University of Southampton

Faculty of Science, Engineering and Mathematics

School of Chemistry

Particle Size and Substrate Effects in Electrocatalysis

by

Jens-Peter Suchsland

Thesis for the degree of Doctor of Philosophy

February 2007

UNIVERSITY OF SOUTHAMPTON

ABSTRACT

FACULTY OF ENGINEERING, SCIENCE AND MATHEMATICS

SCHOOL OF CHEMISTRY

Doctor of Philosophy

PARTICLE SIZE AND SUBSTRATE EFFECTS IN ELECTROCATALYSIS

By Jens-Peter Suchsland

A novel high throughput technique has been developed for the investigation of the influence of supported metal particle size on electrocatalytic activity. This technique was based on a physical vapour deposition (PVD) and has been applied to the synthesis of libraries of supported gold particles on amorphous sub-stoichiometric TiO_x and carbon supports. Array electrodes with a gradation of catalyst particle sizes are fabricated on the different support materials. Simultaneous electrochemical measurements at all electrodes in the array, together with determination of the actual particle size distribution on each of the electrodes by Transmission Electron Microscopy (TEM), then allows rapid determination of the activity as a function of particle size and support.

The TiO_x substrate stoichiometry can be varied or kept constant across a supporting sample, and subsequent deposition of particle sizes on supports are controlled through the nucleation and growth process. TEM measurements indicate nucleation and growth of Au particles takes place, with the smallest particles initially observed with a diameter of 1.4 nm with a maximum density of 5.5×10^{12} cm^{-2} on titania, and 2.6 nm with concomitantly lower density on carbon. Mean gold particle diameter varied in the range 1.4 to 6.6 nm on titania and 2.5 to 7 nm on the carbon support as measured by TEM. The 1.4 nm particles on titania exhibit a binding energy shift in the Au (4f) core level of 0.3 eV from bulk gold, and the shift is ~ 0.1 eV by the time particles grow to a mean size of 2.5 nm. These shifts are associated with final state effects, and the supported gold particles are metallic and appear to be relatively stable in air.

The reduction of oxygen on gold nano-particles supported on the two support materials was studied, as well as on polycrystalline gold, and the conclusions were verified using voltammetry at rotating disc electrodes. At particle sizes below 3 nm, a rapid decay of the catalytic activity for oxygen reduction on both supports was observed.

The electrooxidation of carbon monoxide on titania and carbon supported gold nanoparticles, as well as polycrystalline gold, was studied in acidic media. For the first time evidence for modified properties of metal nanoparticles through support interactions is presented, as well as a particle size effect on the oxide support. Particles supported on carbon were found to behave similarly to polycrystalline gold, while the titania supported nanoparticles showed a decrease in overpotential of almost 200 mV for CO oxidation. The variation of particle size revealed that the maximum enhancement in activity on this oxide support is evident at particles of the diameter of 2.5 to 2.6 nm.

Table of Content

Acknowledgements

The easiest task of this PhD thesis is probably to express my sincere thanks to the people who helped me throughout this time. Firstly I have to start with a thank you to Professor Brian Hayden not only for believing Professor Gregor Hoogers, that I might be able to do a PhD but also for being my supervisor and giving me the great opportunity to work in his laboratory. Special thanks to Professor Derek Pletcher for his supervision, time and advice – I think it is not an overstatement that without him I would have given up. Mike E. Rendall, I have to thank not only for the preparation of many of my samples but also for his high spirits, even when research did not seem to go anywhere. Also I would like to thank my colleagues for making the group a place where it is fun to work and of course for their constant help - Laura J. Williams, Rafael Carmona-Munoz, Duncan Smith, Alexandros Anastasopoulos, Dr Samuel Guerin, Dr Claire Mormiche, Dr Piers Anderson, Dr Christopher Lee and anybody who I might have forgotten. Physical chemistry sometimes feels like learning a trade and without people who are technically skilled to support you it is impossible to get anywhere. Therefore, I would like to thank Alan Glass, Robert Alley and John James for their help. Also I would like to thank Dr Robert Greef and Dr Barbara Cressey for their help with ellipsometry and TEM measurements.

I would like to thank General Motors for the financial support of the project and especially Dr M Frederick Wagner, Dr Hubert Gasteiger and Dr Shyam Kocha for interesting feed back on our progress in the research.

My parents Kurt and Helga Suchsland, I can not thank enough for the support throughout my life.

Christina Grüber I would like to thank for putting up with me during this time when research occupied my brain, reminding me that there are other things worthwhile living for and for her love.

1 Introduction

Generally the aim of a "good" catalyst is to lower the activation energy and/or increase the selectivity [1] for a certain reaction. For the purpose of comparison the characterisation of reactions in heterogeneous catalysis is usually done by quantification of activity. In gas-phase reactions generally the occurrence of a desired reaction per site in terms of the total turnover frequency per unit time (TOF, commonly per second) is used. In Electrocatalysis specific current densities at a fixed overpotential (specific activity) are a common way of quantification. Obviously the highest utilisation from a catalyst is desired, particularly if the catalyst contains precious metals such as platinum or gold. Therefore the highest dispersion in the form of one single monolayer on a support material would suggest itself to be most advantageous. But this does not take into account the observed structure sensitivity of many reactions. This phenomenon was first classified by Boudart [2], who subdivided reactions to be *structure sensitive*, if they depend on the metal dispersion, or *structure insensitive* if they are independent. A structure sensitive reaction could either lead to higher activity with increasing dispersion or deactivation. Insensitive reactions would have the highest mass activity with respect to the metal content if a monolayer could be achieved. A prominent example for structure sensitive reactions in electrocatalysis is probably the deactivation of the oxygen reduction reaction with platinum particle sizes below 3 nm. This has a major impact on the commercialisation of low temperature fuel cells. Particle size effects usually occur when the particle diameter is smaller than ~ 5 nm and therefore the fraction of surface atoms becomes non negligible being ≥ 10 % [2].

One frequently used "particle" only explanation for particle size effects are *geometric effects* such as special geometries of particles having an effect on the activity, such as low coordinated sites, preferential crystallographic orientations with smaller particles and strain in particles changing the bond distance in small particles which has been theoretically suggested to change the binding energies of adsorbates [3]. The latter effect is also regarded as an *electronic effect*. Another electronic effect that was

suggested to influence the catalytic activity at around room temperature is the molecule like behaviour of small particles; the so called "quantum size effect" [4]. Manifestation of this effect is that the valence band was suggested to have discrete energy levels rather than the continuous energy band structures of bulk metals [5], i.e. the density of states close to the Fermi level is believed to decrease and the valence band centre moves towards higher energies[6]. Examples of quantum size effects at gold nanoparticles have been reported for ligand protected gold clusters, titania supported gold particles, as well as for nanometre sized electrodes in electrochemical measurements [4, 7-12]. For gold nanoparticle sizes of smaller ~< 2.5 nm (< 400 atoms) at room temperature the thermal energy (kT~ 0.025eV) is expected to be smaller than the spacing of the energy states near the Fermi energy, which would then lead to a molecule like behaviour [5][1]. Experimentally this effect was for example observed by femtosecond laser pulses [13], scanning tunnelling spectroscopy [4] and electrochemical methods [7-9, 11, 14]. Particle size effects have also been found to depend on the physical properties of the support. Two effects have been observed: *metal support interactions* and *support induced spillover effects* (refer for example to section V. "Particle Size, Support, and Promotional Effects" in [15]). *Strong metal support interactions* have been first reported by Tauster et al [16] for group 8 transition metals supported on titania. The authors [16] used SMSI to explain the observed suppression of chemisorption of hydrogen and carbon monoxide by annealing of the samples. The unexpected high catalytic activity of titania supported gold nanoparticles in gas phase CO oxidation is an example where both strong metal support interactions (charge transfer from gold to titania enhances the stabilisation of an oxygen species on the gold) and support spillover effects (oxygen species is stabilised by the support and reacts at the interface with the CO adsorbed at gold), have both been suggested [17] to be responsible for the surprising catalytic activity of this system (for other explanation refer to chapter 1.3.3).

This thesis describes the application of a combinatorial synthesis and screening method that allowed rapid characterisation of supported gold particles as a function of size

---

[1] "Kubo" criterion describing the spacing of the energy states $\delta(E_F)$ in the vicinity of the Fermi energy E_F for small particles: $\delta(E_F) \approx \dfrac{3}{2} \dfrac{E_F}{N_A z} > kT$, where N_A is the number of metal atoms, k the Boltzman constant, z the valence of the metal (gold =1) and T the temperature.

applied to the electrochemical study of the gold/gold oxide couple, the electrocatalytic reduction of oxygen (ORR) and oxidation of carbon monoxide (CO). In recent years combinatorial approaches have rapidly gained in popularity for optimizing the composition of materials for specific physical or chemical properties in, for example, electrocatalysts or battery materials [18-23]. Recently, a physical vapour deposition system has been developed for the high throughput synthesis of thin film materials [24]. It employs source shutters to achieve controlled gradients of depositing elements across a substrate or an array of pads [24]. This allows, for example, the synthesis of a compositional library of alloys [25] and particle centres supported on homogeneous supports. The system has been applied to the optimization of Pd/Pt/Au [25]. This thesis combines characterisation of arrays of electrodes and compares results with single electrode measurements on rotating disc electrodes to confirm the validity of the results.

Titanium dioxide was chosen for the investigation as support material because of its high conductivity in the sub-stoichiometric or doped forms, its stability in acidic environments and recent studies that showed support induced interactions, which positively influenced the catalytic activity of gas phase CO oxidation on gold nanoparticles.

The following introduction aims to give an overview of the relevant literature. As the reactions studied (ORR and CO oxidation) are relevant to fuel cell application a brief description of the low temperature fuel cell is given. In fuel cells currently carbon supported platinum and platinum alloy nanoparticles are the state of the art catalysts and hence are intensively studied. Some of the recent findings of CO oxidation and ORR on platinum are summarised below as some general concepts of these system will be used in the discussion of the results presented on gold nanoparticles.

1.1 The Polymer Electrolyte Fuel Cell

The operating principle of a fuel cell has been known for nearly two centuries, since the work in 1839 by Sir William Robert Grove. Nevertheless, the first usage of this "cold burning" process of oxygen with hydrogen was made for the outer space missions Apollo and Gemini, in the mid-sixties. Nowadays, fuel cells are experiencing a renaissance due to the high efficiencies compared with internal combustion engines on a

small scale (up to the low MW range). There are a variety of different fuel cell types, which are commonly characterised by their electrolyte, such as: Molten Carbonate, Phosphoric Acid and Alkaline Fuel Cells.

The most promising fuel cell types in terms of commercial potential appear to be the Polymer Electrolyte Membrane Fuel Cell, PEMFC (and its sub form the Direct Methanol Fuel Cell DMFC), Molten Carbonate Fuel cells MCFC and Solid Oxide Fuel Cell, SOFC. Other types of fuel cell have been tested but constraints such as the necessity of very clean fuel gases are a barrier to their application (e.g. the PAFC and AFC require a high purity of hydrogen).

Higher operating temperatures of PAFC's (~200 °C), MCFC's (~650 °C) and SOFC's (~1000 °C) allow their use as combined heat and power units in the power range of low kilo watts to mega watts. The MCFC and SOFC reveal electrical efficiencies greater than 50 % and phosphoric acid fuel cells 40 % [26]. A major advantage of the first two fuel cells is the variability of fuels: hydrogen, CO, methane and other hydrocarbons. Automotive companies (e.g. General Motors, Ford, Toyota, Daimler Benz etc.) are now concentrating on the polymer electrolyte fuel cell. This is mainly because of the low operating temperatures, relatively good "cold start" behaviour combined with a high power/volume ratio.

Figure 1.1 presents a simplified diagram of a Polymer Electrolyte Fuel Cell (PEMFC). The main parts of these devices are the bipolar plates for the gas distribution across the active area of the fuel cell, the membrane electrode assembly (MEA), composed of two gas diffusion layers, a polymer membrane and two catalyst layers. The extension views in the same diagram visualising the "heart" of the fuel cell in greater detail. The gas diffusion layers are normally carbon fibre papers, responsible for distributing the fuel gases homogeneously to the catalyst layer, heat removal from the electrodes and conductor carrying away the electrons formed by the catalyst layer, necessitate a high porosity, heat and electrical conductance. The catalyst layers consist commonly of platinum highly dispersed on a high surface area conducting support material, which is soaked in an ion conducting polymer. Widely used as support material is carbon black such as Vulcan XC 72. Recently metal oxide supported fuel cell catalyst seem to gain some attention as some studies claim enhancements such as CO and methanol tolerance

4

of the supported metal oxide catalyst for both anode (hydrogen oxidation) and cathode (oxygen reduction) reactions over carbon supported catalysts [27-34]. The membrane is a polymer with incorporated ionic groups enabling proton transport from anodic side to the cathode. In a hydrogen/oxygen powered fuel cell at the anode the oxidation of hydrogen would take place and at the cathode the reduction of oxygen to water.

One of the drawbacks of the PEMFC are the high initial costs caused by the high loading of precious metal catalysts required due to the low temperature range. While on the anode (hydrogen or methanol) side contamination from fuels or by-products in the reaction pathway is the major problem, the cathode (oxygen electrode) has to deal with large overpotentials caused by small exchange current density in the low temperature range for oxygen.
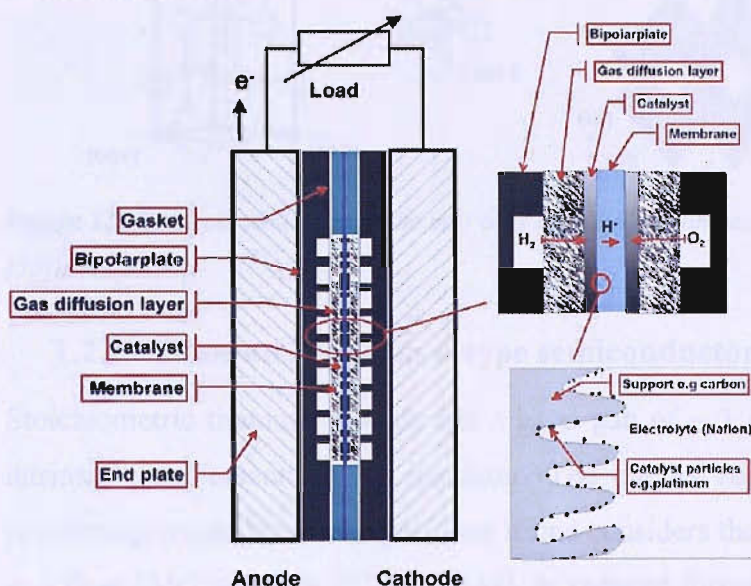
Figure 1.1. *Schematic diagram of a Polymer Electrolyte Fuel Cell (PEMFC).*

1.2 Titanium oxide

1.2.1 Titanium oxide structure

Titania has several crystal structures but the most common ones are rutile, anatase and brookhite [35]. The most widely studied structures are rutile and anatase [35, 36] and the crystal phases are shown in Figure 1.2. "Both crystal structures are tetragonal with each Ti atom octahedrally coordinated to six O atoms, and each O atom coordinated to three Ti atoms. In both structures, TiO_6 octahedra are slightly distorted, but the distortion is larger for anatase than that for rutile. In rutile, four Ti-O bonds of 1.949 Å

and two Ti-O bonds of 1.980 Å are present. For anatase these values are 1.937 and 1.965 Å respectively. Bond angles of O-Ti-O are 81.2° and 90.0° in rutile, whereas for anatase they are 77.7° and 92.6°, respectively [37]."
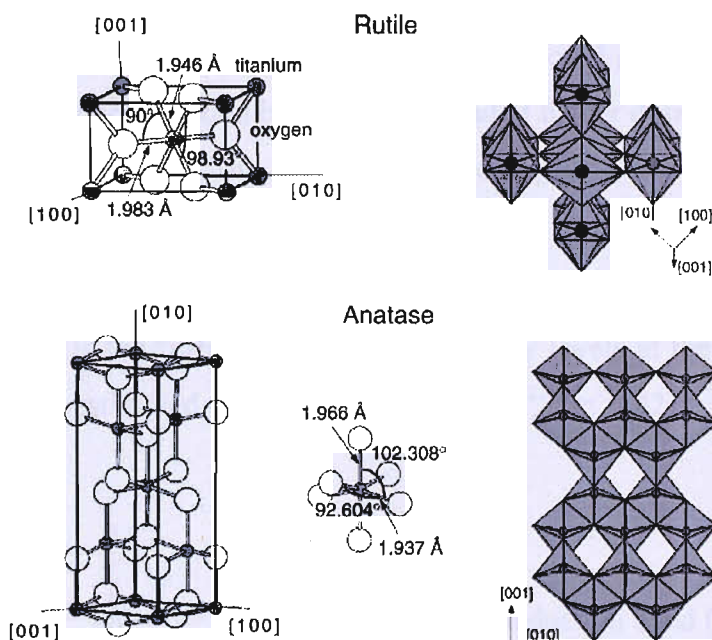
Figure 1.2. *The bulk structures of the unit cells of rutile and anatase titanium dioxide (figure taken from [35]).*

1.2.2 Titanium oxide an n-type semiconductor

Stoichiometric titanium dioxide has a band gab of ~ 3 eV [38] and is therefore in its intrinsic form essentially an insulator. The energy required to make it electrically conducting would be quite significant if one considers that the thermal energy (given by as kT) at 25°C is only 0.0257 eV [39]. In reduced forms of titanium oxide a variety of defects can be formed. Common defects in crystals are oxygen vacancies (doubly charged - oxygen sublattice), titanium interstitials or vacancies (cation sublattice [40]) where Ti is in the oxidation state 3^+ and 4^+ and planar defects like crystallographic shear planes (CSPs) [35]. For the defect equilibria more details are available for example in Bak et al [40]. Which defect form is dominant depends on preparation method and oxygen defect density (stoichiometry) [35]. As a simplification, additional electrons in thereduced form can be imagined to occupy energy states in the band gap region close to the conduction band and act as electron donor levels, n_c (Figure 1.3, n-type SC). The energy position of the conduction band edge E_C for TiO_2 was estimated to be - 4.21 eV and the valence band edge respectively -7.21 eV [41].

Assuming that one oxygen deficient site would contribute one electron n_C to the donor levels, then for a sub-stoichiometric $TiO_{1.95}$ (approximate density ~4 g cm^{-3} for TiO_2 assumed for the calculation), the doping level would contribute charge carriers in the order of ~2.5 x 10^{21} cm^{-3} and for $TiO_{1.9999}$ ~5 x 10^{18} cm^{-3}. For doping levels of 10^{18} to 10^{19} cm^{-3} the position of the Fermi level E_F would shift to a position within less than 0.1 eV of the conduction band edge E_C, and at higher doping levels the system becomes a "quasi-metal" [39]. This can be expressed as [42]:

$$E_F = E_C + kT \ln \frac{n_C}{N_C}$$

(1.1)

Where N_C is the "effective" density of energy levels at the conduction band edge [39] and can be estimated to be on the order of ~10^{21} cm^{-3} [42].
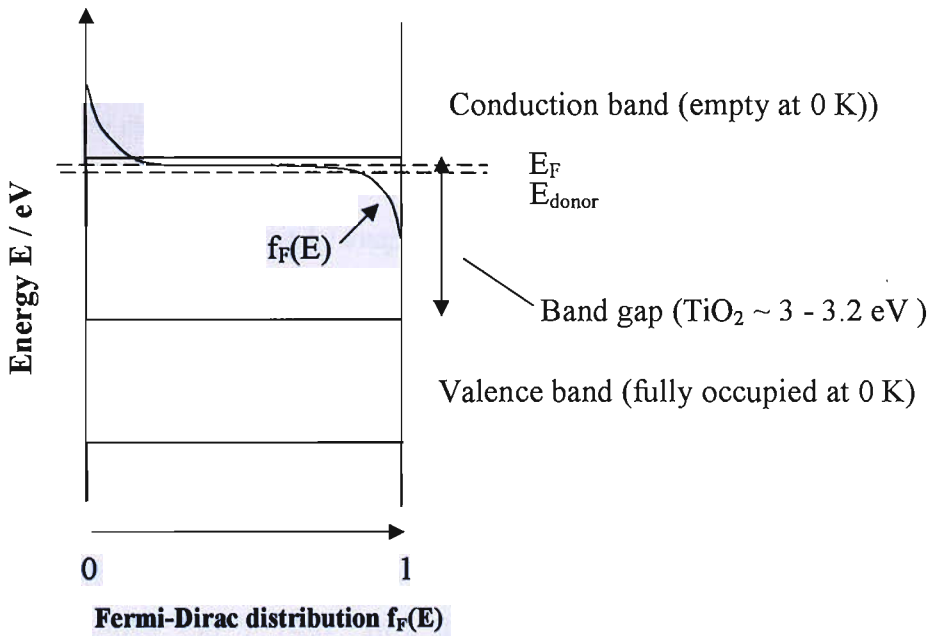
Figure 1.3. *Band scheme of an n-type semiconductor (e.g. sub-stoichiometric titanium dioxide). E_{donor} = electron donor level introduced into material, fF(E) the Fermi-Dirac distribution giving the probability of electrons to occupy an energy state and E_F = Fermi energy (adapted from [43]).*

Titania is an oxide which is easily reducible due to the variety of stable phases available. These are shown in the phase diagram in Figure 1.4 [35]. The phases at O/Ti ratios above Ti_2O_3 to TiO_2 are known as Magneli phases with a structure Ti_nO_{2n-1}. Stoichiometric and hence intrinsic titania is essentially a non-conductor as pointed out before due to the wide band gab of ~ 3 eV, with a resistivity at 300 K in the order of ~

7

10^7 Ω cm (perpendicular to the c-axis of rutile) [44]. In the reduced form the resistivity drops significantly and for example the Magneli phase titania exhibits resisitivities of the order 10^{-1} to 10^{-3} Ω cm [45], and, are therefore, ideal to act as catalyst supports, where high conductivity is required.
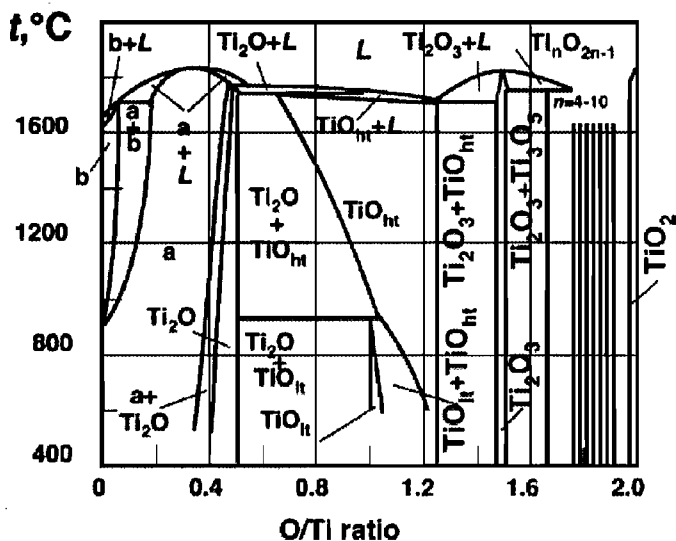
Figure 1.4. *"Phase diagram of the Ti-O system", where a and b are different titanium phases, L – liquid, ht- high temperature and lt-low temperature [35].*

Titanium dioxide: preparation by evaporation techniques

Thin film titanium dioxide has been prepared by several different techniques as for example: plasma enhanced chemical vapour deposition [46], R.F sputtering, magnetron sputtering [47, 48], and physical vapour deposition (PVD) [49]. Generally thin film formation by evaporation of titanium oxide onto room temperature substrates leads to amorphous materials with only a small quantity of anatase and rutile structures [49, 50] and crystallinity is only achieved if annealed or the temperature is raised to temperatures above 350 °C [49]. In a study by Mikhelashvili and Einstein [50] they showed a significant dependence of the flat band voltages with annealing temperature (negative shift by 0.6 V for a 25 nm film and 0.8 V at a 15 nm film).

1.2.3 The Titanium oxide/electrolyte junction

The position of the band edges and therefore band gap is crucial for semiconductor (SC) electrodes and will significantly influence their expected electrochemistry. The energy band edges and Fermi levels E_F of materials are in material science generally quoted against Fermi energy scale or also called the Vacuum scale (Figure 1.5 a) [39]. The

comparison to the electrochemistry energy scale is useful as the redox processes are generally expressed for example against a standard hydrogen electrode in Volts. Therefore the Fermi level for redox couples is defined as the reversible redox potential and the energies of the oxidised and reduced forms are defined as the lowest unoccupied and highest occupied energy states (assuming that the energy states are symmetrically distributed positive and negative to the redox potential)[41]. Following this definition the potential of the standard hydrogen electrode (by definition 0 V in electrochemistry) can be estimated to be close to -4.5 eV vs. the absolute vacuum scale (Figure 1.5 a)[43]. If SC electrodes in electrolyte are biased by a potential for example during the electrochemical experiments the position of the flat band potential is an important parameter, as it determines the ability of electrons to transfer across the interface. The flat band potential is the potential as presented in Figure 1.5 (c), where no charge accumulation (d) or depletion (b) at the SC/electrolyte junction occurs.
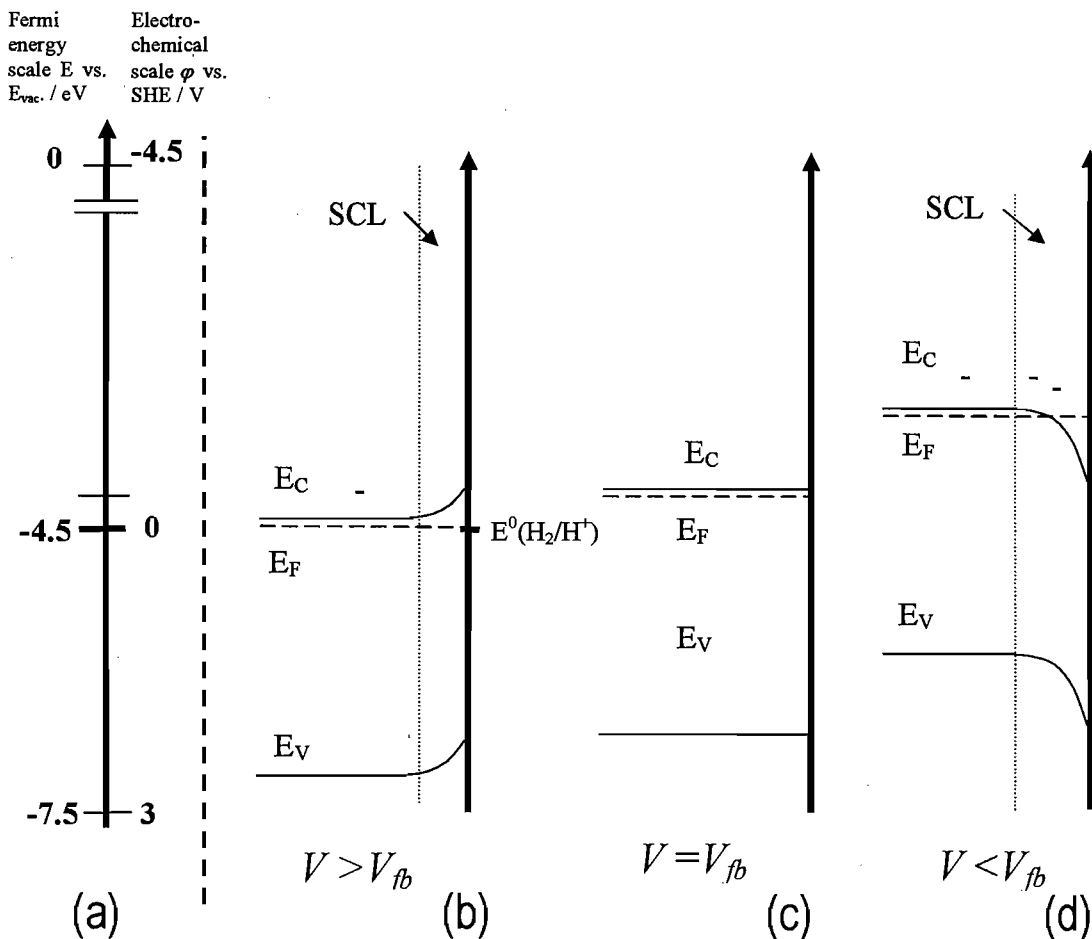
Figure 1.5. *Semiconductor (n-type)/electrolyte boundary (here for a H_2/H^+ couple at a substoichiometric titania surface). (a) Fermi energy scale and electrochemical energy scale. (b) n-type Semiconductor (SC) with a band gap of 3 eV in contact with an electrolyte at positive bias potential to the flat band potential(V_{fb}). The Electrolyte is on the right to the arrow indicating the boundary. In the figure only the band edges of conduction (E_C) and the valence band (E_V), as well as the Fermi energy (E_F) are shown. (c) n-type SC at a potential equal to V_{fb} and (d) n-type SC at a potential negative to V_{fb} (adapted from [39]).*

For titania electrodes a direct correlation of the potential with conductivity (electron transfer ability) was shown [51]. The conductivity drops significantly as expected by several orders of magnitude (Figure 1.5 (b)) positive (SHE scale) of the flat band potential. The flat band potential V_{fl} at the point of zero charge pcz, where the drop across the Helmholtz layer ΔV_H is zero (equal amounts of H and OH on the surface[52]) can be experimentally determined for example using electrochemical impedance spectroscopy by the Mott Schottky analysis [53]. The V_{fl} can be related to the conduction band edge by [39]:

$$V_C = V_{fl} - \frac{(E_C - E_F)}{q}$$ (1.2)

With the E_F being dependent on the doping level according to equation 1.1 [39, 52]. Here V_C is the conduction band edge and q the electron charge. At pH different to the pzc a Nernstian change of the flat band potential with hydronium ion/hydroxide concentration was observed [39]. As the hydroxide and hydronium ion concentration adsorbed at the surface will cause the flat band potential to deviate from the equilibrium at the pzc [39]:

$$V_{fl} = V_{fl(pzc)} - \underbrace{\left(\frac{2.3RT}{F}\right)}_{0.059V \text{ at } 298K}\left(pH - pH_{(pzc)}\right)$$ (1.3)

The conduction band edge of titanium dioxide (as calculated from the electronegativities of titanium and oxygen) was reported to be approximately -4.16 eV and the flat band potential -4.21 at pH_{pzc} (pH ~ 5.8)[41]. It should be noted that the reported flat band potential varies considerably by almost ± 0.25 eV dependent on the reference [36]. In this thesis acid with a hydronium concentration of 0.5 Mol was used which would lead to a flat band potential for crystalline titania using equation 1.3 of approximately -0.015 V.

The electrochemistry will also depend on the crystallinity, doping level and surface states [39, 52, 54]. The crystallographic orientation of anodically grown titanium oxide films has been found to influence the band gap (measured by photoelectrochemistry), where less crystalline, thinner passive films have a wider band gap and amorphous thin films have no direct band gap [55]. The same author proposed that amorphous titania has localised energy states in the band gap region [54] (Figure 1.6 (b)). Surface states (e.g. oxygen vacancies or titanium interstitials) are also known to influence the electrochemistry of titanium dioxide significantly by accessible energy states in the band gap region [39, 52] (Figure 1.6 (c)).
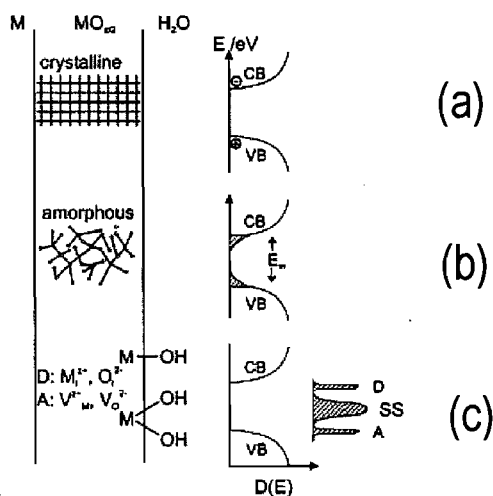
Figure 1.6. *Electronic structures and energy states in metal oxide films (taken from [56]). Band structure in the case of (a) crystalline materials, (b) for amourphous materials and (c) for materials with surface states.*

1.3 Nano-dispersed metal catalysts

1.3.1 Non supported particles

1.3.1.1 The thermodynamically stable form of nanoparticles: Historic view

Particle morphology has been the subject of interest over the last three decades, mainly due to the development of more sensitive surface analytical tools and has been widely theoretically and experimentally studied (reviews [57-59] and references therein). The shape of particles depends strongly on the method of preparation. The rate of deposition, the particle size [2, 60], and the temperature of annealing. Also the interaction with the underlying support materials was shown to strongly influence particle shape and truncation [6, 60, 61]. A few examples of the polyhedra commonly proposed for faceted particles are presented in Figure 1.7 [2]. The coordination number i for atoms at different coordinative environments are presented in Figure 1.7. The particles exhibit mainly two low index planes, (111) with the coordination of the gold atom being 9 and (100) i = 8. Edges and corners are lower coordinated between 3 and 7 depending on the particle shape as well as on the phase boundary. In terms of the

energetics of these idealised shapes total Gibbs free energy G^{total} [2] calculations showed that the lowest and therefore most stable construction would be the truncated octahedron (G^{total} : truncated octahedron < octahedron << cube, valid for particles greater than ~3 nm in diameter) [62].

In this first sub-section a thermodynamically stable particle construction in equilibrium with the surrounded gas phase at low temperatures was assumed. This was characterised as early as 1901 when Wulff described particle shapes in terms of the surface free energies and is consequently known as the "Wulff-construction"[63]. The equilibrium shape for face centred cubic (fcc) metals was concluded to be "... an octahedron with (1,1,1) external facets, which is truncated by a cube having (100) facets and centred on the octahedron and possibly further truncated by a second cube with (100) boundaries"[64] (c.f. Figure 1.7 (d) presents one possible configuration). The surface truncation depends on the ratios of the surface tensions of the low index faces. The optimal shape after Wulff would than fulfil:

$$\frac{\gamma_{(100)}}{\gamma_{(111)}} = \frac{h_{(100)}}{h_{(111)}} \qquad (1.4)$$

where the surface energies γ are given for the low index planes (100) and (111) and h represents the distance of the planes from the centre of the particle for (100) and (111) respectively [57].

Thus particles would preferentially form truncated octahedrons with the truncation depending on their number of atoms and the surface energies of the crystal planes.

---

[2] Calculation of the Gibbs free energy G for gold particles greater 3 nm ignoring edge and corner influences:

$$G^{Total} = G^{bulk} + G^{surface}$$

Where the single terms of the free energy G are sums of the free energy contributions of the bulk and surface respectively [62].
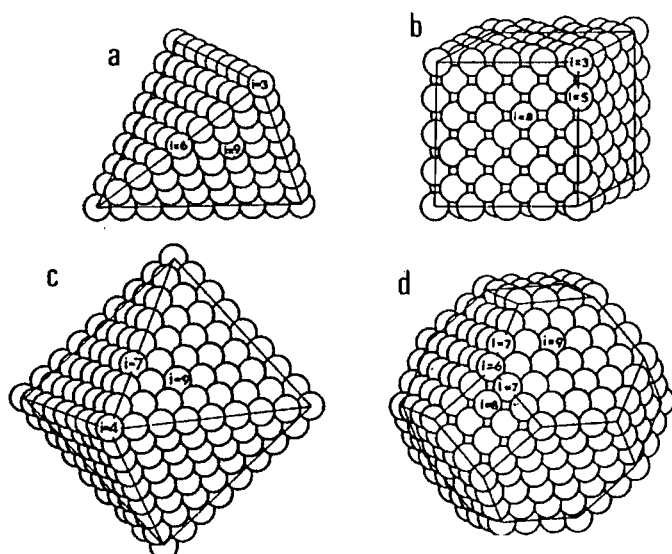
Figure 1.7. *Selected polyhedrons for fcc metals, (a) tetrahedron, (b) cube, (c) octahedron (d) truncated-octahedron, i quote the coordination number of the atoms at different position at the particle surface. Figure taken from [2].*

The statistics of uninfluenced (or supported on non interacting ("inert") supports) particles in polyhedral constructions were calculated by Van Hardeveld and Hartog [65]. In the following Figure 1.8 the relative frequencies of the different phases of a gold "fcc cubo-octahedron" (sic!) [65] as presented in Figure 1.7 (d). As can be seen, the accumulated frequency of edge and corner sites significantly increases when the particle diameter gets smaller ~3.5 nm. At this particle size already ~ 27 % of the surface atoms are at corners or edges and as the diameter further decreases this proportion increases. Another way of looking at this is the average coordination number. For the surface atoms at a particle size of around 3.5 nm, an average coordination number of 8.29 can be calculated which is not significantly different from the 8.63 at particle sizes of ~10 nm. The average surface atom coordination number decreases then rapidly down to 6.75 for particles around 1 nm. Another interesting observation is the relative ratio (100) to (111) low index planes. For particles over 5 nm in size 20 - 23 % of the planes are (100). Below 5 nm this number decreases down to 10 % at ~ 1.8 nm and 0 % at ~1 nm.

A series of closed shell particles of this fcc truncated-octahedron would contain 38, 201, 586, etc. atoms respectively. Any particle that does not reach the close shell "formation" might as consequence form thermodynamically favourable not perfectly truncated-octahedral constructions.
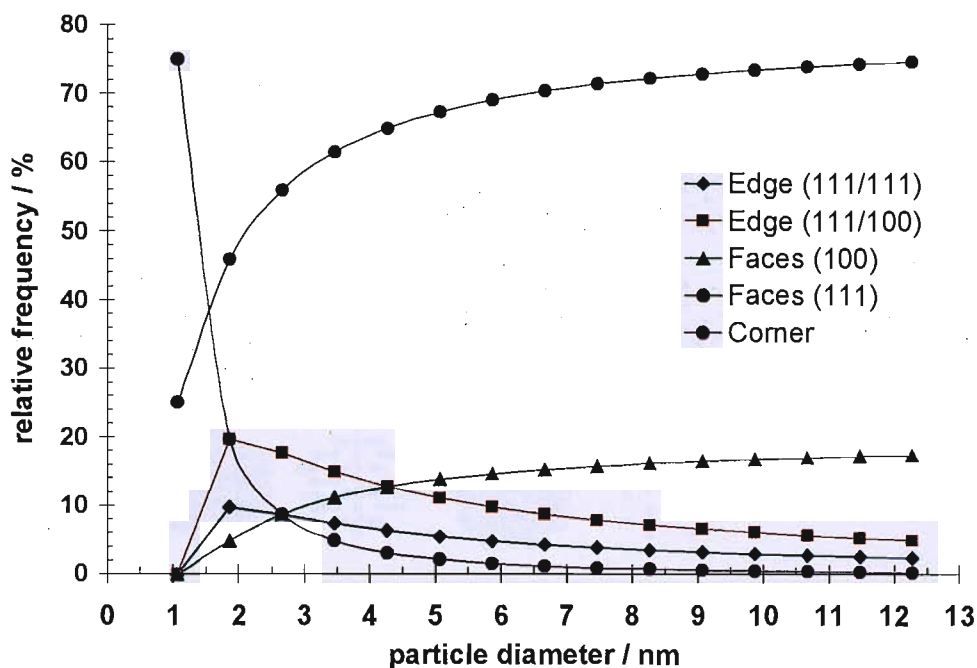
Figure 1.8. *Presentation of the relative frequency of appearance of phases in an fcc truncated octahedron (previous figure (d)) particle. The edges are distinguished by the boundary of the low index planes they are separating (111/111 or 111/100). Calculated after [65], with a constant gold bond length of 0.288 nm. The points on the graphs indicate closed shell configurations.*

1.3.1.2 Nanoparticle morphology: "non crystalline structures"

For small particles, as seen before the surface to volume ratio is high, therefore the energy of corners and edges is likely not to be negligible. Hoare and Pal concluded from their potential energy and thermodynamic calculations that clusters with less than 50 atoms are not likely to exist in their crystalline fcc structure [66]. Non fcc crystalline structures were suggested to be icosahedral and decahedral constructions [58] and were frequently experimentally observed in supported particles [59]. Under non crystalline constructions fivefold rotational axes orientations of atoms are understood, which could not exist in bulk material and the atomic distances are commonly strained [57]. Some of the most common examples of icosahedral and decahedral constructions are shown in Figure 1.9. They show closed packed structures with only (111) like low index planes (if not truncated as in figure 2.3 (b) and (c)) exposed at the surface. Truncated decahedrons expose at the cutting planes (100) like faces. The mentioned strained bonds were quantified for a regular decahedron (Figure 1.9 (a) and (e)) after Ino´s model by Koga and Sugawara [67]. They found the gold bond length along the fivefold axis to be

15

+0.527% elongated, distances normal to the axis are strained by + 1.09% and all other interatomic distances are contracted by - 0.396%.
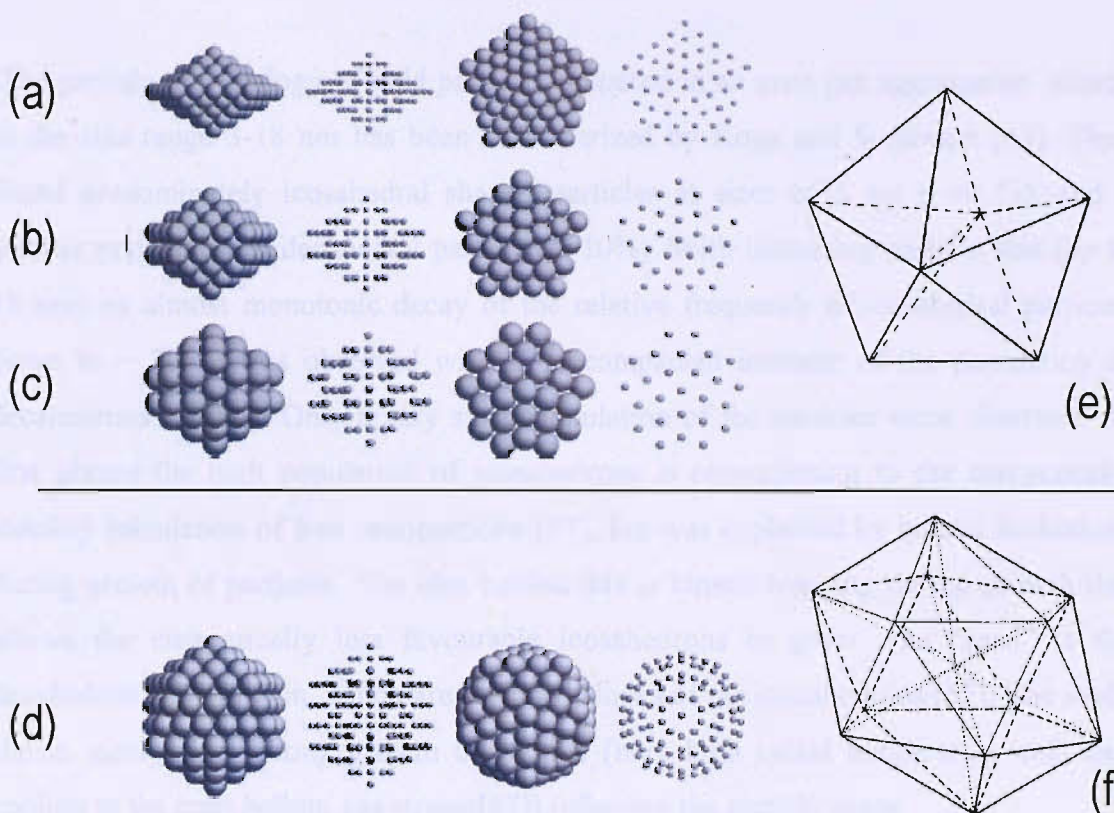
Figure 1.9. *Multiple twined non crystalline particle structures. Decahedrons: (a and e) regular, (b) Ino truncated and (c) Marks truncated decahedron. (d) Mackay Icosahedron (f) "icosahedron, made up of 20 tetrahedral units meeting in a common point at the centre"[68]. Figures (a) to (d) taken from [57]. (e) and (f) taken from [68].*

For "free" nanoparticles [3] theoretical studies suggested the transition from non - to crystalline structures to be *energetically* favoured at around 500 gold atoms (this transition size would be approx. 2.5nm) [69, 70]. The structure for smaller clusters (< 500) was suggested to be a Marks decahedra as shown in Figure 1.9. It must be pointed out that in these theoretical studies particles were "free" (non support influenced). Another conclusion of their calculations was that icosahedral constructions are only possible in the case of clusters smaller 100 atoms of gold (generally not favoured)[57]. Generally very small clusters are assumed to be the most stable as icosahedrons, with a transition to decahedral clusters for the mid range (a few hundred

[3] Free nanoparticles: Particles are experimentally formed without interaction with support materials (e.g. inert gas aggregation sources).

atoms) and then a further transient to truncated octahedrons (as mentioned above 500 atoms for gold).

The particle morphology of gold particles prepared in an inert gas aggregation source in the size range 3-18 nm has been characterized by Koga and Sugawara [67]. They found predominately icosahedral shaped particles at sizes of 3 nm (~90 %), and a smaller population of decahedral particles (~10%). With increasing particle size (up to 18 nm) an almost monotonic decay of the relative frequency of icosahedral particles down to ~ 70 % was observed with an accompanied increase of the population of decahedrons (~30%). Only a very small population of fcc particles were observed. At first glance the high population of icosahedrons is contradicting to the energetically stability calculation of free nanoparticles [57], but was explained by kinetic limitations during growth of particles. The idea behind this is kinetic trapping during growth that allows the energetically less favourable icosahedrons to grow. The "seed" is the decahedron construction, which are building blocks of the icosahedrons [57]. The study shows nicely how strong growth conditions (here high initial temperature and then cooling in the inert helium gas stream[67]) influence the particle shape.

The excess energy differences for the non crystalline and fcc structures are very small [69, 70] making it probable, that under supersaturation (non equilibrated) conditions as present in vapour deposition several constructions are likely to coexist [58]. Experimentally an interesting effect was observed during HRTEM that showed that "gold particles of ~2 nm fluctuating between the cubo-octahedral, icosahedral, and single twined structure" [58]. Two theories arose trying to explain the observed effect. One proposed melting of the particle by energy supplied from inelastic scattering of electrons during microscopy, and subsequent re-crystallisation of the particle. The second theory tried to explain the transition by low energy barriers to convert between local energy minima for different crystal orientations [58].

Some other aspects of nanoparticles
The melting point of gold particles was shown by Buffat and Borel to be a strong function of particle size [71]. At a particle size of ~ 2 to 3 nm they reported a melting point as low as ~300 to 600 K (dependent on model applied and experimental data incorporated in analysis). To the best of my knowledge neither possible influences of

the gold particle/electrolyte interface have been reported, nor the influence of adsorbed species. Structural changes on single crystal surfaces have been reported for gas phase adsorption of species on metals by Somorjai [72] and therefore the suggestion, that from the electrolyte adsorbed species in hte liquid phase might influence metal particle structures seems to be reasonable. In the case that bonding occurs at the surface leading to ionic forms of atoms at the metal atoms the surface change of the radii of the ionic atoms are to be expected (e.g. Au(0) d ~0.288 nm, Au(I) 6 coordinated, ~0.274 nm, and Au((III) 6 coordinated, 0.17 nm [73]), which are also likely to influence the shape.

1.3.2 Supported nanoparticles

The previous discussion of particles did not account for the behaviour of particles which are interacting with a support. If particles would have an isotropic energy distribution they should behave similar to liquids on a surface and consequently could be described by the Young Dupre equation [74]:

$$\cos\theta = \frac{\gamma_{SV} - \gamma_{SL}}{\gamma_{LV}} \tag{1.5}$$

The contact angle θ, as shown in Figure 1.10 (a) is a unique property of an interface of two materials and is described by the angle between the surface and the tangent of the curvature of the drop at the interface. The contact angle therefore is a function of the ratios of surface tensions γ (or energies) of the difference of the support to vapour (surface energy of the support) SV tension and the support/liquid SL (surface particle interaction) to the free liquid/vapour interface LV (surface energy of the particle). This approximation does not adequately describe thermodynamically equilibrated particles (e.g. crystalline particles) as it neglects the surface anisotropic energies due to low index planes and the surface angle does not represent the relative interfacial energies. Therefore as discussed for "free particles" a Wulff like construction was adapted to account for interfacial energies with the support, as presented in Figure 1.10 (b) - the so called Gibbs-Wulff construction. The ratio of the length (vectors) from the centre h to the surface and surface energies γ of the low index planes is a constant (equation 1.4). The particles "sink" into the substrate by Δh. The truncation is therefore dependent on the adhesion energy E_{ad} and the surface plane energies. The interfacial energies can then be expressed as [60, 74]:

$$E_{ad} = \gamma_s^o + \gamma_s^m - \gamma_s^{mo} \tag{1.6}$$

and

$$\frac{\Delta h}{h} = \frac{E_{ad}}{\gamma_s^m} \tag{1.7}$$

Where the superscripts are: oxide O, metal M and metal oxide MO. If adhesion energy would be twice or more than the metal energy, the metal would fully wet the substrate (oxide). This 2D growth mode [75] is often referred to as Frank van der Merwe mode. Weak adhesion energy $(\Delta h \geq 0)$ crystalline particles would be formed without truncation. Individual particle growth in 3D (also with truncation) is also called Volmer-Weber growth [75].
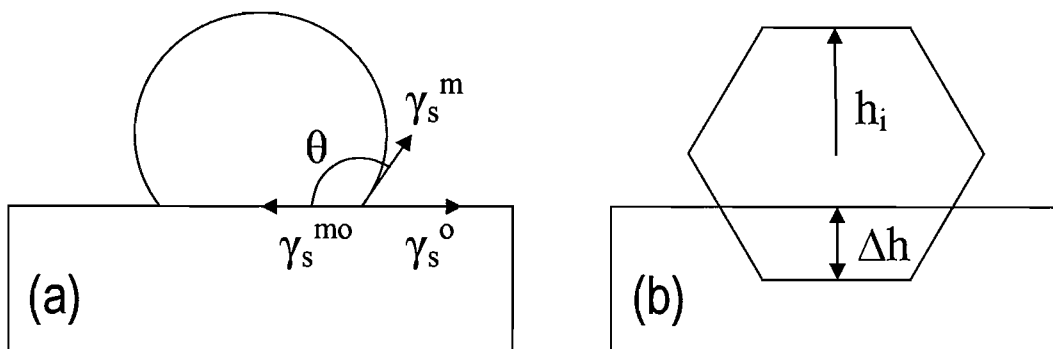
Figure 1.10. *Truncation of particles at the support particle boundary (Reproduced after [60]). (a) Isotropic surface energy as present in liquids (b) anisotropic surface energy distribution, hence Gibbs-Wulff constructed particle interface interplay.*

The interaction of gold with the supports under investigation in this report: carbon (graphite [76-78]) and titania [75, 79, 80] is generally considered to be weak. The interaction of gold with defect free stoichiometric [81] and non-stoichiometric titanium dioxide (rutile) was calculated by several groups [82-85]. The calculations showed that only at very low coverages of gold at stoichiometric TiO_2 considerable binding energies are observed [81, 86] but get weakened by addition of more metal. In reduced titania oxygen vacancy sites have been shown to have larger adsorption energies compared to the defect free surfaces and have been therefore considered to be the main nucleation sites during the growth of gold particles [82-85] this has been directly shown by STM measurements [84, 87]. UHV nucleation and growth studies [75, 80, 88] agree well with the theoretical studies. At very low coverages monolayer growth of gold on titania is observed (higher binding energies) up to a critical temperature and defect density dependent thickness (e.g. the critical coverage for an annealed titania crystal at 293 K is

19

0.15 monolayers of gold [80] and at less defected surfaces 0.093 monolayers) in the low sub-monolayer coverage with subsequent Volmer-Weber 3D growth [75, 80]. The truncation of gold particles on titania was experimentally found to be high; from particles that are initially only one to two atomic layers thick at low coverages with a particle diameter of 0.6 – 2 nm, to hemispherical at particle diameters of 2.5 - 4 nm and finally increasingly spherical at particle diameters above 4 nm [60, 89]. The truncation was also shown to be dependent on the density of surface defect and oxygen vacancies [85].

Nucleation and growth of metal deposited on different support materials have been widely studied. Reference [6, 61, 90, 91] review the literature of transition metal to oxides interfaces. Briefly the main routes of the metal arriving at the surface are presented in Figure 1.11 [61]. Atoms reaching the metal oxide surface have to adsorb or they could, if not thermally accommodated, elastically scatter, which has not yet been observed. The atoms either condense at the surface or could (usually observed at higher temperatures) re-evaporate (desorption). The atoms will subsequently diffuse across the surface until they either reach a surface defect, where they nucleate (heterogeneous) or if no defect is reached within the travelling distance but another atom (homogenous) they could nucleate by aggregation. A critical number of atoms have to be reached to form a stable cluster. Homogenously formed clusters which have not reached the critical size can "redissolve" (atoms in the cluster can be separated) [61]. The number density of particles on the surface is determined for homogenous nucleation by the diffusion coefficient (temperature dependent) across the substrate and the deposition rate. In the case of predominantly heterogeneous nucleation the number density should be independent of deposition rate and diffusion coefficient [61].

After saturation additional surface diffusing atoms will be captured by clusters and particle growth is observed which will eventually coalesce. The growth mode (interfacial energies of the metal and oxide) will now determine the further growth.
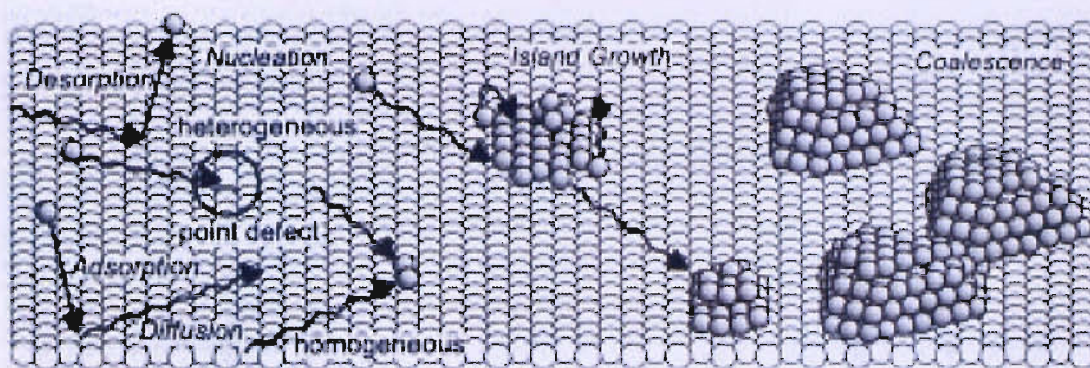
Figure 1.11. *Metal deposition: mechanisms. Figure taken from [61].*

1.3.2.1 The Metal semiconductor boundary - Schottky barrier

Semiconductor/metal boundaries similarly seek to equilibrate their chemical potentials (Fermi energy). In Figure 1.12 a scheme of the band structure of an n-type semiconductor and a thick layer of metal (a) before and (b) after they have been brought to contact is shown. The Fermi energies of both materials are different, and after contact they equilibrate. A depletion layer on the semiconductor will be formed (a similar effect can occur on the metal side but is very small). The driving force is the work function of the metal, which is greater than the electron affinity of the SC [92]. The energy difference of the ("bending") conduction band of the semiconductor to the Fermi energy is called a Schottky barrier. It must be noted that the thickness of the depletion layer (as well as the Schottky barrier) is strongly dependent on the doping level (replacement of the electrons). For high doping levels the thickness would decrease significantly [93].

The Schottky model assumes that the metal energy bands are continuous. The work function of gold measured by different groups was summarised by Trasatti in 1971 [94] and is approximately 4.68 ± 0.12 eV , which would imply that a Schottky barrier of 0.47 eV would be formed with a thick metal layer. In contrast for thin gold films (10-50 nm) on titania a Schottky barrier of 0.9 V (eV) was reported by McFarland and Tang [95]. Kiyonaga et al [96] quote a work function for gold of 5.4 eV significantly different from the one reported by Trasatti [94].

Before contact   **After contact**

semiconductor   metal   semiconductor   metal

E_C

$E_{F,SC}$

$E_{F,M}$

E_C

E_F

Schottky Barrier

E_V

(a)

E_V

Depletion layer   (b)
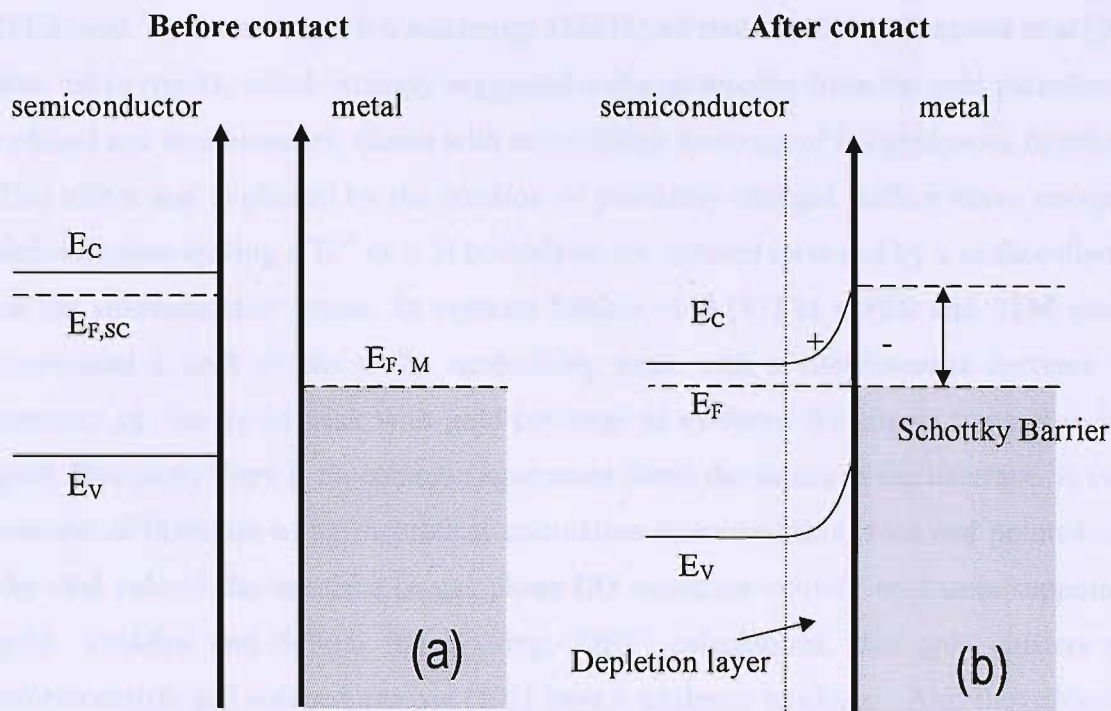
Figure 1.12. *Metal- Semiconductor (n-type) barrier: Schottky barrier. (a) before contact of the metal and semiconductor and (b) after. (adapted from [93])*

For small gold particles coulomb blockage phenomena are reported [9, 11, 97], indicating, that small gold particles do not have continuous energy states that are accessible for electrons, but rather discrete "molecule like" quantizised energy levels, which suggest that the energetics of the barrier should also change. Also electrons transferred to small particles of a metal will probably have quite a significant influence on the Fermi level, as the electron density can be considered to be a finite entity to the entire number of electrons available, while at thicker films the number of electrons will be high compared to the transferred electrons. Indeed Kamat et al [42, 98] reported for UV irradiated titania nanoparticles supported gold nanoparticles a particle size dependence of the apparent Fermi level as characterised by a redox reaction (using C_{60}/C_{60}^-). The biggest effect was observed for the smallest nanoparticles (3 nm) under investigation [42, 98] with a shift of -0.06 V (eV) negative with respect to the apparent Fermi level of pure titania, indicating an electron transfer from the gold to the titania with UV irradiation, while particles of 8 nm only exhibited an apparent Fermi level shift of -0.02 V.

Studies under UHV conditions using synchrotron-radiation light for photo-emission (PES) and medium energy ion scattering (MEIS) on rutile (110) by Okazawa et al [99] also led to results, which strongly suggested a charge transfer from the gold particles to reduced and stoichiometric titania with concomitant lowering of the gold work function. This effect was explained by the creation of positively charged surface states (oxygen deficient sites leaving a Ti^{x+} ($x \leq 3$) behind) on the reduced form and by a surface dipole on the stoichiometric titania. In contrast Minato et al [87] in a PES and STM study interpreted a shift of the O 2p nonbonding peak with a simultaneous decrease in intensity of the Ti 3d peak with gold coverage as evidence for charge transfer to the gold. Obviously there is no common agreement about the nature of the interface. A vast amount of literature using theoretical calculation addressed this issue and pointed out the vital role of the interface to gas phase CO oxidation activity on titania supported gold. Vittadini and Selloni found using "DFT" calculations, that gold clusters on stoichiometric and reduced anatase (101) have a tendency to cluster. Also they showed that the interaction of CO with positively charged gold clusters is stronger than on negatively charged ones [100]. Lopez and Nørskov discuss their DFT results on the Au/TiO$_2$(110) interface in terms of a partial charge transfer from the gold to the titania[81]. Liu et al [101] showed by DFT that positively charged titanium ions at the interfacial region with gold facilitate electron transfer from the gold to oxygen. In contrast Okumura et al. [102], Vijay et al. [83] and Sanchez et al.[103] (on magnesia) all favour, on the basis of their DFT calculations, a charge transfer from the oxide to the gold.

1.3.3 Nano particulate gold in catalysis

Gold was long seen as a metal that is catalytically inactive [104, 105], but after Haruta et al [106] reported that Au nanoparticles supported on metal oxides were highly active for the gas phase oxidation of CO, Au gained a lot of attention. This was in contrast to the bulk form, where Au was known to be non reactive at low temperatures [107], and explained the relative low importance of Au for catalysis before this discovery. Subsequently "activated" Au in the nanoparticulate form was found to catalyse a number of reactions such as: partial oxidations, hydrogenation reactions, decomposition of halogenated compounds, etc. [108]. There was general interest in the phenomena, and a number of explanations were put forward to account for the activity of the supported Au phase ([105, 107, 109, 110] and references therein).

An experimental study by Iizuka et al [111] revealed that small (76 nm) non-supported Au particles showed moderate CO oxidation at temperatures as low as 249-294 K, in contrast to defect free single crystals that did not show any adsorption of O_2 at temperatures up to 500 K, (at pressures of 1400 Torr) and consequently did not catalyse CO oxidation [105]. Valden et al reported the highest activity of CO oxidation at particles sizes of around 3 nm [4]. A correlation of activity with gold particle size has been shown by Haruta and Tsubota [17]. They also point out that freshly prepared titania supported gold particles do not fit the correlation, as they have a one order of magnitude higher in activity, which they believed is the support induced effect [17].

A number of authors [79, 109, 112] favour the argument of an "Au only explanation" for the increased activity towards CO oxidation. They suggest that special geometries of very small Au nanoparticles exist which are stabilised by the metal oxide (non Wulff constructed particles in the range of ~ 1-5 nm) and expose a high density of low coordinated Au sites, and geometries that influenced (i) the adsorption energies of CO and (ii) stabilised small molecules by neighbouring sites [79, 109, 112]. The Au in this explanation was believed to be active in the neutral form (Au^0) with experimental results apparently to confirm this [79].

Support induced effects were a second route to try and explain the reactivity, where the active sites were proposed to be cationic gold atoms at the metal/metal oxide interface [107, 113]. In a comparative study [114] between zirconia (ZrO_2) and titania (TiO_2), positively charged gold atoms were observed at ZrO_2 as well as TiO_2. Interestingly, higher densities of Au^+ sites were observed at the ZrO_2, and this coincided with a smaller number of low coordinated sites in comparison to that for TiO_2.

Another suggested contribution to the catalytic activity was the strain induced due to a mismatch of the lattice parameters at the interface, between the support and metal nanoparticle, leading to variation on the adsorption energies and therefore lower activation energies [115].

Yet another metal support induced contribution to the catalysis of CO is that of "spill-over" of an oxygenated species at the support metal particle interface [116]. This is

believed to occur only at reducible oxides like TiO_2 and Fe_2O_3, [117] either directly at the interface by bridge bonding between the support and metal, or by oxygen that adsorbs exclusively at the support in the vicinity of the Au particle leading in the case of TiO_2 to a minor charge transfer of the oxygen with the CO adsorbed on the gold [109].

Valden, et al attributed the higher activity to quantum sizes effects, i.e. an alteration of the electronic band structure, resulting in a transition from metallic to non-metallic particles in clusters only a few atoms thick [4].

Water vapour was shown to promote the catalysis of CO and was explained by the adsorption of H_2O at the gold with subsequent cleavage to form carbonyl intermediates and adsorbed OH at the particle perimeter (Langmuir-Hinshelwood L-H kind mechanism) [118, 119]. While some authors favour the L-H kind mechanism [118, 119] Bongiorno and Landman [120] showed in their theoretical calculation, that an Eley-Rideal mechanism (CO reacts from the gas phase with an adsorbed oxygen water complex) has a energy barrier as low as 0.5 eV which was similar to the activation energy of a L-H mechanism and hence suggested that both mechanisms would be possible.

Lopez et al. tried to quantify the vast variety of proposed origins of the high catalytic activity of gold towards the CO oxidation and they came to the conclusion that the main contribution and in there eyes most likely origin of the high activity comes from specific low coordinated adsorption sites at neutral gold atoms in small particles [121].

1.4 The surface redox chemistry of gold

The electrooxidation of noble metal such as platinum and gold has been extensively studied, and an excellent review is available [122]. Gold surface oxide formation is believed to proceeds via a place-exchange of electrosorbed oxygenated species (OH) with Au atoms in the vicinity of the surface lattice (see Figure 1.13, further oxidation by deprotonation of the hydroxide not considered in presentation). The effect was explained by relieving the stress or lateral repulsion in the surface layer due to charge accumulation [123].
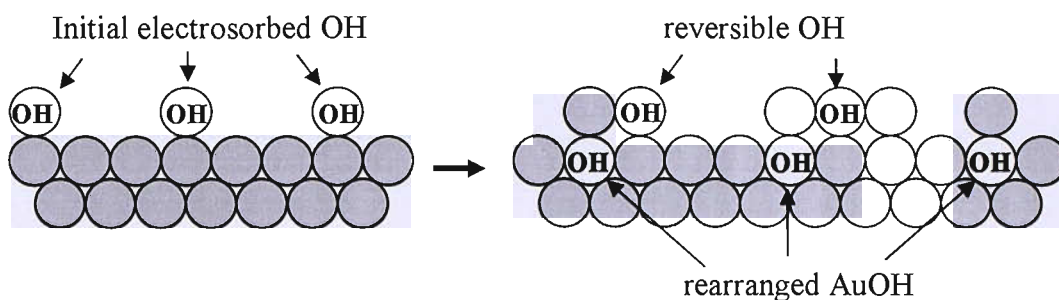
Figure 1.13. *Initial electrosorption of 2 dimensional OH on Pt or Au which subsequently "place exchanges" to form quasi 3 dimensional surface structure (adapted from [122]).*

The structure formed at saturation is a compact AuO (or Au(OH)₂) layer which then further forms multilayered oxide films. The state of the oxide film was found to be a function of the experimental condition and several oxide forms have been suggested for the initial compact layer for different growth conditions (such as AuO, Au(OH)$_2$, Au(OH)$_3$ and Au$_2$O$_3$) [123-127]. The subject of this section will only be the initial oxide growth and not discussed are "aggressively" formed oxide films (e.g. extended cycling with very positive potential limits or those formed potentiostatically at very positive potentials) often referred to as β oxide or hydrous oxides (reviews of this are available from Burke [123, 128, 129]). These "β oxide" films formed at very high overpotentials and extended times, form less dense structures and eventually form thick yellow films, which can "peel off".

The following steps of initial oxide formation in aqueous electrolytes (0.5 M H$_2$SO$_4$ and KOH) seem to be accepted [130]:

$$Au + H_2O \longrightarrow AuOH + H^+ + e^- \tag{1.8}$$

$$AuOH \xrightarrow{\;place\;exchange\;} AuO + H^+ + e^- \tag{1.9}$$

At the very initial oxide formation stages water gets activated at the surface to form a gold hydroxide species with subsequent lattice place exchange in the surface atomic layers. Further oxidation to form Au$_2$O$_3$ or AuOH$_3$ (Au^{3+}) requires significantly higher overpotentials (well above 1.5 V vs. SHE) or prolonged holding times at oxidative potentials:

$$2AuO + H_2O \longrightarrow Au_2O_3 + 2H^+ + 2e^- \tag{1.10}$$
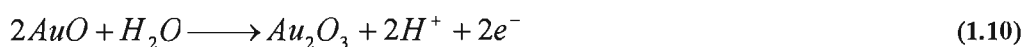
This stoichiometric reaction equation for the oxide formation has been chosen for the convenience of presentation. Even so stoichiometric oxides are only to be expected for

"thicker" films as argued by Conway [122] and, therefore, a presentation that accounts for non-stoichiometryic films would be more accurate. Also hydrated oxide forms are not covered in the reaction schemes.

The onset of gold oxide formation is still under discussion and generally the formation of irreversible (at very initial stages some reversible adsorption of OH involved) oxide in 0.1 M $HClO_4$ occurs at ~ 1.22 V vs. RHE and for 0.05 M H_2SO_4 at ~1.36 V [131]. The potential region below the onset of gold oxide formation is often referred to as the double layer (DBL) region where charges are solely due to the surface charging. Careful investigation showed that this is not the case. For example it was convincingly shown by electrochemical radioactive labelling [132] and STM measurements [133] in acidic solution that anion (sulphate) adsorption takes place. Anion adsorption in the double layer region (onset as low as 0.4 V vs. RHE) should according to Angerstein-Kozlowska et al [134, 135], be treated in terms of a pre-oxidation of the surface, due to the competition for adsorption sites of the anion with OH and they suggested the involvement of OH in the surface adsorbates. In fact surface-enhanced infrared adsorption spectroscopy supplied direct evidence that perchlorate adsorption begins at 0.4 V (at highly orientated Au (111)) [136] as has been claimed on basis of electrochemical analysis earlier by Angerstein-Kozlowska et al. [137]. The former study [136] did not show evidence for the presence of surface OH formation in the double layer DBL region, but rather show ice like water orientation (hydrogen ends orientated towards electrolyte and hydrogen bonded to a second layer) at potentials greater than the potential of zero charge ($\leq$ 0.55 V) and strongly hydrogen bonding at potentials $\leq$ 0.9 V, caused by the interaction with perchlorate anions (one hydrogen is blocked by weak interaction with one anion). In alkaline solution, where no water activation is required, reversible adsorption of OH was found with an onset as early as 0.3 V (vs. RHE in 0.1 M KOH) [138]. Interestingly in the potential range where anion adsorption was observed on single crystals a surface reconstruction effect was observed (lifting of the surface from hex to (1x1) orientation) in both alkaline as well as acidic electrolytes [139-142].

Electrochemical quartz crystal microbalance measurements (EQCM) [126, 143-145] and Ellipsometry measurements [126, 127, 146] have been employed to characterise the nature of the oxide films and their thicknesses respectively. Interpretation of the data is

difficult, as EQCM measures the incorporation of water (hydrous oxides) and binding of water at the oxide film as well as dipole coordinated water to adsorbates and anion adsorption, as pointed out by Conway [122]. In sulphuric acid (0.1 M) [126] as well as in perchloric acid (0.1 M) [145] a reduction of the crystal frequency, hence a mass increase was observed commencing from approximately 0.4 V to 0.7 V vs. RHE . The mass increase at the onset of the irreversible oxide formation was not found to be greater than the mass increase in the pre-oxidation region [126, 145]. The mass increase in the pre-oxidation region was rationalized as anion adsorption (neutral electrolytes) [144] or hydroxide/water (water H bonding to a OH species at the surface) adsorption [126, 145]. The oxide species in the potential range (below 2 V, where hydrated multilayered oxide structures are formed) of irreversible oxide was dedicated to the formation of α oxides either of the nature of AuOH or AuO [143, 145]. Xia and Birss [126] concluded from a combined ellipsometry and EQCM study that the irreversible oxide in 0.1 M sulphuric acid must be of the form of AuO (thickness 0.3 nm) in the potential range of 1.3 to 1.5 V vs. RHE and of a mixed AuO and Au_2O_3 (thickness of 0.5 nm) nature between 1.5 and 1.7 V. A similar α oxide film thickness using ellipsometry was found by Tremiliosi-Filho et al. [127], but they believed it to be solely the formation of either AuO or $Au(OH)_2$. At potentials of 1.7 V vs. SHE in 0.5 M H_2SO_4 Juodkazis et al [124] concluded from XPS measurements, that gold in the oxidation state 3+ is present from the beginning of the irreversible gold oxide formation, and that this is most likely to occur as the hydroxide $(Au(OH)_3)$.

To the best of my knowledge, there are no investigations exclusively on the gold oxide formation/reduction behaviour on supported gold nanoparticles.

1.5 The oxygen reduction reaction (ORR)

The oxygen reduction reaction (ORR) has been widely studied in recent years because of its role in the cathode reaction of fuel cells. Even if a precious metal such as platinum is used as cathode catalyst, which is known to promote almost exclusively the four electron reduction of oxygen to water, relatively high overpotentials and low exchange current densities are observed. Platinum appears to be one of the most effective catalyst for the oxygen reduction reaction (especially in the low temperature range), but due to the high price it is not suitable as catalyst from an economic point of view [147, 148].

For commercialisation of fuel cells to be realised, catalyst prices have to be significantly reduced.

More conservative approaches are carbon supported high surface area catalysts. The aim is to maximize the active surface area of platinum while reducing the platinum loadings [147]. This approach yields a significant cost reduction but at the same time exhibits quite significant potential losses of < 0.4 V during operation (fuel cell potentials under load are commonly in the range of ~ 0.6 V to 0.85 V), due to the associated low kinetics and hence high overpotentials. To increase the mass activity the metals used as catalysts are usually finely dispersed, but in the case of platinum there seems to be "critical" particle size (approx. 3 nm in diameter), where further dispersion leads to a loss in mass activity and hence an economic penalty [149]. The ongoing catalyst research for a more effective catalyst for oxygen reduction faces catalyst material dependent reaction pathways, which either lead to direct or indirect reduction to water. In this work only the ORR in acidic electrolytes is investigated and three reduction reactions with associated standard potentials E^0 (vs. SHE) are involved [43]:

The direct reduction:

$$O_2 + 4H^+ + 4e^- \longrightarrow 2H_2O \qquad\qquad E^0 = 1.229\ V \qquad\qquad (1.11)$$

Indirect reduction:

$$O_2 + 2H^+ + 2e^- \longrightarrow H_2O_2 \qquad\qquad E^0 = 0.695\ V \qquad\qquad (1.12)$$

$$H_2O_2 + 2H^+ + 2e^- \longrightarrow 2H_2O \qquad\qquad E^0 = 1.763\ V \qquad\qquad (1.13)$$

E^0 values after [150] at standard conditions.

The pathways are also strongly dependent on the surface reaction kinetics of the adsorbed oxygen or hydrogen peroxide, i.e. further reduction from hydrogen peroxide to water, must be fast compared with the loss into bulk solution.
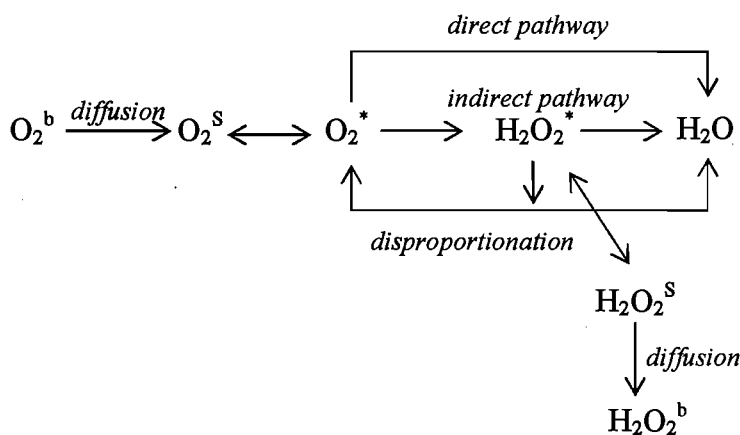
$$O_2^{\ b} \xrightarrow{\ diffusion\ } O_2^{\ S} \longleftrightarrow O_2^{\ *} \longrightarrow H_2O_2^{\ *} \longrightarrow H_2O$$

direct pathway

indirect pathway

disproportionation

$$H_2O_2^{\ S}$$

diffusion

$$H_2O_2^{\ b}$$

Figure 1.14. *Reaction scheme of the oxygen reduction reaction (adapted after [43, 151]).*

In Figure 1.14 a simplified reaction scheme of the reduction of oxygen is presented [43, 151]. Oxygen dissolved in the bulk, b, of solution diffuses towards the electrode vicinity s, where it subsequently adsorbs, *, followed by either a two electron reduction to hydrogen peroxide (often referred to as the indirect pathway), or a direct four electron reduction to water (direct pathway). During indirect reduction the hydrogen peroxide intermediate disproportionates at the surface and then either undergoes further two electron reduction to water or desorbs from the surface and diffuses to the bulk of the solution. As an example gold, carbon [152-154], and titania [155, 156] are known to promote the 2 e⁻ or indirect pathways of ORR, whereas bulk platinum and silver promote almost exclusively the 4 electron reduction to water [157] (the series of the four electrons transferred during the reduction is not yet fully understood and the exact reaction mechanism is still under discussion) at potentials positive to the hydrogen underpotential deposition region [152].

Analogous to the simple system of the hydrogen oxidation reactivity, where it was shown that the activity is a function of the hydrogen adsorption strength [158, 159] on different metal surfaces the ORR shows a characteristic peak like shape (volcano plot); the oxygen adsorption strength as calculated using DFT calculations [160] led to a volcano type plot as shown in Figure 1.15. The authors [160] used a simplified ORR mechanism, where oxygen adsorbs dissociatively (equation 1.14), hydrogenates in a second subsequent step (equation 1.15) and forms water in a last reaction step:

$$\frac{1}{2}O_2 + * \to O^*$$ (1.14)

$$O^* + H^+ + e^- \to HO^*$$ (1.15)

$$HO^* + H^+ + e^- \to H_2O + *$$ (1.16)
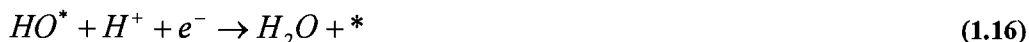
The stability of the intermediates was estimated from the energies involved in water splitting at the different metals (equations 1.17 and 1.18):

$$H_2O + * \to HO* + \frac{1}{2}H_2$$ (1.17)

$$H_2O + * \to O* + H_2$$ (1.18)

In all reaction equations * signifies a metal surface site. The authors point the role of surface coverage out and used for apporximation a coverage with oxygenated species of 0.25. They also compared a mechanism, where the dissociation of oxygen (equation 1.15) takes place after the hydrogenation (they proposed the name "associative mechanism"). They concluded that the free energy path of this ORR mechanism has a similar energy pathway and hence would not dramatically change the volcano plot (for more details of their calculation refer to [160]). Evidently from their calculations the platinum group elements are the most favourable metals for the ORR. They point out that gold is so inactive for the ORR because of the instability of oxygen at the surface and that due to weak oxygen bonding at the gold surface the dissociation barrier of oxygen is high (see also for the importance of the stability of intermediates as given by the chemisorption energy, Nørskov et al. [161]). Rao et al pointed already in 1963 the vital role of the d band electrons to the activity of oxygen reduction (in the case of gold no unpaired d-band electrons are present)[162], and there seems to be a clear correlation with the d-band electrons and chemisorption strength [163]. The shape of the volcano plot (Figure 1.15) is very similar to that found experimentally for some of the metals if the adsorption potential of –O or –OH during CV's vs. the activity of oxygen reduction at 800 mV is plotted [158].
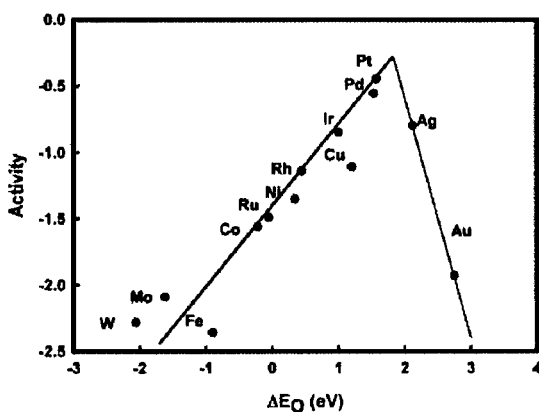
Figure 1.15. *Volcano plot of the oxygen reduction activity as a function of oxygen binding energy at 0.25 coverage of the surface with oxygenated species (taken from [160]).*

ORR on platinum

As mentioned above platinum is the most widely studied catalyst for the reduction of oxygen, due to its high importance in low temperature fuel cells. Many reaction steps and hence intermediates during oxygen reduction on platinum have been suggested (e.g. [164, 165]) for the purpose of presentation one (Pt-(OHOH)) is shown in equations (1.19) to (1.22), which was identified to be the lowest energy pathway as calculated by Anderson et al. using ab-initio DFT calculations [166, 167]:

$$Pt - O_2 + H^+(aq) + e^- \rightarrow Pt - OOH \tag{1.19}$$

$$Pt - OOH + H^+(aq) + e^- \rightarrow Pt - (OHOH) \tag{1.20}$$

$$Pt - (OHOH) + H^+(aq) + e^- \rightarrow Pt - OH + H_2O \tag{1.21}$$

$$Pt - OH + H^+(aq) + e^- \rightarrow Pt - OH_2 \tag{1.22}$$
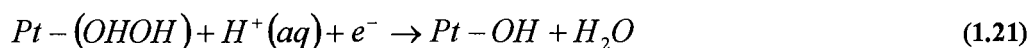
They concluded that the oxygen dissociation during ORR on Pt takes place during the second electron transfer (equation 1.20), which is supported experimentally for example by Markovic and Ross et al. [168].

A significant electrolyte dependent oxygen reduction activity on platinum was reported and explained by specific anion adsorption [169]. The activity was found to increase in the order of $H_2SO_4 \sim CF_3SO_3H < H_3PO_4 < HClO_4$. To elucidate the mechanistim of the ORR on platinum, investigations have been undertaken at several systems, including studies on polycrystalline electrodes (e.g.[170-174]), low Miller index single crystal Pt(h,k,l) (reviewed in [168]) and supported platinum particle electrodes [19, 149, 175-178].

Damjanovic et al proposed a mechanism for oxide free platinum in 1967 [165], where they concluded from Tafel analysis that at high overpotentials the oxygen coverage is low and hence the oxygen adsorption follows the Langmuir isotherm and the rate determining step is the addition of the first electron to the oxygen (again probably the protonation step of the oxygen equation 1.17) with an associated Tafel slope of 120 mV dec^{-1}. They found that the reaction is first order with respect to the oxygen pressure as well as pH. At low current densities and hence low overpotentials the surface coverage with oxygenated species (probably O_{ads}, OH_{ads} and O_2H_{ads} [178]) is high and the kinetics follow Temkin isotherm like behaviour with a Tafel slope of 60 mV dec^{-1} and a reaction order of 1.7 with respect to pH. Interestingly Gewirth et al [179] could identify a Pt-OH intermediate in the reduction of H_2O_2 by surface enhanced Raman spectroscopy in the region where platinum is usually OH (oxide) free.

The Damjanovic mechanism did not account for surface anion adsorbed species and therefore a rate law was proposed including this effect which seems to be generally accepted [164, 168, 180]:

$$j = nFKc_{O_2}\left(1 - \theta_{ad}\right)^x \exp\left(-\frac{\beta FE}{RT}\right)\exp\left(-\frac{\gamma r \theta_{OH_{ad}}}{RT}\right) \qquad (1.23)$$

Where n is the number of electrons, F the Faraday constant, K the chemical rate constant, θ_{ad} the coverage of anions (H_{upd}, OH, O_2, O_2^{2-}, H_2O_2 and spectator anions from the electrolyte), $\theta_{OH_{ad}}$ the hydroxide coverage, x either 1 or 2 for the surface site requirement of the adsorbates, E the electrode potential, β and γ are the symmetry factors (assumed 0.5) and r accounts for the coverage dependent adsorption isotherm behaviour with increasing coverage.

The oxygen reduction on platinum is a structure sensitive reaction with respect to the Pt(hkl) planes [181, 182]. The activity in weakly adsorbing perchloric acid was found to increase in the order (100)<(110)≈(111) with only small differences in the rate of ORR, while in sulphuric acid, where strongly adsorbing HSO_4^- is present, the difference between highest and lowest activity was two orders of magnitude following the order (111)<<(100)<(110).

Measurements on stepped single crystal electrodes in sulphuric acid showed higher activity, which was explained by a lowering of (bi)sulphate adsorption, whereas in perchloric acid the activities of the stepped surfaces were not found to be enhanced significantly, in agreement with the single crystal Pt(hkl) [183, 184]. Electrochemical reduction of oxygen on platinum nanoparticles represents surfaces with a high density of steps, i.e. several crystallographic orientations c.o. have to be expected, as summarised in Chapter 1.3. The correlation between mass-activity and dispersion of platinum has been reported to b non-linear in sulphuric, and strong phosphoric (T = 180 °C, 97 - 98%) as well as perchloric acid electrolytes [19, 149, 178]. This phenomenon is often referred to as the particle size effect. It must be noted, that there is an ongoing dispute, about possible reasons and recently it was convincingly reported, that in weakly adsorbing electrolytes like perchloric acid no particle size effect was observed, when particles with similar crystallographic orientations are used (as determined by the relative XRD intensities of the different planes) [185]. The authors [185] argued on the basis of NMR measurements, that only small electronic perturbation of the surface atoms for particles as small as a mean particle size of 1.6 nm are observable and therefore the activity (rate constants) remained unchanged to bulk platinum. They reported apparent activation energy of 37 kJ mol^{-1} at overpotential of -0.525 V vs. E^0. The recent findings from Yano et al [185] find support in Stonehart's earlier work [177], where it was found that the specific ORR activity was independent for particles separated at least 10 times the size [186].

Nevertheless there is little doubt, that in electrolytes containing anionic adsorbents (like HSO_4^- or PO_4^{3-}) a particle size effect occurs. Kinoshita [149] explained this effect using the statistics for small particles presented in Chapter 1.3. He reports, that the activity drop for particles smaller than 3-5 nm is a function of the decrease of higher active (i.e. (100)) surface planes. Markovic et al [181, 182] showed that the activities for the different crystallographic orientations of Pt(hkl) agree well with this argumentation. Some author's emphasise the possible influence of the OH adsorption on the ORR activity. Generally the OH adsorption strength seems to decrease as the particle size decreases, i.e. the platinum oxide formation/reduction was found to become more irreversible [19, 176, 178, 181] and also a progressively positive shift in binding energy of the f –states of platinum was observed for smaller particles [176].

Figure 1.15 implies that further improvement of activity could be achieved if the oxygen binding energy is slightly weakened. Such an effect was achieved by alloying platinum with transition metals like Ni, Co,V, Fe and was studied on bulk alloys [187-192], supported particles [193-197]. Theoretical calculations seem to confirm the experimental findings [198-202].

1.5.1   ORR on gold

Gold in contrast to platinum is oxide free in the potential range where oxygen reduction occurs. It is significantly less studied than platinum because of the lower impact on energy conversion technology due to the two electron reduction of oxygen in acidic media following equation 1.12 with hence a lower free energy change. Even so studies have been carried out on polycrystalline [203-206], single crystal [207-210] and supported nanoparticle electrodes. The oxygen reduction on gold was found, as on platinum, to be dependent on the crystallographic orientation of the low index Miller planes in alkaline [207, 208], neutral [209] and in acidic media [210].

The activity decreased at all pH's in the order [207-211]:

(100) >> (110) >(111)   (1.24)

Special attention was given to the (100) crystallographic orientation of gold [207, 212-216] because of the ability to catalyse oxygen in a four electron reduction to water over a pH range of   3 > pH > 14 [214] at potentials where OH appears to be stable at the surface. This was generally explained by specific adsorption of an intermediate (possibly a superoxide) which is favoured on the "missing row" configuration of Au (100) (bridge adsorption with prolonged O-O bond). It was shown in several studies, that ad atom such as lead and bismuth on Au (111) can create bridge sites to promote four electron oxygen reduction [204, 210, 217].

The reaction scheme was generally concluded to follow an indirect pathway (as shown in Figure 1.14) using electrochemical linear sweep experiments in rotating ring disc electrode (RRDE) experiments. Also from the kinetic data obtained in electrochemical experiments the addition of the first electron was interpreted to be the rate determining step (Tafel slope -2RT / F) in the reduction to from hydrogen peroxide [205, 216]:

$$O_2 + e^- \rightarrow O_{2,ad}^-$$ (1.25)

Recent studies using infrared spectroscopy techniques during the reduction of hydrogen peroxide [179, 203] and oxygen [204, 218] on roughened [179, 203, 204] and thin film

gold [218] revealed some interesting aspects of the oxygen reduction on gold: Unlike on platinum (as quoted before) no OH stretching bond was observed in the potential range of the reduction of hydrogen peroxide showing, that no or little bond cleavage of the O-O bond occurred. At potentials as low as 0 to 0.2 V during oxygen reduction (mass transport controlled potential region) a superoxide (HO_2^-) stretching bond was observed which suggested that this is a reaction intermediate [204]. And Shao and Adzic [218] observed a very weak band for such a superoxide in acidic media and concluded therefore, that this might be an indication, that the lacking stability of the this intermediate and fast protonation might be the reason for the 2 e$^-$ reduction of oxygen.

1.5.1.1   ORR on gold particles

Only recently the number of publications treating the oxygen reduction reaction on supported gold nanoparticle electrode rose [219-235]. Deab and co-workers studied the ORR on electrodeposited gold nanoparticles on gold [219, 222] and glassy carbon [221, 223, 225, 236] supports in acidic, neutral and basic solutions. The particles studied are tens to hundreds of nanometre in size [236]. They observed, that in acidic media on very low coverages of electrodeposited gold on a gold electrode a positive shift could be observed over bulk gold, i.e. lower overpotential leading to higher activity [219, 222]. A similar increase in activity they observed on gold nanoparticles supported on glassy carbon in acidic [223] and alkaline media [225]. Also they believe that a further reduction of hydrogen peroxide to water takes place on small Au particles [219, 222] on gold electrodes. A similar effect they observed on glassy carbon supported gold nanoparticles in alkaline and acidic media[223, 225]. In neutral media they observed a selectivity enhancement towards the hydrogen peroxide formation inhibiting the further reduction to water on glassy carbon supported small gold particles [221]. They explained there results by the specific tuning of their nanoparticles by controlling the growth conditions achieving particles exposing the more active planes at the surface electrolyte interface such as (100) and (110) which then effects the structure sensitive reduction of oxygen. Hernandez et al. [226, 227] reported another study on carbon supported gold nanoparticles, leveraging from the possibility of controlling the specific planes exposed at the electrolyte surface interface by the addition of iodide and sulphides during reduction of gold chloride from a water-in-oil micro emulsion. The mean particle size under investigation was 3.7 to 4.8 nm [226] and in the presence of iodide they were able to synthesise nanoparticles with preferential (100) orientation as

analysed by lead underpotential deposition and enhanced catalytic activity with a shift towards four electron reduction of oxygen.

The oxygen reduction of evaporated [228] and electrodeposited [229, 230] gold deposited nanoparticles has been studied on boron doped diamond electrodes by two groups. Both groups claim that they observed an increase in activity over bulk gold. There is no conclusive information given about the particle sizes studied in these investigations. Tammeveski et al.[231, 232] studied the reduction of oxygen at gold deposited on glassy carbon and multi walled carbon nanotubes. They have seen no change of oxygen reduction activity and mechanism on glassy carbon (no conclusive information about the particle sizes at equivalent thicknesses were particle growth is to be expected has been given) for equivalent gold coverages (thicknesses) in the range 0.25 nm till 50 nm and bulk gold [232]. Whereas they observed slightly higher activities at the multiwalled nanotubes supported gold particles (no information is given for the particle size) but no change in mechanism[231].

Recently Baker et al. [235] reported the ability of tin dioxide supported gold nanoparticles (particle diameter d ~ 1nm) to reduce oxygen in 0.1 M perchloric acid to water. The RRDE measurements indicate, that only very little hydrogen peroxide was formed. They speculated that either an electronic effect or a "bifunctional" mechanism might be responsible for this behaviour. The electronic effect, they explain by the charge transfer from the support to the gold particles, which then influence the ability of stabilising oxygen and reaction intermediates. During their proposed "bifunctional mechanism" oxygen adsorbs and forms an O_2^- radical at the support and the reaction takes place at the perimeter with the gold particle. This is to the best of my knowledge the first study that shows a significant change (enhancement) of the oxygen reduction reaction due to metal support interactions.

Some metal oxides are known to promote the oxygen reduction reaction and are found in solid oxide fuel cells at higher temperature [237-239]. Nonetheless most possible candidates which show high degradation stability in acidic media, high surface area and required conductance at room temperature such as titanium dioxide are known being poor catalyst for the oxygen reduction in alkaline solution [155, 240] and non active in acidic media.

The results on the gold nanoparticle catalysed oxygen reduction are scarce at best as evident from the summary of experimental investigations as presented before. In summary:

- Nanoparticles can be grown with specific crystallographic orientations.
- Particles with preferentially (100) were successfully synthesised which reduce oxygen at least in alkaline solution in a sequential reduction to form water
- In acidic solution there were claims that, at least partially, oxygen might undergo sequential four electron reduction on gold particle gold electrodes as concluded from the number of electrons involved in the reduction as determined by Levich analysis varying between 2 and 4 [219].
- Convincing four electron reduction data in acid was only presented for SnO_x supported gold nanoparticles. This was explained by metal support interactions [235].
- There is little information about mechanistics involved in the reduction of oxygen at gold nanoparticles.

Van Brussel and co workers [241, 242] present a method to prepare gold supported platinum particles by electrodeposition. They claim that a four electron reduction of oxygen takes place which exhibit a higher activity in the oxide free scan than a smooth platinum surface. A significant hysteresis between positive and negative going scan was observed, so that the negative going sweep (platinum oxide formed on the surface) showed the same or slightly lower activity then smooth platinum.

1.6 The electrochemistry of carbon monoxide oxidation

The oxidation of carbon monoxide (CO) in the gas phase and in electrochemical systems is an important reaction for example for the removal of the catalyst poisoning CO from reactant stock gases in fuel cell applications. Traces of CO can significantly affect the performance of a Polymer Electrolyte Membrane Fuel Cell (PEMFC) due the strong CO adsorption on the catalyst commonly (platinum) used. Almost monolayer coverage of platinum arises if traces of CO (~10 ppm) are present in the feedstock gas hydrogen in fuel cell application at temperatures below 100 C [243]. Blyhoder [244] explained the strength of adsorption of CO (for linearly bounded CO) by a back donation concept. In this electrons are donated from the 5 σ orbital of CO to the metal

and back donated from the metal d band to the 2 π^* antibonding orbital of CO. For platinum the adsorption energy was found to strongly dependent on the CO surface coverage, which also influences the adsorption type. Three adsorption types on platinum (111) were identified by infrared reflection absorption spectroscopy: atop, 2-fold bridge and threefold bridge [141]. The overall electrocatalytic oxidation of CO could be expressed as:

$$CO + H_2O \longrightarrow CO_2 + 2H^+ + 2e^- \qquad E^0 = -0.106 \qquad (1.26)$$

With a standard potential of $E^0 = -0.106$V (SHE) [245] which is a slightly corrected value ([150, 245][4]). The detailed mechanism, especially the form of the oxygenated species, at different catalyst materials is still under discussion. For the *platinum* catalysed CO oxidation Gilman proposed in 1964 a Langmuir Hinshelwood[5] (L-H, see [246]) like "reactant pair mechanism" [247], where CO and water are adsorbed at surface sites and a hydroxycarbonyl like reaction intermediate ("activated complex") is formed, that than oxidises to form CO_2. The dissociation of water takes place in this proposed mechanism during the activated complex step [247].

As mentioned above, the reaction intermediates especially the role of the oxygenated species is not yet fully understood, but widely a L-H like mechanism is accepted for polycrystalline as well as single crystal platinum surfaces [168, 248]. The general simplified reaction mechanism can be written as:

$$H_2O \leftrightarrow OH_{ads} + H^+ + e^- \qquad (1.27)$$

$$CO_{ads} + OH_{ads} \rightarrow CO_2 + e^- + H^+ \qquad (1.28)$$

In a first reaction step water dissociation at a surface site on platinum takes place (1.27) and in a second reaction step surface adsorbed CO and OH react to form CO_2.

The L-H mechanism might not account for the preoxidation wave region during CO stripping experiments on platinum with almost CO saturated surface at potentials $\sim <$

---

[4] The uncorrected potential using the enthalpy and entropy from reference [150, 245] would lead to a standard potential of $E^0 = -0.098$ V.

[5] Langmuir-Hinshelwood mechanism: Reaction educts are adsorbed at the surface, prior to the surface catalytic reaction. The reaction should follow a second order law and the rate v is a function of the rate constant k and the surface coverage θ of the educts (here CO and OH): $v = k\theta_{OH}\theta_{CO}$ [246].

0.4 (RHE), where no oxygenated species is believed to be present at the surface. As a consequence an Eley-Rideal like mechanism has been suggested by Bergelin et al [249, 250].

A mechanism having a hydroxycarbonyl intermediate similar to the "reactant pair mechanism" from Gilman [247] seems to be more and more agreed [251]:

$$H_2O \leftrightarrow OH_{ads} + H^+ + e^- \qquad\qquad (1.29)$$

$$CO_{ads} + OH_{ads} \rightarrow COOH_{ads} \qquad\qquad (1.30)$$

$$COOH_{ads} \rightarrow CO_2 + e^- + H^+ \qquad\qquad (1.31)$$

Again water dissociation takes place (1.29), but then an intermediate reaction step forming hydroxycarbonyl (1.30) is needed to form finally the CO_2 (1.31). This mechanism was proposed on basis of spectroscopic evidence for an COOH [252, 253] reaction intermediate during the reaction, as well as on basis of slower reaction kinetics (Tafel slope of around 75 mV dec^{-1} e.g. [254, 255]) as would be present at a simple L-H mechanism (equations (1.25) and (1.26)).

Herrero and Feliu report an apparent activation energy of 132 kJ mol^{-1} [256] for the oxidation of adsorbed CO on Pt(111) surface, which was in good agreement, as they report, with molecular orbital theoretical calculation by Anderson and Grantscharova [257], where an activation barrier of 135 kJ mol^{-1} was found assuming a hydroxycarbonyl intermediate. CO oxidation occurs on almost fully CO pre-covered surfaces at overpotentials $\sim< 0.4$ V. Assuming a L-H mechanism the activation of water has to take place at Pt sites on the almost fully covered surface. Experimental evidence of McCallum and Pletcher on the basis of chronoamperometric measurements [248] suggested that CO "monolayer" oxidation proceed via a nucleation and growth, where nucleation "seeds" in form of oxidised platinum is formed and then the oxidation propagates across the surface as fronts (with increasing PtOH domains), which eventually overlap. In this mechanism the reacting species are considered to be immobile [258]. Recent studies showed that CO oxidation can be analytically fitted by the "mean field approximation" [259], which works on the assumption, that the CO surface mobility is higher than the reaction rate and hence a homogenous mixture of the reactants forms [260]. The authors of this studies assume an active site concept, where the OH formation occurs at surface defects with lower coordination number [260-262]

CO oxidation can be enhanced by adatoms at platinum or alloys PtM, such as PtSn [263, 264], PtGe [265] and the most active alloy appears to be PtRu [266-272]. Generally two different explanations are formulated. The first often referred to as a "ligand effect" explains the higher CO oxidation activity by an electronic modification of the CO Pt interaction and hence lowering in CO adsorption strength due to the second metal [273-276]. The second so called bifunctional mechanism [277, 278], proposes, that the less noble second element activates water at lower potentials and supplies in a L-H mechanism the OH required for the oxidation of CO to CO_2 [263].

The platinum particle size effect on the CO oxidation was recently intensively studied ([19, 279-284] and literature therein). Generally in CO stripping experiments multiple peaks with a general displacement towards higher potentials at particles below ~ 3 nm have been observed [19, 281, 285].

1.6.1 CO oxidation on gold

The electrocatalytic oxidation of CO on supported Au nanoparticles, unlike on Pt is not very extensively studied [15]. While the oxidation on polycrystalline [286, 287] and single crystal Au surfaces [138, 141, 288] has been studied, in both alkaline and acidic electrolytes in great detail, studies of supported gold nanoparticles are rare. In contrast to the adsorption of CO on platinum the interaction with gold is weak; hence surface coverages are low. Weaver et al. [288-290] only observe very low coverage at single crystal Au surfaces by surface infrared spectroscopy ($\theta < \sim 0.1$ ML), while Blizanac et al. using forced convection techniques (high rotation rate in RDE experiments : 2500 rpm during adsorption at -0.05 V vs. RHE) achieve almost full coverage of 0.95 ML on Au(110)-(1 x 2), 0.72 on (100)-"hex" and 0.3 on (111)-(1 x 23) [141] in 0.1 M $HClO_4$ (CO stripping experiment). Guesta et al. studied CO adsorption by an electrolyte electro reflectance (EER) method on gold and suggested that electrons are donated to the 2 π^* orbital of the CO (antibonding) from a Au surface state positive the Fermi level [291]. They concluded that the potentials required to adsorb CO are very negative in acidic electrolytes and hydrogen evolution hence would prevent CO adsorption. It must be noted that they suggested an inhibition of CO adsorption for Au(100)-hex which has been proven to adsorb CO up to a coverage of 0.72 at potential of -0.05 V [141].

For the mechanistic of gold catalysed CO electrooxidation on single crystals a Langmuir-Hinshelwood mechanism was suggested by Weaver et al [290] in analogy to metal complex catalysed CO oxidation in homogenous solution:

$$CO_{ads} + H_2O \leftrightarrow COOH_{ads} + e^- + H^+ \qquad (1.32)$$

$$COOH_{ads} \rightarrow CO_2 + e^- + H^+ \qquad (1.33)$$

They found the reaction order to be unity with pH, i.e. the kinetics is directly correlated to the OH⁻ concentration over a wide range of pH: 4 to 13.5. The water activation was shown experimentally by a deuterium isotope deprotonation experiment to only taking at place pH's lower than 4 (equation (1.32)), apparently no water activation is required for higher pH. They also observed a unity reaction order with pH range 0 - 2 which would be inconsistent to a rate determining step (rds) being reaction (1.32) and hence suggested that the rds might be the decomposition of the hydroxycarbonyl intermediate (1.33). In contrast to the water activation argumentation by Weaver, Blizanac et al suggested that the real onset of OH formation on gold surfaces takes place as low as 0.3 V vs. RHE in both in alkaline (0.1 M KOH) as well as acidic (0.1M HClO₄) environment [138, 216] and hence the difference in activity are mainly due to competing adsorption of perchlorate with hydroxide.

A structure sensitivity of the CO oxidation activity towards the crystallographic orientations was observed on single crystal gold electrodes [141, 288] with the activity decreasing in the order:

Au (110)≥ Au(100)>Au (111) $\qquad$ **(1.34)**

As already outlined in chapter 1.4 a potential dependent surface reconstruction takes place at single crystal surfaces to form (1x1) (unreconstructed structures) surfaces both in alkaline [138, 292] and acidic electrolytes [216] as measured by STM and surface X-ray scattering (SXS). It was found that CO oxidation is sensitive to this transition with the unreconstructed surfaces appear to be more active, i.e. the CO oxidation activates in repetitive cyclic voltammetry experiments from the first (fully reconstructed) to second cycle (transition to unreconstructed surface) both in alkaline and acid [138, 290]. This was explained by the increased number of low coordinated sites during transition [138].

1.6.2 CO oxidation on supported gold nanoparticles

Very view publications cover the CO electrooxidation on supported gold nanoparticles. Jaramillo et al claimed in their studies [293, 294] that an enhancement of the electrochemical CO oxidation activity takes place on iridium/tin oxide (ITO) with decreasing particle size in alkaline solution. Kumar, et al. report on a very similar system that higher current densities (referred to the "real electrochemical surface area") are non catalytic effects, and show lower activities on smaller particles [295]. The former group also published a combinatorial electrochemistry study of TiO_2 supported gold nanoparticles, and claimed to observe an enhancement in catalytic activity towards CO oxidation [293].

1.6.3 CO tolerance at fuel cell anodes

Due to the aforementioned catalyst poisoning effect of CO research has tried to increase the catalyst tolerance ([296, 297] and reference therein) for CO poisoning and to lower the usage, as far as possible, of expensive precious metals and/or the need to clean reformate gases of CO.

The common methods applied for reformate gas cleaning are methanation, preferential oxidation, water gas shift or cleaning by permeation through a palladium membrane [298, 299]. The common disadvantages of these techniques are that they employ precious metal catalysts and are energy consuming.

The second approach is to make the fuel cell catalyst more CO tolerant or to have "partial oxidation" of CO. Four methodologies to solve this problem have been practically applied: Increasing the temperature of the PEMFC, use of alloying metals to alter the CO tolerance, use of an air bleed and use of CO tolerance altering supports.

Increased temperature would lead to a much higher CO tolerance, from around 10 ppm at 80 °C to 1000 ppm at 130 °C [243]. The operating temperature of a PEM fuel cell is currently restricted to between 50 and 100 °C, due to the lack of heat stability of most of the polymers, and problems of lowering the humidification at higher temperatures leading to a higher membrane resistance and therefore voltage losses [300].

The approach of an *air bleed* is based on the idea that oxygen is added to the fuel gas, which then reacts with the catalyst to inhibit the CO poisoning [301, 302]. However, this non specific reaction does not only oxidise CO but also the hydrogen, leading to exothermic heat production which sinters the catalyst particles and leads to degradation of the catalyst.

Another approach to enhance CO tolerance of the catalyst is a supportive effect by *metal oxide* semiconductors. Recent studies by Tseung et al have shown higher CO tolerance of platinum particles supported on tungsten oxides (on carbon) over platinum/ruthenium [29, 303]. These results seem to be confirmed in a very recent study by Maillard et al [304]. Another promising oxide support material for the anodic oxidation of impure hydrogen and methanol seems to be molybdenum oxide [28]. Recently a combination of gold (Au) supported on titania (TiO_2) combined with a Pt/Ru as a methanol electrocatalyst was proposed [305], which apparently increased the activity.

2   Experimental

This chapter describes the experimental instrumentation and parameters that were used throughout this work for the sample preparation and characterisation. Descriptions are generalized and subsequent results chapters include more specific information when parameters deviated from the description below.

2.1   Physical Vapour Deposition

The samples for the surface characterisation and electrochemical experiments were prepared in an ultrahigh vacuum (UHV) molecular beam epitaxy system (MBE, DCA Instruments) modified, to allow the parallel synthesis of thin films (co-deposition), as well as controlling their deposition rate [24]. In Figure 2.1 a schematic of the system is shown. The system consisted of two physical vapour deposition (PVD) chambers, one low pressure chemical vapour deposition (LPCVD) chamber (not used in this work)), and a surface characterisation chamber (CC), all interconnected by a transfer chamber (TC). The entire system was kept under UHV with the base pressure in the range 1 to 5 x 10^{-10} mBar. Sample access was achieved through a load lock, which could be vented to atmospheric pressure. All samples could be transferred between chambers by a transfer "Railway" and transfer arms. The "railway" consisted of two trolleys on rails transporting the samples along the TC. Next to each chamber a pick up mechanism allowed changeover to the transfer arms. Once picked up and placed on the transfer arm they could be brought into the chambers for deposition. The PVD deposition chambers were cryo- (Helix Tech. Corp.) and titanium sublimation (Varian) pumped, the TC and CC was ion- (Varian) and titanium sublimation pumped. The load lock was pumped by an oil free rotary pump (Pfeiffer) and a turbo-molecular pump (Pfeiffer).
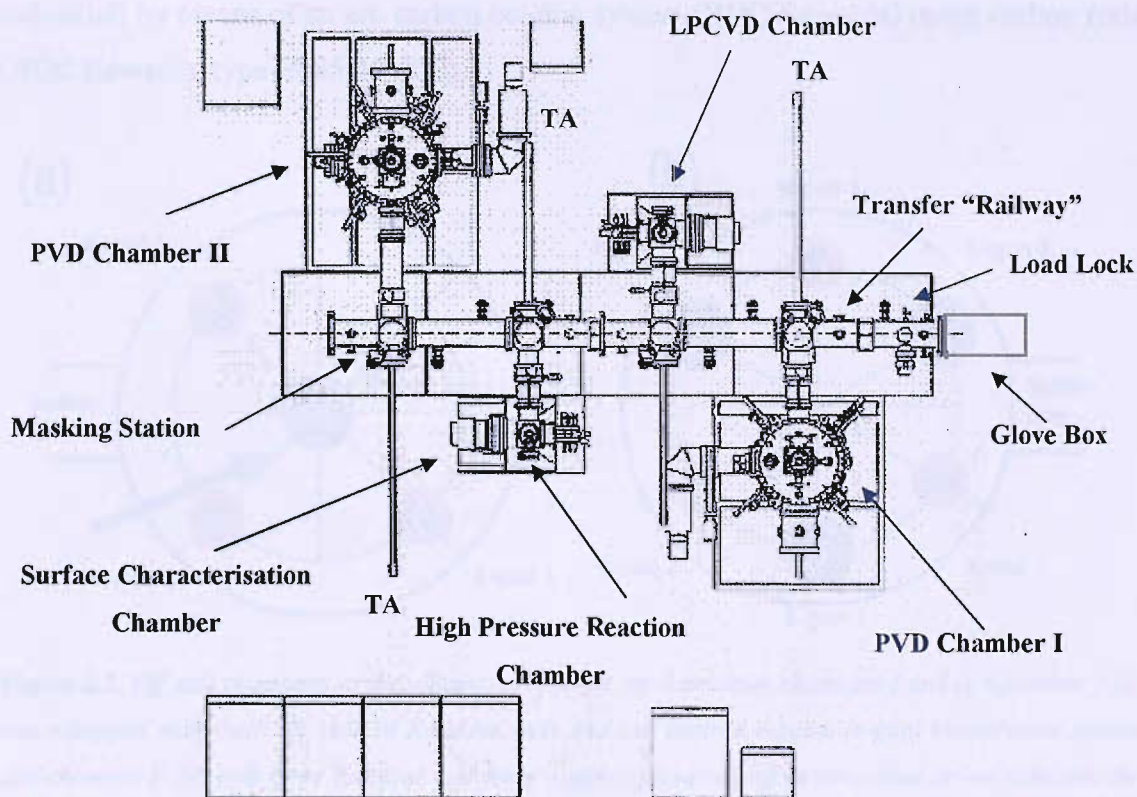
Figure 2.1. *Schematic presentation of the UHV deposition system. TA: transfer arm.*

The deposition by PVD was undertaken in the growth chambers incorporating evaporation sources as presented in Figure 2.2. Chamber I was equipped with three off axis Knudsen Cells (K-Cell, DCA HTKS) and one centred electron-beam (e-gun, Temescal) evaporator. Chamber II consisted of six off centred sources, three K-Cells and three e-gun evaporators. Mainly the off axis K-Cell 1 (titanium) and K-Cell 2 (gold) of chamber I were used for sample preparation in this work. Gold was also deposited from K-cell 3 in chamber II using a low temperature source. The effusion source for the titanium (granules 99.95 %, Goodfellow Metals) was a high temperature cell for operation up to 2000 °C using a pyrolitic graphite 10 cm³ (Sintec Keramik) crucible. Gold (pellets 99.99 %, Goodfellow Metals) were evaporated from a low temperature K-cell for operation up to 1400°C equipped with a 30 cm³ Fabmate crucible (Kurt Lesker). Sub-stoichiometric TiO_x layers were deposited by the oxidation of the titanium during deposition by a beam of molecular oxygen (BOC Special Gases, N6 Grade) directed at the sample face (the collimating molecular oxygen source is shown in Figure 2.2 as an arrow). Carbon layers were deposited using the centred e-gun 1 evaporation source and graphite rods (Alfa Aesar, type 231-955-3). Carbon layers were also deposited (where

46

indicated) by means of an arc carbon coating system (BOC Edwards) using carbon rods (BOC Edwards, type E085-19-030).
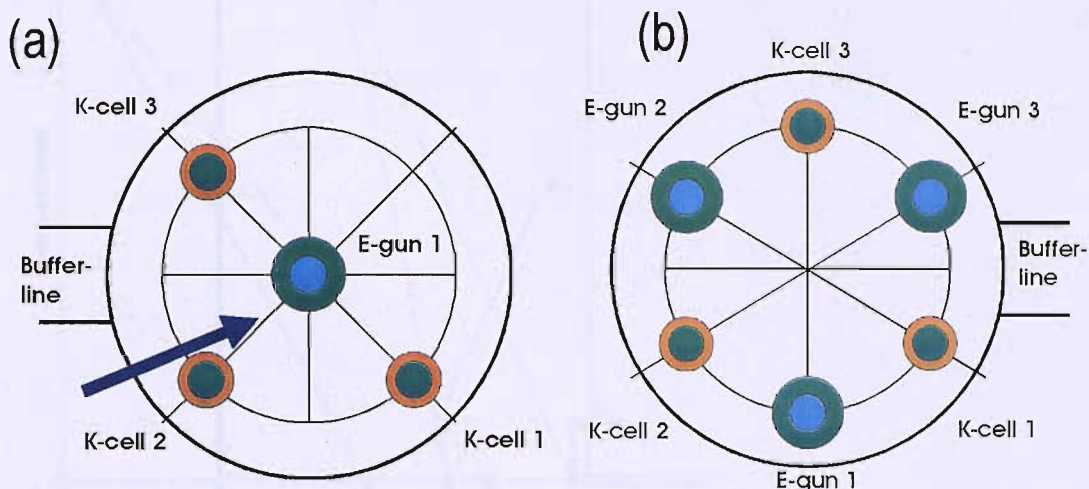

Figure 2.2. *Off axis alignment of the effusion sources in the deposition chambers I and II. Chamber I (a) was equipped with three off centred Knudsen cells and one centred e-beam (e-gun) evaporation source and chamber II (b) with three Knudsen and three e-gun sources (all off centre). Blue arrow indicates the position of the molecular oxygen source.*

The graduation of material across a wafer was achieved using "wedge shutters". Figure 2.3 presents the methodology. Guerin and Hayden described the methodology in detail [24]. Every off axis source was equipped with a movable aperture (also called wedge shutter), which could be shifted into the free atomic stream of evaporated material. Due to the finite size of the source, C, and the sample, A, the aperture, will shadow the free pass of atoms from the source to the sample depending on the length, B, in Figure 2.3. If we considered one possible scenario, where the aperture was thought to be set to position B1, the sample at position A1 would "see" all the material from the source size C1 to C2. At the position B2, the atomic flux from the source position C2 would not reach the sample, and only material from the vicinity of C1 would be deposited. The result would be a linear gradient and, taking the chamber geometries into account, a graduation of material of ~ 98% at position A1 would be expected and ~ 61% at position A2 (for a detailed trigonometric/mathematical description see [24]). Experimental results demonstrating the method will be presented in chapter 2.3.2 for the deposition of gold. For uniform depositions such as carbon and titania support materials the sample holder was equipped with a motor drive which allowed rotation of the substrate during deposition.
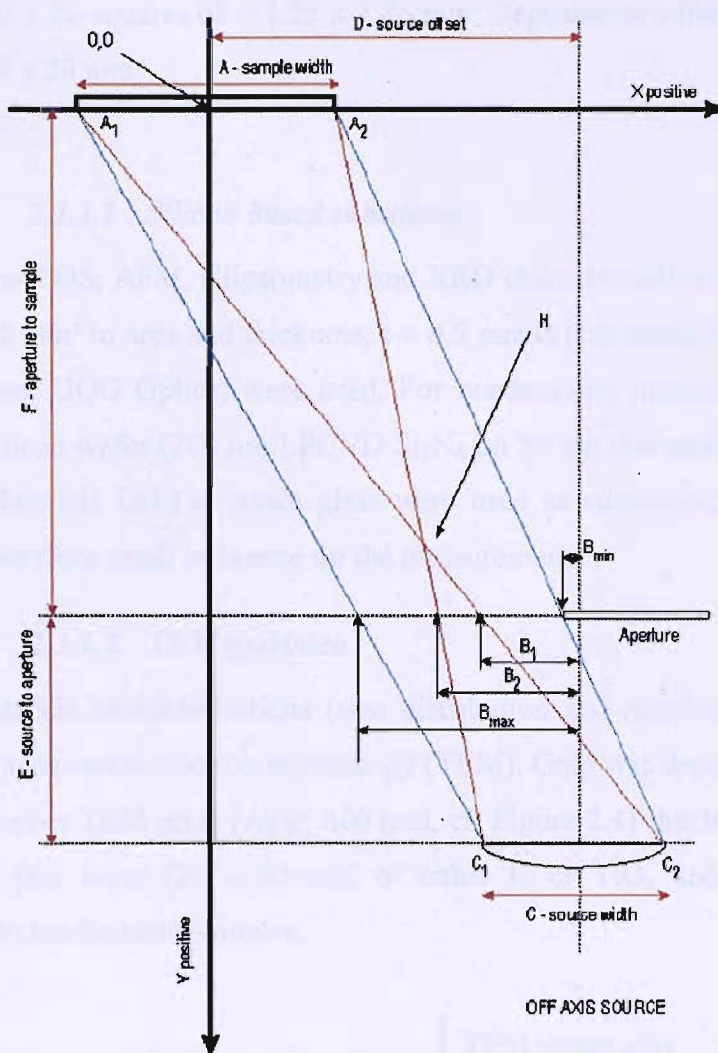
Figure 2.3. *Off-axis evaporation source/sample schematic with shutter aperture [24].*

2.1.1 Analytical substrates

Depositions were carried out onto (a) silicon (Nova Electronic Materials Ltd); (b) silicon nitride on silicon (Nova Electronic Materials Ltd); (c) a micro-fabricated silicon (10 x 10) array of gold electrodes (applied Microengineering LD.) for electrochemical measurements [25] and (d) Ti (Goodfellow, 99.6 % titanium rod) or glassy carbon (SIGRADUR G, glassy carbon rods) discs. Glassy carbon and titanium rods (diameter 5 mm) have been cut into 4 mm length discs and subsequently polished on a microcloth® (Buehler) to a mirror finish using alumina (particle sizes 1, 0.3 and 0.05 μm, Buehler). The substrate choice depended on the intended experiment and the analytical tool used to characterise them. Samples could be masked by a 10 x 10 matrix contact mask giving

10 x 10 squares of ~ 1.25 x 1.25 mm. Depositions without the mask were squares of ~ 28 x 28 mm.

2.1.1.1 *Silicon based substrates*

For EDS, AFM, ellipsometry and XRD characterisation either silicon wafers (squares ~ 32 mm² in area and thickness, t = 0.5 mm in), or normal glass (squares ~ 32 mm², t = 1 mm, UQG Optics) were used. For conductivity measurements silicon nitride-covered silicon wafer (200 nm LPCVD Si_3N_4 on 50 nm thermally grown SiO_2, Nova Electronic Materials Ltd.) or again glass were used as substrates, to ensure high resistivity and therefore small influence on the measurements.

2.1.1.2 *TEM specimen*

Particle characterisations (size distribution and number density) were determined by transmission electron microscopy (TEM). Gold was deposited onto small carbon coated, copper TEM grids (Agar, 400 grid, cf. Figure 2.4) that had previously been coated with a thin layer (20 – 60 nm) of either C or TiO_x under identical conditions as the electrochemical samples.
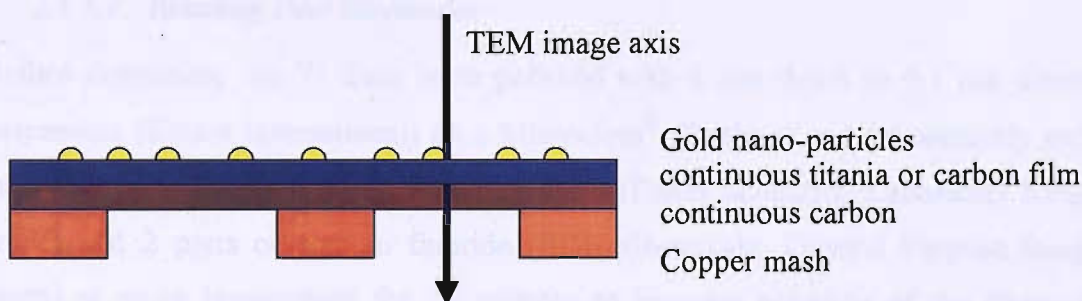

TEM image axis

Gold nano-particles
continuous titania or carbon film
continuous carbon
Copper mash

Figure 2.4. *Schematic of a TEM specimen.*

2.1.1.3 *Array electrodes*

Experiments have been carried out on materials deposited by PVD on silicon microfabricated arrays of gold pad electrodes [25]. The substrate is made up of a square silicon nitride wafer (31.8 x 31.8 mm) which has an array of 100 individually addressable gold pad electrodes. These electrodes make up a square matrix on the wafer, which can be masked when placed in a physical vapor deposition chamber allowing deposition of thin films on the gold electrodes.

49

Figure 2.5, below, shows a schematic drawing of the configuration. Small electrical contact pads in gold for the individual addressing of electrodes (0.8 x 0.8 mm) are placed on the boundaries.
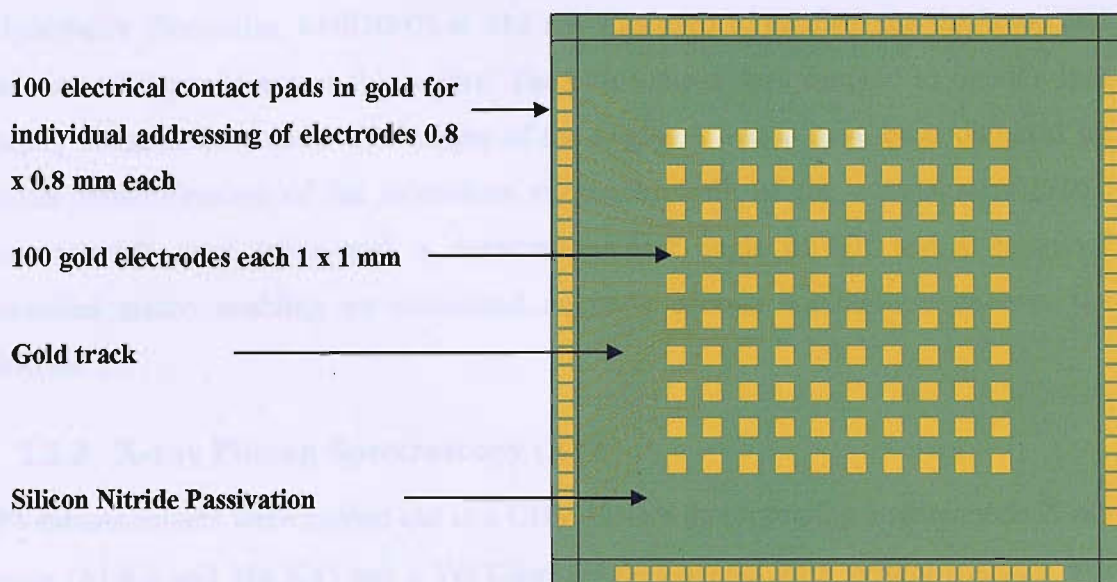
100 electrical contact pads in gold for individual addressing of electrodes 0.8 x 0.8 mm each

100 gold electrodes each 1 x 1 mm

Gold track

Silicon Nitride Passivation

Figure 2.5. *Silicon nitride sample wafer containing individual addressable square gold electrodes.*

2.1.1.4 Rotating Disc Electrodes

Before deposition, the Ti discs were polished with 6 μm down to 0.1 μm diamond suspension (Kemet International) on a Microcloth® (Buehler) and subsequently etched in a solution of 80 parts water, 18 parts HNO_3 (Fisher Scientific; Laboratory Reagent grade) and 2 parts of sodium fluoride (BDH Chemicals; General Purpose Reagent grade) at room temperature for 20 minutes to improve adhesion of the films. The titanium discs (5 mm diameter) were mounted in a holder that allowed 16 discs to be coated simultaneously in the PVD system.

2.2 Surface analytical tools

2.2.1 Atomic Force Microscopy (AFM)

AFM (Veeco, Autoprobe M5) was carried out in tapping mode using a silicon cantilever with a resonance frequency of ~ 180 kHz, spring constant of 5 N m^{-1} and approximate tip curvature radius of 1 nm (μ-mash; DP14/HI'RES/AIBS) or in non-contact and

50

contact mode (ThermoMicroscope Ultralever UL06A and UL20A) for particle height determination.

2.2.2 Ellipsometry

Ellipsometry (Nanofilm, i-elli2000) at 532 nm was used to confirm the thickness and gradation of deposits across the wafers. The ellipsometer was adapted to operate in a rotating compensator mode. The values of the angles Δ and ψ have been obtained by Fourier transformation of the intensities vs. the azimuth of the compensator [306]. Measurements were taken with a constant incident angle of 60° and a computer controlled macro enabling an automated mapping of one hundred points over the substrate.

2.2.3 X-ray Photon Spectroscopy (XPS)

XPS measurements were carried out in a UHV system incorporating a twin anode X-ray source (Al Kα and Mg Kα) and a VG Clam Single Channel XPS system analyser. For reference purposes a gold foil was placed in the UHV chamber that was subsequent to the samples of interest measured. Measurements were taken by Laura J. Williams.

2.2.4 Four Point Conductivity Measurements

Uniformity of the resistance of the deposited films was demonstrated by four point probe resistivity measurements at multiple points over the surface (hundred points were measured at a square of 19x19 mm following the area of interest on the array electrodes) using a Four Dimensions 280DI automated conductivity mapping system. A four point probe head (Jandel, A-type, < 60g tip pressure) with 1 mm spacing or a square array head (1 mm spacing, Jandel) were used to measure the film sheet resistances. The tips where cleaned prior to experiments by lowering them down on a rough ceramic slice. A diagram of the technique is presented in Figure 2.6. A current is applied through the two outer probe tips and the voltage drop due to the resistance of the sample across the inner tips is measured. The sheet resistance (or resistance per square in $\Omega_{/sq.}$) is given by,

$$R_{/sq} = \frac{\rho}{t} \tag{2.1}$$

where ρ (Ω cm) is the resistivity (material constant) and t the sample thickness (in m).

Since the sample thicknesses in our research were sufficiently small (t << s/2), the current distribution could be assumed to be in ring form [307], which led to the expression for the resistivity, as follows,

$$\rho = \frac{\pi \cdot t}{\ln(2)} \cdot \frac{V}{I}$$ (2.2)

where V is the voltage and I is the current.

Further corrections for the lateral sample dimension and the placement of the probe head regarding the edges is much more complicated and a summary of different methods can be found in reference [308]. However, the error obtained for homogenous thin layers of titanium and carbon was < 1 %, and therefore was assumed not to affect our results substantially.
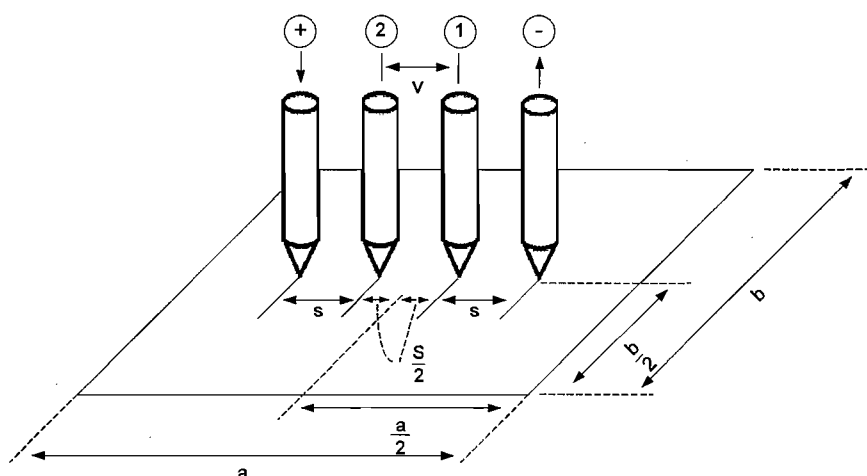

Figure 2.6. *Measurement arrangement for the four point probe on a rectangular sample [309].*

2.2.5 Energy Dispersive Spectroscopy (EDS)

Energy dispersive microscopy was carried out at a scanning electron microscope (Jeol, JSM 5910) equipped with an energy dispersive X-ray micro analyser (Oxford Inca 300). An acceleration voltage as low as 7 kV was chosen to minimize the void volume penetrated by the electrons. For analysis, the K-line intensities were integrated and results are presented in atomic percentage to the total number of elements, e.g. for a sample of gold nanoparticles deposited on an amorphous carbon C coated silicon, results would be presented as the atomic percentages of at % C, at % Au and at % Si and also the relative ratios of gold to the sum of Si, Au and C. A macro was

programmed to measure 100 points on a wafer, following the 10x10 matrix of the contact masked samples.

2.2.6 Transmission Electron microscopy (TEM)

TEM images were obtained using a Jeol 3010 with an accelerating voltage of 300 kV and incorporating a Gatan CCD camera for recording images. Measurements were supported by Barbara Cressey.

2.3 Deposition calibration

2.3.1 Support materials: Carbon and sub-stoichiometric titanium dioxide

Figure 2.7 shows the deposition rate variation of titanium with changing source temperature as determined by AFM. The rate of deposition as expected increases with increasing temperature. If not otherwise quoted, sub-stoichiometric titanium dioxide films were prepared with a titanium source temperature of T_{dep} =2073 K for 30 min. The deposition rate of titanium was 1.6 ± 0.2 nm min^{-1}. A pressure of 1×10^{-7} mBar (Ion Gauge) was maintained during deposition, by constantly leaking oxygen into the chamber (collimating oxygen source). Final thicknesses of titania always fell into the range of 60 - 100 nm. Carbon depositions from the e-gun source were found to have final film thicknesses in the range of 30 - 60 nm. Approximately 60 nm thick films were also achieved using the arc deposition carbon coater (15 seconds deposition time).

During physical vapour deposition using the Knudsen source, substrate temperatures ranged between 298 – 308 K. The electron gun evaporators were found to increase the temperature to slightly higher values but with the maximum temperature never being higher then 323 K.
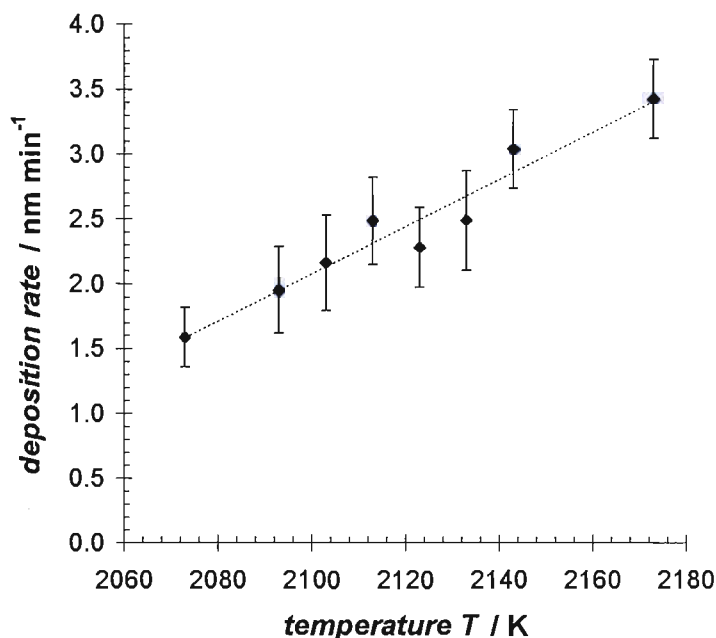
Figure 2.7. *Titanium source calibration. Deposition rate of TiO$_x$ (nm min^{-1}) as determined by AFM vs. the source temperature T.*

2.3.2 Gold calibration

The gold particles were deposited from a low temperature K-cell with source temperatures of T$_{dep}$ = 1548 K or 1623 K. These temperatures were found to yield a highly stable Au flux, equivalent to the deposition of 0.16 ± 0.015 nm min^{-1} and 0.51 ± 0.05 nm min^{-1}. Deposition rates were calculated by the deposition of several thick layers over extended times (1800 – 7200 seconds) and demonstrating that the thickness (as determined on contact masked samples by AFM) was proportional to the deposition time. Due to very low fluxes of gold, the source characteristic did not change over extended periods of time (several months) because the fill level remains almost constant and the deposition characteristics were frequently checked by test wafers.

To achieve particle covered surfaces, the deposition times were short leading to nominal thicknesses < 3 nm (see chapter 3).

Variable coverages over the substrate were deposited under the same conditions using the fixed "wedge" shutter technique [24]. The characteristics of the "wedge" growth were established (Figure 2.8) from AFM and ellipsometry measurements of gold deposited for times sufficient to achieve continuous films, and concomitantly lower times were used subsequently to achieve the lower equivalent coverages required for particle growth.
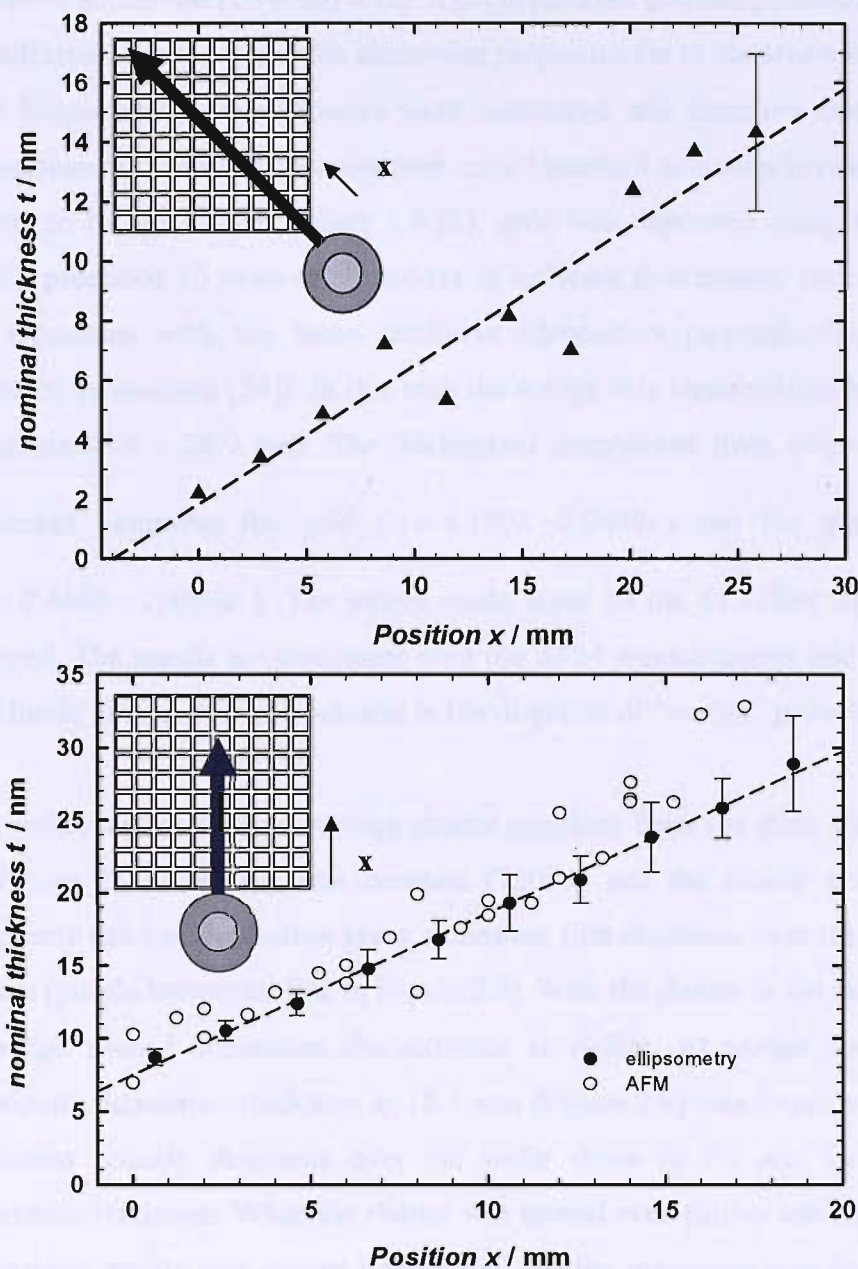
Figure 2.8. *Thickness determination of gold deposition onto a bare silicon wafer using a 10 x 10 contact mask in two geometries (see inset) using (a) AFM along the diagonal of an array of 100 electrodes, and (b) using AFM and ellipsometry for a deposition geometry which allowed an averaging 10 fields of identical thickness across the "wedge"(see insets). The source temperatures and deposition times were (a) 1548 K, 7200 s and (b) 1623 K and 4500 s.*

Two examples are shown in Figure 2.8, with different orientations of the source with respect to the substrate (samples deposited in chamber I show a diagonal deposition profile and from chamber II perpendicular), and different shutter positions. In Figure 2.8 (a), a uniform thickness of ca. 18 nm would be achieved in the absence of the wedge shutter. AFM measurements show a variation of a factor of seven in coverage is

achieved across the (10 x 10) array. This deposition geometry produces electrodes with 19 different coverages and the electrodes perpendicular to the arrow should be identical. The Ellipsometry measurements were automated and therefore faster then the AFM measurements. Also the measurement error (standard deviation between measurements) seems to be smaller. In Figure 2.8 (b), gold was deposited using a geometry (inset) which produced 10 rows of electrodes of different thicknesses, each row consisting of 10 electrodes with the same thickness (deposition perpendicular to the "wedge" direction is constant [24]). In this case the wedge was characterised by less variation of thickness (8.9 – 28.9 nm). The thicknesses determined from ellipsometry have been estimated assuming for gold ($\tilde{n} = 4.1502 - 0.0449i$) and for the silicon substrate ($\tilde{n} = 0.4666 - 2.4083i$). The native oxide layer on the Si before deposition has been ignored. The results are consistent with the AFM measurements and indicate a smooth and linear change in film thickness in the direction of "wedge" growth.

The influences of different wedge shutter positions from the same source are presented in Figure 2.9. The time was constant (7200s.) and the shutter position was varied. Evidently the free deposition gives a constant film thickness over the silicon wafer of ~ 61 nm (purple horizontal line in Figure 2.9). With the shutter in the atomic beam of gold a wedge shaped deposition characteristic is visible. At wedge position of 65% the maximum deposition thickness at 18.6 mm (Figure 2.9) was found to be 28.1 nm. This thickness linearly decreases over the wafer down to 8.2 nm, i.e. to 29 % of the maximum thickness. When the shutter was moved even further into the atomic beam the deposition profile was moved downwards and the maximum was found to be 21.1 nm linearly decreasing to ~ 0 % at the position closest to the source. Note that the 70 % fit excluded the measurements at 0.6 and 2.6 mm, because they deviated from the expected linear behaviour, this is probably because of different optical properties at very low coverage of gold (grain boundaries, surface roughness, particle sizes etc.[310-314]). Also the native oxide on silicon (on substrates used here typical oxide thicknesses of 0.5 nm and 1.5 nm have been found) influences the measurements more strongly.
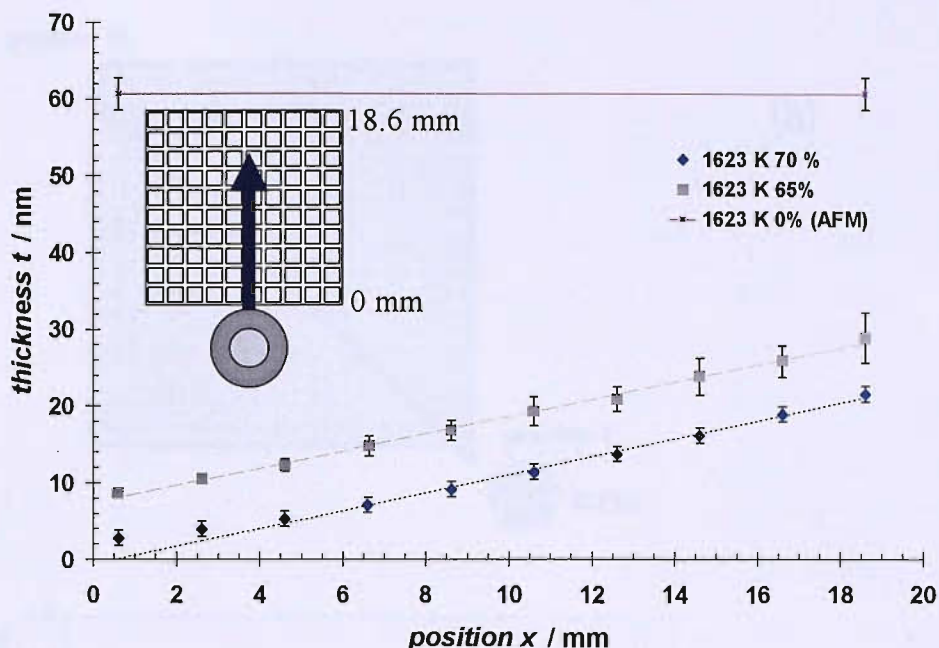
Figure 2.9. *Thickness t determination of masked gold samples on Silicon wafers applying different wedge shutter positions. The thickness of the free uninfluenced measurement (wedge shutter 0%) was measured by AFM, due to the opaque film thickness and the wedge position of 65 and 70% were analysed by Ellipsometry. Temperature of the source 1623 K and the deposition time was 7200s.*

Alternatively the samples were analysed by energy dispersive spectroscopy. Figure 2.10 (a) shows a set of results for the ratio of the atomic percent of gold to the sum of all elements (Silicon, carbon and gold). Measurements were taken at one hundred points. The carbon was deposited from the e-gun for 1800 s and gold was deposited from a K-cell placed at an angle of 120° in respect to the wafer at 1548K for 3600s. The percentages varied as expected from the source position from the minimum at the bottom right corner with 0.1% to the maximum in the top right corner with 1.2 %. In Figure 2.10 (b) the average of the pads perpendicular to the deposition axis of the wafer are shown. The wedge shaped deposition characteristic is clearly visible. This technique is able to show qualitative trends, but is lacking in accuracy at lower coverage, because of the signal to noise ratio during the measurement. For alloy particle work it would be a powerful tool to analyse the relative compositions of the particles.
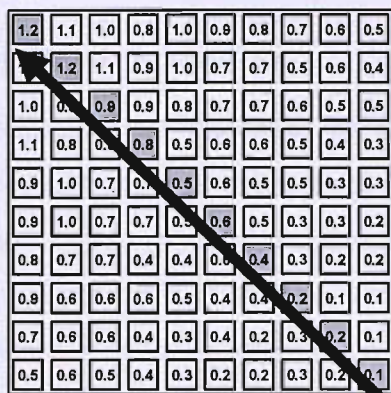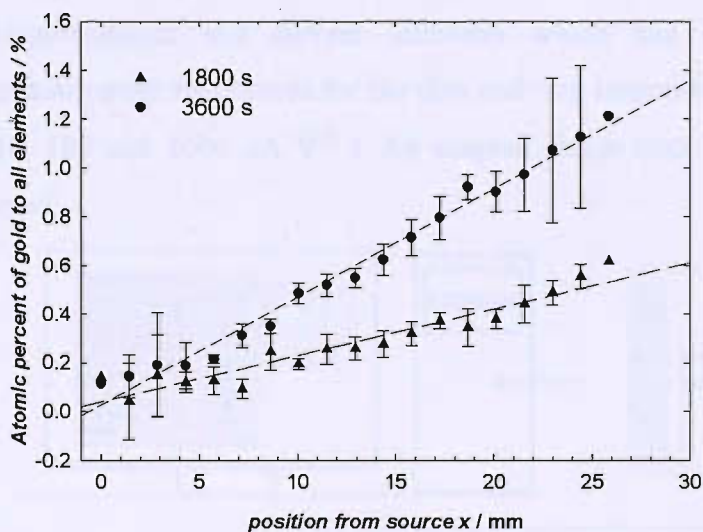
Figure 2.10. *Energy dispersive spectroscopy measurement of carbon supported gold samples. The gold was deposited at 1548 K for either 1800 or 3600 s. (a) Shows the ratio of the atomic percent of gold at the 100 measurement points at the wafer to the sum of all atomic percentages (carbon, silicon and gold). The source and deposition axis is also shown. In (b) the average of the pads perpendicular to the deposition axis of the wafer are shown. The errors are given as the standard measurement error of the pads with the same coverage as calculated from $\mu = \dfrac{t \cdot \sigma}{\sqrt{n}}$, where t is the student factor, σ the standard deviation and n the number of measurements.*

2.4 Electrochemical measurements

2.4.1 Instrumentation

The electrochemical responses of the 100 electrodes in the array were measured simultaneously using a potentiostat, two 64 channel current followers and two data acquisition cards controlled/monitored by a PC as shown in Figure 2.11. The data was then visualised with software written in the laboratory. The software allowed simultaneous monitoring either of the current, or single cyclic voltammograms (CV) or potential step experiments at each of the 100 electrodes. This instrumentation has been described previously [19], but the sensitivities of the current followers used here were 10 $\mu A\ V^{-1}$. A similar set up was used for the single electrode measurements, but with a bi-potentiostat and current followers which had the ability to switch between measurement resistances for the disc and ring responses and therefore the sensitivity (1, 10, 100 and 1000 $\mu A\ V^{-1}$). An adapted single electrode version of the software was used.
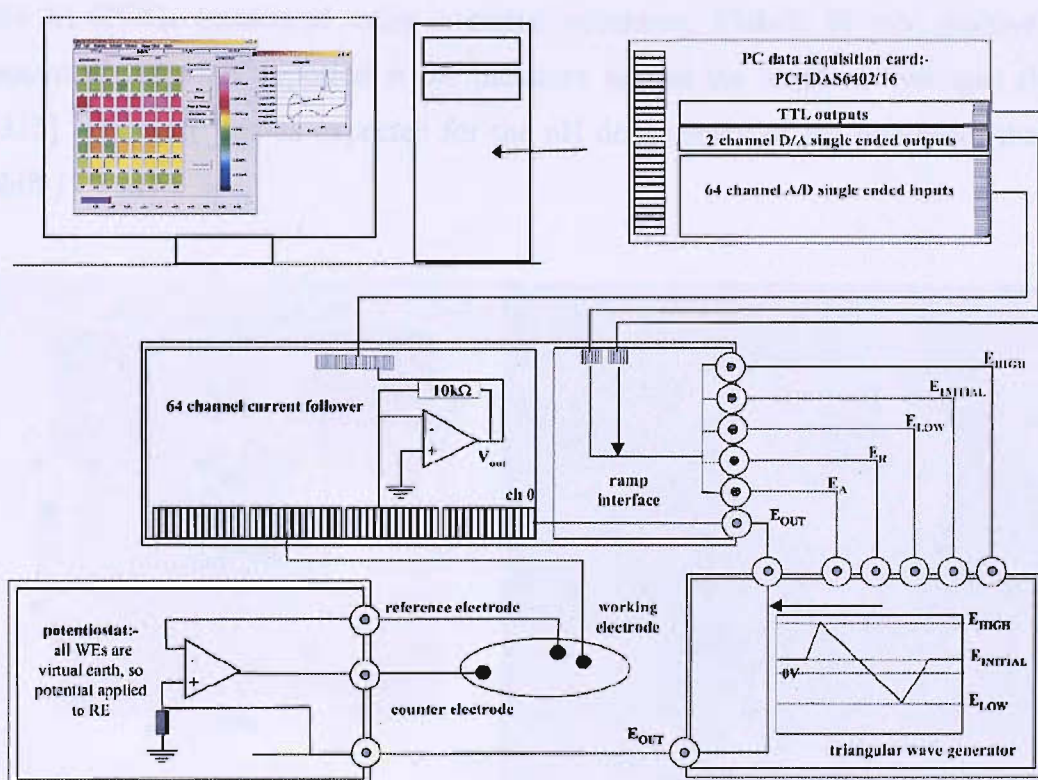
Figure 2.11. *Electrochemical screening instrumentation, consistent of wave generator, potentiostat, current follower and a PC with a data acquisition card [19].*

2.4.1.1 Array electrode cell

The electrochemical experiments with the arrays were carried out at room temperature in a cell where the body of working electrode compartment is made from PTFE (c.f. Figure 2.12 (b)). The Au gauze counter-electrode (Goodfellow, Au-mesh 99.9%) is in a glass compartment separated from the working electrode compartment by a glass sinter. The array as shown in Figure 2.12 (a) was situated in an indentation of a PTFE plate to ensure precise positioning. Electrical contact was made by pressing modified IC connectors fitted on a circuit board onto the electrical pads of the array wafer (c.f. chapter 2.1.1.3.). Note that the PTFE cell (round, white part in the centre of Figure 2.12 (b) is sealed against the sample wafer using a Viton® seal. The gasket was boiled before experiments in ultra-pure water for 30 minutes to prevent contaminant leaching. The experimental reference electrode was a commercial (Sentec) mercury/mercuric-sulphate electrode (0.5 M H_2SO_4) whose tip was placed close to the array. All potentials presented in this thesis, however, are reported against the reversible hydrogen electrode in 0.5 M $HClO_4$ (RHE). Typically the potential was close to 0.698 ± 0.009 V vs. RHE in 0.5 M $HClO_4$ (measured using a digital voltmeter, Fluke), 18 mV positive to the potential of 0.68 V reported in the literature against the standard hydrogen electrode [315]. The shift was as expected for the pH dependency of the reference (theoretical shift 17.8 mV).
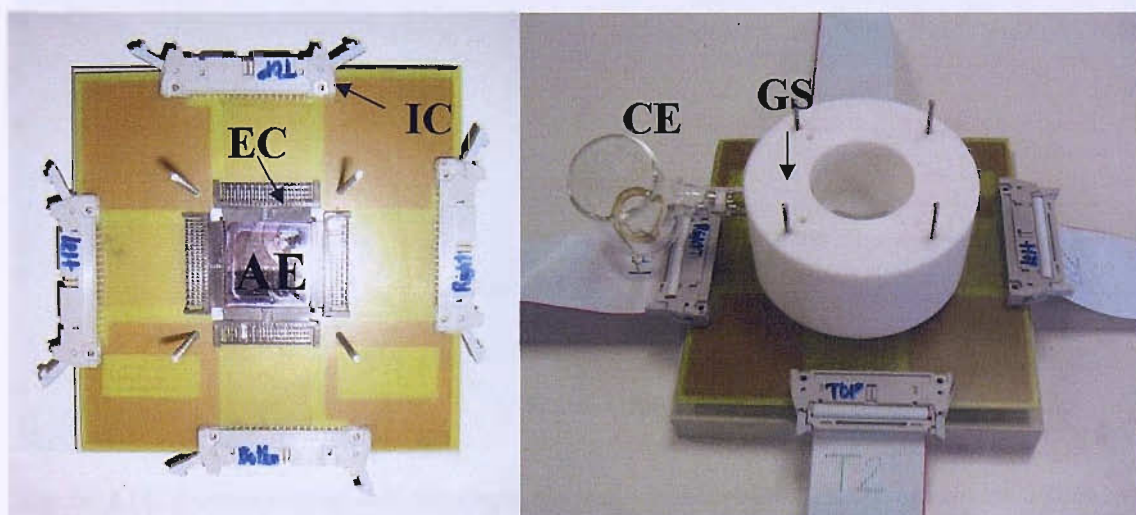

Figure 2.12. *(a) Circuit board and array electrode wafer. Abbreviations: EC-modified IC connector for the electrical connection to the wafer, IC-IC-connector (b) Cell assembly: PTFE cell, Counter electrode compartment (CE) and electrical connections.*

2.4.1.2 *Electrochemical cell and rotator for single electrode measurements*

The rotating disc electrode measurements were carried out in a standard three electrode/three compartment, glass cell with a Haber-Luggin capillary. It also had a water jacket to maintain a constant temperature of 298 K, water being pumped from a thermostatically controlled water bath (Grant). In Figure 2.13 the three compartment cell used for the measurements is presented. The gold counter electrode compartment (counter electrode: Goodfellow Au-mesh, 99.9 %) was separated from the working electrode compartment by a glass frit. Gases (like argon, oxygen and carbon monoxide) can either be bled over the surface for measurements in quiescent solution or by turning a switching valve to "bubble" them through the solution. A glass sinter ensures fine dispersion of the gases. The experimental reference electrode was again a commercial (Sentec) mercury/mercuric-sulphate electrode (0.5 M H_2SO_4) placed in the Reference compartment. All potentials presented in this thesis, however, are reported against the reversible hydrogen electrode in 0.5 M $HClO_4$ (RHE).
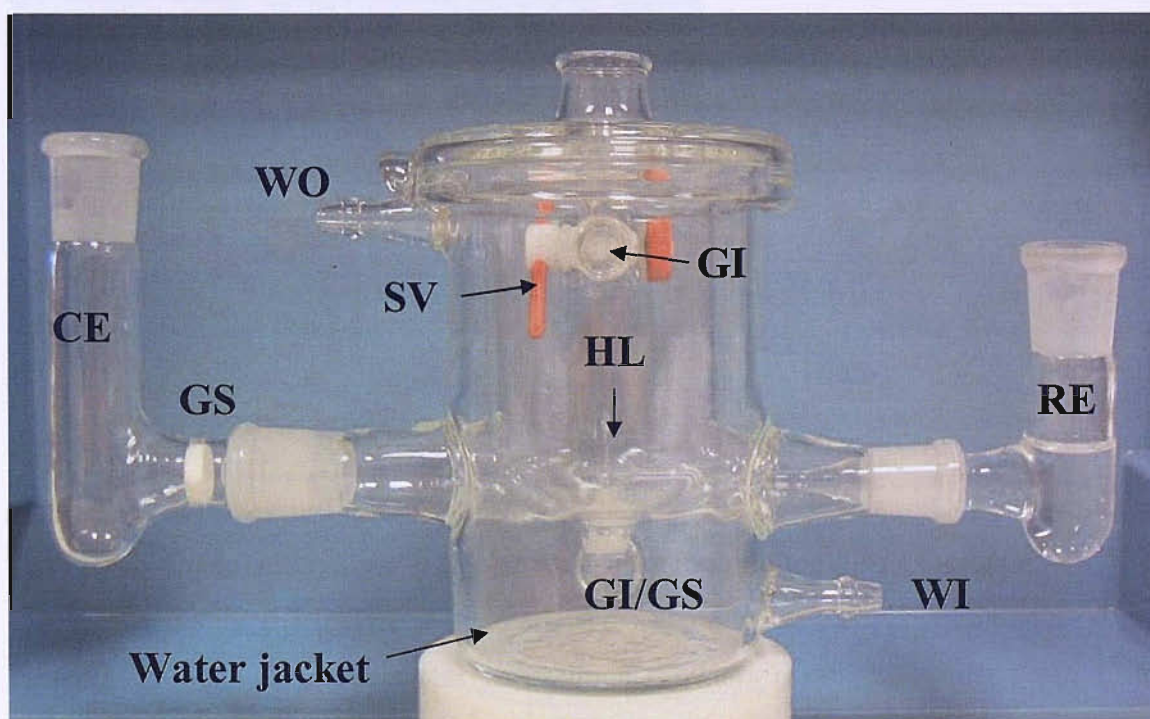

Figure 2.13. *Electrochemical cell for single electrode measurements. Abbreviation explanation: CE-Counter electrode compartment, GS - glass sinter, WO - water outlet, HL - Haber-Luggin capillary, GI/GS - glass inlet with glass sinter, WI - water inlet, SV - switching valve and RE - reference electrode compartment.*

In Figure 2.14 the rotator and the exchangeable disc system are shown (all Pine Research Instrumentation: Modulated Speed Rotator (MSR) and E4 Series ChangeDisk RDE Tips or E6 Series ChangeDisk RRDE Tips). For measurements on "polycrystalline" gold, referred to later as a bulk gold a disc was prepared by melting gold foil (Alfa Aesar, Premion® 99.9985%) and machining it to a 2.5 mm length, 5 mm diameter Au-rod. One end of the cut rod was then abraded using sand paper (400 and 600 grit) and then polished manually using alumina powder (Buehler, grain sizes of 1, 0.3, 0.05μm).
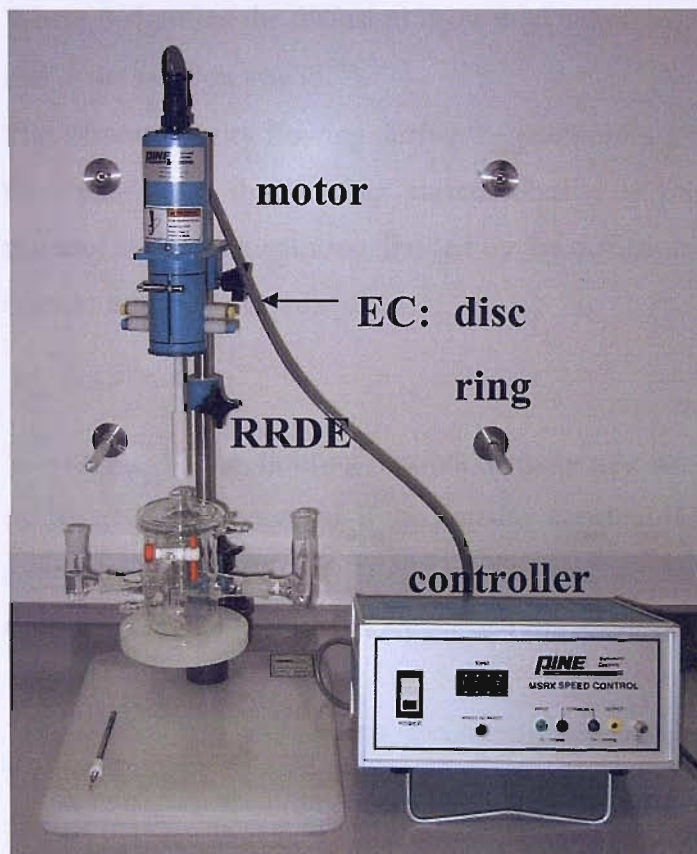

Figure 2.14 *Pine instrument rotator with controller unit.*

In order to obtain purely kinetic information from the rotating disc experiments (RDE), one has to distinguish between mass transport and kinetic control component of the currents during electrochemical experiments. The mass transport regime in electrochemistry is subdivided into: (i) diffusion, due to a gradient in concentration following Fick's laws (ii) convection, defined as a flow of species provoked by a mechanical force, (iii) migration, provoked by a potential gradient in solution. If the mass transport regime of an experiment is exactly known, interpretation of reaction kinetics are possible.

In RDE experiments the convection to the electrode is well defined, dominating all other forms of mass transport, and mathematical solutions can be found in a number of electrochemistry texts (e.g. [315]). In brief, a laminar flow to the electrode is forced by the rotation velocity. This convection control allows the derivation of equations which describe the solution flow and therefore the variation of diffusion layer thickness with the rotation rate. In the steady state the Nernst diffusion layer thickness is given by:

$$\delta = 1.61\omega^{-\frac{1}{2}}\nu^{\frac{1}{6}}D^{\frac{1}{3}} \qquad\qquad (2.3)$$

Where δ signifies the diffusion layer thickness (cm), ν the kinematic viscosity ($cm^2\ s^{-1}$) and ω the rotation rate (s^{-1}).

The current density flowing during the reaction is limited by the transport of reactant to the surface, i.e. the limiting current density is proportional to the concentration of reactant in the bulk solution divided by the diffusion layer thickness in case the reaction is mass transport controlled:

$$j_{lim} = nFD\frac{c_o}{\delta} \qquad\qquad (2.4)$$

Where j_{lim} is the limiting current density ($A\ cm^{-2}$), n is the number of electrons exchanged in the reaction, F the Faraday constant ($C\ mol^{-1}$), D the diffusion coefficient ($cm^2\ s^{-1}$), A the area (cm^2) and c_0 the bulk concentration of reactant ($mol\ cm^{-3}$). If equation 3 is incorporated in equation 4 the result is the so called Levich equation:

$$j_{lim} = 0.62nFD^{\frac{2}{3}}\omega^{\frac{1}{2}}\nu^{-\frac{1}{6}}c_o \qquad\qquad (2.5)$$

To obtain pure kinetic information from polarization data the Koutecký-Levich equation is used [315].

$$\frac{1}{j} = \frac{1}{j_k} + \frac{1}{j_{lim}} = \frac{1}{j_k} + \frac{1}{0,62nFD^{\frac{2}{3}}\omega^{\frac{1}{2}}\nu^{-\frac{1}{6}}c_o} \qquad\qquad (2.6)$$

Here j_k is the kinetic current density ($A\ cm^2$) uninfluenced by mass transfer. The inverse current density j observed at each potential is plotted against the square root of inverse rotation rate $\omega^{-1/2}$. By extrapolation of the resulting linear plots to $\omega^{-1/2} \rightarrow 0$, (i.e. infinite rotation rate) the intercept represents the inverse kinetic current.

Specific activities measured by RDE were always quoted as the kinetic current density calculated from equation 6 normalized for the "real" surface area of the catalyst. The real surface area was either determined by TEM measurements (as described in chapter 3) or electrochemically by integrating the gold oxide reduction peak from the

voltammogram. The potential, where a monolayer of gold oxide was assumed to be formed at 1.63 V vs. RHE and the associated charge was ~ 400 mC cm^{-2}.[6]

2.4.2 Electrochemical measurements: parameters and techniques

Generally cyclic voltammetry and chronoamperometry (potential step experiments) were carried out at both the arrays and discs. The scan rate v was commonly 100 mV s^{-1} during RDE experiments and 50 mV s^{-1} at the array electrodes. The activities for oxygen reduction and carbon monoxide oxidation at the array of electrodes were assessed by chronoamperometry. The step potentials during chronoamperometry were reaction dependent, i.e. dependent on the gas used to saturate the electrolyte (0.5 M HClO$_4$) and are listed in Table 2.1.

Table 2.1. *Parameters used during Chronoamperometry.*

Reaction	Initial potential[*1] / V	Ht[*2] / s	Step 1 / V	Step 2 / V	Step 3 / V	Step 4 / V	Step 5 / V	Hts[*3] / s
Oxygen reduction	0.8	45	0.5	0.4	0.3	0.4	0.5	90
CO oxidation	0 or 0.05	45	0.3	0.35	0.4	0.5	0.6	90

[*1] potential where no reaction is expected to occur. For the ORR the initial also is the final potential
[*2] Ht - holding time at initial potential
[*3] Hts - holding time per step

At rotating disc electrodes, steady state voltammograms were recorded at a scan rate of v = 20 mV s^{-1} at rotation rates of 400, 900, 1600 and 2500 rpm. The potential limits varied for the different reactions. For the oxygen reduction reaction the potential range varied between the upper potential limit around E_u = 1.0 V and the lower E_L = - 0.3 V. For activity measurement, the currents during the negative going scan at 0.5, 0.4 and 0.3

---

[6] As discussed in the background section gold paticles mainly expose (111) and (100) low index planes to the electrolyte. The assumed charge of 400 mC cm^{-2} is just an approximation.

low index planes of Au	surface Atoms cm^{-2}	Charge associated with a monolayer gold oxide / μC cm^{-2}
111	1.38 x 10^{15}	442
100	1.19 x 10^{15}	381
110	0.84 x 10^{15}	269

V analogously to the step experiments were measured and corrected for mass transport influences using a Koutecký-Levich correction as described above. The limiting current was measured at potentials between 0 V and - 0.1 V, where the limiting current densities were similar and independent of the gold surface area.

The combinatorial electrochemical experiments are best clarified by an example. Figure 2.15 illustrates a convenient presentation of electrochemical experiments at an electrode array that allows a rapid preliminary assessment of the data and identification of trends; more detailed and quantitative analysis requires different presentations. The figure shows both a set of cyclic voltammograms in deoxygenated 0.5 M perchloric acid and a set of potential step experiments in oxygen saturated 0.5 M perchloric acid. In both Figure 2.15 (a) and Figure 2.15 (b), the arrow shows the direction from the source during deposition. Here the highest coverage can be found in the top left hand corner and the lowest in the bottom right hand corner (in fact, in this array the upper left hand corner corresponds to a nominal gold thickness of 1.8 nm and the lower right hand corner to a nominal thickness of 0.21 nm). Perpendicular to this arrow, the Au coverage should be uniform and the surfaces should be identical. In this study of particle size effects, the single array gives 19 data points since the electrodes immediately adjacent to those on the diagonal provide intermediate particle sizes to those on the diagonal.
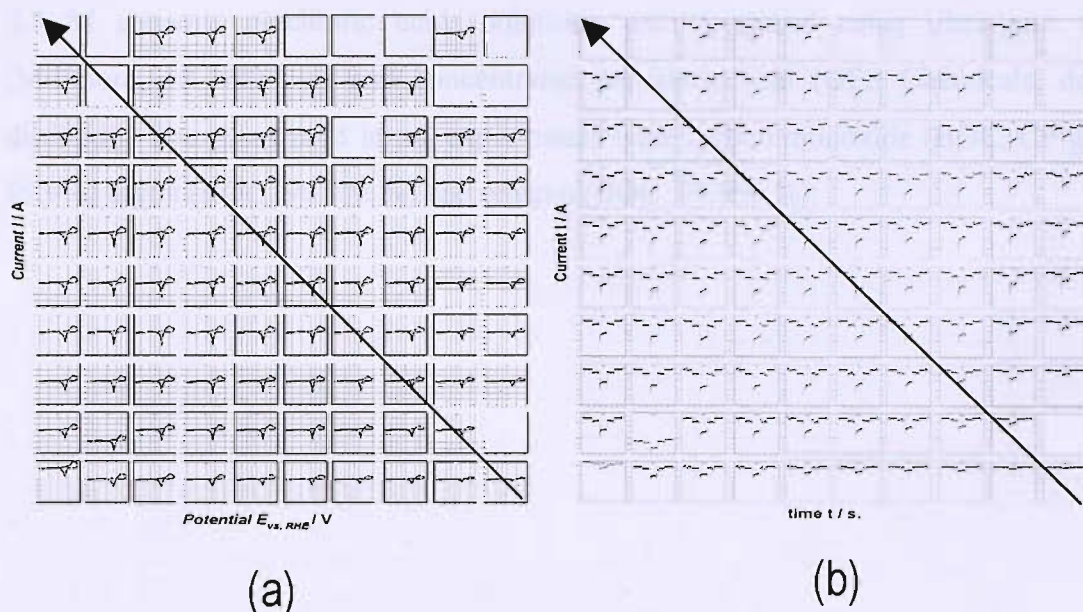
Figure 2.15. *(a) Cyclic voltammetry (v =100 mV s⁻¹, between 0 V and 1.63 V) on a 100 electrode array of carbon supported gold particles in argon purged solution (b) Oxygen reduction at the same array electrode as determined by potential step measurements from 0.8 V (baseline, 60 s.) to 0.5 V (90 s.), 0.40 V (90 s.) and 0.3 V (90 s.) in oxygen saturated solution. All measurements were made in 0.5 M HClO₄ electrolyte at room temperature. The arrows indicate the direction of the graduated flux; in this array the upper left hand corner corresponds to a nominal gold thickness of 1.8 nm and the lower right hand corner to a nominal thickness of 0.21 nm.*

From the magnitude of the gold oxide formation/reduction peaks on the cyclic voltammograms of Figure 2.15 (a), it can clearly be seen that, qualitatively, the surface area of the gold centres is decreasing down the diagonal while perpendicular to the arrows the voltammograms are similar. Empty panels are electrodes, where electrical contact has been lost during measurements. Similarly, it can be seen from the potential step experiments that, at least quantitatively, the oxygen reduction currents reflect this trend in surface area. Figure 2.15 also shows some limitations of the cell used for the electrochemical experiments in this project. Firstly, the blank positions in the presentation of the array shown indicate electrodes where electrical contact has been broken during positioning of the array within the cell and then sealing the cell. Secondly, in the oxygen reduction experiments, see Figure 2.15 (b), the electrodes at the edges of the array often give lower currents and this results from the proximity of a wall perpendicular to these electrodes. In consequence, the cell has since been redesigned to overcome these limitations and also to allow temperature control.

2.4.2.1   *Chemicals and gases used for electrochemical measurement*

0.5 M aqueous perchloric acids solutions were prepared using ultra-pure water (Millipore, 18 MΩ cm) and concentrated perchloric acid (GFS Chemicals, double distilled). The gases used in the experiments were carbon monoxide (BOC, CP grade, 99.9%) argon (BOC, 99.998 %) and oxygen (BOC, 99.999 %).

3 Sample characterisation

3.1 Deposition of TiO$_x$ layers

TiO$_x$ layers were initially deposited onto silicon nitride coated silicon using the Ti (K-Cell) and molecular oxygen (10^{-10} - 10^{-5} mBar) directed at the substrate using a collimating oxygen source positioned to one side of the sample as shown in the experimental section. The variation of stoichiometry was qualitatively indicated by the change in colour [35, 38] of the synthesised film with oxygen pressure and power of the atomic source radiofrequency P_{rf}. TiO$_x$ deposited with an molecular oxygen pressure of 5 x 10^{-6}, 10^{-7} and 10^{-9} mBar produced green, blue and brown (not shown) films respectively. Films deposited using atomic oxygen varied from almost transparent (high P$_{rf}$ = 400W) to green at (200 to 300W, see Figure 3.1).
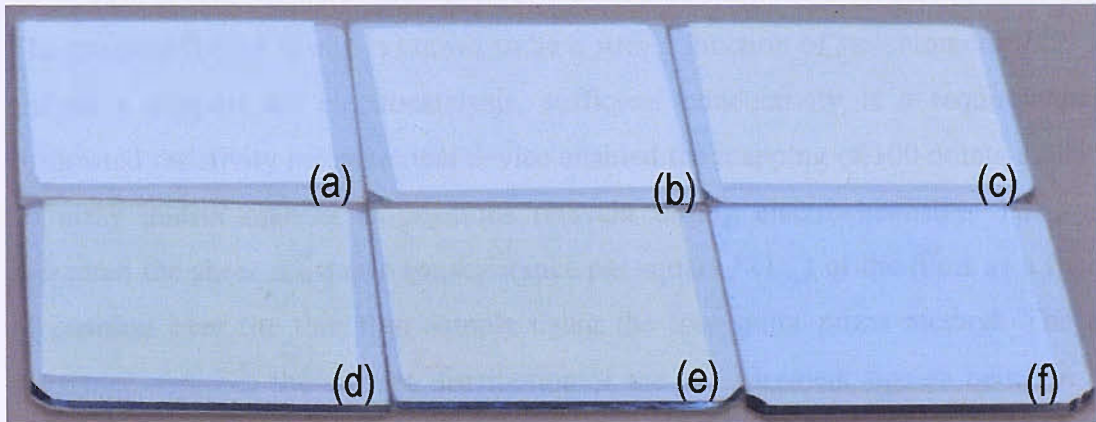

Figure 3.1. *Variation of the degree of stoichiometry of titanium dioxide films deposited on glass, prepared at a titanium source temperature of 2073 K (constant thickness) using molecular and atomic oxygen. Top left corner to bottom right: radiofrequency Power P_{rf} = 400W, (a), 300 W, (b), 250 W, (c), 200 W, (d), (films deposited by Dr Piers Anderson) and molecular oxygen at ppO$_2$ of 5 x 10^{-6}, (e), and 1 x 10^{-7} mBar, (f).*

XRD indicated that the titania films were largely amorphous at all oxygen partial pressures (see Figure 3.2), which is consistent with findings elsewhere [49]. To achieve crystalline structures Lottiaux reported that a substrate temperature of at least 623 K was necessary for thicker TiO$_2$ layers [49] (the films in their study were 35 - 70 nm). As we deposited the films at substrate temperatures of 298 - 308 K, we would expect amorphous structures.
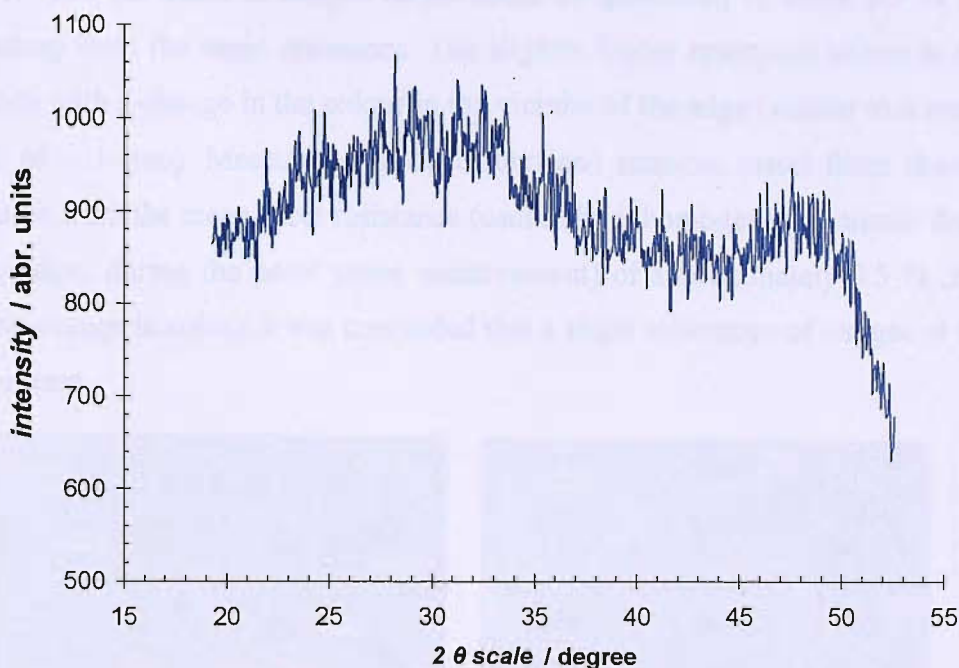
Figure 3.2. XRD measurement on sub-stoichiometric titanium dioxide (ppO2 = 5 x 10⁻⁶). X-ray exposure time 1800s (measurement taken by Dr Piers Anderson).

The conductivity of titania is known to be a strong function of stoichiometry [45, 316], and as a support for electrocatalysis, sufficient conductivity is a requirement. An automated resistivity measurement device enabled the mapping of 100 points in the 10 x 10 array matrix manner at positions relevant during electrochemistry. The system measured the sheet resistance (or resistance per square / $\Omega_{sq.}$) of the films as a function of position over the thin film sample using the four point probe method. The sheet resistance assumes the current distribution at the measurement tips as being in rings (because of the thin film geometry, see experimental section) and the material constant resistivity is then calculated by multiplication by the thickness. Figure 3.3 (a) shows a resistance map for a 66 nm thick TiO_x film prepared with an oxygen pressure of 10^{-7} mBar. There is a variation in the sheet resistance across the sample associated with a variation in stoichiometry due to the anisotropic exposure to oxygen of the titania during growth. This observation provides evidence that if optimised, collimated molecular oxygen beams may be used to synthesise graded stoichiometries of oxides for high throughput thin film synthesis. Note that the total change of resistivity would be on the same order of magnitude. The oxygen anisotropy could be overcome by rotation of the sample as shown in Figure 3.3 (b). Titania films rotated during synthesis showed a largely homogeneous stoichiometry as evident by the small resistance change across the

sample. The deviation at sample edges could be quantified to about 2.5 % (standard deviation) from the mean resistance. The slightly higher resistance values at the edges coincide with a change in the colour in the vicinity of the edge (similar to a mark with a width of ~ 1 mm). Measurements on carbon and titanium metal films showed edge deviation from the mean sheet resistance (caused by inhomogeneous current distribution at the edges during the point probe measurement) of approximately 0.5 %. From this and the change in colour it was concluded that a slight anisotropy of oxygen at the edges was present.
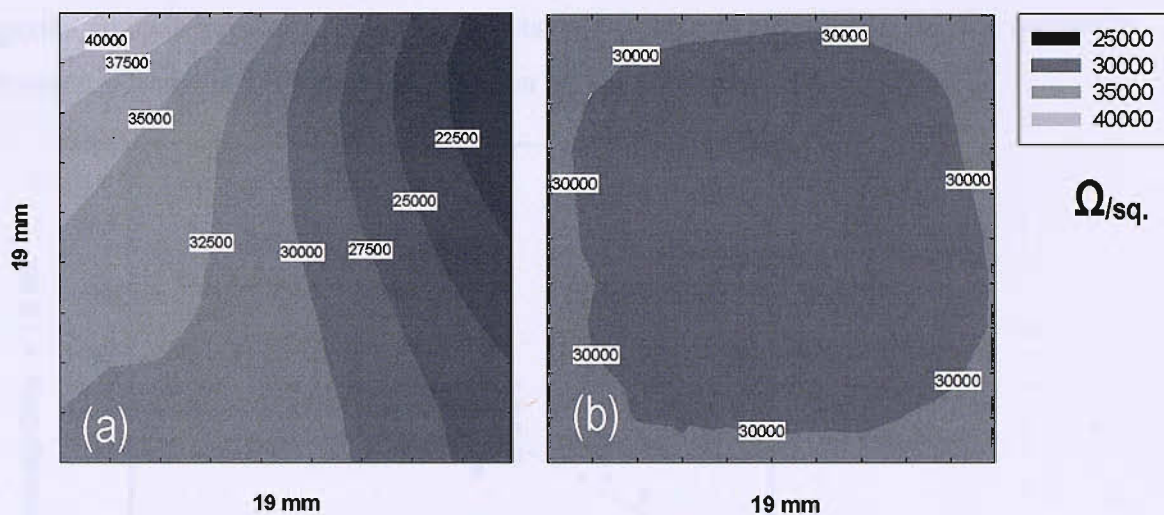

Figure 3.3. *Sheet Resistance (Ohms per square) contour plots of 100 measurement points on titania thin films. Samples prepared at a partial pressure of molecular oxygen of 1 x 10^7 mBar at a Ti K-cell temperature of 2073 K over 1800 seconds. (a) Anisotropic oxygen flow: (b) Sample rotated during deposition.*

Figure 3.4 shows the variation of the conductivity of the TiO_x film (calculated from the sheet resistances and the film thicknesses determined by AFM) as a function of the synthesis oxygen pressure. The conductivity varies over five orders of magnitude over the pressures of molecular oxygen used for synthesis. The conductivities may be associated with oxygen defects within the structure [316] that increase as the oxygen pressure is lowered during deposition. In order to estimate the stoichiometry of the TiO_x, the results were compared (Figure 3.5) to materials where both stoichiometry and conductivity are known [45, 316, 317]. For example, a significant amount of data is available because of the interest in the Magneli phases of titanium oxides, particularly Ti_4O_7 and Ti_5O_9, as corrosion resistant materials with conductivities high enough to be considered as electrodes in massive form. We conclude that the titania thin film synthesis carried out in this study using molecular oxygen produced stoichiometries in

the range x ~ 1.7 - 1.9999. We have also been able to synthesise near stoichiometric titania thin films using a plasma atom source, with concomitantly much higher resistivity (sheet resistance ~ 15 M$\Omega_{/sq.}$ $\rightarrow$ conductivity ~ 0.01 S cm^{-1}). The experimental data in Figure 3.4 was the result of measurements taken during the entire time of the project (3 years) and the scatter might be partially influenced by different base pressures in the deposition chambers, which made the determination of the partial pressure of oxygen difficult. Partial pressures of oxygen $\geq$ 1 x 10^{-7} mBar were determined by the Ion Gauge, while partial pressures below this value are referred to the partial oxygen pressures given by a mass spectrometer as the sum of the molecular (weight 32) and atomic (mass 16) oxygen partial pressures.
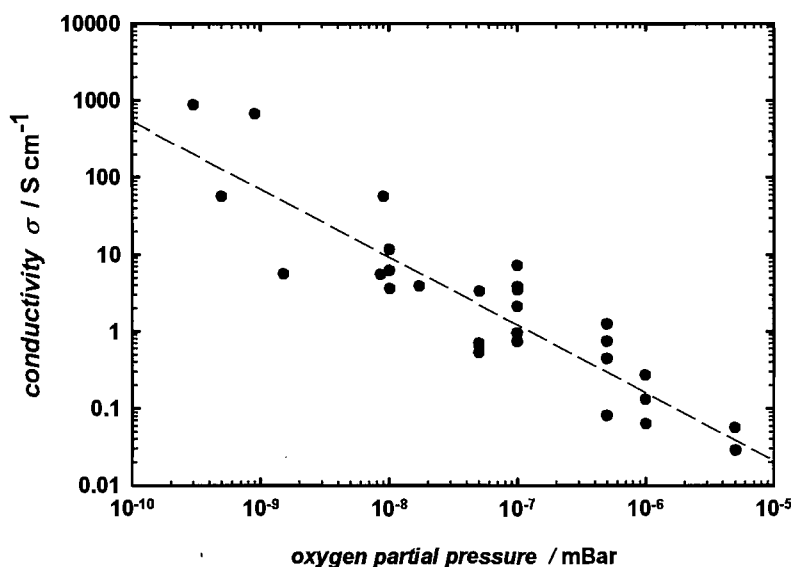

Figure 3.4. *Experimentally determined conductivities (calculated from film thickness and measured sheet resistance) of various sub-stoichiometric titania films prepared at different partial pressures of oxygen.*
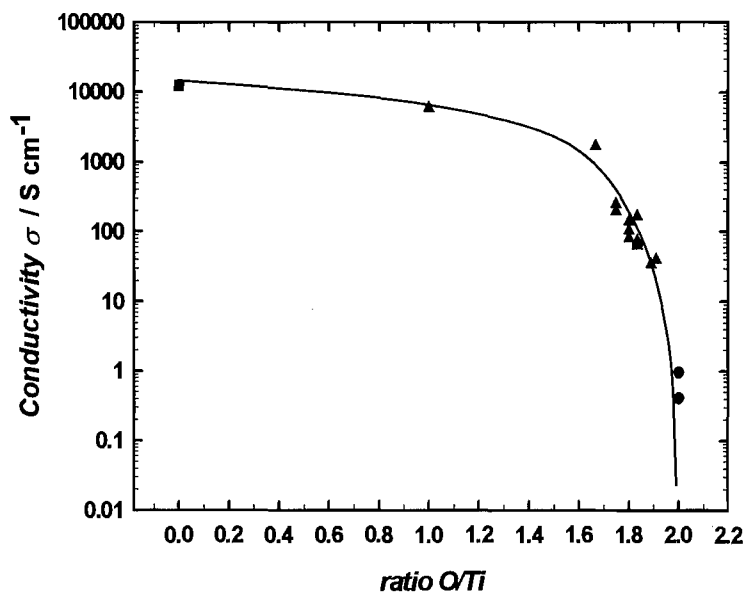
Figure 3.5.*Comparison of titania conductivities from the literature vs. the ratio of oxygen over titanium. Data taken from ■ [317] ▲ [45] ● [316].*

For the titania supported gold samples, the titania was synthesised using 1×10^{-7} mBar of molecular oxygen, corresponding to a average conductivity σ of ~ 3 S cm^{-1} and a stoichiometry of $x > \sim 1.96$ estimated from comparison with materials produced elsewhere (Figure 3.5). A linear regression of the data in (Figure 3.4) would lead to a slightly lower conductivity value of $\sigma \sim 1.2$ S cm^{-1}. Comparing this fitted conductivity value to the literature value of $\sigma \sim 1.04$ and 2.48 S cm^{-1} [316] for $TiO_{1.9999}$ and $TiO_{1.9996}$ respectively, points out a weakness of this method in determining the stoichiometry accurately. Titania with stoichiometries close to 2 varies significantly in conductivity making an exact determination of the oxygen defect concentration difficult. The stated stoichiometry for TiO_x might be better given as a range of x between 1.96 to 1.99 with a tendency to be closer to 1.99.

In Table 3.1 an attempt was made to quantify the density of oxygen deficient sites in an equivalent cubic centimetre of titania at different stoichiometries. It must be noted that the oxygen deficiencies are not exact values as the density for amorphous titania is to the best of my knowledge not quantified. Crystalline densities vary between 3.83 (anatase) and 4.24 (rutile) g cm^{-3} [35]. Also neglected was the expected change of density with varying stoichiometry. Anyway, the order of magnitude of the defect sites should be approximately correct. The striking conclusion from this calculation is that the change of conductivity of ~ 5 orders of magnitude (Figure 3.4) correlates with a

change of five orders of magnitude of the oxygen deficient sites (Table 3.1). This observation is reasonable as the oxygen deficient sites (Ti III) will act as electron donors in the band gap region of the n-type titania semiconductor.

Table 3.1. *Estimated quantity of oxygen deficient sites of selected stoichiometries of titanium dioxide (TiO$_x$)*

x	Oxygen deficient[*] sites in a cubic centimetre N$_d$ / cm^{-3}	Oxygen deficient sites at the surface (approximation no surface structure was assumed) / cm^{-2}
1.70	1.5 x 10^{22}	6 x 10^{14}
1.96	2.0 x 10^{21}	2 x 10^{14}
1.9996	2.0 x 10^{19}	7 x 10^{12}
1.9999	5.0 x 10^{18}	3 x 10^{12}

[*]Basis for the calculation of the oxygen deficiency was an assumed density of 4 g cm^{-3} (real density difficult to estimate as it varies for the different crystal structures) and a molar mass of TiO$_2$ of 80 g mol^{-1}

3.2 Deposition of carbon layers

Amorphous carbon layers have been deposited and the uniformity and resistivity of the films were investigated by four point probe measurements. The films exhibited a conductivity of ca. 3 x 10^2 S cm^{-1} (arc sputtered carbon), or 4 x 10^3 S cm^{-1} (PVD e-gun deposited) and the variation across the substrate was found to be as small as 0.5 % (Figure 3.6). The variation was found at samples edges and therefore ascribed to the edge, effecting the four point probe measurement by inhomogeneous current distribution.
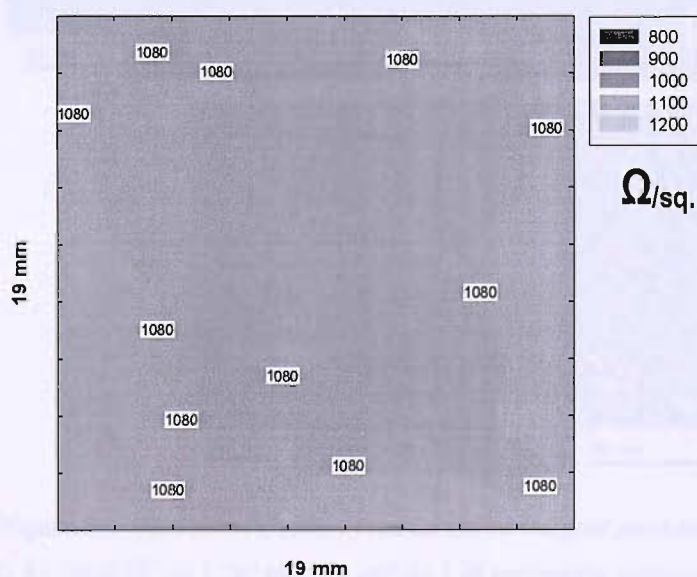

Figure 3.6. *Sheet resistance of an amorphous carbon film synthesised by arc sputtering.*

3.3   Deposition of gold nanoparticles on TiO$_x$ layers

For electrochemical studies gold was deposited using conditions defined in the "experimental" section. Gold particles were deposited onto TiO$_x$ and carbon on both arrays and Ti discs using the conditions described above, but with proportionally reduced deposition times to achieve low coverages and particle growth. Particle size distributions were measured by TEM. Both titania and carbon (ca. 20 - 60 nm thickness), and subsequently the gold, were deposited on TEM microscope grids under identical conditions to those used for other substrates (support materials were deposited for shorter times to ensure passage of the electron beam of the microscope). Figure 3.7 shows TEM images for five deposition times (50, 300, 600, 900 and 1200 seconds) corresponding respectively to nominal thicknesses of 0.13, 0.8, 1.6, 2.3 and 3.2 nm of Au on TiO$_x$ estimated from the known rate of gold deposition. The light field image clearly allows the identification of the gold particles where the base of the particle is round. Hence, it was assumed that the particles were hemispherical, distributed randomly at low coverages, and they coalesce at higher coverages (Figure 3.7 (e)).
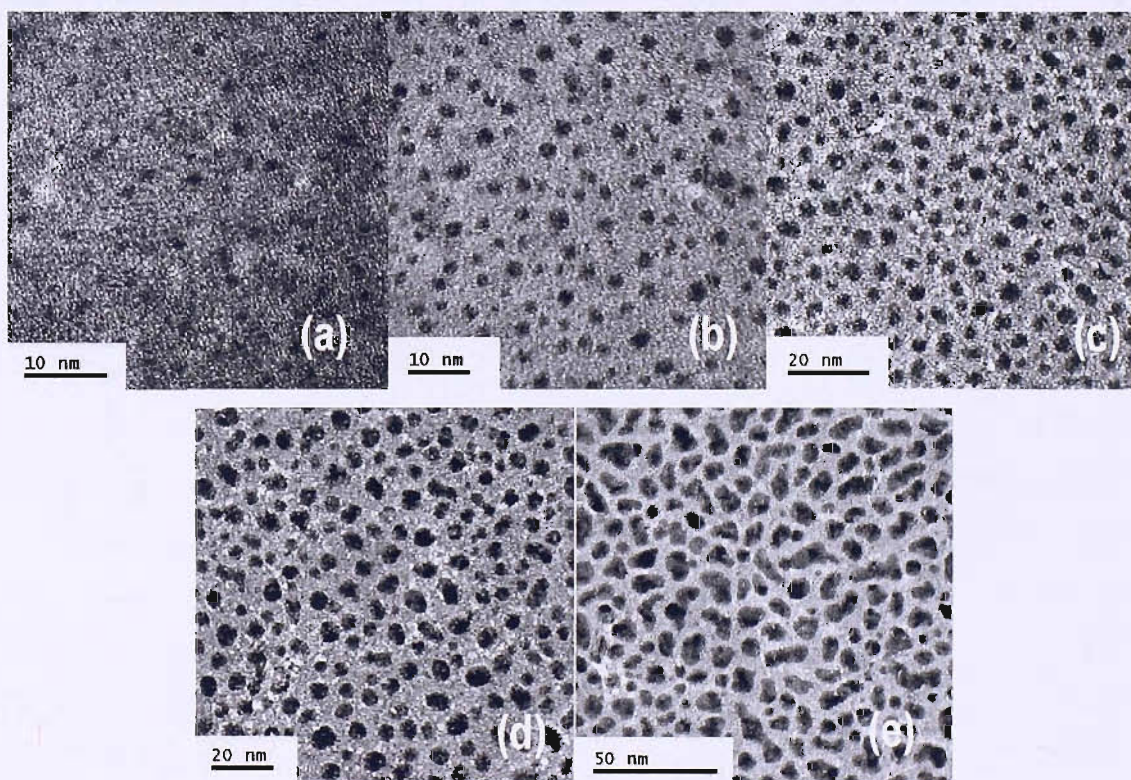

Figure 3.7. *TEM micrographs of titania supported gold particles. The nominal thickness of gold was (a) 0.13; (b) 0.78; (c) 1.56; (d) 2.33 and (e) 3.16 nm and the deposition rate was 2.6 x 10^{-3} nm s^{-1}.*

Figure 3.7 shows clearly, that the particles were randomly distributed and the approximate sizes could be estimated (see below). But the clusters at the presented magnification appeared to be round and no structural information could be obtained. The literature as summarized in the introduction described the possibility of crystalline and non crystalline morphologies of particles. Closer inspection at higher magnification allowed (for a few particles) to give some further insight to the morphology of the particle (Figure 3.8). It must be noted that there was a compromise to be made between maximum resolution and equal behaviour during nucleation and growth of the particles. For high resolution transmission electron microscopy (HTEM) the support thickness used here was 20 - 60 nm (TiO_x), i.e. relatively "thick". This support thickness was selected to obtain best resolution at similar nucleation and growth behaviour as on the electrochemistry samples.

Figure 3.8 (a) shows a titania supported gold particle of approximately 5.8 nm diameter. This image showed evidence of lattice fringes. Two orientations in an angle of approximately 100 to 110° were visible. Figure 3.8 (b) shows a possible profile and (c) presents the corresponding fast Fourier transform (FFT) pattern. The profile suggested an octagon. Another particle is shown in Figure 3.8 (d), which had a diameter of ~ 5.2 nm (vertically measured). Only very weak lattice fringes were observed. The profile of the particle appeared to have a hexagonal shape (Figure 3.8 (e), possible profile highlighted).
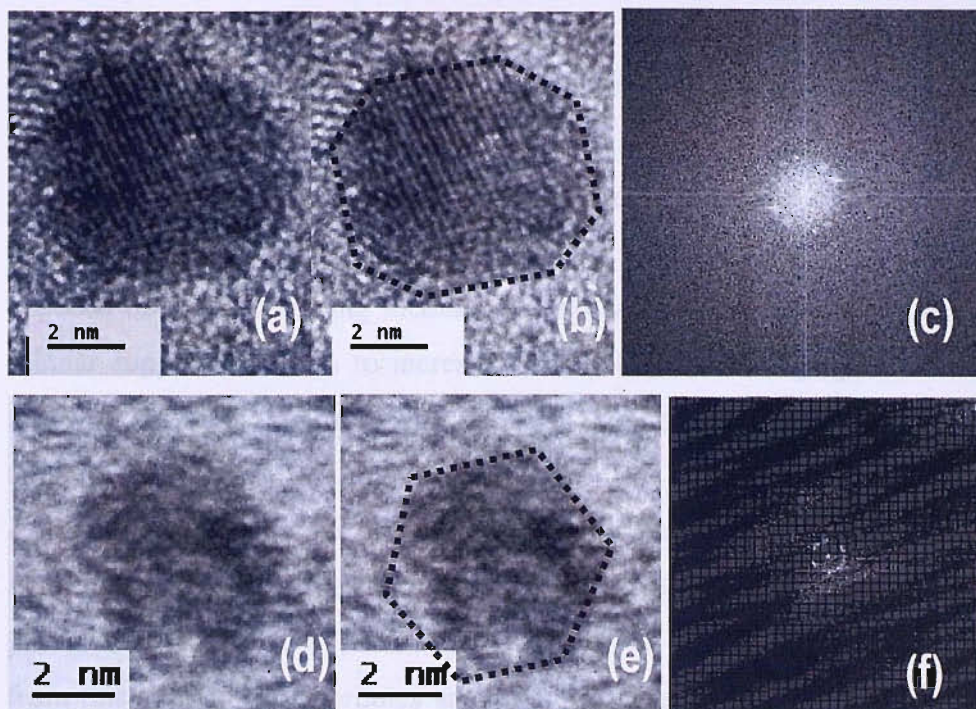
Figure 3.8. *HTEM images of titania supported gold particles. (a) Particle with a diameter d~ 5.8 nm, (b) possible profile of the previous particle with respect to the image axis, (c)FFT of the particle shown in (a and b), (d) particle with d~5.2 nm and (e) highlighted profile of (d). (f) FFT of a truncated cubo octahedral (taken from reference [319])*

The observed lattice fringes suggest that the beam along the images axis (beam strikes the atomic lattice exactly at their Bragg angle) had a crystalline orientation. As lattice fringes would not be expected in amorphous materials (particles) it could be concluded, that the particles are crystalline.

The angle between the different lattice fringes in Figure 3.8 (a and b) was close to the angle observed elsewhere for carbon supported cubo-octahedral gold particles in high resolution electron microscopy (HREM) [318]. The shape of the profile of the particle and the micrograph FFT are close to experimental as well as modelled particles with cubo-octahedral shape (in the zone axis 113 see Figure 3.8 (f) [319] or figure 14 in [320]). Therefore it was concluded that the particles might be Wulff (polyhedral) constructed as it was also suggested for titania supported gold particles by Mavrikakis et al. [321].

Clearly from the analysis of only a few particles, a general conclusion for the particle shape is not possible, i.e. the true particle shape would be for example influenced by the

number of atoms per particle (different particle sizes favour thermodynamically different structures, see Chapter 1). Presented here is evidence for crystallinity of the core of particles of around 5 nm. For non annealed particles it was reported, that the particle shell was isotropic (round, not equilibrated) while the core of the particle showed crystalline orientations [60]. Here we have seen profiles that are polygonal, suggesting anisotropic surface energy distributions, i.e. particles with low index planes exposed to the surrounding medium are likely. Further work has to be carried out on thinner support materials to increase the resolution of imaging and different imaging angles are essential to analyse the real particle shape.

A typical particle size distribution obtained from three TEM images with a nominal gold thickness of 0.78 nm is presented in Figure 3.9. For the distribution a total of 349 particles were analysed. The average particle size was found to be 2.5 nm. As evident from this example the particles are normally distributed and in the following analysis are fitted with a normal Gaussian function.
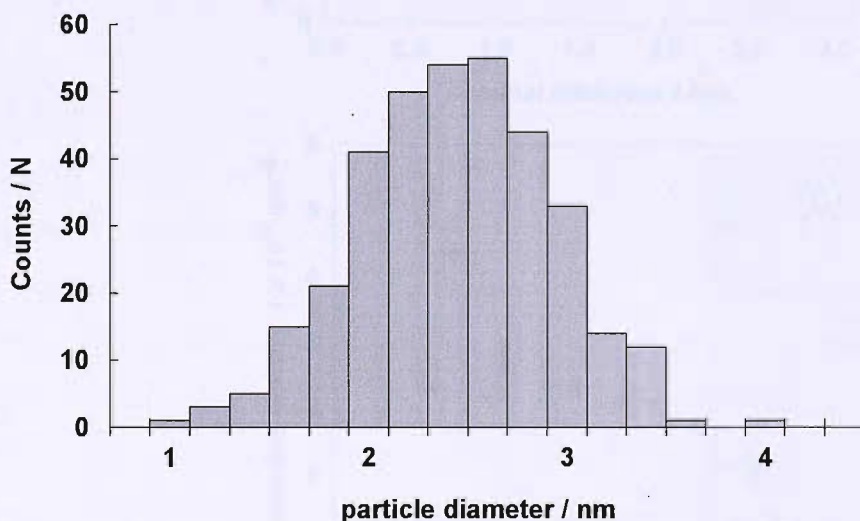
Figure 3.9. *Particle size distribution of a titania supported gold sample ($t_{nom.}$ = 0.78 nm)*

Figure 3.10 provides a quantitative analysis of the particle sizes as a function of deposition time. From the particle size distributions in Figure 3.10 (a) it is evident that at low nominal Au thickness ($t_{dep.}$ = 50 s. → $t_{nom.}$ = 0.13 nm) mean particle diameters are about 1.4 nm and fall in a narrow range of sizes. As the nominal thickness becomes higher the particle size increases and the distributions becoming broader.

77

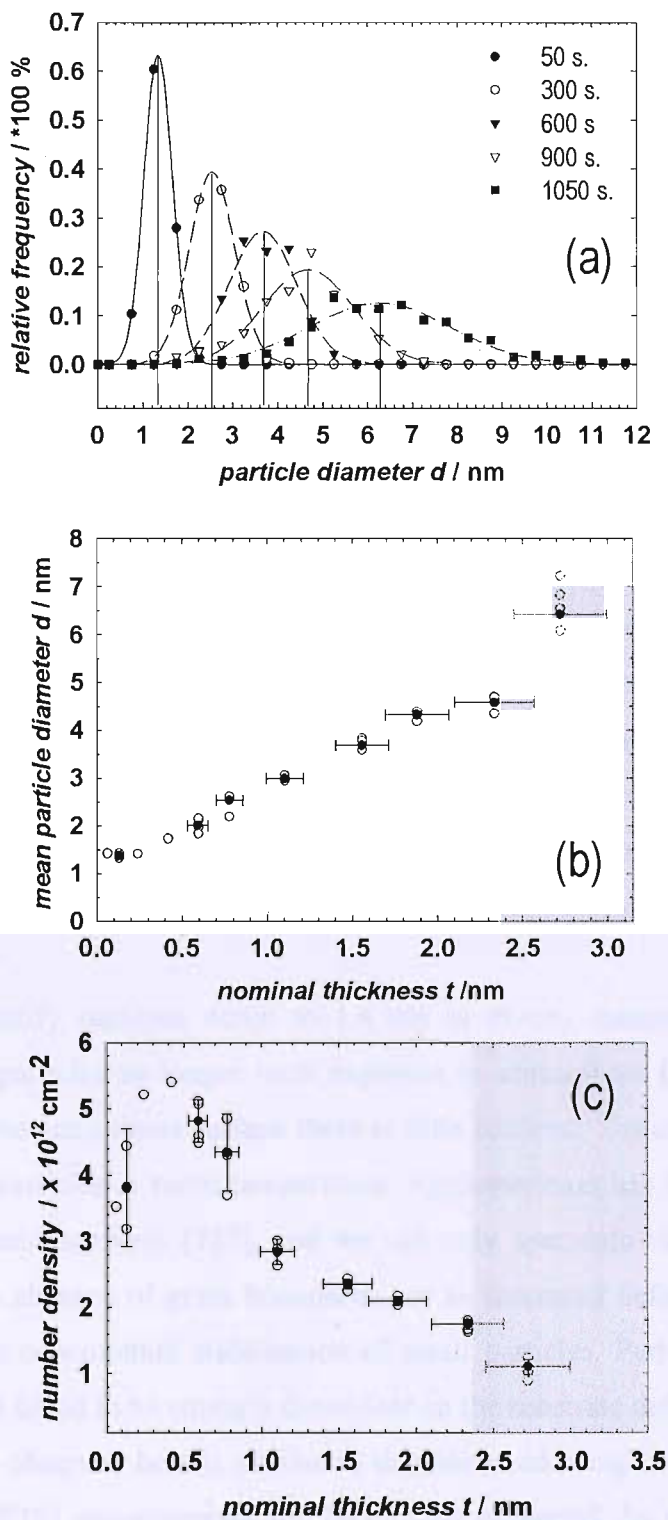**Figure 3.10.** *(a) Particle size distributions of gold particles grown on TiO$_x$ obtained from TEM measurements. Gold deposition times are shown in the figure. The data was fitted to a normal Gaussian function. (b) The mean particle size of gold. (c) The number density of particles per cm^2. The grey areas in (b) and (c) indicate nominal thicknesses where particle coalescence is likely.*

78

The change in mean particle size as a function of nominal thickness is shown in Figure 3.10 (b), and the number density is shown in Figure 3.10 (c). Initial stages of growth are characterised by an increase in the number of particles at near constant particle size (1.4 nm) in the range of nominal thickness of gold of 0.06 to 0.24 nm. This is followed by a linear increase in particle size and reduction in number density. This initial growth stage is associated with Au particle nucleation at titania defect sites. Several authors report that the binding of gold to stoichiometric titania is weak [81, 83] and binding is only favoured by higher adsorption energies to surface oxygen deficient sites (oxygen vacancies) [83-85]. Therefore the observed growth mechanism is best described by a Vollmer-Weber growth mode (refer to introduction). The maximum density of particles at one centimetre square was found to be 5.5 x 10^{12} cm^{-2}. The comparison of the maximum particle density with the above concluded range of stoichiometry (1.96 to 1.99) and the rough estimate according surface oxygen deficient sites (Table 3.1) shows that the number of surface vacancies and the particle number density are on the same order of magnitude for stoichiometries closer to 1.99, assuming one oxygen vacancy site per particle. Higher stoichiometries would lead to the conclusion that there is a possibility that particle are bound to more than one oxygen deficient site.

The ability to identify particles down to 1.4 nm in ex-situ measurements, and the stability of these particles to longer term exposure to atmosphere (over six months) indicates that on the amorphous surface there is little tendency towards migration and agglomeration of particles at room temperature. Agglomeration has been observed on polycrystalline titania supports [322], and we can only speculate that this difference may be due to the absence of grain boundaries, or an increased defect density on our substrates, and the concomitant stabilisation of small particles. Particle sintering and hence stability was found to be strongly dependent on the substrate defect density [323]. The growth mode observed here is similar to that observed using in-situ Low Energy Ions Scattering (LEIS) measurements for TiO$_2$ (110) supported Au particles [75] and subsequently ex-situ high resolution SEM [88], with the main difference being that the number of nucleation sites is larger and the observed particle sizes are smaller on the amorphous titania substrates. The latter may simply be associated with the higher defect density on the amorphous titania, and interestingly they also report that the particles are stable in air [88].

Figure 3.11 reports the titania surface coverage by gold for the different samples. Nominal thicknesses higher than ~ 10 monolayers (ML) were excluded due to starting coalescence of the particles and therefore inaccurate calculation of the coverage. Also shown is a layer growth pattern[7] (2D), where the gold would grow layer by layer. This presentation suggested again, that only at the initial growth (fraction of a monolayer) stages a 2D growth pattern with subsequent particle thickening. At a nominal thickness of ~ 0.5 nm the slope changes coinciding with the maximum density of particles observed (Figure 3.10 (c)). Parker at al. reported a monolayer growth pattern only at the initial stages of synthesis [80]. They concluded that energetically a monolayer growth is favoured over thickening (associated energy barrier of an atom stepping up to form multilayered structure is less favourable) of gold clusters until a critical thickness. For gold on sputter induced defected titania (110) surfaces at 293 K they found a critical coverage of 0.22 ML.
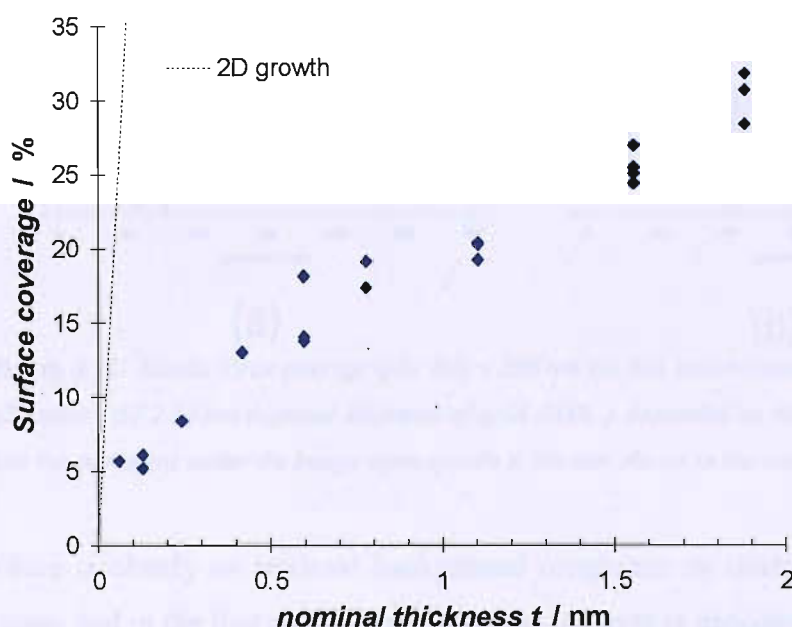
Figure 3.11. *Surface coverage of gold at different nominal thicknesses. Dashed line shows a 2D growth pattern.*

Figure 3.12 shows atomic force micrographs of (a) sub-stoichiometric titania, prepared at a partial pressure of oxygen of 1×10^{-7} mBar and (b) gold nanoparticles of a mean

---

[7] The 2D growth was based on a gold (111) monolayer with a thickness of 0.235 nm, i.e. at a nominal deposition thickness of 0.235 nm the surface coverage following a "Frank van der Merwe" like growth mode would be 100%.

particle diameter of 4.58 nm prepared on the same support. Both samples have been prepared on silicon wafer substrates and the imaged area was 500 x 500 nm.

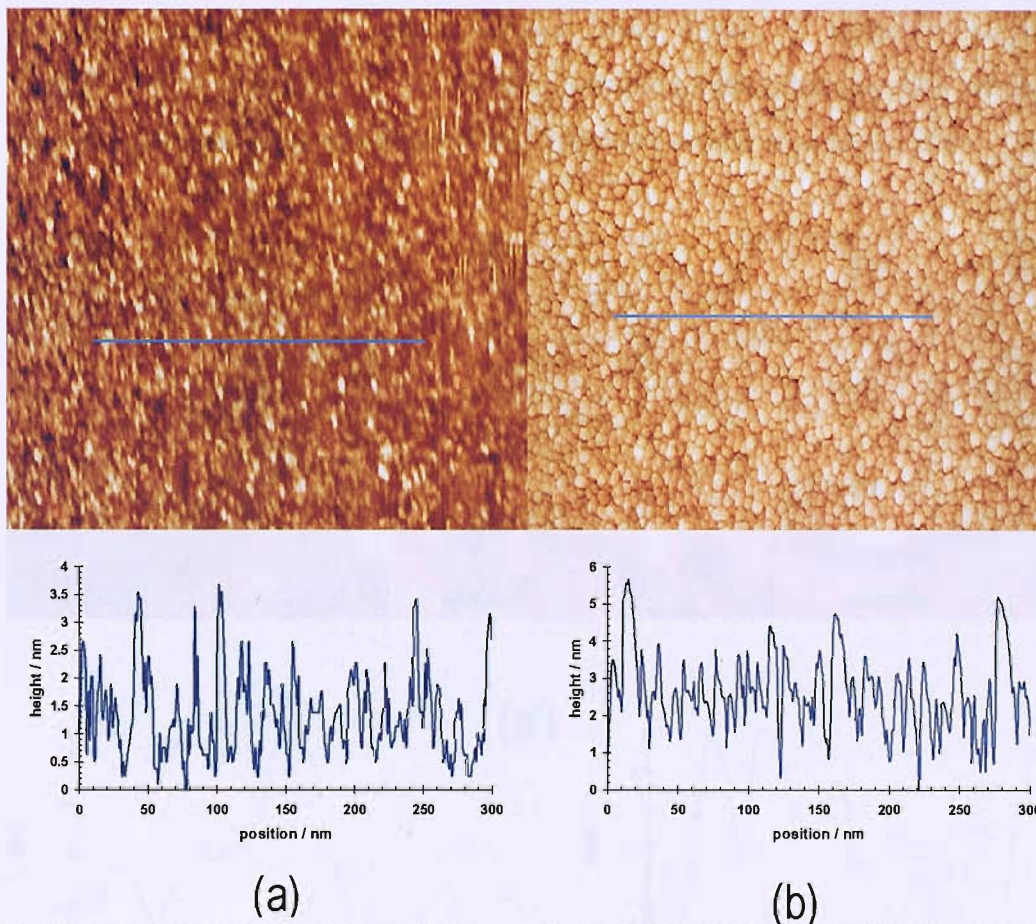**Figure 3.12.** *Atomic force micrographs 500 x 500 nm (a) Sub stoichiometric titanium dioxide (ppO$_2$ 1 x 10^{-7} mBar) (b) 2.33 nm nominal thickness of gold (900s .) deposited on titania (ppO$_2$ 1 x 10^{-7} mBar). The line measurement under the image corresponds to the line shown in the image above.*

There is clearly an intrinsic background roughness on titania that can be seen in the image and in the line plot (Figure 3.12 (a)). As gold is deposited the appearance changes and the surface showed a higher density of features. Also the surface roughness is slightly increased as determined by the RMS roughness (Table 3.3). The major problems as mentioned above were the tip convolution and an apparent loss of the accuracy of lateral dimensions. For imaging in the micrometer region a so called "scan-master" corrects the inaccuracies of the piezo-element by previous calibration measurements on a grid with known dimensions. For scan sizes in the sub micrometer range the "scan-master" has to be switch off, as it limits the lateral resolution. This leads to a loss of the calibration and hence the exact lateral dimensions of the image are unknown. This effect becomes clear at even higher resolution imaging of 100 x 100 nm

as shown in a series of micrographs in Figure 3.13 for titania (a), 0.78 nm gold on titania (b) and 2.33 nm gold on titania. The comparison for example of Figure 3.13 (b) representing a gold coverage of 0.78 nm on titania with a TEM image with the same coverage (Figure 3.7 (b)) shows a much lower density of particles, suggesting an inaccurate lateral resolution. A further constraint restricting the use of AFM was features in the morphology of titania that appeared similar to gold particles.
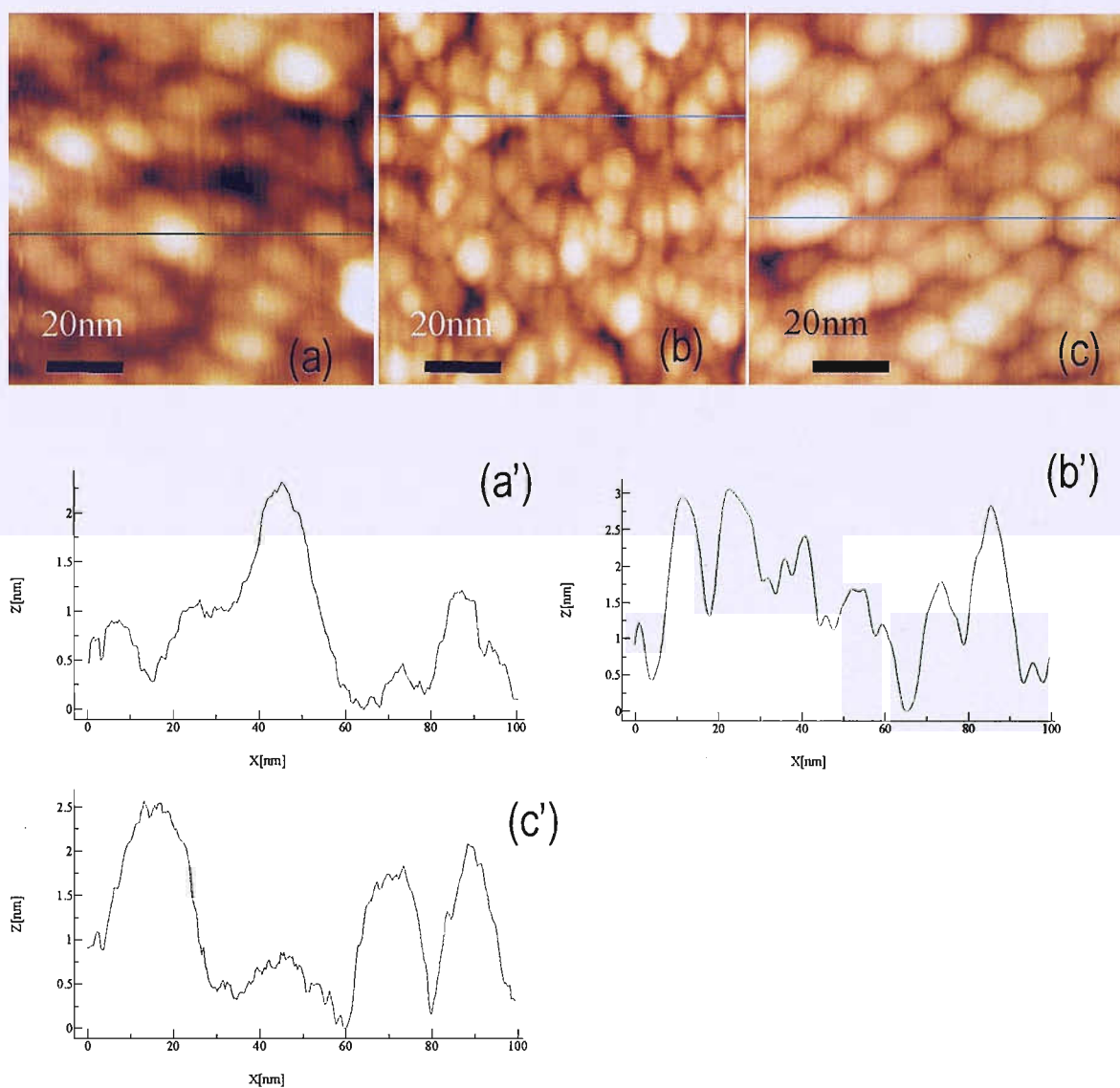
Figure 3.13. *Tapping mode AFM images 100 x 100 nm taken with a High resolution tip (compare experimental section). (a) sub-stoichiometric titania (prepared at 1 x 10^-7 mBar) (a') the according line measurement as indicated in the image (b) 0.78 nm gold deposited on titania (b') line measurement and (c) 2.33 nm gold deposited on titania (c') line measurement.*

And a further observation was made for example for the highest gold coverage of 2.33 nm (Figure 3.13 (c and c')) that indicated that the tip did not image the background

(titania). TEM images with the same coverage (Figure 3.7 (d)) revealed that the inter-particular distance were smaller than 10 nm.
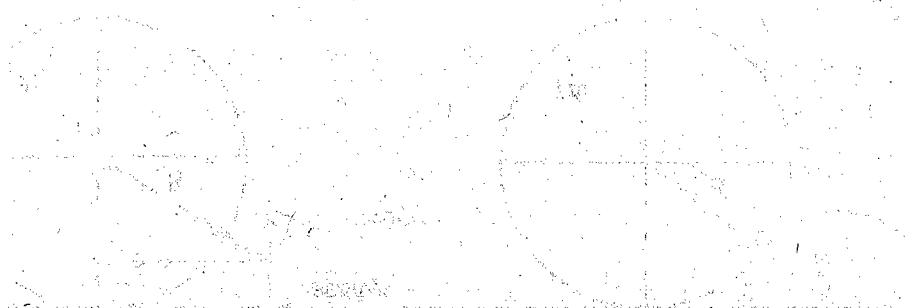
Table 3.2 showed the height and width for some size selected gold particles. Also shown in the same table were the widths calculated for a simplified model of either spherical or hemispherical particle shape (cf. Figure 3.14), assuming the supplier specified tip radius of 1 nm and tip radii calculated for the simplified model (a similar model was applied in [324]). The widths in the measurements were found to be broader than predicted by both models assuming a tip radius of 1nm. "Real" radii for the tips appeared bigger than specified between 2.9 – 9.2 nm. This lead to the conclusion that the AFM tips would not be able to image accurately the background, if the particles were not sufficiently spaced (as in higher coverage samples).

$$W = 4\sqrt{R \cdot \left(\frac{H}{2}\right)} \qquad\qquad W = 2\sqrt{H^2 + 2H \cdot R}$$

Figure 3.14. *Simplified model of Tip/particle interactions – the tip convolution effect. (a) Spherical particle (b) Hemispherical particle. H - particle height, W- apparent particle width and R - tip radius.*

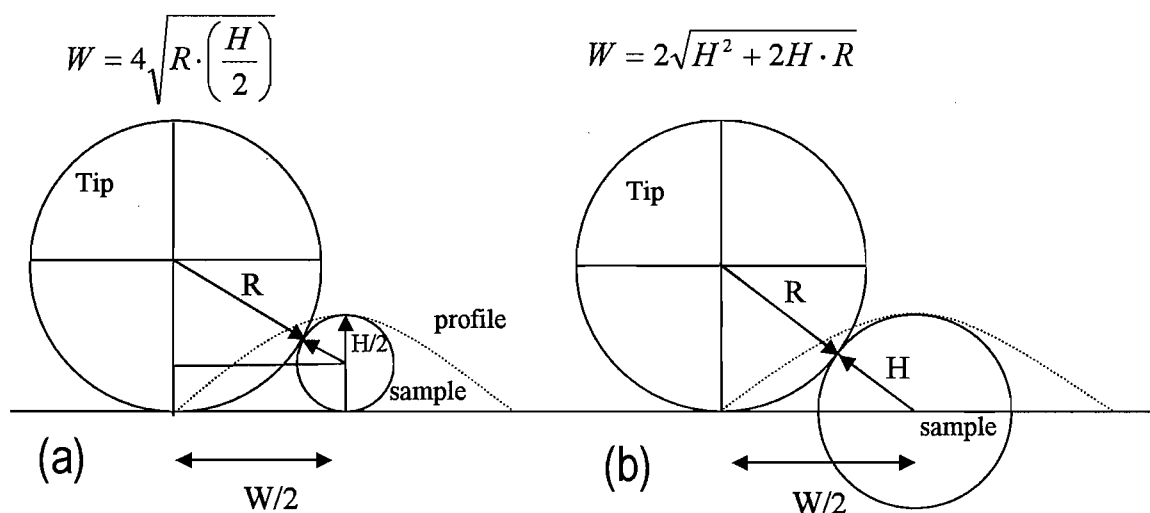**Table 3.2.** *Comparison of particle heights and width as measured by AFM of a few particles with a simplified model.*

measurements		W_{cal} HS / nm	W_{cal} SP / nm	R_{cal} HS / nm	R_{cal} SP / nm
Width W / nm	Height H / nm				
14.9	4.2	9.2	5.8	9.2	6.7
12.9	4.1	9.1	5.7	6.2	5.1
8.1	2.8	6.6	4.8	2.9	2.9
10.3	1.6	4.0	3.5	*15.4*	8.5

W_{cal} HS: calculated width from the measured particle height for a hemispherical model

W_{cal} SP: width - spherical model

R_{cal} HS: Calculated tip radius from measured width and height using the hemispherical model

R_{cal} SP: calculated tip radius –spherical model

Bearing in mind the described restrictions only an estimate of the particle height from the measurements was attempted, as AFM was not able to provide sufficient lateral resolution to confirm neither particle sizes nor particle densities as a result of tip broadening and inaccurate handling of lateral sizes of the image.

Table 3.3 summarizes roughness factors, and heights taken as a random sample N, from a number of AFM images. Results are included for the root mean square roughness of the titania substrate, and for several nominal thicknesses of gold. The root mean square roughness increases with increasing gold coverage. For gold particle height analysis line measurements were taken at arbitrary positions of the image and it was assumed that all features in this measurement were associated with the Au particles. Clearly this is an approximation since the titania also exhibits a finite roughness. Comparing the ratio of the particle diameter from TEM versus the "height" of the particle as measured by AFM, we consistently find values close to two.

Table 3.3 *Summary of AFM characterization of titania, and titania supported Au, surfaces.*

Nom. thickness gold t / nm	image size / nm	Random sample N	RMS[8] roughness/ nm	TEM particle d /nm	AFM height H / nm	Ratio diameter/ height
0	500	-	0.78	-	-	-
0	100	-	0.67	-	-	-
0.78	100	34	0.75	2.53	1.29	**1.96**
1.56	500	75	1.31	3.68	2.17	**1.70**
2.33	500	62	1.14	4.58	2.17	**2.11**

We conclude because of a lack of other independent measurements, such as STM, that the observed Au particles are hemispherical, which is consistent with previous conclusions on $TiO_2(110)$ for a particle diameter range of 2.5 – 4 nm [88]. Mavrikakis et al. suggested, from theoretical calculation, that the thickness of titania supported gold nanoparticles would be ~ 0.7 – 1.4 nm for particles with diameters of ~ 3 - 7 nm on TiO_2, which would be less than hemispherical [321]. Also Lopez et al. suggested a similarly strong truncation by the interaction with the support. They base their results on theoretical calculation and confirmed it by experiments on "real" catalyst (high surface area Au/TiO_2) [85].

Later in this work evidence for non bulk gold like oxide formation/reduction behaviour will be presented. This made an electrochemistry independent estimation of the "real" surface area necessary. Therefore the particle density, diameter and the assumption of hemispherical shape were used to calculate the "real" surface area (c.f. Figure 3.15). This value is important, for example, in establishing specific electrocatalytic activity in reactions investigated on these model catalysts.

---

[8] RMS roughness is defined as the square root of the mean value of the squares of the distance of the points from the image mean value: $R_{ms} = \sqrt{\dfrac{1}{N}\sum_{i=1}^{N}\langle Z_i - Z \rangle^2}$
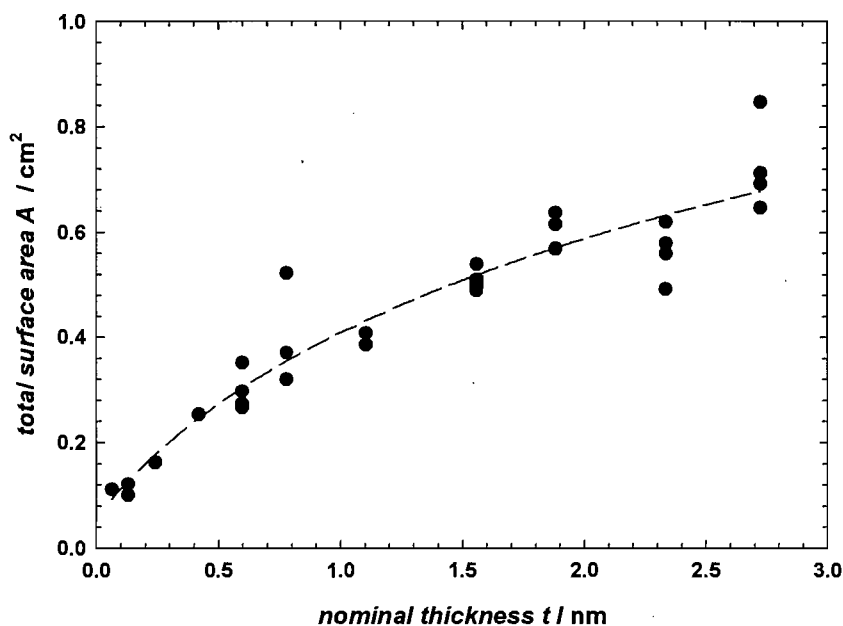
Figure 3.15. *Titania supported gold surface area estimated from the particle density and diameter for hemispherical particles.*

The estimation of the surface area was based on the assumption that the particles are hemispherical and if they deviate from this morphology the surface area exposed to the electrolyte would change. As discussed above, at higher coverages tip convolution effects might not reveal the real height of particles. In the literature a change of gold particle truncation on titania (110) was observed [60]. For three size ranges, different truncations are reported: for particle diameters between 1.5 – 2.5 nm a quasi 2D growth was observed (not hemispherical, only a few atomic layer thick), 2.5 - 4 nm hemispherical growth and > 4 nm spherical 3D growth (small contact area, almost spherical) [60]. To elucidate if a similar effect was present with the particles studied here, the estimated cube root of the number of atoms in the particles[9] was plotted against the particle diameter (Figure 3.16). The experimentally found data points followed linear behaviour (particle > 5nm excluded due to particle coalescence) with an intercept very close to zero.

---

[9] $N = \dfrac{\dfrac{t_{nom}}{t_{ML}} \cdot N_{ML}}{N_{TEM}}$, where t_{nom} is the nominal gold thickness, t_{ML} the thickness of one monolayer

Au(111) $\sim$ 0.235 nm, N_{ML} the number of atoms in a monolayer and N_{TEM} the number density of particles.
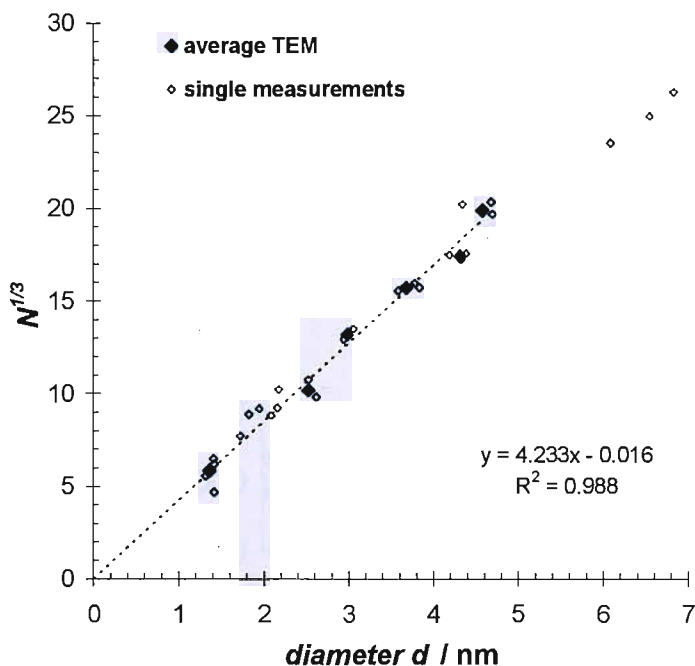
Figure 3.16. *Cube root of the number of atoms per particle versus the average gold particle diameter (TEM). The legend "average TEM" refers to the average of each of the respective deposition thicknesses.*

Figure 3.17 (a) and b show XPS spectra (Au(4f)) of titania supported Au particles of 1.4 nm and 2.5 nm mean diameter. The peak positions of a gold foil, measured under the same conditions as the particles, has been included, and provides a calibration reference for the Au $4f_{7/2}$ peak of bulk Au at 84.0 eV [325]. A shift in the peaks for the 1.4 nm particles of ~ 0.3 eV to higher binding energy is observed, and this shift decreases to ~ 0.1 eV for 2.5 nm particles. The upward shift in binding energy for the small particle is similar to that found for Au on TiO_2 (110) during the initial growth stages, and was associated with final state effects (electron screening in a small cluster) rather than any initial state effect [326]. The shift is also similar to that found for 2 nm particles on polycrystalline titania [322] where it was not quite clear whether a final state effect or initial state effect contributed to the shift from the bulk value.
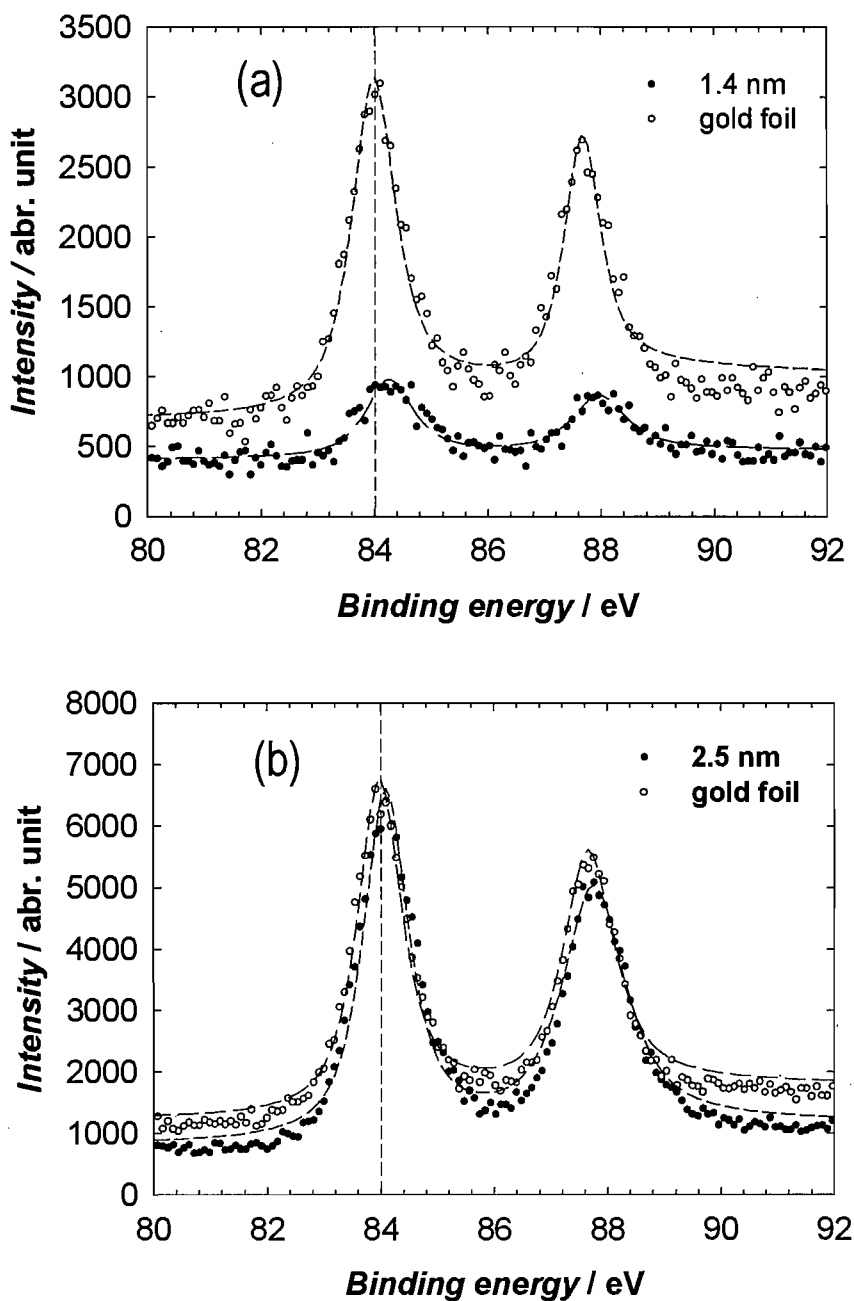
Figure 3.17. *XPS spectra of the Au(4f) core level for titania supported particles with a mean diameter of (a) 1.4 nm and (b) 2.5 nm . The calibration spectrum from a gold foil is also shown. (XPS measurements by Laura J. Williams)*

3.4 Deposition of gold nanoparticles on carbon layers

Gold was deposited, using the conditions described in the experimental section at a deposition rate of 0.16 nm min^{-1} onto carbon coated TEM grids on which a 30 nm carbon film was deposited to ensure the same substrate and nucleation behaviour.

Figure 3.18 shows the TEM images for gold particles on carbon with deposition times of 50, 300, 600 and 900 s (nominal thicknesses 0.13, 0.8, 1.6 and 2.3 nm).

Figure 3.18. *TEM micrographs of carbon supported gold particles. The nominal thickness of gold was (a) 0.13; (b) 0.78; (c) 1.56; (d) 2.34 nm and the deposition rate was 1.7 x 10^{-3} nm s^{-1}.*

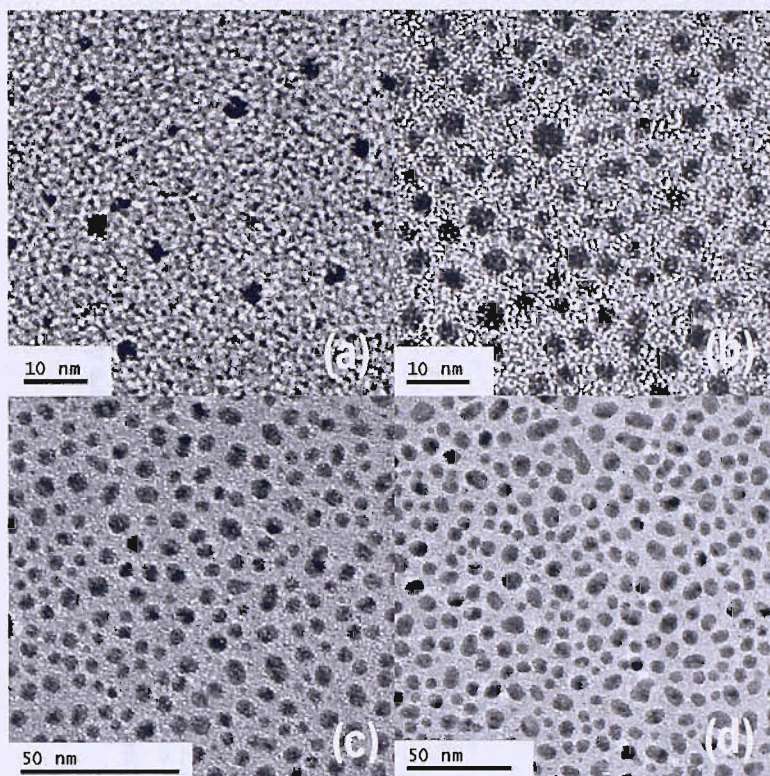These images were analysed to give the particle size distributions shown in Figure 3.19 (a), while Figure 3.19 (b) reports the variations of the mean particle diameter and Figure 3.19 (c) the number density as a function of the nominal thickness. Comparison of these data with those in Figure 3.10 for the deposition of gold particles on TiO_x indicates a number of differences on the carbon support. The initial number of nucleation sites on carbon is considerably smaller than on titania during the initial Au deposition resulting in larger particle sizes. As the number of nucleated particles grows at low nominal thickness, the average particle size is 2.5 – 3 nm. Particles coalesce at higher nominal thicknesses (at particles sizes where coalescence is observed on titania), and a concomitant reduction in particle number density is observed. At substrate temperatures of ~ 300 K, we were not able to observe particles of Au on carbon below 2.6 ± 0.7 nm average particle size. The observed "critical size, compared to a fcc truncated-octahedron was close to the steep increase of the relative frequency of corner sites and close to the maximum of edges, leading to a higher density of low coordinated gold sites (c.f. Figure 1.8). The average particle diameter was with 2.6 ± 0.7 nm close to a closed shell configuration which would exhibit in the truncation presented in Figure 1.8

diameter of 2.66 nm. For other shapes (e.g. differently truncated octahedron) a similar steep increase of surface atoms with low coordination number have to be expected.
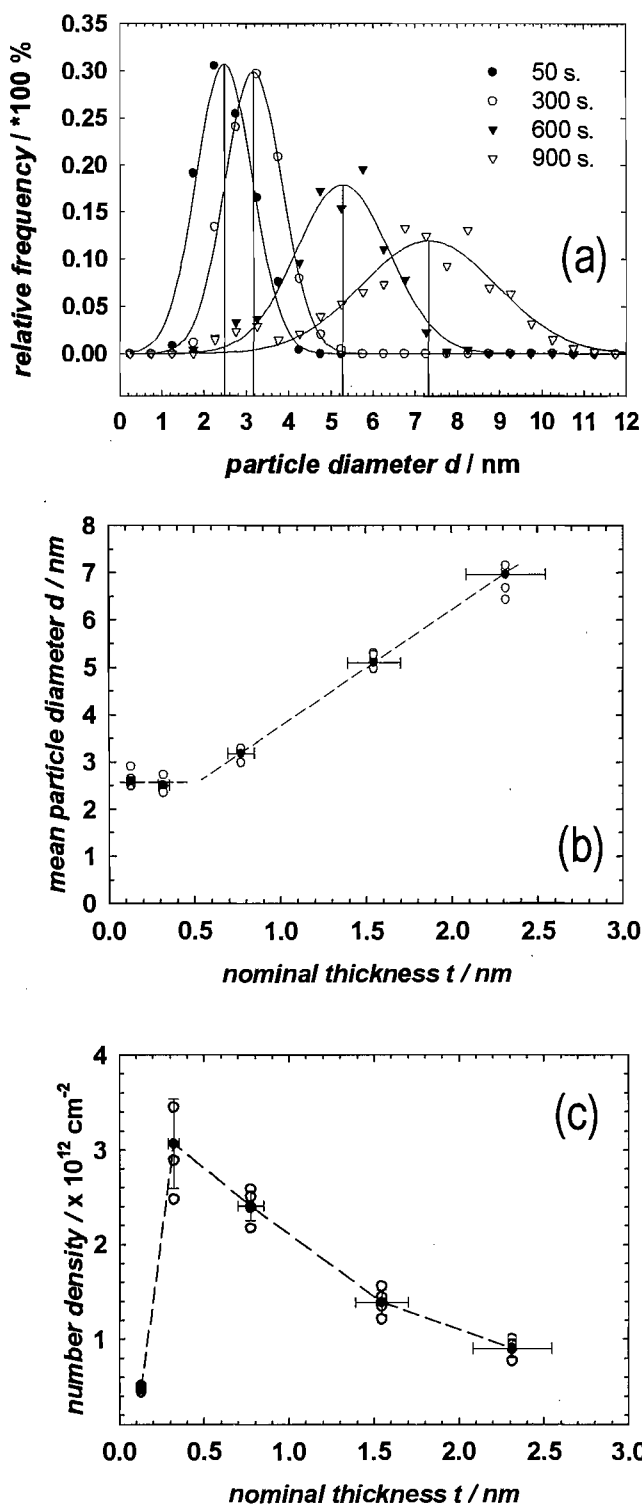

Figure 3.19. *(a) Particle size distributions of gold particles grown on carbon obtained from TEM measurements. Gold deposition times are shown in the figure. The data was fitted to a normal Gaussian function. (b) The mean particle size of gold. (c) The number density of particles per cm².*

91

As for the titania supported gold particles, high resolution TEM measurements on carbon supported gold particles revealed polygonal shaped particles (Figure 3.20). The particle profile in Figure 3.20 (a) was highlighted in the same picture in (b). One could draw a hexagonal profile. The profile Figure 3.20 (c) and then highlighted in (d) could be drawn as an octagonal.

The partially visible lattice fringes in the Figure 3.20 (a) and (c) provide evidence, that the particles are crystalline, even so they where grown at room temperature. The presented particles provide evidence of crystallinity, but it was not possible to elucidate which particle shape was present at the sample.

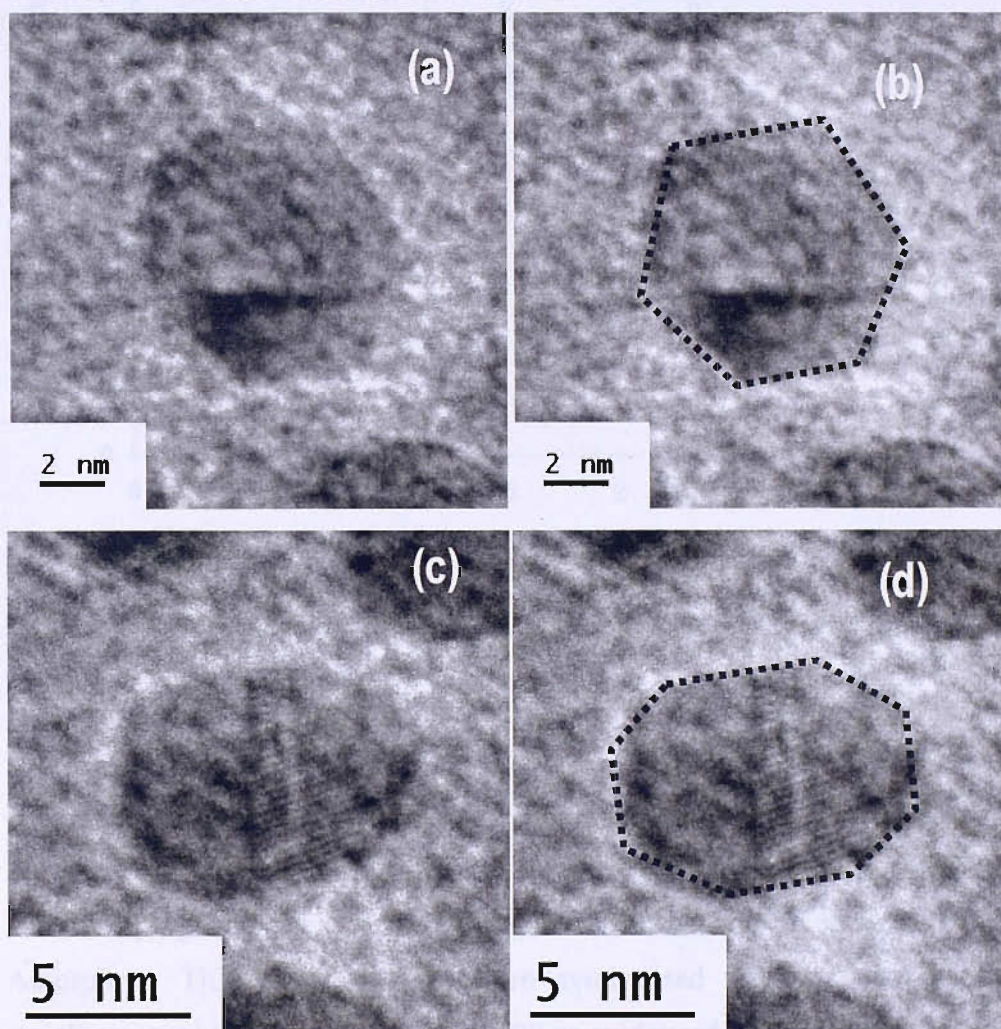**Figure 3.20.** *High resolution TEM images of carbon supported gold particles.*

The "total" gold surface area per centimetre square of geometric electrode area was again estimated the same way as for titania supported gold. Hemispherical particles were assumed and the diameter from TEM and the number density lead to the plot of the particle diameter dependent surface area shown in Figure 3.21. The particle height

was attempted to be measured by AFM, but due to the high intrinsic background roughness of roughness, it was even more difficult to conclude heights. To ensure uniformity between data sets, the specific electrochemical activities for the different reactions discussed below were corrected under the assumption of hemispherical particle shape. For carbon supported samples also the electrochemical determined surface area was used and results were presented for both normalisations.

$y = 0.20446 Ln(x) + 0.48170$
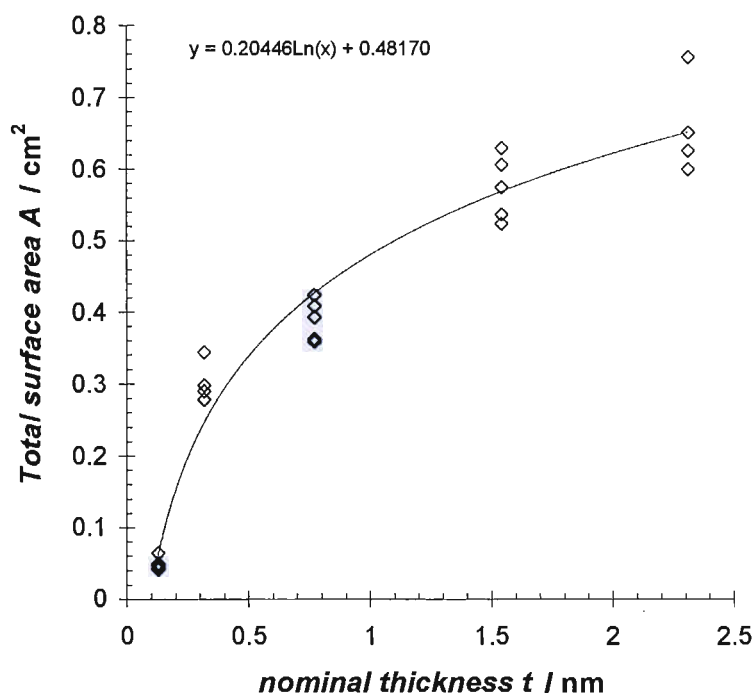
Figure 3.21. *Calculated surface area of carbon supported gold particles using particle diameter, number density and hemispherical particle shape.*

3.5 Conclusions

A system designed for high throughput physical vapour deposition (HT-PVD) of materials [24] has been applied to the synthesis of libraries of supported metal particles. Amorphous TiO_x supports have been synthesised with a controlled variation in stoichiometry in the range $x = 1.7 - 1.99$ as evidenced by their range of conductivities. A range of Au nanoparticles have been synthesised as a function of position across titania substrates at a temperature of ca. 300 K. TEM measurements indicate that during nucleation, a mean particle size of 1.4 nm is observed, and increasing coverage leads to an increased number of such nuclei to a maximum density of 5.5×10^{12} cm^{-2}. Particle sizes increase at higher Au coverages with a concomitant decrease in density. The small

particles exhibit a binding energy shift in the Au(4f) core level of 0.3 eV from bulk gold, and the shift is 0.1 eV by the time particles grow to a mean size of 2.5 nm. Nucleation and growth of Au on carbon support is also observed, but the initial particle size is significantly larger at ca. 2.5 nm and the maximum particle density (3.1 x 10^{12} cm^{-2}) lower when compared to titania. The HT-PVD technique is a powerful method of producing supported metal samples of controlled particle size, and when combined with multiple source deposition [24] should allow similar control of supported alloy particles as a function of particle size and alloy composition. When combined with suitable screening methods [24] the methodology provides a powerful route to the elucidation of particle size effects in catalysis on well characterised model catalysts.

4 Electrochemistry of the support materials titanium, titania and carbon

4.1 Introduction

This chapter briefly summarises the electrochemical response of the substrate materials titanium, titania and carbon in $HClO_4$. The aim was to compare the electrochemical behaviour of the substrate with reported behaviour and to investigate possible contributions of the substrate to oxygen reduction on the catalysed surfaces.

4.2 Electrochemical behaviour of a pure titanium disc

The electrochemical measurements were carried out on a polished titanium disc (area 0.196 cm^2, preparation described in the experimental section). Figure 4.1 shows the first six potential cycles after immersion into the deaerated electrolyte at 50 mVs^{-1} and then scanned to more positive potentials (upper potential limit 1.63 V). The first cycle shows an oxidation wave associated with the oxidation of Ti to TiO_2. The charge passed during the scan from the initial potential to the upper potential was 7.5 mC cm^{-2}. Assuming 4 electrons for the oxidation of one titanium atom to titanium dioxide would indicate that 4.5 x 10^{-16} titanium atoms were oxidised. Assuming a density of atoms of ~ 1.5 x 10^{15} atoms cm^{-2} an area of 7.9 cm^2 would have been oxidised. The electrochemical titanium surface area oxidised was hence much higher than the geometric surface area and therefore multiple layer oxidation could be concluded. Subsequent cycles (2nd to 6th) did not show significant charge transfer that could have been associated to oxide thickening and were rather ascribed to the double layer charging. Hence a higher overpotential would be required to thicken the titania layer formed on the surface.
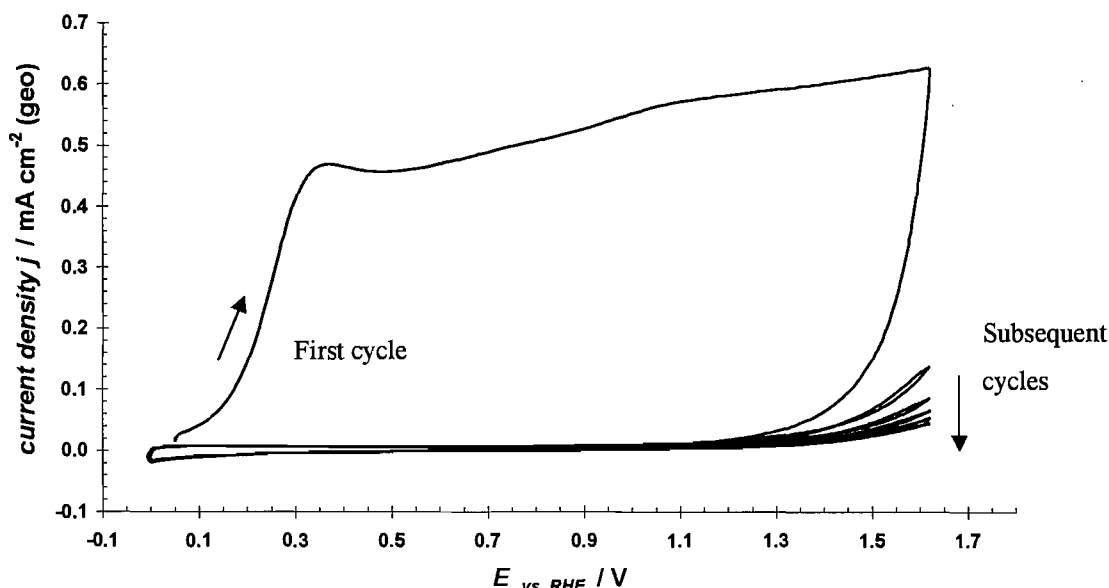
Figure 4.1. *Cyclic voltammetry (six cycles) on a polished titanium disc in argon purged 0.5 M HClO₄ at a scan rate of v= 100 mV s⁻¹. The temperature was maintained at 298 K.*

Standard potentials for titanium oxidation to TiO_2 are difficult to determine [327], but are known to be significantly lower than the potential range investigated here (> - 0.5 V vs. SHE) [327] .

4.3 Electrochemical behaviour of sub-stoichiometric titanium dioxide

Titania samples (prepared at a pp O_2 of 1 x 10^{-7} mBar on an etched titanium disc) have been measured and results are shown in Figure 4.2. Shown are the first three potential cycles. The first cycle showed a similar oxidation wave at potentials > 0.5 V as on the polished titanium disc but the oxidation wave was shifted towards more positive potentials. The subsequent cycles again showed only small oxidation charges. Measurements on the 10 x 10 array electrodes (and therefore smooth gold substrates) did not show significant oxidation charge. Furthermore the disc colour did not change from before and after electrochemical modification. This indicates that no significant change of the thin film stoichiometry occurs. Therefore it was concluded that the oxidation charge was mainly due to oxidation of titanium metal exposed to the electrolyte. Before the deposition the titanium disc have been etched to insure adhesion of the deposit. The etched surface has a much higher roughness and hence holes could

have been formed, which were not entirely covered by the TiO_x and oxide formation/thickening occurred at free sites during the first potential cycle.
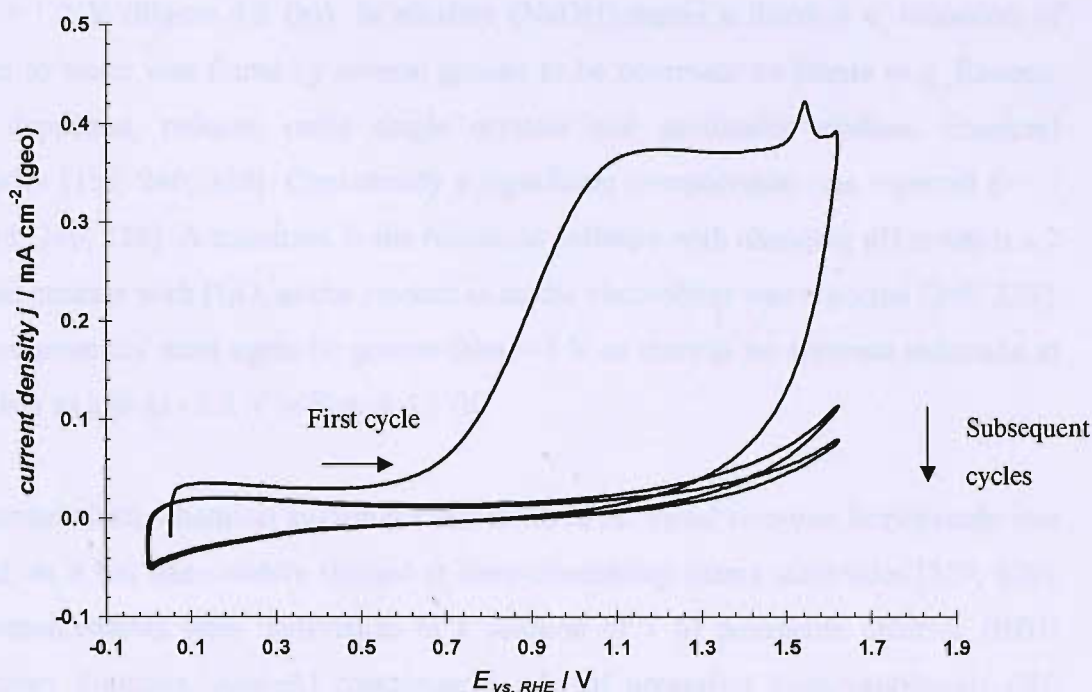
Figure 4.2. *Cyclic voltammetry (first three cycles) on sub- stoichiometric TiO_2 in argon purged 0.5 M $HClO_4$ at a sweep rate of $v = 100\ mV\ s^{-1}$ and 298 K. The electrode was transferred into solution under potential control at 50 mV.*

Figure 4.3 (a) shows a voltammogram (one cycle) again on a titania electrode, but this time cycled to more negative potentials. The voltammetry did not change with cycling after approximately 10 cycles (as shown in the figure).
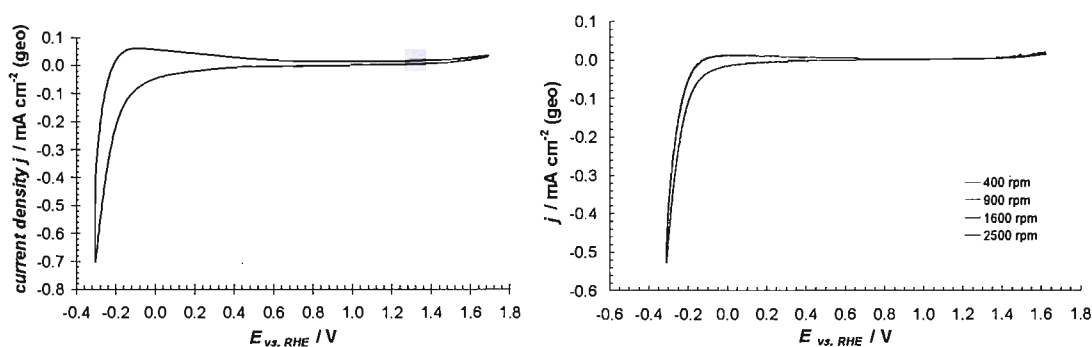
Figure 4.3. *(a)Cyclic voltammetry (10th cycle) on a titanium dioxide disc at a scan rate of $v= 100\ mV\ s^{-1}$. The electrolyte was purged with Argon. (b) Steady state voltammetry (continous cyling, 13th cycle onwards) in oxygen saturated electrolyte at a scan rate of $v = 20\ mV\ s^{-1}$. The rotation rate was varied between 400 and 2500 rpm as indicated in the figure. The electrolyte was 0.5 M $HClO_4$ and the temperature was maintained at 298 K.*

Substoichiometric titanium dioxide did not show any activity towards the oxygen reduction reaction in acidic ($HClO_4$) media in the potential range of E_{lower} = - 0.3 V and E_{upper} = 1.2 V (Figure 4.3 (b)). In alkaline (NaOH) media a direct 4 e⁻ reduction of oxygen to water was found by several groups to be dominant on titania (e.g. Ebonex, CVD deposited, reduced rutile single crystals and anodically oxidised titanium) electrodes [155, 240, 328]. Consistently a significant overpotential was reported (>> 1 V) [155, 240, 328]. A transition in the reduction pathway with changing pH towards a 2 electron process with H_2O_2 as the product in acidic electrolytes was reported [240, 328]. The overpotential must again be greater than ~ 1 V as there is no apparent reduction at potentials as low as - 0.3 V in Figure 4.3 (b).

As a model electrochemical system the reduction of the metal complex ferricyanide was studied, as it has been widely studied at semi-conducting titania electrodes [329, 330]. The measurements were undertaken in a solution of 1 M potassium chloride (BDH Laboratory Supplies, AnalaR) containing 5 mM of potassium hexacyanoferrate (III) (Fisons Scientific Equipment, Analytica Reagent). The reference electrode was a Saturated Calomel Electrode (SCE, Cole Parmer) and the results are presented against the standard hydrogen electrode (corrected for 0.241V).

The redox potential of the ferro/ferricyanide couple is E^0 = + 0.361 V (SHE) [331]. This potential will be strongly influenced by the supporting electrolyte [331]. Therefore cyclic voltammetry of 5 mM ferricyanide in a 1 M supporting electrolyte of potassium chloride on a stationary gold disc was measured (Figure 4.4). The voltammetry has the typical shape reversible shape and the peak separation was found to be 64 mV, close to the theoretical 59 mV. The „apparent" redox potential[10] of the ferri/ferrocyanide couple during the measurement was 0.46 V close to the potential of 0.469 ± 0.002 V (vs. SHE) found elsewhere [332] in 1 M KCl. Note that the exact position of the peak potentials is not very accurate and an error of ± 10 mV associated to them was estimated.

---

[10] $E_{app}^0 = \dfrac{E_p^C + E_p^A}{2}$, where E_{app}^0 is the apparent redox potential, E_p^C the cathodic peak potential

(potential at maximum peak current and E_p^A the anodic peak potential.

The peak current density (j_p=1.18 mA cm^{-2}) allowed the estimation of the concentration using the Randles Sevčik[11] equation and lead to a concentration of 5.05mM close to the expected 5 mM (as prepared).
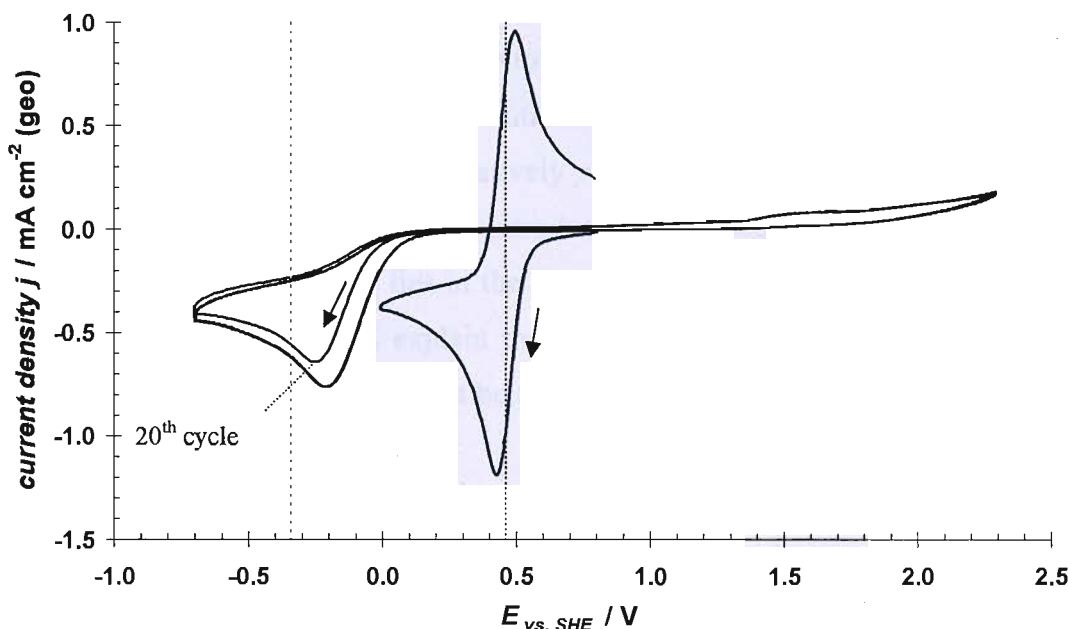
Figure 4.4. *Cyclic voltammetry on titania (black solid curve- three cycles, cycle No. 20 to 22) and on a bulk gold disc (blue solid curve- first cycle) in 5mM K$_3$Fe(CN)$_6$ in 1M KCl supporting electrolyte. Also shown are the flat band potential [41](red dotted line, pH$_{pzc}$ 5.8) and the apparent redox potential E$^0_{app}$ ~0.46 V (black dotted line). The temperature was maintained at 298 K, the scan rate was v=100 mV s^{-1} and the electrolyte was purged with argon prior to experiments.*

The comparison of the voltammogram on the gold with a titania electrode (Figure 4.4) revealed some major differences. At TiO$_x$ the reduction peak potential was ~690 mV negative during the first cycle and 650 mV during subsequent cycles compared to the peak observed on gold. There was a 50 mV activation after the first cycle. The maximum peak current density on titania was approximately 35 % less of that observed at gold and the peak was much more drawn out, as would be expected for an irreversible electron transfer. Furthermore during the anodic potentials scan direction no re-

---

[11] $j_p = -0.4463nF\left(\dfrac{nF}{RT}\right)^{1/2} c^0 D^{1/2} v^{1/2}$, where n is the numbers of electrons transferred (n = 1), F the

Faraday constant, R the universal gas constant, c^0 the bulk concentration of the electro active species, D the diffusion coefficient (D[Fe(CN)$_6$]$^{3-}$ = 0.76 x 10^{-5} cm^2 s^{-1} in 1M KCl) and v the scan rate.

oxidation peak was observed at currents below 0.8 V. At more positive potentials a small amount of charge was transferred. This charge is most likely associated to the re-oxidation of ferrocyanide to ferricyanide. It does not approach diffusion control.

The electrochemistry of a model redox system on the TiO_x electrodes prepared in this work was found to be similar to the behaviour reported literature [36, 330].

The literature value for the flat band potential of - 0.34 V at pH = 5.8 [41][12] is shown as a red dotted line in Figure 4.4. The relatively wide band gap of ~ 3 eV (or 3 V) would extend positive to this value (see Introduction). The standard potential of the ferro/ferricyanide couple hence lies in the band gap region. A simplified band bending model (see Introduction) could explain the electron transfer from the electrode to the redox couple by an electron that must be transferred from the conduction band (CB) to the electroactive species:

$$[Fe^{III}(CN)_6]^{3-} + e^-_{CB} \rightarrow [Fe^{II}(CN)_6]^{4-}$$

This simplified model explains why the reduction peak was shifted significantly negative towards the flat band potential, were electrons are available due to the thermal excitation. The similar band bending model could also apply to re-oxidation where a hole must be created in the valence band at the surface to allow an electron transfer into the electrode.

$$[Fe^{II}(CN)_6]^{4-} + h^+_{VB} \rightarrow [Fe^{III}(CN)_6]^{3-}$$
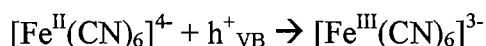
The observed small oxidaiton charge seen in the voltammetry hence must be due to the creation of holes at the semiconductor surface. The premise for this explanation would be that a thin space charge layer, so that electrons can tunnel from the highly bended valence band edges at the electrolyte/semiconductor interface into the conduction band of the bulk. Not discussed in this discussion is the influence of a ferri/ferrocyanide surface species stabilised by the titania [36, 329, 330].

---

[12] Finklea [36] summarised 187 reported values and the fit through them is at the same pH very close to the potential of - 0.34 V but the scatter ± ~ 0.25 V was significant. The flatband potential was reported to depend on the doping.

4.4 Electrochemical behaviour of amorphous carbon

In Figure 4.5 the electrochemical response of amorphous carbon as prepared by physical vapour deposition (MBE), is shown. In Figure 4.5 (a) the potential was cycled in the potential range 0 V and 1.3 V in deaerated electrolyte. The current density (based on the geometric surface area) is in the order of $\mu A\ cm^{-2}$. The voltammetry was similar to that reported in the literature [154].

In oxygen saturated solution at different rotation rates (Figure 4.5 (b)) slightly increasing currents towards the negative limit attest to a small activity to the reduction of oxygen, but yet again the currents are very small compared to metal electrodes like platinum.
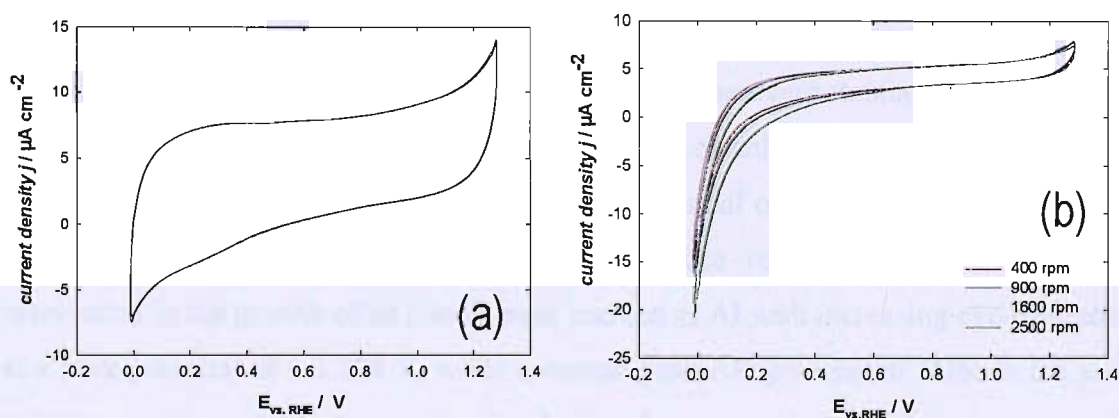
Figure 4.5. *(a) Electrochemical response of titanium supported carbon in nitrogen purged 0.1 M HClO₄ at a sweep rate of v = 100 mV s⁻¹ and 298 K. (b) Steady state voltammograms of carbon in oxygen saturated 0.1 M HClO₄ at a sweep rate of v = 20 mV s⁻¹.*

4.5 Conclusions

The electrochemistry of the support materials titania and carbon was found to be in good agreement with the literature (e.g.[39, 52, 154]) . In the potential region where the reactions of interest in this investigation, i.e. gold oxide formation/reduction, oxygen reduction and CO oxidation, no or little electrochemistry of the supports is observed, which would make the interpretation of data more difficult.

5 Electrochemistry of gold oxide

5.1 Gold oxide formation on polycrystalline gold

The oxidation of gold to gold oxide (AuO) has been intensively studied and the influence of the positive potential limit, scan rate etc has been reported; a brief summary can be found in the Introduction. Figure 5.1 (a) reports the cyclic voltammetry on a freshly polished bulk gold electrode after immersion into a deaerated solution of 0.5 M HClO$_4$. The first nine cycles showed an anodic peak with an onset potential of $\sim$ 1.225 V for the AuO formation (see Figure 5.1 (b)). This onset potential was similar to potentials reported in the literature; it was pointed out that adsorption of anions compete with the gold oxide formation and this may increase the overpotential [131]. The onset potential was taken therefore as a measure of system cleanliness. On the reverse scan an AuO reduction peak was observed with a peak potential of $\sim$ 1.142 V. Evidently from the changing voltammetry a "clean up" or surface reconstruction was observed, manifested in the growth of an anodic peak marked as AI with increasing cycle numbers at a peak potential of $\sim$ 1.324 V, while a second peak AII got smaller. Also in the same voltammogram in the reverse scan the AuO reduction peak seemed to increase with cycle number. In the 30th and 31st cycle as shown in Figure 5.1 (c) the voltammogram was totally reproducible and all subsequent experiments on bulk gold, such as CO oxidation and oxygen reduction were subjected to this pre-treatment of the surface. Throughout the cycles, the total anodic charge and the total cathodic charge appear to be equal.

The AuO reduction peak was found not to be perfectly symmetrical and showed a shoulder at $\sim$ 1 V. Charge observed at potentials negative to the gold oxide features in acid was mainly due to double layer (DBL) charging (see Figure 5.1 (d)), although the voltammogram in this potential range was not featureless. On the positive going scan a maximum was observed (denoted DAI) as well as on the negative going scan (denoted DAII). On single crystal Au(110) three waves in the DBL regions were identified [137] and have been ascribed to the adsorption of hydrated perchlorate anions (approx. peak potential 0.4 V), discharge of adsorbed anions (approx. peak potential 0.7 V) and metal

anion hydroxide complex formation (approx. peak potential 0.9 V). In contrast to this interpretation of anion adsorption, Burke suggested [129], that hydrous oxide might form in this potential region with an estimated standard potential of 0.33 V vs. SHE as was evident from a peak in cyclic voltammetry on "activated" surfaces in 1 M sulphuric acid. These activated surfaces exhibit gold sites which are highly active and undergo oxidation at very low potentials.
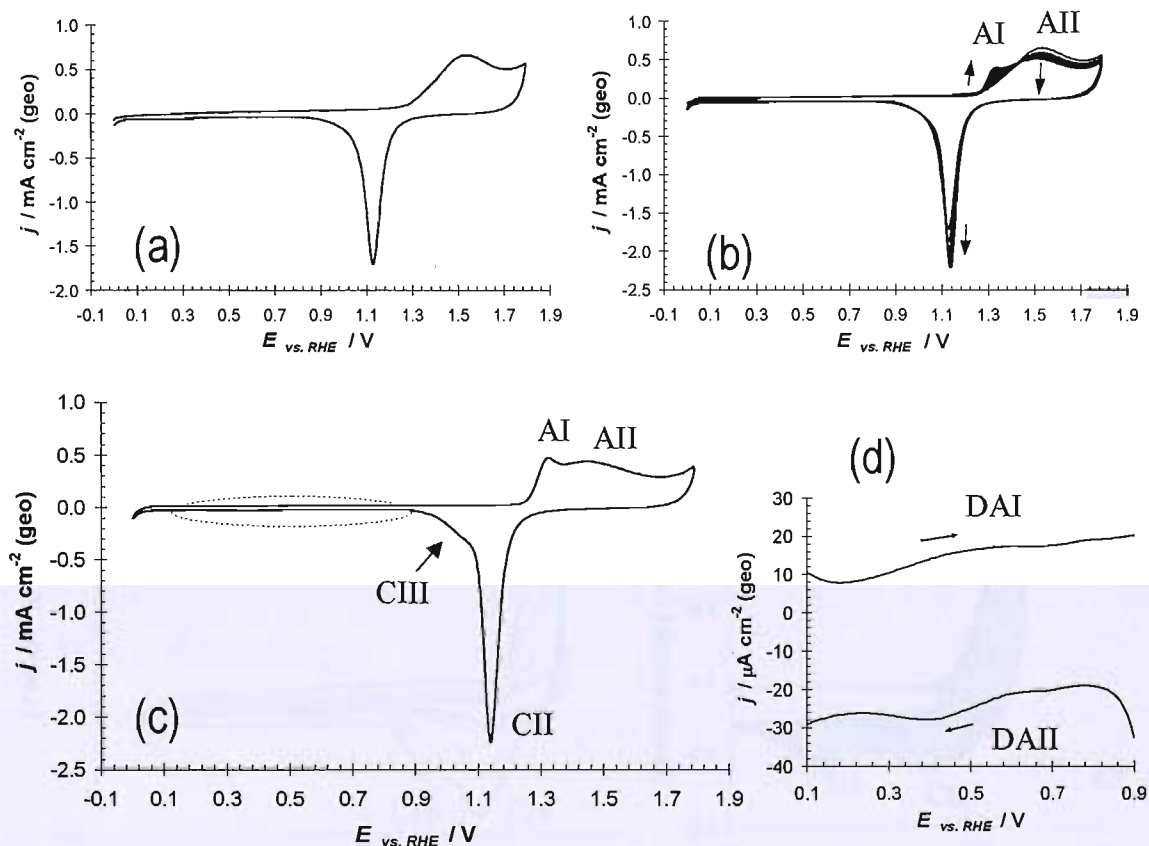
Figure 5.1. *Cyclic voltammetry on a bulk gold disc. (a) first cycle (b) first to 9th cycles shown. (c) 30th and 31th cycle (d) double layer charging region of (b) blue dotted line surrounded region. Measurements were taken in argon purged 0.5 M $HClO_4$ at a temperature of 298 K and a scan rate of $v = 100\ mV\ s^{-1}$.*

Figure 5.2 (a) shows a series of cyclic voltammograms, where the scan rate was varied, using 100, 200, 500 and 1000 mV s^{-1}. The upper potential limit was chosen to be 1.5 V. The positive going scan showed the oxide formation with an onset potential being just above ~ 1.2 V, in good agreement with the literature [131]. With increasing scan rate, as it would be expected, the current density increases. On the negative going cycles two AuO reduction peaks are evident (CII and CIII). The oxygen species which is reduced in peak CIII was reported to be limited to the formation of oxide at a certain number of surface sites [333] and will be dominated by the peak CII as the coverage with

oxygenated species is increased. This was evident in the CV of Figure 5.1, where a surface coverage with oxygenated species of greater 1 is to be expected.

In a potential opening experiment (Figure 5.2 (b)) a third cathodic peak numbered CI could be identified at the very early stages of AuO formation. The wave formed during positive sweep was mirrored on the negative scan, in a reversible manner, acting electrochemically like a surface adsorbed species. This reversible peak was also found elsewhere at very short time scales of oxidation of a gold electrode at a potential held in the AuO formation region [333]. All three peaks can be resolved in 0.5 M sulphuric acid, but with the major difference being that CIII has a significantly smaller influence (experiments not shown). This was attributed to the inhibiting adsorption of bisulphate to sites that are reduced in CIII [122]. The peak nomenclature AI, AII, CI, CII and CIII will be used hereafter.
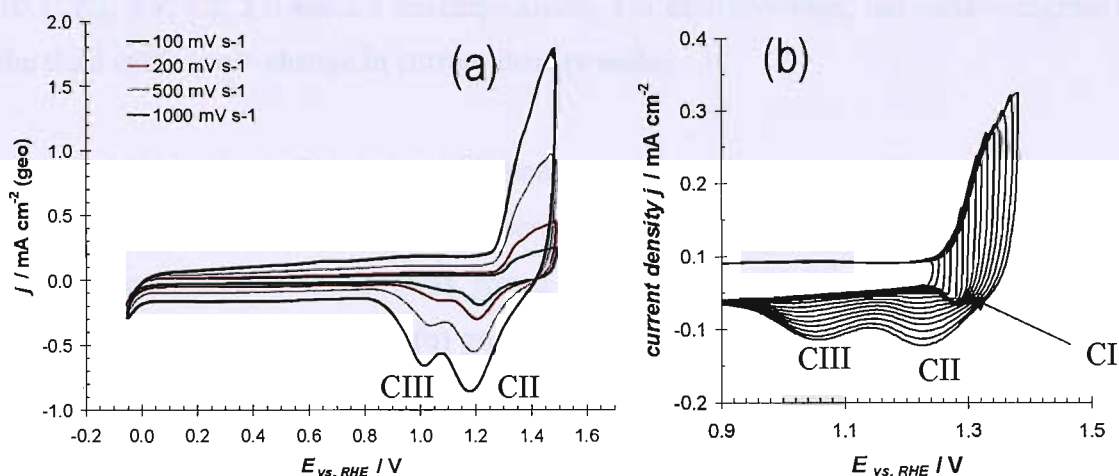
Figure 5.2. *Cyclic voltammetry on a bulk gold disc in argon purged 0.5 M HClO₄ at 298 K. (a) The scan rate was varied as indicated on the graph. (b) Potential opening experiment (10 mV each cycle) at a scan rate of 100 mV s⁻¹.*

In the literature the determination of the "real" gold surface area by integration of the charge transferred during reduction of an oxide layer is a common measure of gold surface area, but it disputed wheather or not a monolayer of gold oxide is formed. Many different potentials or holding times at oxidising potentials have been suggested [334]. Also the formation of gold oxide is temperature, electrolyte (gold oxide formation competes with anion adsorption) and surface structure sensitive [131, 134, 141, 335, 336]. The electrochemically measured surface area here was built on the assumption,

that gold forms a monolayer of its oxide if cycled to an upper potential limit of 1.63 V versus RHE and that a charge of ~ 400 μC per cm^{-2} surface area is required (see experimental section) to form it. This assumption was chosen in the range of potentials suggested and is applied throughout this study for comparison. It must be noted that throughout the experiments on bulk gold a charge balance between the anodic and cathodic gold oxide features was found (at potentials before oxygen evolution).

5.2 Gold oxide formation on carbon supported gold nanoparticles

Figure 5.3 reports the behaviour during cyclic voltammetry in argon deaerated 0.5 M HClO$_4$ of varying gold nanoparticle sizes deposited on carbon array electrodes. Figure 5.3 (a) and (b) present six voltammograms with nominal gold coverages of 3.6, 2.4, 1.5 nm (all (a)) and 0.78, 0.58, 0.33 nm (all (b)). The corresponding mean particle sizes are 10.1, 7.1, 4.9, 3.2, 3.0 and 2.8 nm respectively. For each coverage, the voltammogram is the third cycle (note change in current density scale).

As the gold coverage decreases and hence the gold surface area (refer to chapter 3) the charge passed in the Au/AuO region decreased. For coverages shown in Figure 5.3 (a) the electrochemical response was found to be bulk gold like. At the three lower coverages shown in Figure 5.3 (b) gold oxidation appears to become more difficult. A gradual decrease of the anodic peak AI in favour of AII appeared to occur. Also the gold oxide reduction peak CII shifts to slightly more negative potential, as the peak potential for the nominal gold coverage of 3.6 nm is ~ 1.175 V and for 0.33 nm ~ 1.152 V. Both the relative gain in influence of the peaks AII over AI and the slight shift of CII by ~ 23 mV to more negative potentials are evidence of slightly more irreversible redox behaviour of the electrochemically formed gold oxide. There seemed to be a charge balance between anodic and cathodic cycle in the third cycle. Cycles thereafter were found to be reproducible and were stable upon cycling.
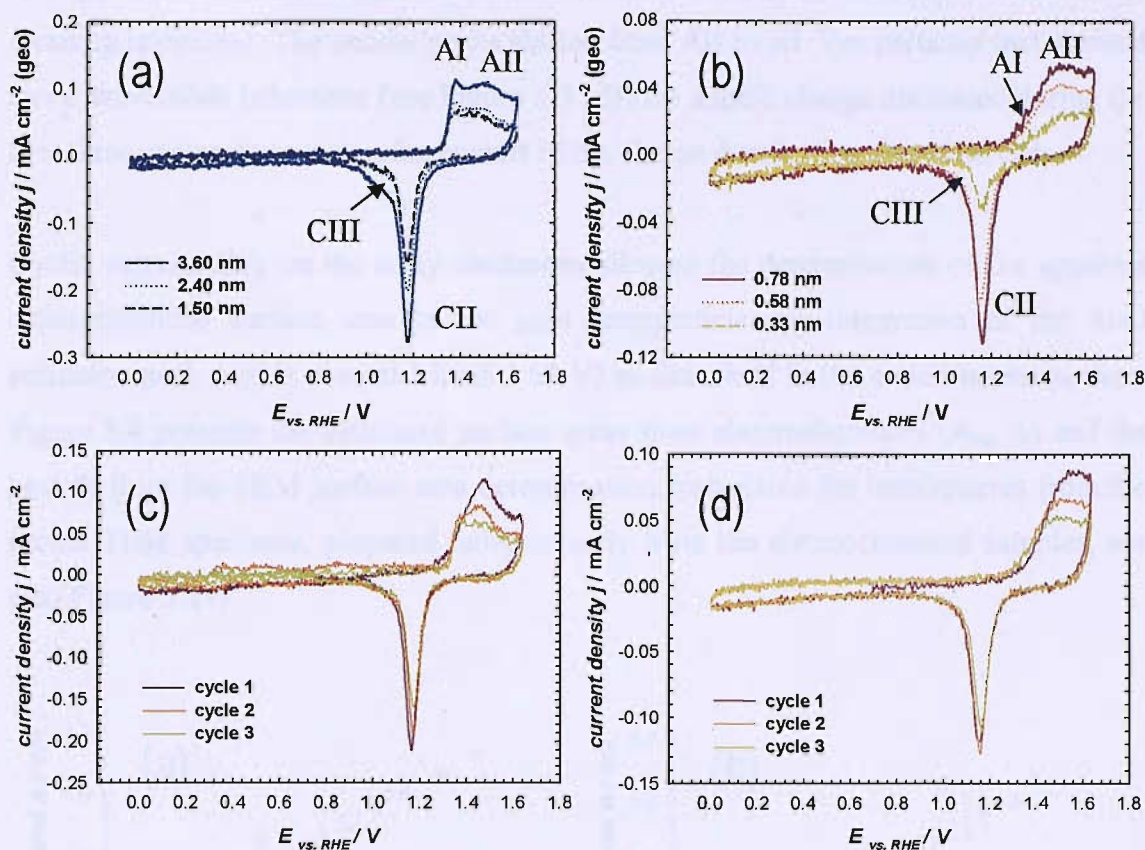
Figure 5.3. *Cyclic voltammograms on carbon supported gold nanoparticles on selected electrodes of an array of electrodes. (a) and (b) show third cycles of voltammograms of electrodes with a varying nominal gold coverage of $t_{nom.}$ = 3.6 nm, 2.4 nm, 1.5 nm, 0.78 nm, 0.58 nm and 0.33 nm as indicated in the legend. (c) first three cycles of an electrode with $t_{nom.}$ of 1.5 nm (d ~ 4 .9 nm), (d) first three cycles of an electrode with $t_{nom.}$ = 0.78 nm (d ~ 3.2 nm). The scan rate was 50 mV s^{-1}. All measurements taken in argon purged 0.5 M HClO$_4$.*

The transition from bulk gold like behaviour to more irreversible formation reduction behaviour seemed to occur between nominal gold coverages of 1.1 nm and 0.94 nm or mean particle sizes 4.0 and 3.6 nm. These particle sizes coincide with a beginning of oxygen reduction activity (cf. chapter 6).

The voltammetry of the carbon supported gold nanoparticles has been found to be reproducible after three potential cycles. During the first three cycles the surface was found to undergo changes as shown in Figure 5.3 (c) and (d) for particle sizes above (d ~ 4.9 nm) and below (d ~ 3.2 nm) the apparent transition diameter. A slight charge imbalance was observed, where more charge was transferred during oxidation of the gold surface, then during the reduction. It is not certain whether all charge transferred is due to the oxidation of gold, or if some carbon oxidation occurs. Again as in the case of

bulk gold, in the voltammograms shown in Figure 5.3 (c), a surface reconstruction or cleaning is evident. The anodic peaks shifted from AII to AI. For particles that showed more irreversible behaviour (see Figure 5.3 (d)) the anodic charge decreased during the first three cycles, but no significant shift of the charge distribution was observed.

Cyclic voltammetry on the array electrodes allowed the determination of the apparent electrochemical surface area of the gold nanoparticles by integration of the AuO reduction peak (upper potential limit 1.63 V) as described in the experimental section. Figure 5.4 presents the estimated surface areas from electrochemistry (A_{ec}, Δ) and the best fit from the TEM surface area determination (calculated for hemispheres from the model TEM specimen, prepared independently from the electrochemical samples, see also Figure 3.21).
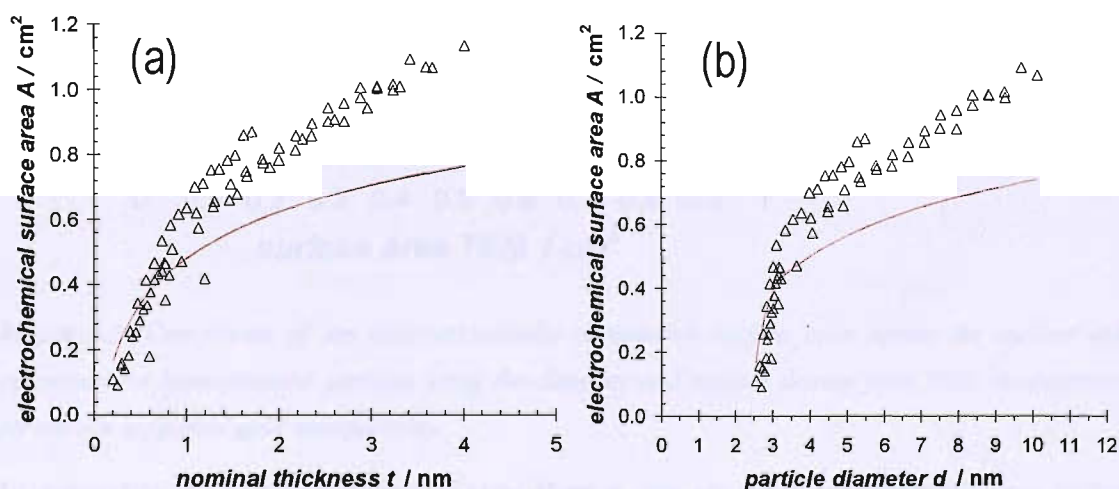
Figure 5.4. *Comparison of the surface areas as determined by TEM (red line, only the best fit is presented as determined in the sample characterisation chapter on model TEM specimen, shown are the areas for hemispherical particles) and by electrochemical determination from the CV of carbon supported gold nanoparticles. The data was taken at six different array electrodes.*

In Figure 5.4 (a) the surface area is plotted against the nominal gold thickness and in (b) against the particle diameter as measured by TEM. The surface areas measured by electrochemistry and TEM follow a similar trend, but the TEM derived areas are slightly lower than the electrochemically determined surface areas. The reasons for this mismatch might be that a monolayer of gold oxide is formed earlier than the potential of 1.63 V.

The deviation of plots at higher Au coverages results from overlap of the centres, The plot of Figure 5.4 (b) reflect the absence of centres of < 2.5 nm on the Au on C surface.

In Figure 5.5 a correlation plot of the electrochemistry surface area versus the TEM surface area for hemispheres is presented (data taken from Figure 5.4). The correlation is linear but the slope is not one.
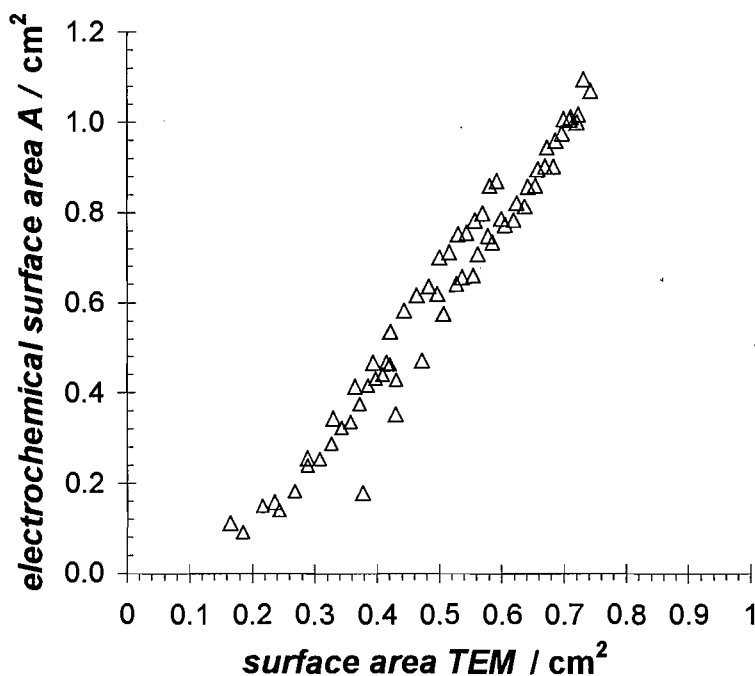
Figure 5.5. *Correlation of the electrochemically determined surface area versus the surface area calculated for hemispherical particles using the diameter and number density from TEM measurements for carbon supported gold nanoparticles.*

In summary gold nanoparticles bigger than 4 nm in diameter deposited on carbon behave similar to bulk gold. For smaller particles (d ~ 2.6 nm) a slight irreversibility was observed. Unfortunately particle sizes below a critical size of ~ 2.5 nm could not be prepared, due to their nucleation and growth mechanism (see chapter 3) and therefore no statements about their behaviour can be made.

5.3   Gold oxide formation on TiO_x supported gold nanoparticles

In Figure 5.6 (a) the electrochemical response of titania supported Au nanoparticles (deposited on a titanium disc electrode) in a potential sweep experiment is shown. The electrode was immersed under potential control at 50 mV and the first 10 potential cycles in 0.5 M $HClO_4$ are shown. The behaviour shown is typical for all gold

coverages under investigation. The nominal gold thickness presented was 0.78 nm which corresponds to a particle diameter of $\sim$ 2.4 nm (according to the calibration on model TEM specimen). The first cycle showed during the positive going scan an oxidation wave that contained two regions. The first region in the potential range of approximately 0.7 to 1.225 V showed a similar shape as the wave observed on a RDE covered with a $\sim$ 80 nm titania film as presented in chapter 4. In the second potential region (1.225 to upper potential limit of 1.63 V) where gold oxide formation occurs on bulk gold, a further increase in current density is observed which seems to be dedicated to the charge transferred during oxide formation and is "mirrored" in the charge transferred during the negative going cycle in the gold oxide reduction peak. The second cycle was lacking the first wave of the support influenced electrochemistry and showed only the gold electrochemistry. During this cycle the peak AII was dominant over the AI peak. Subsequent cycles showed a general decrease in charge transferred during the gold oxide formation, while the ratio of the anodic peak AII to AI seemed to change in favour of AI. On the negative going scans the current density of the gold oxide reduction peak CII ($E_p \sim$ 1.117 V) decreased with cycling and a peak broadening arose. This could be seen as an increasing gain of influence of the oxide states reduced in CIII ($E_p \sim$ 0.98 V). The peak broadening, the decreased oxidation and reduction charge and apparent splitting of the reduction response into two overlapping peaks, where the CIII appeared to gain influence all give evidence for a strong modification of the gold particles. Throughout the anodic and cathodic charges associated with Au/AuO are always equal.
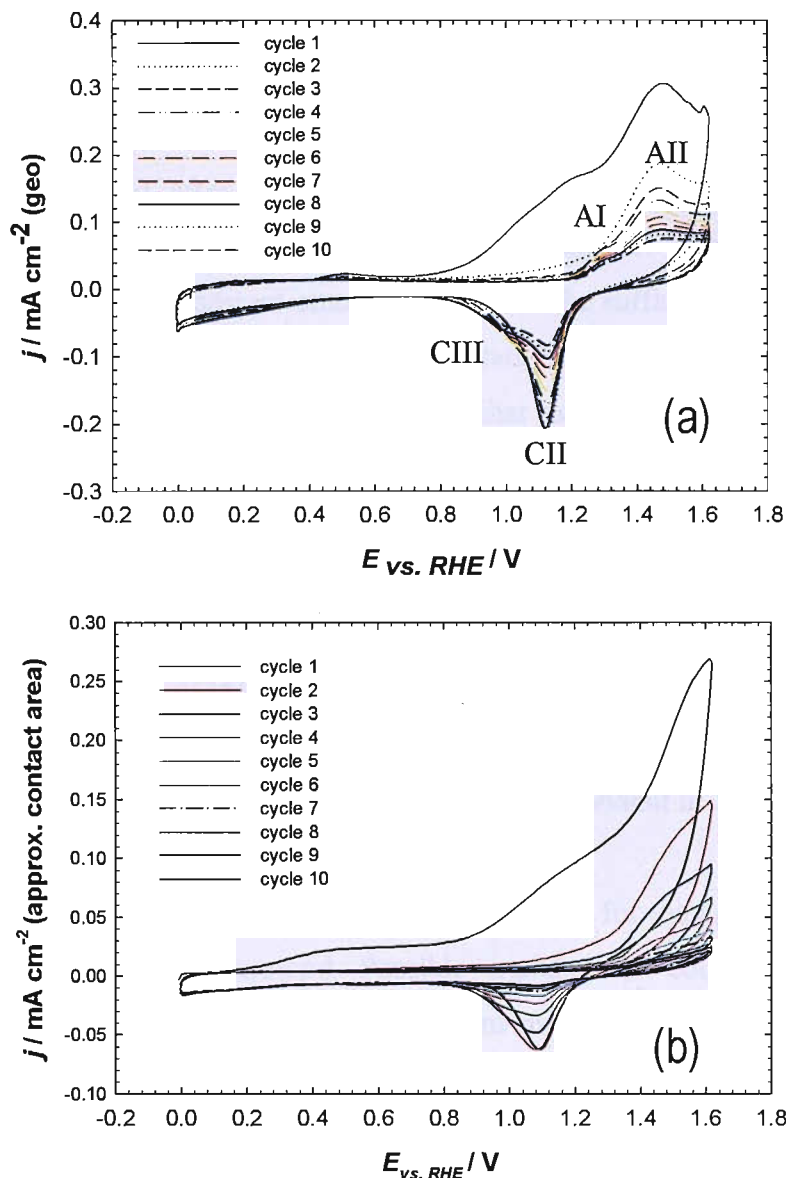
Figure 5.6. *Cyclic voltammogram (v = 100 mV s⁻¹) on titania supported Au in argon purged 0.5 M HClO₄ (a) and 0.5 M H₂SO₄ (measurements taken by Laura J. Williams using a meniscus contact cell), (b). The first 10 cycles are shown. The nominal thickness of gold were $t_{nom} = 0.78$ nm (which corresponds to a particle size of approx. 2.5 nm as determined by TEM measurements on model samples).*

For comparison an analogous experiment of a disc with the same nominal gold coverage on titania measured in 0.5 M H₂SO₄ using a meniscus contact cell is presented in Figure 5.6 (b) (for detailed experimental description compare Laura J. Williams: Transfer report [337]). The voltammogram is presented to point out that in sulphuric acid a similar peak broadening (double peak) was observed with a relative increase of the oxide species reduced in CIII. This is surprising as the oxide species reduced on bulk gold in at similar potentials was strongly inhibited in sulphuric acid, because of competing adsorption of sulphate anions [122, 333]. It is therefore only speculative that

110

the peak CIII formed on the Au/TiO$_x$ samples has a common origin in comparison with bulk gold. The measurements presented in Figure 5.6 (b) show that the gold features are getting smaller with continuous cycling until they vanish. XPS measurements [337] before and after the cycling experiment presented in Figure 5.6 (b) showed no difference in binding energy (BE) of the gold nor a decrease in the intensity of counts, suggesting a constant amount of gold on the surface and no change of oxidation state. The determination of the oxidation state by XPS has to be taken with care because of a diversity of interpretation of effects that can cause initial state effects (effects that were made responsible for positive core level shifts: e.g. lattice strain increase with small particles, metal insulator transition of small clusters, particle geometry and coordination number, etc.) as well as the problem that initial and final state effects might be overlaid and final state effects are known to be a strong function of substrate conductivity (e.g. [75, 76, 326, 338]). For example Fu et al. were able to identify gold oxide species on titania supported gold nanoparticles using a time-of-flight secondary ion mass spectroscopy technique [339] which are not evident in XPS.

Therefore, it has to be noted that the reasons for the apparent increase in irreversibility are still not understood. Possible explanations could include particle loss of Au, sintering or spreading of the Au atoms over the surface to form thinner layers, a loss of conductivity of the support, encapsulation or conversion of the gold to an oxidised form which is not apparent in a shift towards higher BE in the XPS. Particle sintering seems to be unlikely, as bigger gold particles supported on carbon at similar nominal gold coverage show clearly gold oxide formation and reduction features (see Figure 5.9 and accompanied discussion). Also the unchanged BE position seems to be weak evidence, that no dramatic loss of conductivity occurred [326]. The XPS also rules out massive Au corrosion and further conclusive evidence will be presented later.

The third cycle of voltammetric measurements on RDE's with different equivalent gold film thicknesses (0.13, 0.39, 0.78, 1.17, 1.95, 3.16 nm) and hence different particle sizes (diameter ~ 1.4, 1.7, 2.4, 3.1, 4.5 and 6.6 nm (particles coalesce)) have been overlaid in Figure 5.7. The AuO reduction peaks decrease as expected in the particle size range of 2.4 to 6.6 nm with the surface area. At the particle sizes of 1.7 nm a peak broadening was observed from the first cycle onwards and at the third cycle the peak almost disappeared. At the smallest particle size no gold redox behaviour was observed.
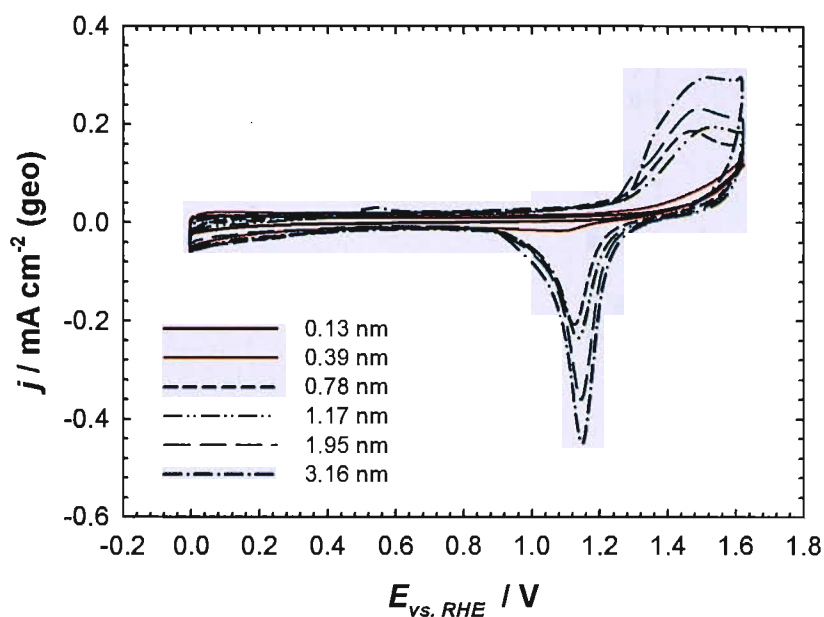
Figure 5.7. *Cyclic voltammogram (v= 100 mV s⁻¹) on titania supported Au different coverages (thicknesses as indicated in the legend) in Argon purged 0.5 M HClO₄ (3ʳᵈ cycle shown).*

Quantification of these trends with particle size are presented in Figure 5.8 where the electrochemical surface area and surface areas as calculated from the TEM (A_{TEM}) images are plotted against nominal gold thickness (a) and particle size (b). The data led to similar plots as presented for the carbon supported gold nanoparticles (see Figure 5.4). For particle sizes above approx. 2 nm the electrochemical surface area followed a similar trend as the surface areas as determined by TEM for hemispheres. At particle sizes below ~ 2nm (see Figure 5.8 (b)) the surface area was found to be almost zero (this was confirmed by array electrode measurements - plots are not shown). Particles below this critical diameter were therefore concluded to behave in non bulk gold like manner. Unfortunately particles of these diameters could not be synthesised on carbon for direct comparison.
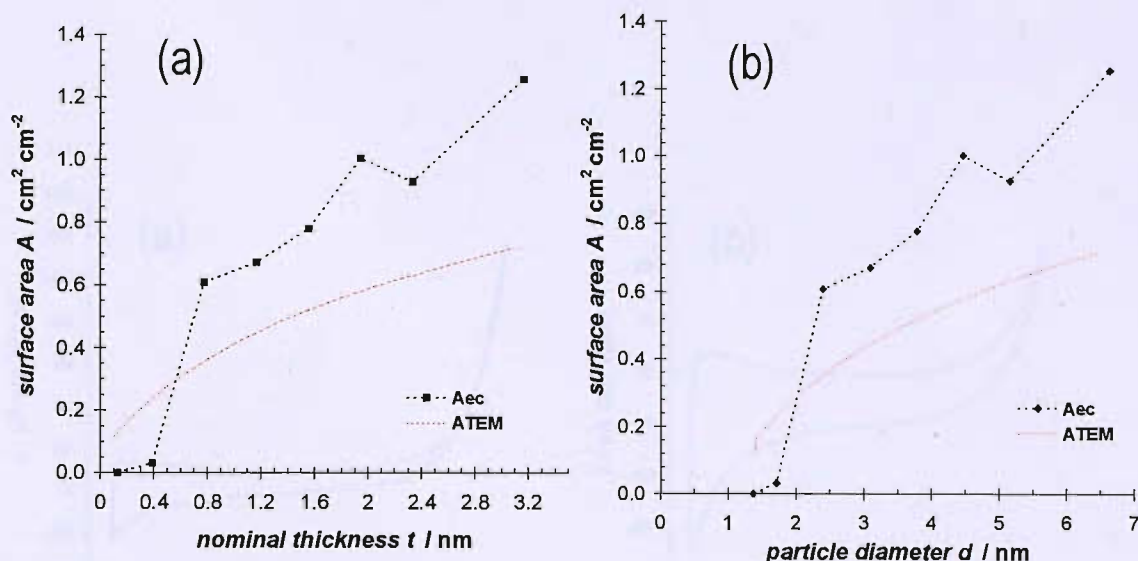
Figure 5.8. *Comparison of the surface areas as determined by TEM (only the best fit is presented as determined in the sample characterisation chapter, shown are the estimated for spherical and hemispherical particles) and by electrochemical determination from the CV for titania supported gold nanoparticles deposited on RDE's.*

An attempt is made in Figure 5.9 to compare equivalent gold thicknesses of 0.13 nm on the support materials under investigation. Figure 5.9 (a) and (b) shows a voltammogram of the second and tenth cycle of 1.4 nm gold nanoparticles supported on titania and Figure 5.9 (c) and (d) equivalent voltammograms of the second and tenth cycle of 2.5 nm gold nanoparticles supported on carbon are shown. The voltammogram of the titania supported sample had the appearance of a thin titania layer without Au (see chapter 4), while the voltammogram of the carbon supported sample shows clear Au/AuO response albeit more irreversible than on bulk Au. The estimated surface areas from TEM for hemispheres are 0.1 cm^2 for the titania sample and 0.06 cm^2 for the carbon sample. The higher surface area for the titania supported sample results from a higher dispersion of the gold as evident in the TEM images (see chapter 3). Again these voltammograms clearly show the loss of metallic behaviour for titania supported gold nanoparticles. The initial conductivity can be assumed to be sufficient to oxidise and reduce the gold (as shown before for bigger particles) and it appears therefore to be unlikely, that this effect was triggered by a resistive substrate effect. The carbon voltammetry showed again slightly higher charge transferred during the first three cycles accompanied with a charge imbalance. Cycle 10 and subsequent cycles appeared not to change further and charge balance was observed.

113
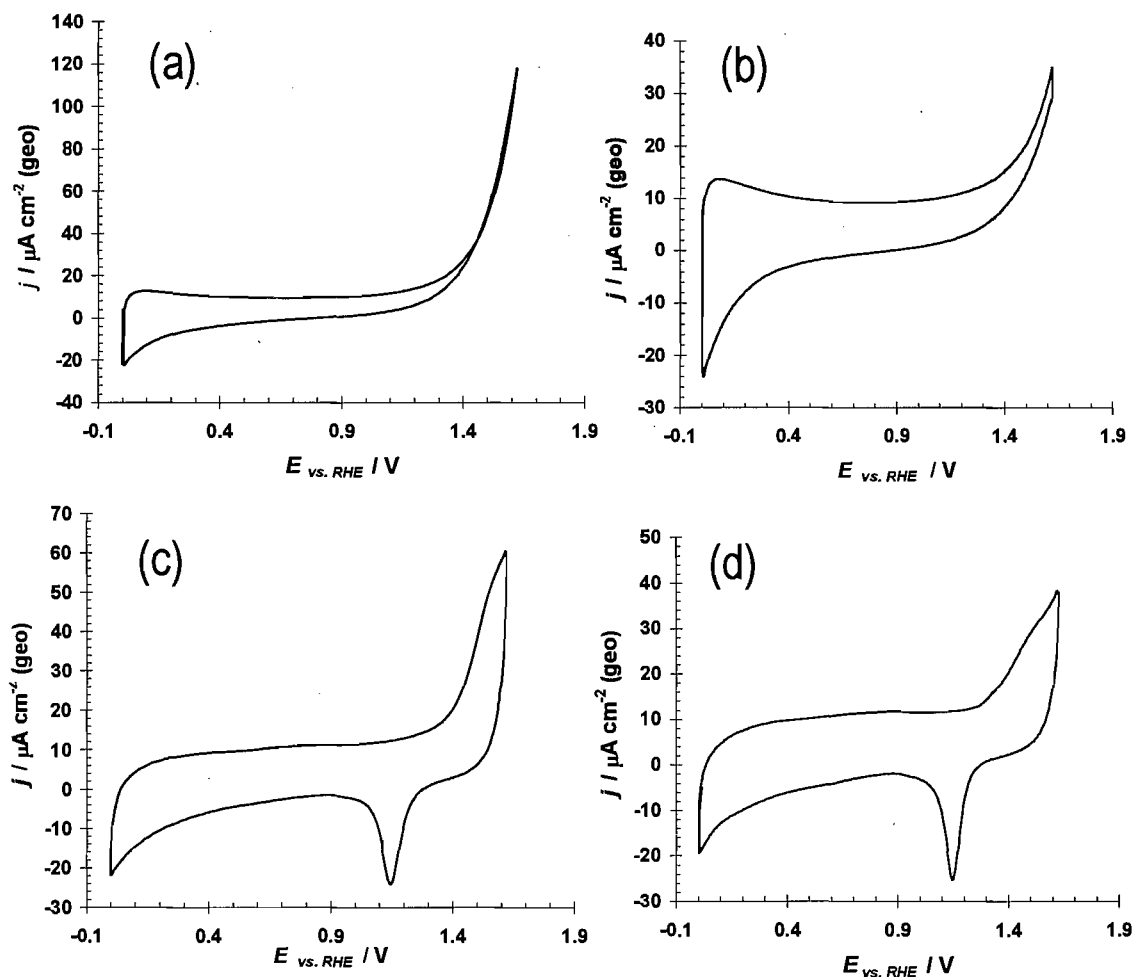
Figure 5.9. *Comparison of titania (a), (b) and carbon (c), (d) supported gold particles on RDE electrodes. The nominal gold thickness on both disc samples was 0.13 nm and the particle diameter 1.4 nm and 2.5 nm respectively. (a) and (c) show the 2nd cycle and (b) and (d) the 10th cycle. Both voltammograms were measured in argon purged 0.5 M HClO$_4$ at a scan rate of 100 mV s^{-1}.*

Not surprising on the basis of the above presented data a correlation between surface areas determined by electrochemistry and TEM do not follow linear behaviour as shown in Figure 5.10. For surface areas (TEM) below ~ 0.28 cm^2, no apparent gold oxide reduction peak was observed and hence no electrochemical gold surface area could be designated to the electrodes. This coincides with a particle diameter of 2 nm in array measurement in good agreement with RDE samples. Thereafter a steep increase of the electrochemical surface area or charge during AuO reduction is evident in the plot. Interestingly the plot seems to be linear at surface areas above ~ 0.55 cm^2.
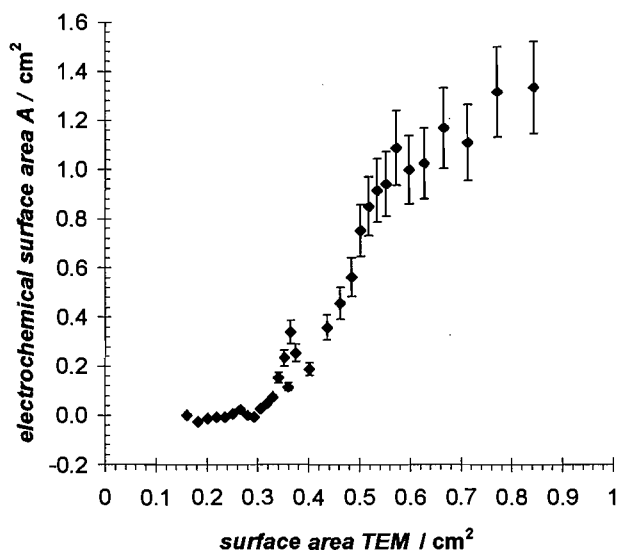
Figure 5.10. *Correlation of the electrochemically determined surface area versus the surface area calculated for hemispherical particles using the diameter and number density from TEM measurements for titania supported gold nanoparticles (data from five arrays, first cycle).*

In chapter 4, it was established, that titania does not exhibit significant oxygen reduction activity below a particle size of approximately 2 nm. The question arose as to whether the surface modification as shown in Figure 5.6 leads to catalytically inactive gold for the oxygen reduction. An experiment was designed to test this on a titania supported Au sample with diameters of 5.1 nm. A series of experiments was conducted, where the RDE electrode was immersed into oxygen saturated 0.5 M $HClO_4$ and chronoamperometric measurements were made between repetitive cycling between 0 V and 1.63 V at 100 mV s^{-1} to modify the electrode. The step experiments were undertaken before any cycling (0 cycles) and after 1, 11, 22 and after 44 cycles (see Figure 5.11 (a)). For the chronoamperometry, the potential was stepped from an initial potential of 0.8 V where no oxygen reduction is expected (holding time 45 s) to 0.5, 0.4, 0.3, 0,4 and 0.5 V (holding time 90 s) and back to the initial potential (see Figure 5.11 (a)). For a more thorough discussion of the oxygen reduction behaviour on gold and supported gold nanoparticle the reader is referred to chapter 6. The results from this experiment are summarised in Figure 5.11 (b). The primary y-axis shows the oxygen reduction activity in terms of the current density (geometric electrode area) of the last ten seconds of the steps to 0.5 and 0.4 V in dependence of the cycle number. On the secondary y-axis the apparent electrochemical surface area was plotted. The first step experiment showed low oxygen reduction activity but activation occurred after one potential cycle. The activity thereafter remained constant, while the gold oxide

reduction peaks diminished. Apparently the electrodes modified by potential cycling remained active for oxygen reduction.
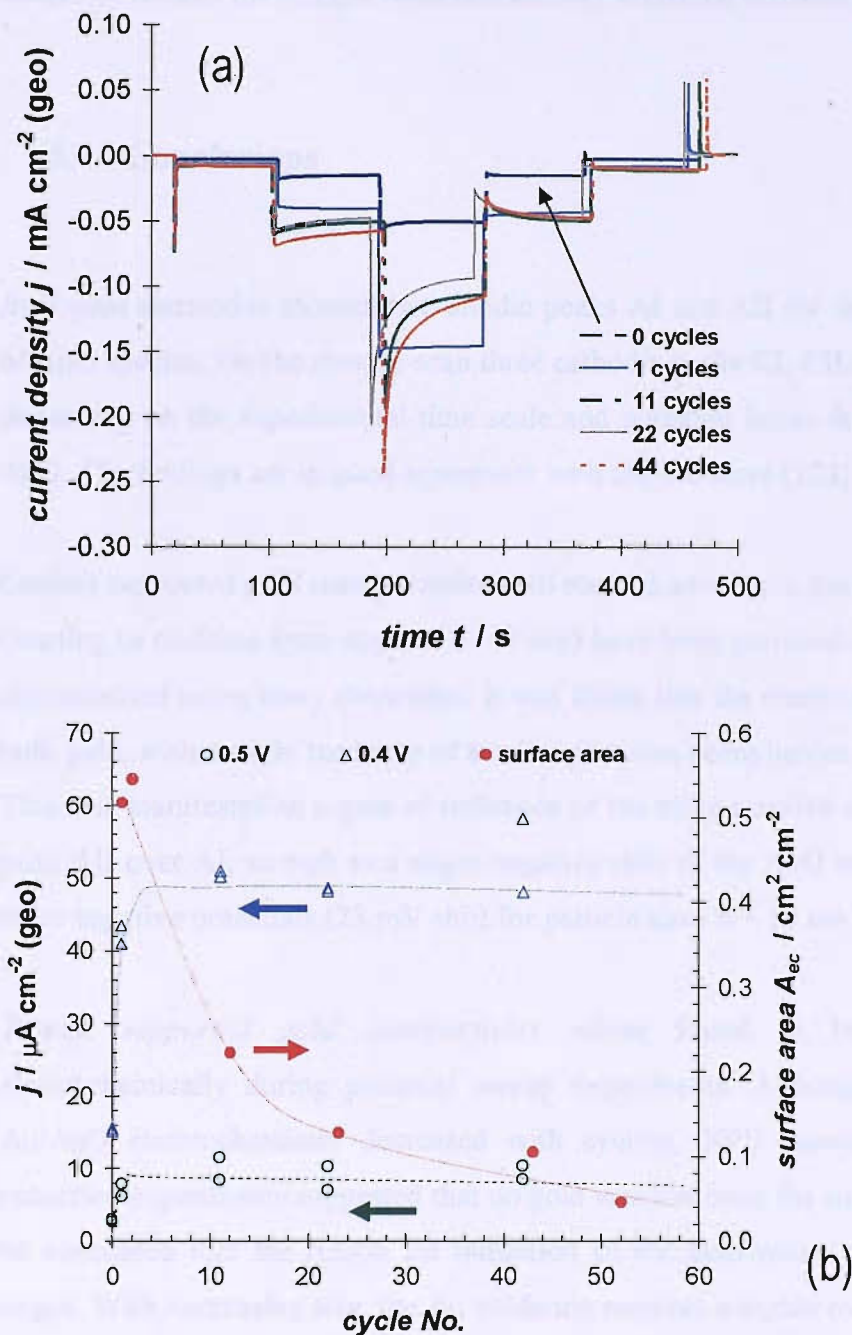
Figure 5.11. *(a) Potential step experiments on an Au/TiO$_x$ disc electrode sample (gold nominal thickness 2.34 nm) in oxygen saturated 0.5 M HClO$_4$. The step potentials were 0.8, 0.5, 0.4 and 0.3 V (holding time t ~ 90 s. per step). (b) Average of the current densities of the last 10 seconds of the steps at 0.5 and 0.4 V (primary y-axis). In between the potential step experiments the disc has been cycled between 0 and 1.63 V in the same electrolyte (oxygen saturated) at a scan rate of 100 mV s^{-1}. On the secondary axis the apparent electrochemically determined surface area with increasing cycle number is shown.*

The described experiment was also conducted on a TiO_x/Au disc electrode, with a mean Au particle size of 1.4 nm. There was no apparent charge transfer due to the redox couple of Au and the oxygen reduction activity remained constant.

5.4 Conclusions

Bulk gold electrodes showed two anodic peaks AI and AII for the oxidation/formation of AuO species. On the reverse scan three cathodic peaks CI, CII and CII are resolvable depending on the experimental time scale and potential limits during the formation of AuO. The findings are in good agreement with the literature [122].

Carbon supported gold nanoparticles with mean diameters in the range of 2.6 to 10 nm (starting to coalesce from approx. d ~ 7 nm) have been prepared and electrochemically characterised using array electrodes. It was found that the electrochemistry is similar to bulk gold, with a slight tendency of smaller particles being harder to oxidise and reduce. This was manifested in a gain of influence of the more positive anodic AuO formation peak AII over AI, as well as a slight negative shift of the AuO reduction peak towards more negative potentials (23 mV shift for particle sizes d ~ 10 nm to d ~ 2.5 nm).

Titania supported gold nanoparticles where found to be strongly modified electrochemically during potential sweep experiments. Although the charge for the Au/AuO electrochemistry decreased with cycling, XPS measurements and oxygen reduction experiments suggested that no gold was lost from the surface. Therefore it can be concluded that the reason for inhibition of the gold redox couple has a different origin. With decreasing size, the Au oxidation requires a higher overpotential and below a critical particle size of ~ 2 nm, the centres were found to exhibiy non-metallic behaviour in potential sweep experiments throughout the characterisation, i.e. they showed no characteristic gold oxide electrochemistry.

Later studies must attempt to elucidate possible electronic changes to the substrate (loss of conductivity), particles (oxidation state) and/or possible morphology changes.

6 Electrochemistry of the oxygen reduction reaction on supported gold particles

6.1 Results and Discussion

6.1.1 ORR on polycrystalline gold

Voltammograms taken in oxygen saturated electrolyte at a scan rate of 20 mV s^{-1} (Figure 6.1) showed three peaks in addition to those for gold in deaerated solution. On the negative going second scan a cathodic wave associated with the reduction of oxygen was evident (marked as peak I). The peak potential E_{pI} was found to be approximately 0.37 V and the peak current density 0.3 mA cm^{-2}. A second peak convoluted with the first one (peak II) was evident at potentials negative to the first at $E_{pII} \sim 0.06$ V and $j_{pII} \sim 0.4$ mA cm^{-2}. On the positive going scan peak (III) was observed. The peak potential was approximately $E_p^A \sim 1.045$ V and the peak current $j_p^A \sim 0.1$ mA cm^{-2}. A linear sweep voltammogram was also recorded for a solution of 1 mM H_2O_2 in 0.5 M $HClO_4$. A reduction peak with potentials close to those for peaks II and III in the oxygen reduction experiment was observed (the inset to Figure 6.1 shows the reduction peak for H_2O_2).
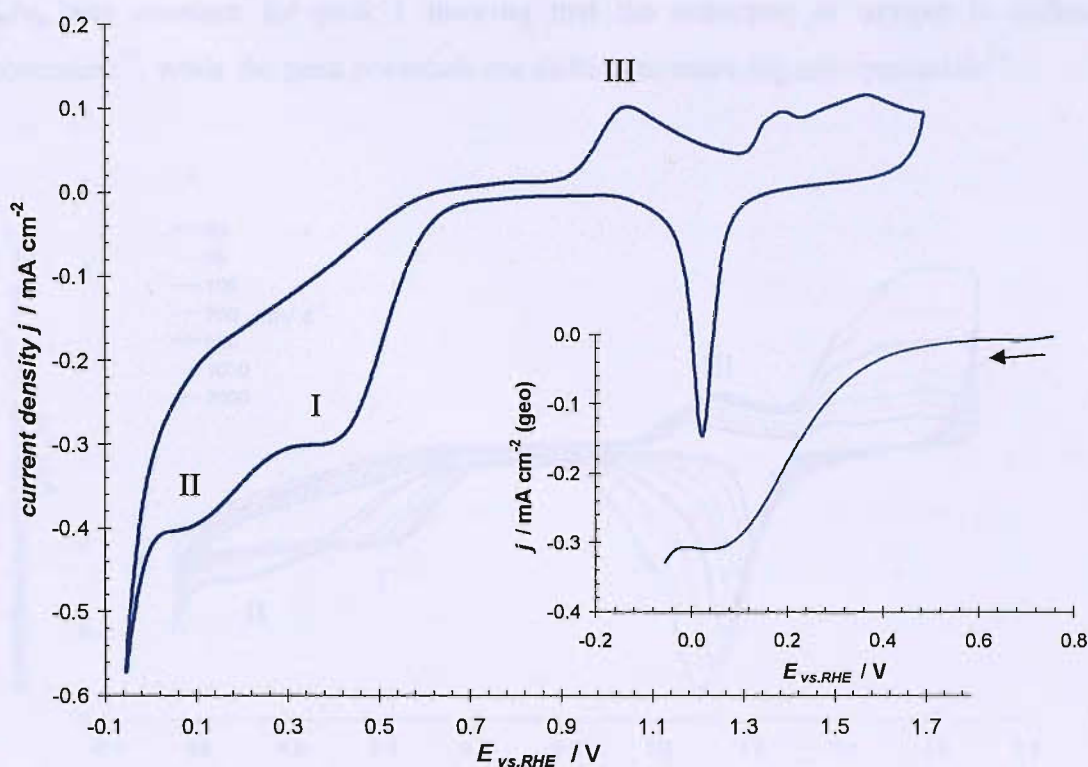
Figure 6.1. *Bulk gold cyclic voltammogram in oxygen saturated 0.5 M HClO₄. The second cycle is shown. The inset shows the negative going scan of a cyclic voltammogram of in Argon purged electrolyte to which ~ 1 mM H₂O₂ was added. The scan rate was 20 mV s⁻¹ and the temperature 298 K.*

In Figure 6.2 scan rate normalised cyclic voltammetry is shown, where the current densities was divided by the square root of the scan rate. The scan rate in oxygen saturated solution was varied over three orders of magnitude. Respectively the second cycles of cyclic voltammetry at scan rates of 0.02, 0.05, 0.1, 0.2, 0.5, 1 and 2 V s⁻¹ are shown. The peaks dedicated to the gold oxide behaviour were discussed in the previous section. The peaks associated with the solution oxygen electrochemistry are again signed by roman numbers (I, II and III).

J_p/v_p was constant for peak I showing that the reduction of oxygen is diffusion controlled[13], while the peak potentials are shifting to more negative potentials[14].
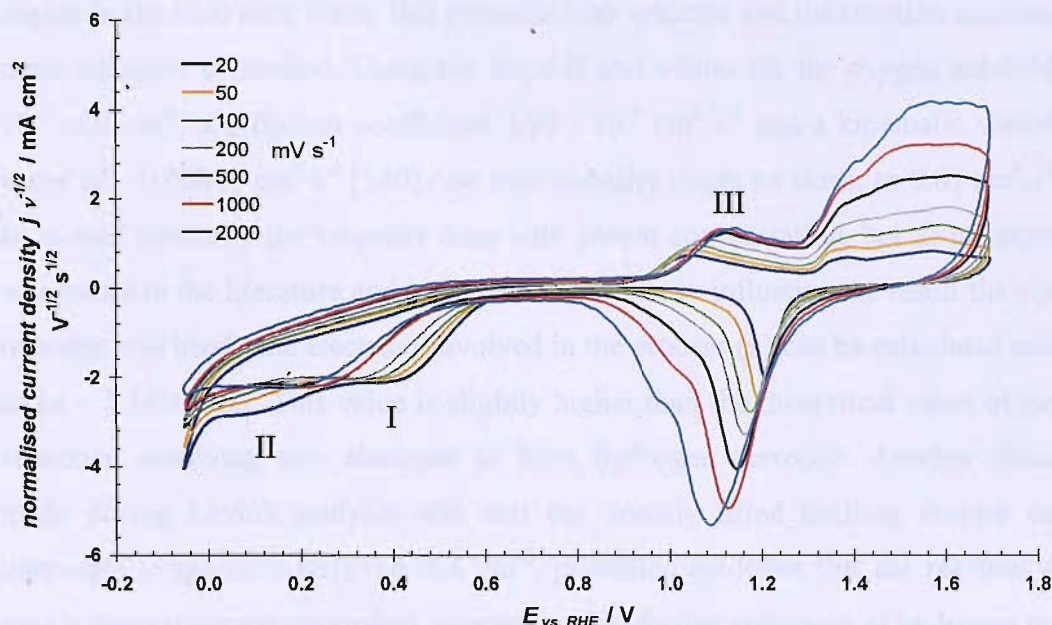
Figure 6.2. *Scan rate normalised cyclic voltammetry (second cycle) at a bulk electrode in oxygen saturated 0.5 M HClO₄. The scan rate was varied to be 20, 50, 100, 200, 500, 1000 and 2000 mV s⁻¹ and the temperature was 298 K.*

Figure 6.3 (a) shows voltammograms of bulk gold RDE in oxygen saturated 0.5 M HClO₄ maintained at a temperature of 298 K at a sweep rate of 20 mV s⁻¹. The rotation rate was varied to 400, 900, 1600 and 2500 rpm. The slow scan gold voltammograms at all rotation rates showed the onset of the oxygen reduction waves at potentials < 0.65 V.

---

[13] During irreversible voltammetry the peak current density j_p follows:

$$j_p = \left(-2.99 \cdot 10^5\right) n \left(\alpha_c n_\alpha\right)^{\frac{1}{2}} c^0 D^{\frac{1}{2}} v^{\frac{1}{2}}$$, where n is the number of electrons involved in the

reaction, α_C the transfer coefficient for the reaction, n_α the number of electrons involved in the rated determining step, c^0 the bulk concentration (here the oxygen solubility in the electrolyte), D the diffusion coefficient (of oxygen) and v the scanrate. [Electrochemistry Textbooks]

[14]The peak potential changes according to: $E_p^C = K - \dfrac{2.3RT}{2\alpha_c n_\alpha F} \log v$ where

$$K = E^0 - \frac{RT}{\alpha_c n_\alpha F}\left(0.78 - \frac{2.3}{2}\log\left(\frac{\alpha_c n_\alpha FD}{\left(k^0\right)^2 RT}\right)\right)$$

The limiting current densities (geometric surface area) should be a function of the square root of the rotation rate at mass transport dominated overpotentials. The inset presented in Figure 6.3 (a) showed the Levich plot at 0 V. Due to the lack of a plateau region in the reduction wave, this potential was selected and the reaction assumed to be mass transport controlled. Using the slope B and values for the oxygen solubility, $1.3 \cdot 10^{-6}$ mol cm^{-3}, a diffusion coefficient $1.93 \cdot 10^{-5}$ cm^2 s^{-1} and a kinematic viscosity for water of ~ 0.00891 cm^2 s^{-1} [340] (the true viscosity might be closer to 0.01 cm^2 s^{-1} [341] as in acid generally the viscosity rises with proton concentration, but as no exact value was found in the literature and it did not significantly influence the result the viscosity, of water was used), the electrons involved in the process (n) can be calculated and found to be $\sim 2.14 \pm 0.03$. This value is slightly higher than the theoretical value of two for a reduction involving two electrons to form hydrogen peroxide. Another observation made during Levich analysis was that the linearly fitted limiting current densities intercepts at approximately 0.6 mA cm^{-2}, providing evidence that the reaction was not purely mass transport controlled, suggesting that further reduction of hydrogen peroxide contributes to the currents.
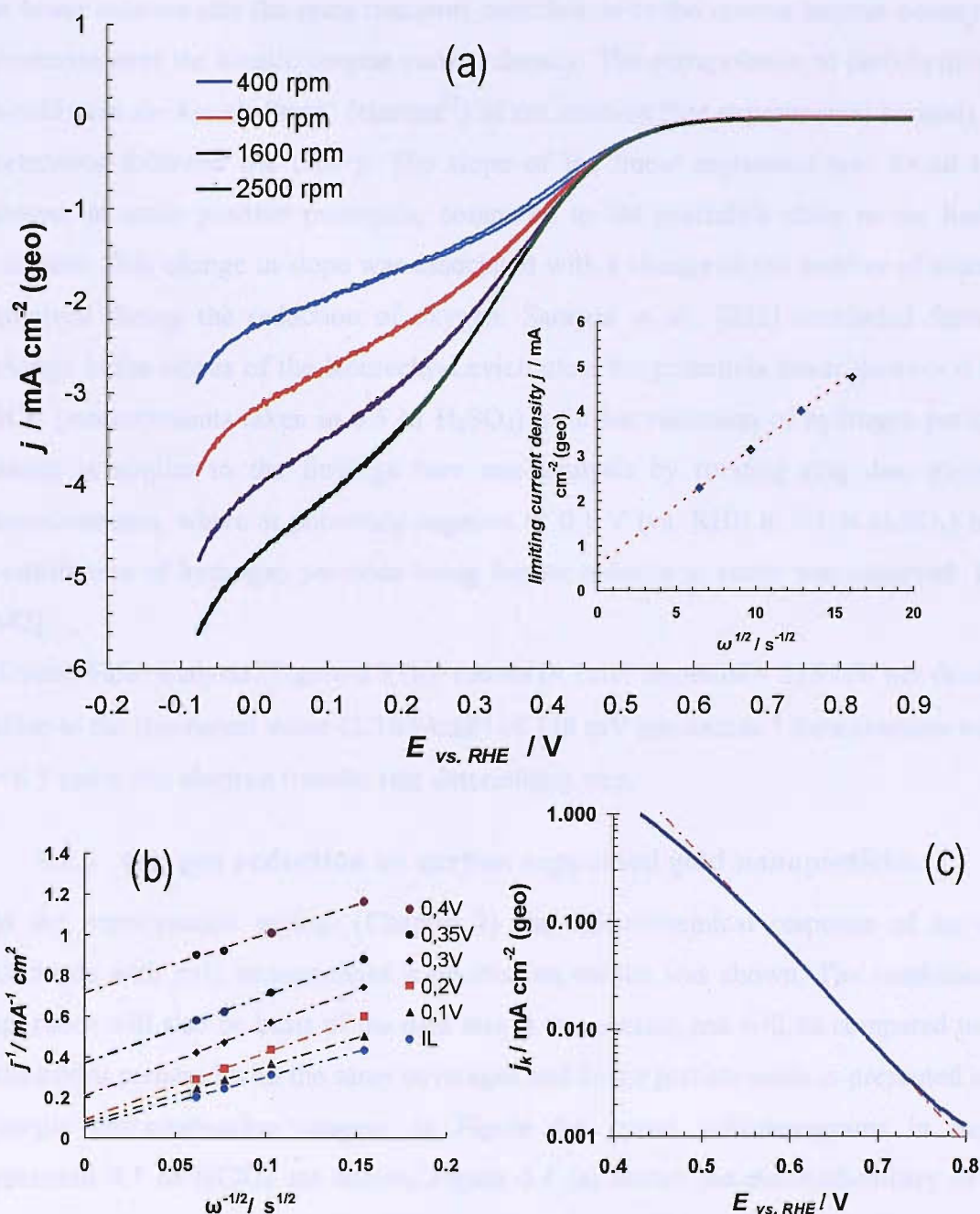
Figure 6.3. *(a) Steady state polarization curves under an oxygen atmosphere at a bulk gold disc electrode in 0.5 M HClO₄ at a scan rate of v = 20 mV s⁻¹ and a temperature of 298 K. The rotation rates are 400, 900, 1600 and 2500 rpm. The inset presents the Levich plot for an assumed mass transport limited potential of 0V during the negative scan direction. (b) Koutecký-Levich plot at the potentials 0 (IL), 0.1, 0.2, 0.3, 0.35 and 0.4 V. Again on the negative going scan. (c) mass transport corrected Tafel plot (limiting current assumed to be 0 V) of the negative going potential sweep at 900 rpm.*

Figure 6.3 (b) shows Koutecký-Levich plots at the potentials 0, 0.1, 0.2, 0.3, 0.35 and 0.4 V. The currents were taken from the polarisation curves shown Figure 6.3 (a). The inverse current densities (geo) increased with the inverse square root of rotation rate; i.e.

at lower rotation rate the mass transport contribution to the inverse current density was dominant over the kinetic inverse current density. The extrapolation to zero in this plot would give the kinetic "rate" (current[15]) of the reaction (see experimental section). The behaviour followed the theory. The slope of the linear regression was found to be steeper at more positive potentials, compared to the potentials close to the limiting currents. This change in slope was associated with a change in the number of electrons involved during the reduction of oxygen. Sarapuu et al., [232] concluded from the change in the slopes of the Koutecký-Levich plots for potentials lower than ~ - 0.1 vs. SCE (measurements taken in 0.5 M H_2SO_4) a further reduction of hydrogen peroxide, which is similar to the findings here and analysis by rotating ring disc electrode measurements, where at potentials negative of 0.3 V (vs. RHE in 0.1 N H_2SO_4) in the contribution of hydrogen peroxide being further reduced to water was observed [205, 342].

Kinetic Tafel analysis (Figure 6.3 (b)) results in Tafel slopes of ~ 115 mV per decade^{-1}, close to the theoretical value ($2.3RT/\alpha nF$) of 118 mV per decade^{-1} for a reaction with α = 0.5 and a one electron transfer rate determining step.

6.1.2 Oxygen reduction on carbon supported gold nanoparticles

In the experimental section (Chapter 2) the electrochemical response of an array electrode with gold nanoparticles supported on carbon was shown. The combinatorial approach will also be basis of the data sets in this section and will be compared to disc electrodes prepared with the same coverages and hence particle sizes as presented in the sample characterisation chapter. In Figure 6.4 cyclic voltammograms in oxygen saturated 0.5 M $HClO_4$ are shown. Figure 6.4 (a) shows the electrochemistry of disc

---

[15] For comparison of the electrochemistry conducted in this work one might want to compare the activities at a fixed potential. In this work the specific activity j_k (surface area and mass transport corrected at the negative going scan) of the oxygen reduction reaction on bulk gold at 0.4 V vs. RHE (at 900 rpm rotation rate) was found to be 0.46 ± 0.04 mA cm^{-2} in 0.5 M perchloric acid and 0.06 ± 0.005mA cm^{-2} 0.5 M sulphuric acid (Aldrich, 99.999%). The surface area was estimated from cyclic voltammetry measurements, where the upper potential limit was 1.63 V vs. RHE and the scan rate 100 mV s^{-1}. The charge transferred during gold oxide reduction was then determined by integration and to determine the charge was subsequently divided by 400 μC cm^{-2} for normalisation (compare experimental section).

electrodes of gold nanoparticles supported on amorphous carbon (arc-sputtering system) on glassy carbon discs. The coverages were 0.13 nm, 0.78 nm and 2.33 nm. At all three samples, oxygen reduction is observed as an irreversible peak/wave in the potential range 0.4 V – - 0.2 V. The limiting currents were found to decrease, the response becomes less steep, and shifted negative as the gold loading was decreased, i.e. the overpotential for O_2 reduction increases with diminishing gold loading. In the positive going cycle hydrogen peroxide formed during the oxygen reduction is oxidised in the potential range 0.85 to the upper potential limit during the cyclic voltammetry (here 1.63 V and 1.7 V). In this potential range a peak was observed typical for a diffusion controlled electrode process. At potentials higher ~ 1.25 V gold oxide formation has to be expected (refer to chapter 5 gold oxide electrochemistry) and the CV showed that the currents recorded did not decay as expected for a change of diffusion profile after passing the peak maximum by the increase of the diffusion layer thickness, suggesting a convoluted peak ascribed to the gold oxide formation. In addition, the peak at ~ 1.16 V on the negative going scan is characteristic of the reduction of the oxygen covered surface back to gold.

Figure 6.4 (b) shows an equivalent experiment on carbon supported gold nanoparticles prepared by the wedge shutter method across an array electrode. The main diagonal of the electrodes is shown. This presentation clearly presents the great advantage of the combinatorial approach. All electrodes have exactly the same conditions such as scan rate, potential limits, mass transport and temperature. The nominal thicknesses of gold as determined by calibration samples were of 0.21, 0.39, 0.56, 0.74, 0.92, 1.09, 1.27 and 1.44 nm. The features were the same as discussed above for the disc samples (see Figure 6.4 (a)). For comparison Figure 6.4 (c) presents a CV on a bulk gold disc using the same conditions. The charge ratio transferred during ORR and H_2O_2 oxidation was found to be within experimental errors the same on bulk gold and carbon supported gold (Figure 6.4 (d), primary y-axis). With decreasing particle size the potential of the H_2O_2 oxidation peak maximum shifted positive, i.e. the overpotential increased (Figure 6.4 (d), secondary y-axis). Respectively the peak maximum during oxygen reduction did move negative with decreasing particle size (see Figure 6.4 (b)).
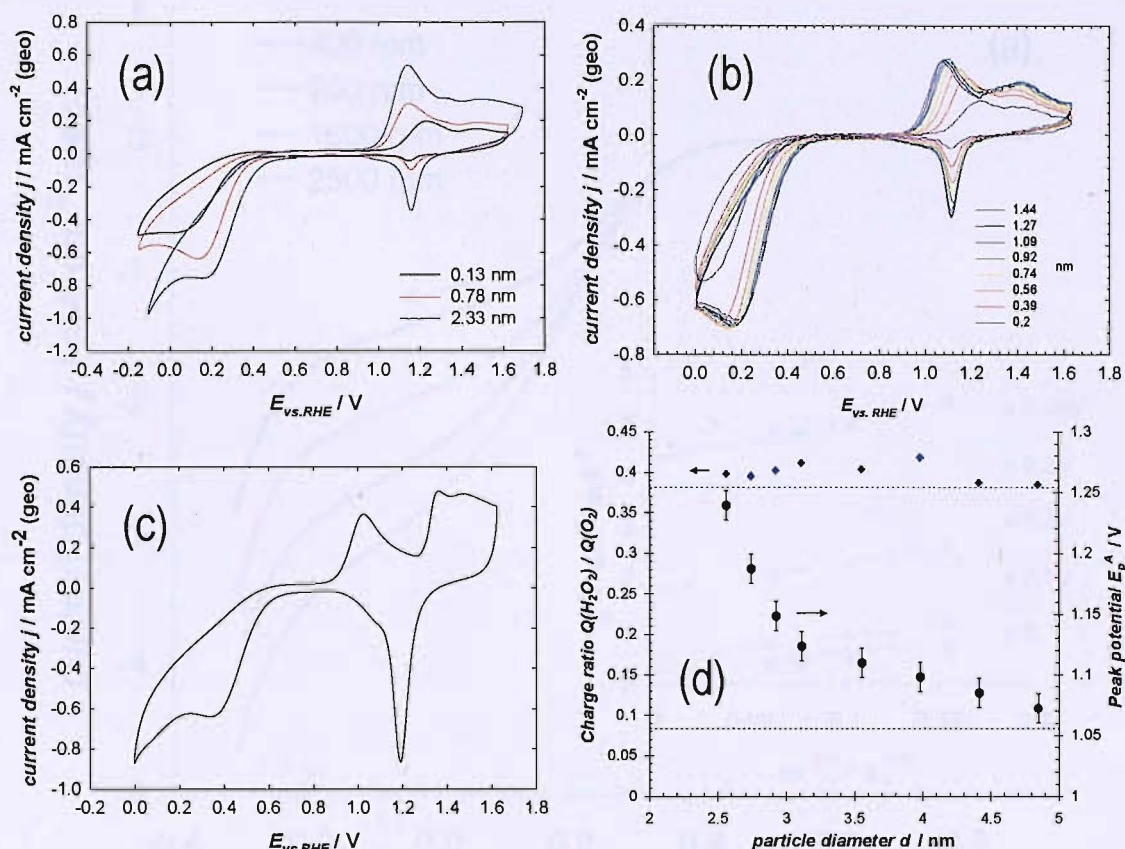
Figure 6.4. *Cyclic voltammograms of carbon supported gold particles in O_2 saturated 0.5 M $HClO_4$. (a) Glassy carbon disc samples (nominal thicknesses 2.33 nm, 0.78nm and 0.13 nm). (b) Selected electrodes in an array electrode (nominal thicknesses 1.44 nm, 1.27 nm, 1.09 nm, 0.92 nm, 0.74 nm, 0.56 nm, 0.39 nm and 0.21 nm). (c) bulk gold disc (d) primary axis oxygen reduction to hydrogen peroxide oxidation charge ratio of the voltammograms in(b) and on the secondary axis the peak potentials E_p^A of the hydrogen peroxide oxidation. Also shown as dotted lines are the according values for the bulk gold voltammogram in (c). The Potential scan rate was $v = 100$ mV s^{-1}. The responses shown are the second cycles. The temperature was thermostated to 298 K (a) and (c) and room temperature (d).*

The oxygen reduction/hydrogen peroxide oxidation became more irreversible. At higher coverages, i.e. bigger particles, the peak potential converged close to bulk gold like behaviour. Moreover, the steady state voltammetry showed bulk gold like behaviour (Figure 6.5) with a Tafel slope at 900 rpm of 112 mV dec^{-1} close to the 115 mV dec^{-1} observed on bulk gold.
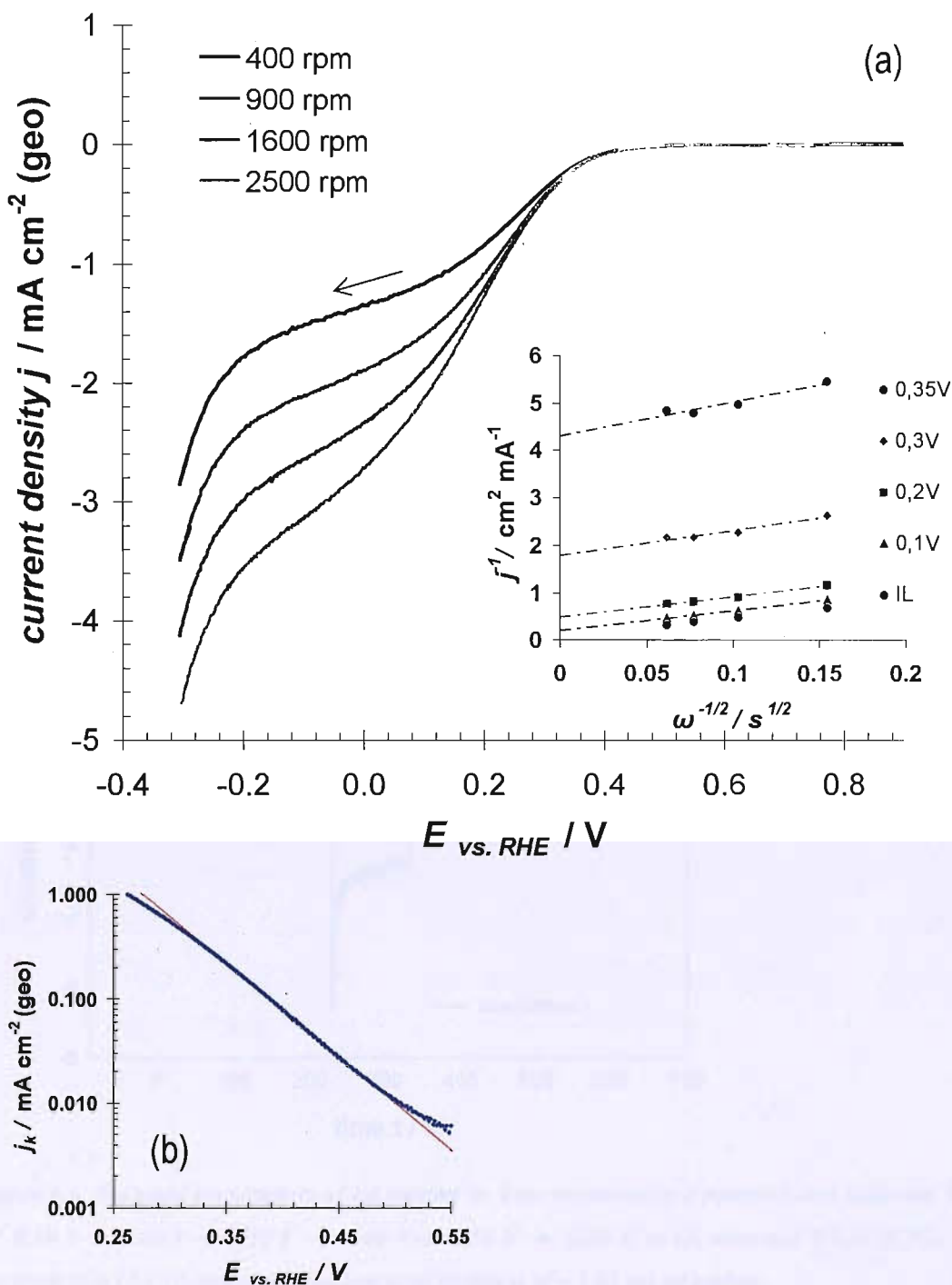
Figure 6.5. *Carbon supported gold nanoparticles (d ~ 7 nm) (a) Steady state polarisation curves (negative scan) under an oxygen atmosphere in 0.5 M HClO₄ at a scan rate of v= 20 mV s⁻¹ and a temperature of 298 K. The rotation rates are 400, 900, 1600 and 2500 rpm. The inset presents the) Koutecký-Levich plot at the potentials -0.05 (IL), 0.1, 0.2, 0.3 and 0.35 V. (b) mass transport corrected Tafel plot (limiting current assumed to be -0.05 V) of the negative going potential sweep at 900 rpm.*

For quantitative definition of the effect of the particle size upon the oxygen reduction reaction chronoamperometric measurements have been taken. Surface area corrected current densities enabled quantitative analysis. In these experiments the potential was

stepped from an initial potential, where no reaction occurs (0.8 V) to oxygen reducing potentials (0.5, 0.4 and 0.3 V). The electrode potential was held constant for a period of 90 seconds at reducing potentials and 45 seconds at the initial potentials. In the experimental section (Figure 2.15), a set of one array electrode step experiment on all 100 electrodes was shown. For a more detailed presentation one electrode out of an array of electrodes of carbon supported gold nanoparticles is shown in Figure 6.6. At 0.3 V, there is a small initial decay in current perhaps due to some influence of non-steady state diffusion. The figure also confirms that when the direction of the potential steps is reversed, the same constant currents are obtained at both 0.4 V and 0.5 V. The data at 0.5 V was not further analysed because of the small magnitudes of the currents compared to the noise and the currents at 0.4 V and 0.3 V were used as a measure of oxygen reduction activity.
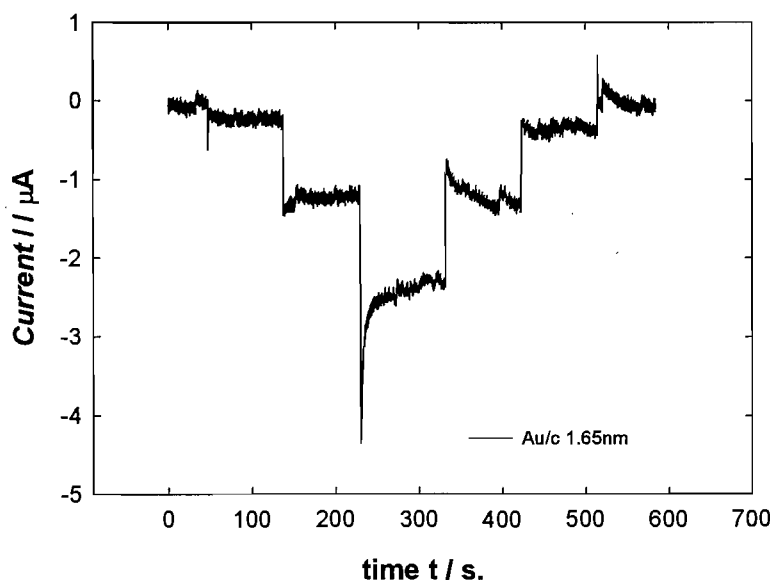
Figure 6.6. *Enlarged presentation of the current vs. time responses to a potential step sequence, 0.80 V → 0.50 V→ 0.40 V→ 0.30 V → 0.40 V→ 0.50 V → 0.80 V, in O_2 saturated 0.5 M $HClO_4$ at an electrode in a 10 x 10 array with nominal gold thickness of ~ 1.65 nm on carbon.*

Every experiment on the array electrode produced a complete data set of measurements at one hundred electrodes of the type presented in Figure 6.6. For analysis an in house written Matlab® program was used. The software allowed analysis of the potential step experiments in the following way. The baseline was set to the current at 0.8 V and outputted the average of a time interval at each step (in here the average of the last 10 seconds of each step was used). Figure 6.7 shows the current densities normalised for the geometric surface area of carbon supported gold particles at 0.4 and 0.3 V

depending on the particle sizes. Evidently the current density (geo) increased with increasing particle size. This statement is not valid, however, as the coverage increased and the surface area also increased.
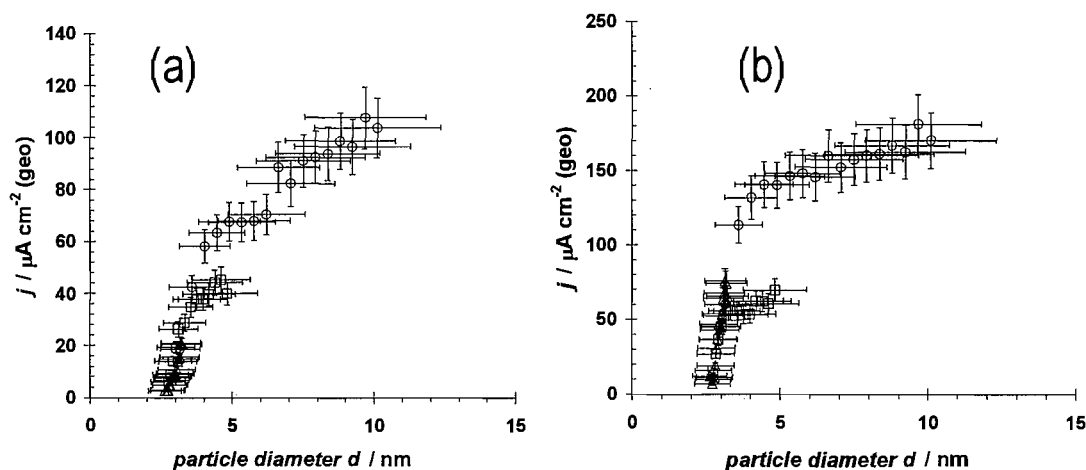
Figure 6.7. *Oxygen reduction activities obtained from potential step experiments at 0.4 (a) and 0.3 V (b). The x error bars indicate the standard deviation of the particle size distribution and the y error was the standard deviation of the main diagonal (n=10) of the array of electrodes.*

For more quantitative analysis mass normalisations and real surface area corrections of the current densities are common. Figure 6.8 shows three different ways of correcting the geometric current densities at 0.4 and 0.3 V: Mass activity j_m, electrochemical surface area normalised specific activity j_A (ec) and TEM surface area normalised specific activity j_A (TEM).
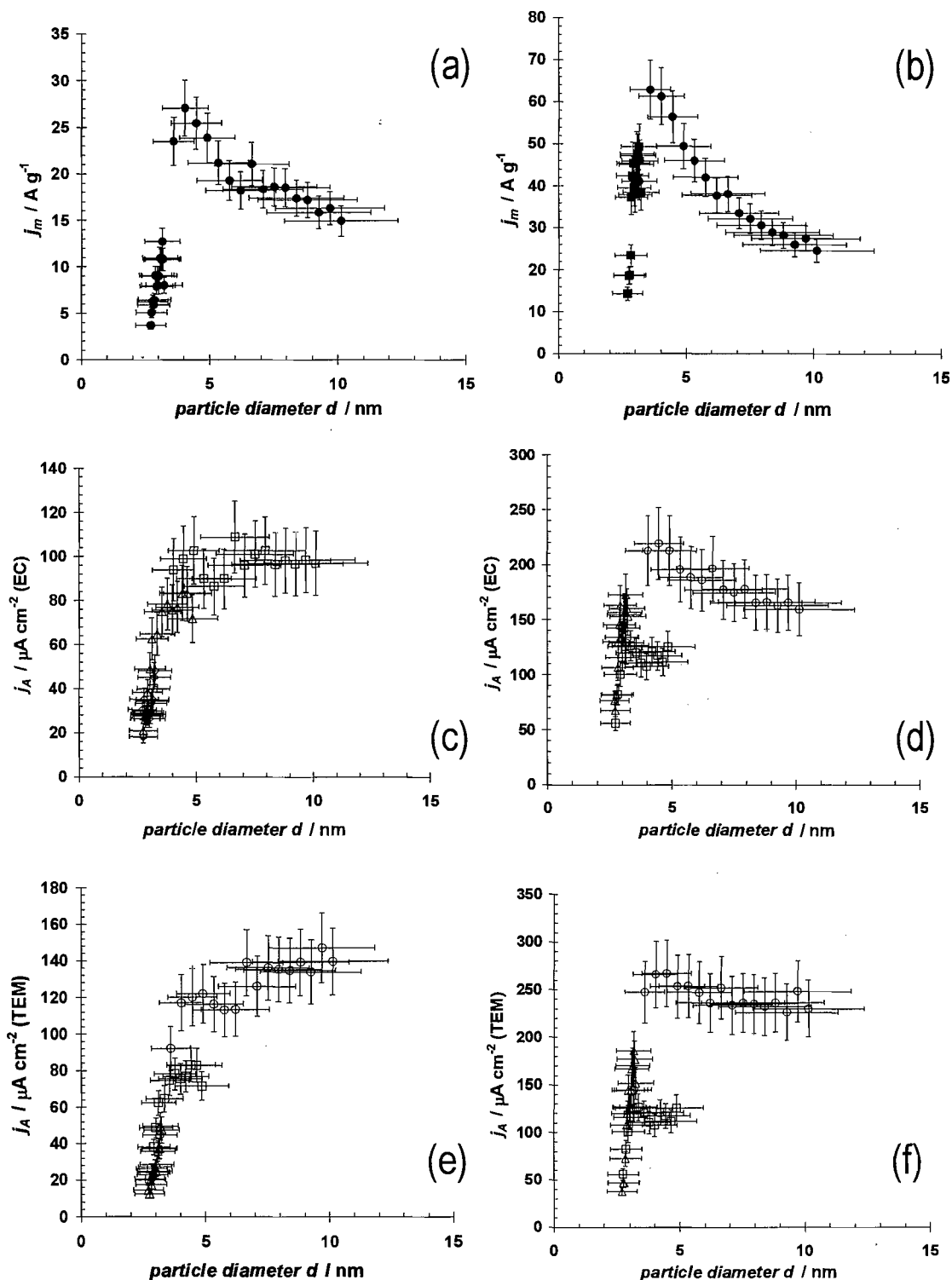
Figure 6.8. *Analysis of ORR on carbon supported gold nanoparticle. (a) Mass activity at 0.4 and (b) 0.3 V. (c) electrochemical surface area corrected "specific activities at 0.4 and (d) 0.3V. (e) TEM determined surface area corrected "specific activities" at 0.4 and (f) 0.3 V. The error bars along the particle size axis indicate the range of particle size (in fact, the standard deviation of the particle size) observed by TEM. The error bars on the specific activity axis reflect the standard deviation of the currents measured at the 10 electrodes on the array with a mean particle size.*

129

The mass activity was calculated from the volume of an equivalent thin gold film on the electrode area multiplied by the density of gold. The error bars indicate (i) the standard deviation of the particle size distribution resulting from each deposition and (ii) the variation in the currents at the arrays as estimated from the standard deviation of the currents across the row of electrodes with the same particle size.

Evidently the mass activity was a function of particle size as can be seen in Figure 6.8 (a) and (b). The data has a peak shape with a maximum of 27.1 A g^{-1} at particle diameters 3.6 nm at 0.4 V. At higher overpotentials (step potential 0.3 V) the peak seems to be at slightly bigger particle diameters ~ 4 nm and a maximum mass activity of 62.9 A g^{-1} was observed. The activity showed a steep drop at smaller particle sizes, being only ~ 13 % (0.4 V) or ~ 23 % (0.3 V) of the maximum activity at a particle size of 2.7 nm. At bigger particle sizes, the mass activity decays as a smaller % of Au atoms are exposed to electrolyte. This effect was more pronounced at 0.3 V, where as seen in Figure 6.6 by the decay of current with time the mass transport gains influence on the current. The steep decay of mass activity at smaller particles indicates a structure sensitive reaction.

Figure 6.8 (c) and (d) show the particle size dependent "specific activity", where the current density was corrected for the electrochemical determined surface area as described in the experimental section. At 0.4 V the specific activity remained constant in a range of particle sizes with a diameter of ~ 4 – 10 nm. At particle sizes below a critical diameter of ~ 3.1 nm a steep decrease in activity was observed. The same trends where observed at 0.3 V, where the kinetic currents are influenced by the mass transport effects as evident by slightly less deactivation. The steep decay of activity lies at a particle size between 3.1 and 4 nm.

Figure 6.8 (e) and (f) shows the particle size dependent "specific activity", where the current density was corrected for the surface area determined by TEM assuming hemispherical particles as described in the experimental section. The trends are qualitatively the same as for the electrochemically determined surface area. The steep decay in specific activity started in this characterisation method at particle sizes of ~ 4 nm (0.4 V) or 3.6 nm (0.3 V). In the gold oxide section (Chapter 5) the surface area

determined by the two characterisation methods (TEM and EC) was compared and it was found that they differed for the hemispherical particle assumption. Therefore the specific activities as determined by TEM are about 20 % higher at the maximum activity than for the electrochemically corrected specific activities.

6.1.3 ORR on TiO$_x$ supported gold nanoparticles

Figure 6.9 shows expansions of cyclic voltammograms for an O$_2$ saturated 0.5 M HClO$_4$ recorded at three electrodes in an array of Au/TiO$_x$ electrodes, as well as on three disc electrodes. The scan rate was 50 mV s^{-1} at the array electrode and 100 mV s^{-1} at the disc electrodes. The three voltammograms in Figure 6.9 (a) and (b) correspond to surfaces with different nominal thicknesses of gold as indicated in the legend, corresponding to similar particle sizes on the array as well as on the disc electrodes. At all three surfaces, oxygen reduction is observed as an irreversible peak/wave in the potential range 0.4 V – 0.0 V. The limiting currents are very similar (as expected for a diffusion controlled process) but the reduction of oxygen clearly shifts to a more negative potential as the gold loading, hence the particle size decreased, i.e. the overpotential for O$_2$ reduction increases with diminishing gold loading and particle size. With the highest loading of gold (particle sizes ~ 4.6 (array) or 5.2 (disc) nm), the features on the voltammogram are similar to those at a bulk gold electrode; the positive scan showed a peak with an peak potential at the current maximum of approx. ~ 1.2 V for the oxidation of the hydrogen peroxide formed during the reduction of oxygen. At more positive potentials, charge for the oxidation of the gold surface was observed. In addition, the peak at 1.18 V on the negative going scan at the array electrode was characteristic of the reduction of the oxygen covered surface back to gold. The gold oxide reduction peak at the disc with the same coverage showed a slightly more negative shifted peak (1.12 V). Also the sizes were smaller than on the array. It must be noted, that on titania supported samples the behaviour of the gold oxide was very sensitive to electrochemical modification and any slight differences in the pre-treatment lead to significantly different responses (see chapter on gold oxide).

At the lower loading Au surfaces, the responses at more positive potentials are more surprising. Firstly, the anodic current for the oxidation of hydrogen peroxide is much diminished. This is partly because less hydrogen peroxide is formed in the experiment

but more importantly the oxidation appears to become more irreversible on the lower loading of gold. Secondly, the oxidation of the gold surface appears to become more irreversible.
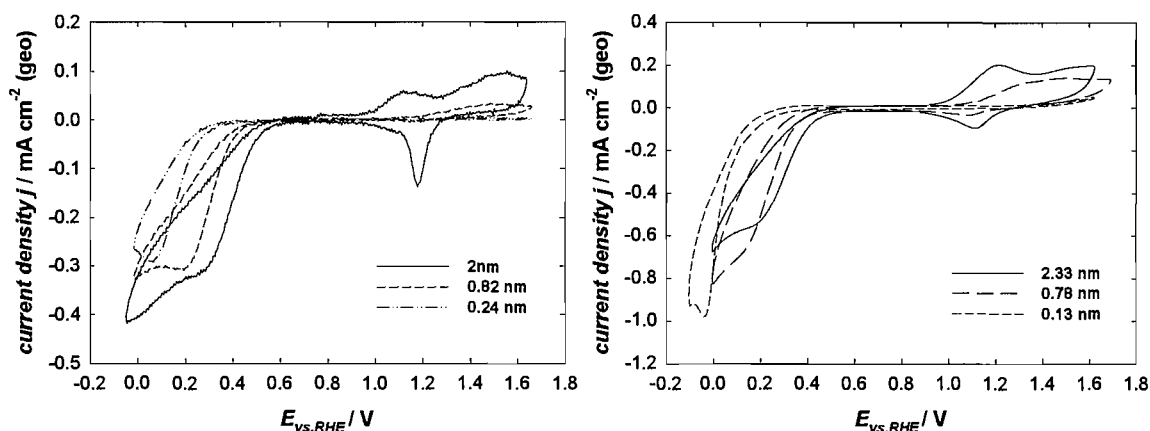
Figure 6.9. *Cyclic voltammograms of TiO_x supported gold particles (a) array electrodes (nominal thicknesses 2.0 nm, 0.82 nm and 0.24 nm → respectively particle sizes of 4.6, 2.5 and 1.5 nm). Potential scan rate 50 mV s^{-1}. (b) (nominal thicknesses 2.33 nm, 078 nm and 0.13 nm → respectively particle sizes 5.2, 2.4 and 1.4 nm). Potential scan rate v = 100 mV s^{-1}. All measurements were taken in O_2 saturated 0.5 M $HClO_4$. The third cycle were shown*

Oxygen reduction was examined as a function of gold centre size using rotating disc voltammetry. Figure 6.10 (a) reports a set of steady state voltammograms as a function of rotation rate for a Ti/TiOx/Au disc (mean Au centre diameter is 1.7 nm) in O_2 saturated 0.5 M perchloric acid. Each voltammogram has a well formed wave for the reduction of oxygen with $E_{1/2}$ close to 0.2 V and a mass transport controlled plateau negative to 0 V. This is close to the response at a massive gold electrode although the waves are slightly shifted towards more negative potentials. The inset shows Koutecký-Levich plots at a series of potentials confirming by their linear behaviour model system like behaviour. Figure 6.10 (b) showed the Tafel plot at 900 rpm. The slope was found to be close to the theoretical slope of 118 mV per dec^{-1} ($\alpha = 0.5$) for a one electron rate determined reaction with 117 mV dec^{-1}. Voltammograms were also recorded in O_2 saturated 0.5 M $HClO_4$ solution for eight further Ti rotating disc electrodes with TiO_x substrate layers but gold deposits with different nominal thicknesses ranging from 0.13 nm to 3.1 nm or particle sizes varying between 1.4 and ~ 6.6 nm. It must be noted that at the biggest particle size of 6.6 nm the particles start to coalesce. Figure 6.11 reports voltammograms obtained at 900 rpm for five selected coverages with nominal gold thicknesses (and particle diameters d) of 0.13 nm (d ~ 1.4 nm), 0.78 nm (d ~ 2.4), 1.17 nm (d ~ 3.1), 1.56 nm (d ~ 3.8 nm) and 1.95 nm (d ~ 4.5 nm). It can be seen that the

limiting current density for oxygen reduction (based on the geometric area) is independent of the amount of gold on the surface. Also, with the thicker deposits (nominal thicknesses 1.17 – 1.95 nm), the response is very similar but with the thinner gold deposits, the reduction wave shifts to significantly more negative potentials. The kinetic currents at 0.4 V and 0.3 V as determined by Koutecký-Levich correction (refer to experimental section) were again taken as a measure of activity of the surfaces for oxygen reduction. In addition, the kinetic currents as a function of potential were used to construct Tafel plots. At all surfaces studied, the log j_k vs. E plots were linear with a slope of $(120 \pm 12 \text{ mV})^{-1}$ and this is the Tafel slope reported for other gold surfaces in the literature [205, 232]. This confirms that the mechanism for oxygen reduction at the small gold centres was the same as at bulk gold and that the reaction is initiated by the transfer of a single electron.
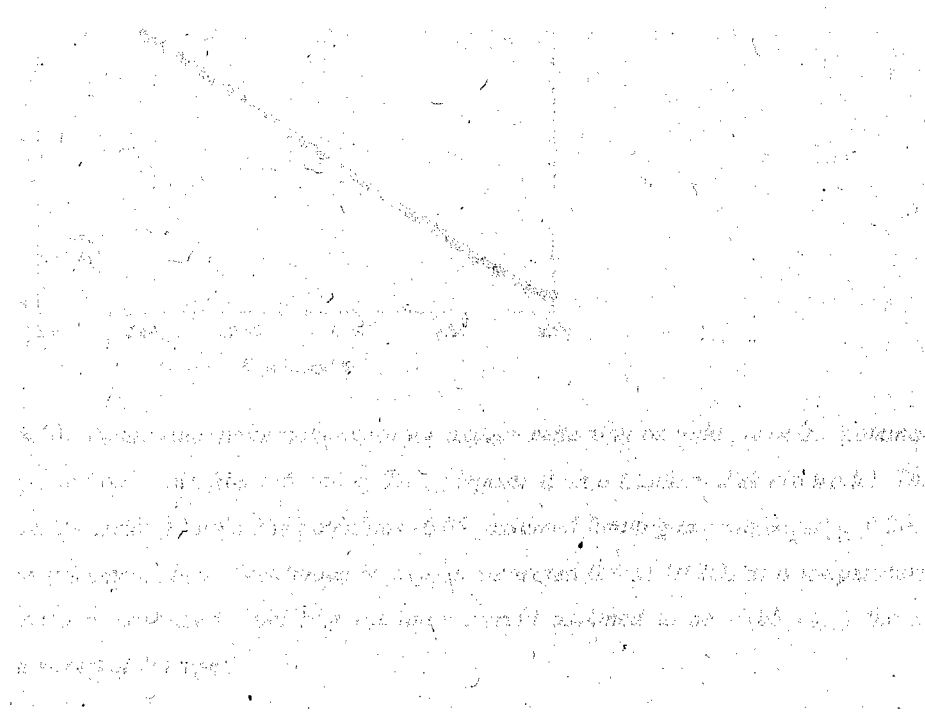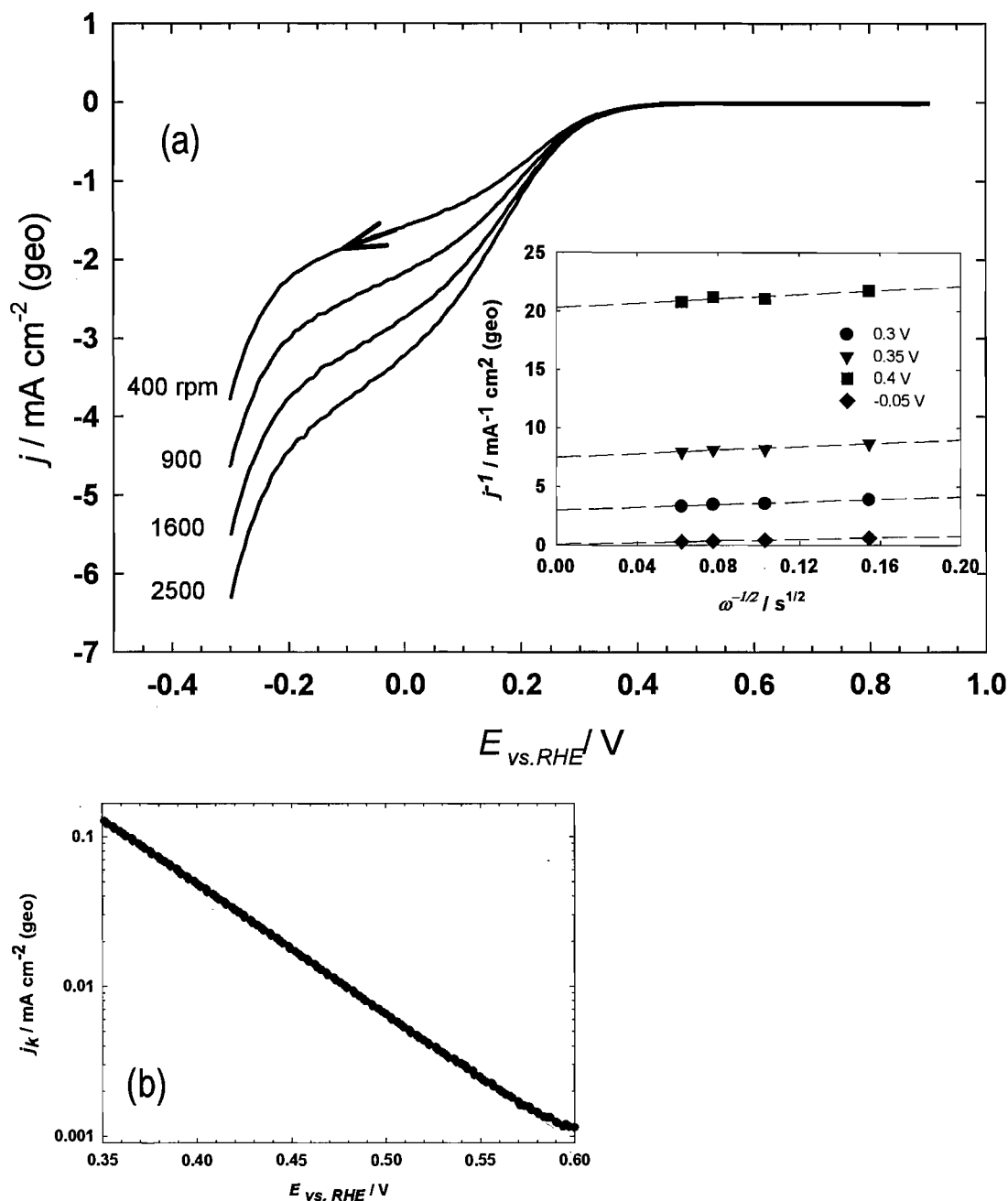
Figure 6.10. *Steady state polarizations (a) for oxygen reduction on gold particles (nominal thickness 0.4 nm) supported on a thin film (66 nm) of TiO_x (deposited on a titanium disk electrode). The insert shows the Koutecký-Levich Plot for the potentials -0.05 (assumed limiting current density), 0.30, 0.35 and 0.40 V. All measurements have been made in oxygen saturated 0.5 M $HClO_4$ at a temperature of 298 K. (b) Mass transport corrected Tafel plot (limiting current assumed to be -0.05 V) of the negative going potential sweep at 900 rpm.*
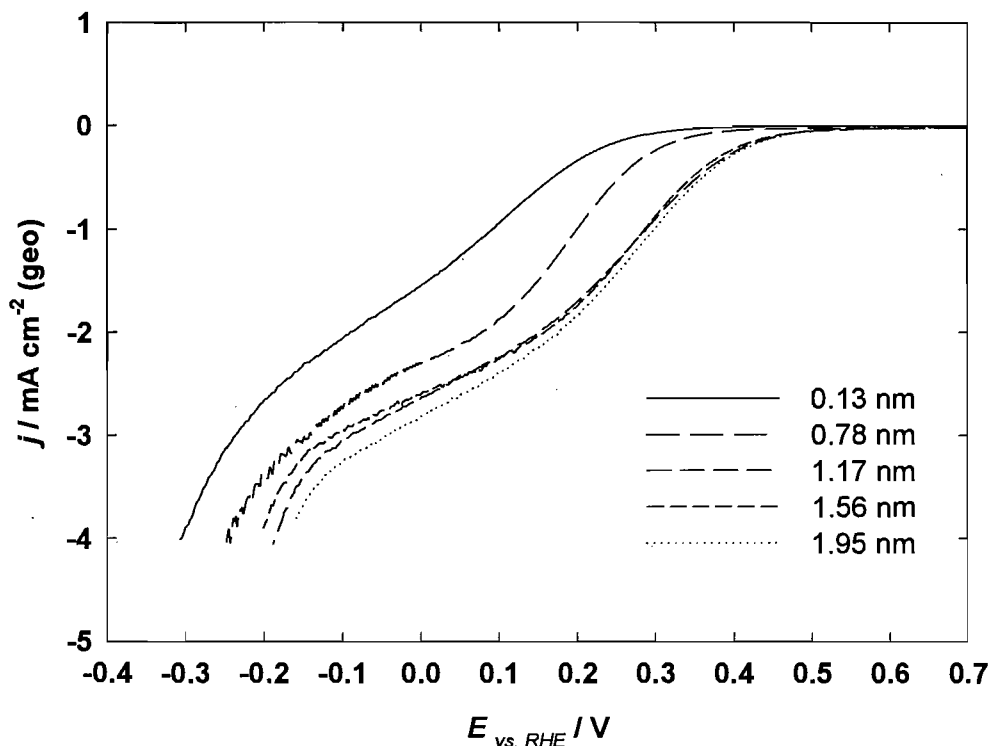
Figure 6.11. *Polarization measurement (v = 20 mV s⁻¹) for oxygen reduction on Au/TiOₓ RDE electrodes with different gold coverages, nominal thicknesses shown in the figure legend. TiOₓ film thickness 66 nm. Rotation rate 900 rpm. O₂ saturated 0.5 M HClO₄. Temperature of 298 K.*

The most appropriate measure of catalytic activity is the current density based on the exposed gold/electrolyte interface. In order to interpret the data in terms of the mean diameters of the gold centres and real surface area, it is necessary to characterise the surface structure. The characterization of the gold deposits for such an analysis was achieved by TEM and is reported in more detail in the sample characterisation section. For TiOx supported gold particles solely the surface area correction from TEM data was undertaken, because as discussed in the previous chapter the gold oxide formation/reduction behaviour, did not allow one to estimate the electrochemical surface area for small particle sizes. The following Figure 6.12 (a) shows the kinetic mass activity[16] $j_{k,m}$ for the eight different coverages at a potential of 0.4 V. The mass activity was found to be maximal at a particle size of ~ 3.1 nm. At particle sizes bigger and smaller $j_{k,m}$ decayed. The surface area (TEM) corrected specific kinetically

---

[16] Kinetic correction using the Koutecký-Levich equation: $\dfrac{1}{j} = \dfrac{1}{j_k} + \dfrac{1}{j_L}$, (compare experimental section)

135

corrected activity $j_{k,A}$ is shown in Figure 6.12 (b). Again the maximal activity was observed at ~ 3.1 nm particle diameter, steeply decreasing at smaller particle sizes. At bigger particles (> 3nm) a slight decrease was observed.
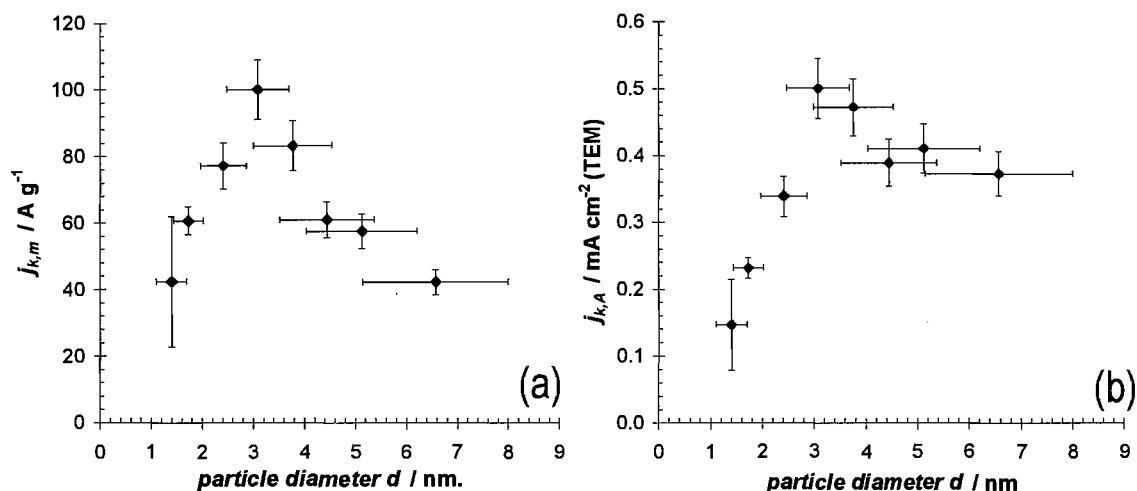
Figure 6.12. *Kinetically (Koutecký-Levich equation) corrected mass activity at rotating disc electrodes $j_{k,m}$ (a) and kinetic specific activity $j_{k,A}$ (b) for the negative scan direction in oxygen saturated 0.5 M $HClO_4$. The x- error bar is the standard deviation of the particle size distribution and the y error bar the standard deviation of three measurements at the same coverage.*

The activity for oxygen reduction was also assessed quantitatively using the potential step technique as described above for carbon supported gold. Figure 6.13 shows one electrode out of an array of electrodes at a similar coverage of gold as the carbon supported sample in Figure 6.6. The current time response had a similar appearance to that at the carbon electrode.
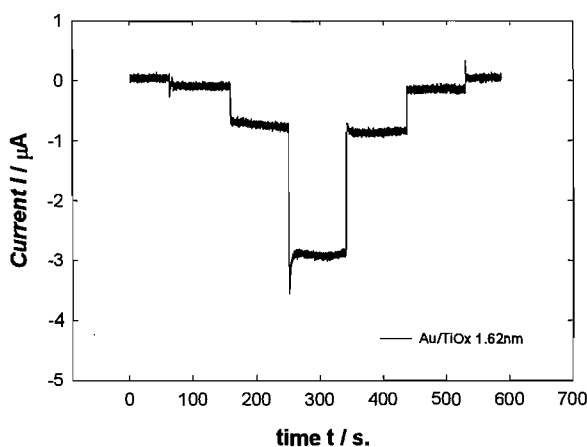
Figure 6.13. *Enlarged presentation of the current vs. time responses to a potential step sequence, 0.80 V → 0.50 V→ 0.40 V→ 0.30 V → 0.40 V→ 0.50 V → 0.80 V, in O_2 saturated 0.5 M $HClO_4$ at electrodes in a 10 x 10 array with nominal gold thickness of ~ 1.62 nm (particle size d ~ 3.9 nm) of Au on TiO_x.*

Figure 6.14 presents the data from a 10 x 10 Au/TiO$_x$ array as contour plots. Figure 6.14 (a) shows the amount of gold deposited over an array of Au/C at the same wedge shutter position as for the titania supported array as estimated by EDS; the decrease in gold from the top left to the bottom right is clearly seen while perpendicular to the arrow the relative uniformity is apparent. Figure 6.14 (b) reports the specific activity for oxygen reduction (from chronoamperometric measurements), in fact the current densities for oxygen reduction at 0.30 V (based on the geometric surface area of the electrode), again as a contour plot. The correlation between the two figures is clear and it can again be seen that the oxygen reduction rate drops off with the amount of gold on the TiO$_x$ support.

(a)   (b)
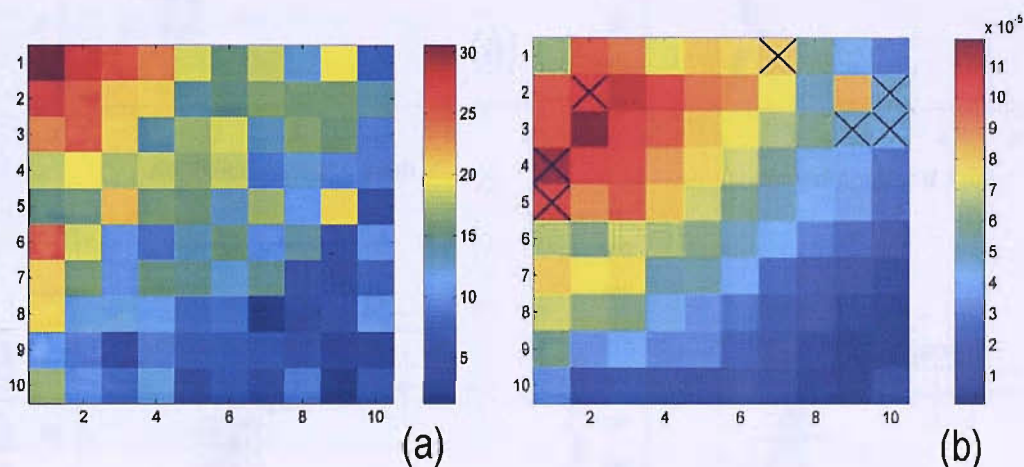
Figure 6.14. *Comparison of (a) the amount of gold as determined by EDS (arbitrary units) in calibration and (b) the oxygen reduction current density (A cm^{-2}) (based on geometric area) at 0.3 V. 10 x 10 titania array. The nominal gold thicknesses ranged from 0.6 nm to 0.07 nm. The crosses indicate electrodes where electrical contact has been broken.*

Again the current responses at 0.4 and 0.3 V during chronoamperometry (Figure 6.13) have been used for the quantitative analysis (geometric current densities as presented in Figure 6.14 divided by the "real" surface area) of the activity. Figure 6.15 therefore summarises the data from the array electrode experiments for the activity of the surfaces (TiO$_x$/Au) for oxygen reduction as a function of the mean particle diameter. Figure 6.15 (a) and (b) show the mass activity at 0.4 and 0.3 V and (c) and (d) the specific activity based on the total real area of gold exposed to the solution as calculated from the number density and mean diameter of the gold particles as described in the sample characterisation chapter for the potentials 0.4 V and 0.3 V respectively. Again in the mass activity a maximum was observed at ~ 3nm particle size at 0.4 V and at a higher overpotential at ~ 2.5 nm particle size at 0.3 V. The mass activity decreased at higher

dispersion smaller particles as on the disc electrode. At bigger particles again a decrease was observed (Figure 6.15 (a) and (b)). The specific activity reached a maximum at ~ 3 – 3.5 nm particle diameter. At smaller particles a dramatic decrease in activity was observed.
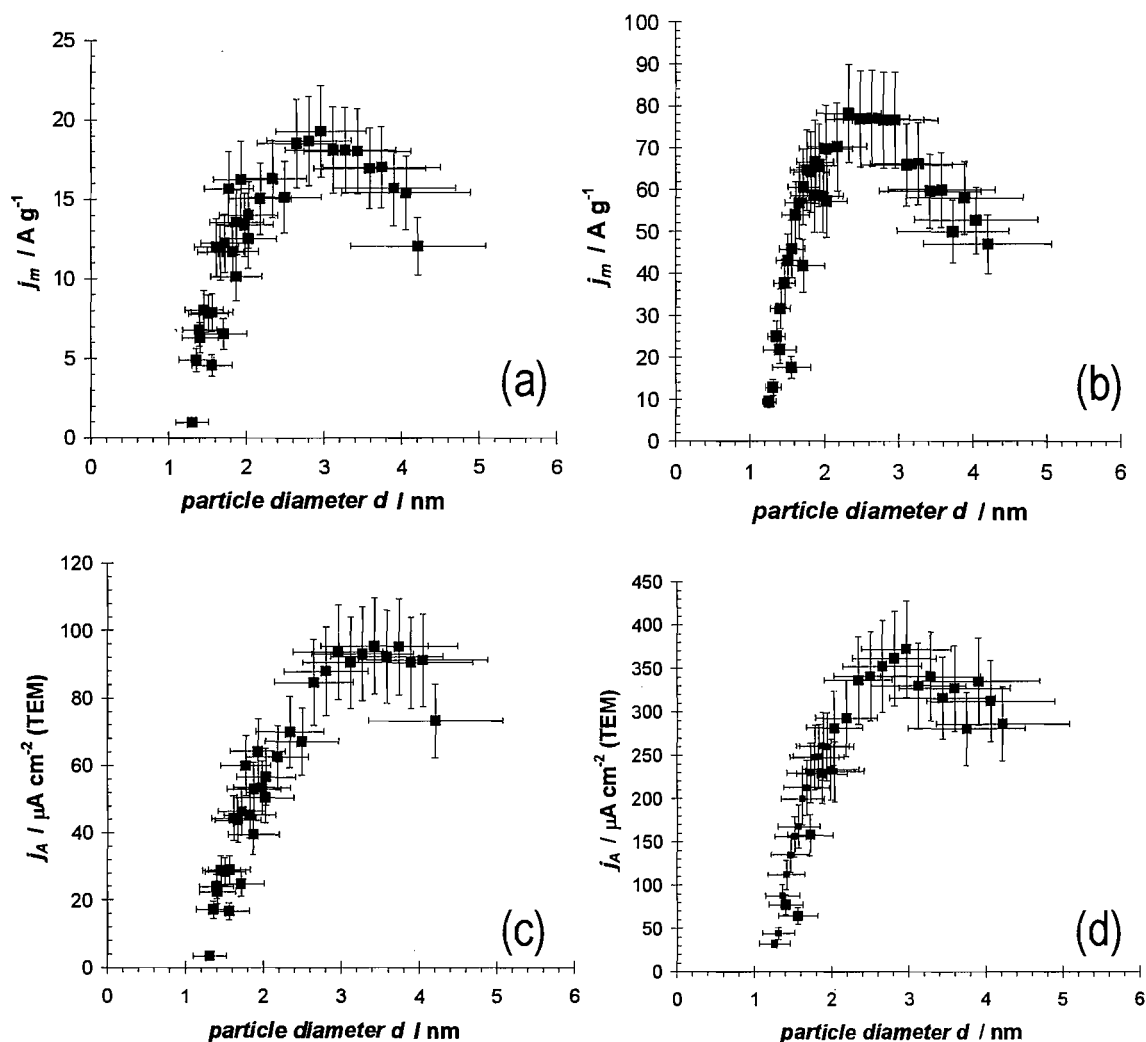
Figure 6.15. *The mass oxygen reduction activity of TiO_x supported gold particles at (a) 0.40 V and (b) 0.30 V vs. RHE. (c) Specific activity (TEM corrected) at 0.4 V and (d) at 0.3 V. The error bars along the particle size axis indicate the range of particle size (in fact, the standard deviation of the particle size) observed by TEM. The error bars on the specific activity axis reflect the standard deviation of the currents measured at the 10 electrodes on the array with a mean particle size.*

The trends identified from the array and the rotating disc electrode experiments are identical. At both potentials, the dramatic conclusion is the loss of activity for oxygen reduction (as measured at the constant potentials) for gold centres smaller than 2 nm. In addition, the plot shows a maximum in activity at a mean diameter of 3 nm.

6.2 Conclusions

The combinatorial approach to the study of particle size effects in catalysis/electrocatalysis was successfully applied to characterise the reduction of oxygen of dispersed gold on titania and carbon. Trends in the activity vs. particle size could be identified and data from the array and the disc electrodes on titania supported samples are identical. It was found that particles of gold with diameters below $2.5 - 3.0$ nm are less active for oxygen reduction, independent of the supporting material. In both cases a steep deactivation of the ORR was observed. For commercial application the mass activity is an important measure. The presented technique allowed identification of mass normalised catalyst activity trends. For a structure sensitive reaction, an optimum dispersion of the catalyst might be desired to avoid an economic penalty in using more precious metal. In here a maximum of the oxygen reduction to hydrogen peroxide at particle sizes around 3 nm was found on titania supported samples and at 4 nm on carbon supported gold particles.

The electrochemical reduction of oxygen was found to be support independent and to undergo mainly a two electron reduction to hydrogen peroxide. At higher overpotentials a further reduction of a small fraction of the hydrogen peroxide seems to undergo further reduction to water as identified by a non zero intercept of the Levich plot and the number of electrons n (as determined by the slope of the Levich plot) being always slightly higher than two with 2.3.

The mechanism of the ORR on titania supported samples seems to be support and particle size independent, as the Tafel slope was always within experimental errors similar to the one found on bulk gold.

7 Electrochemical oxidation of carbon monoxide on gold

7.1 Introduction

In this chapter, the electrocatalytic oxidation of CO on polycrystalline and both carbon and sub-stoichiometric titanium dioxide (TiO_x) supported gold nanoparticles will be discussed.

7.2 Results and Discussion

7.2.1 CO oxidation on polycrystalline gold

Figure 7.1 shows a set of rotating disc electrode measurements at a slow scan rate $v = 20$ mV s^{-1} (to ensure steady state polarisation) at rotation rates of 400, 900, 1600 and 2500 rpm on a polycrystalline gold electrode (in the following called bulk gold). The measurement was carried out in CO saturated 0.5 M $HClO_4$ at a temperature of 298 K. The positive and negative scans are marked by an arrow in the figure. During the positive sweep, the current density associated with CO oxidation rises rapidly in the foot of the wave at around 0.5 V. The Tafel plot (kinetic current versus potential) in Figure 7.1 (b) was linear for this initial rise with a slope of 118-150 mV dec^{-1} (900 rpm) in the range of 0.5 to 0.7 V which was close to the theoretical value of 118 mV dec^{-1} (T = 298K and $\alpha = 0.5$) for an electron transfer reaction, where one electron is transferred in the rate determining step. In the potential range of 0.7 and 1.0 V a mixed mass transport and kinetically controlled region was evident. Subsequently between 1 and 1.35 V a well defined mass transport controlled limited plateau was evident. At ca. 1.35 V a steep decay of the current is observed and is result of the formation of non-reactive gold oxide overlayer, as suggested by Blizanac et. al. [141], and which is completed at ~ 1.6 V. The overlaid cyclic voltammogram in Figure 7.1 (a) confirmed that the observed current at potentials higher than 1.6 V, may be mainly attributed to further oxidation of the gold.
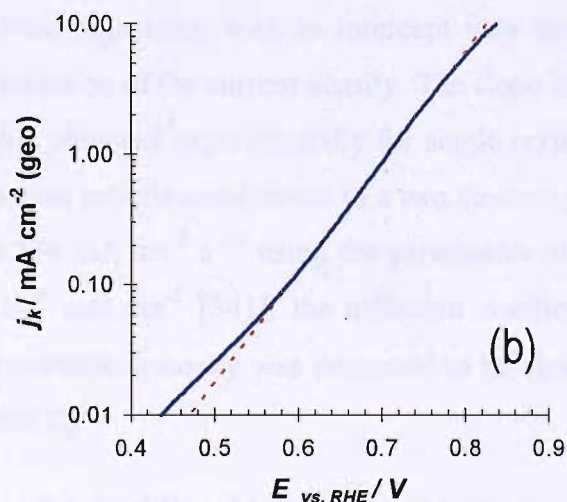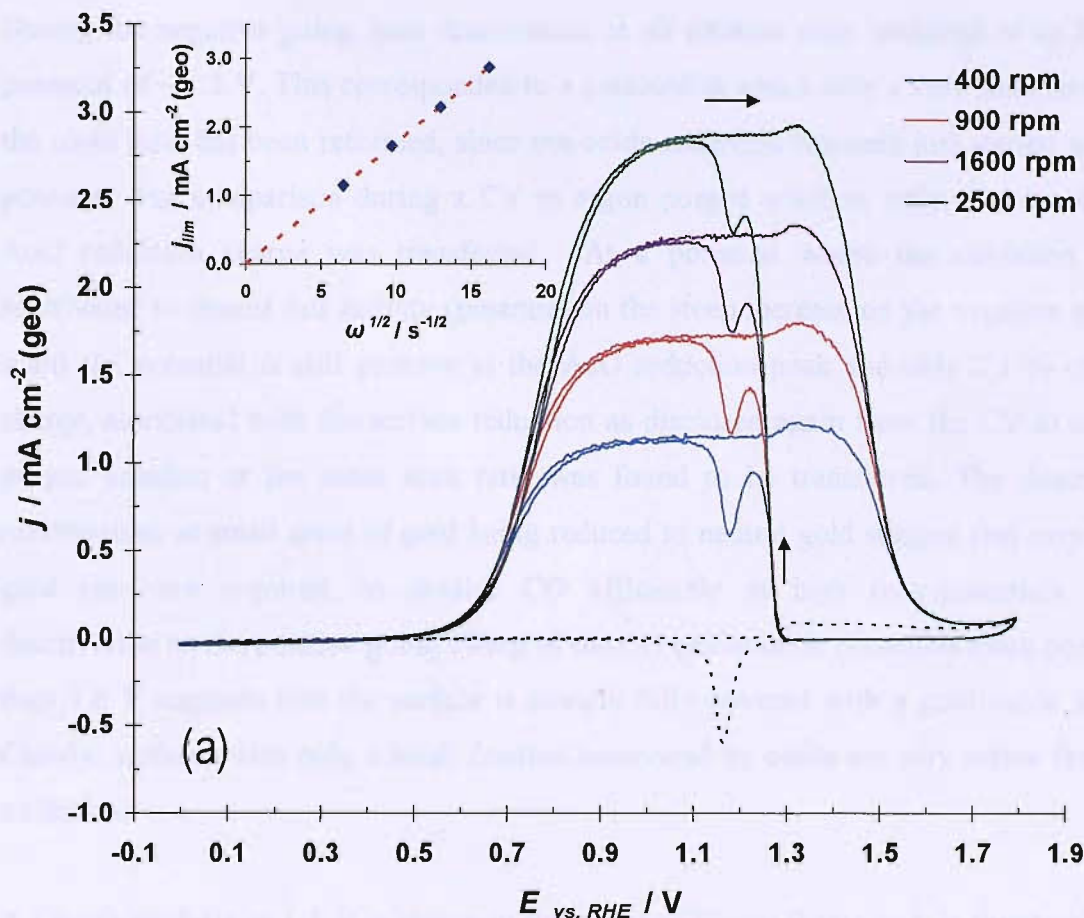
Figure 7.1: *(a) Steady state polarisation for the carbon monoxide oxidation on a polycrystalline gold electrode. The insert shows the Levich plot at 1.2 V for the anodic sweep. The measurement was taken at $v = 20 \text{ mV s}^{-1}$ in CO saturated 0.5 M $HClO_4$. The dashed voltammogram shown is a base voltammogram of the same electrode in an Argon deaerated electrolyte under identical conditions at a stationary electrode. (b) Mass transfer corrected (limiting current density at 1.2 V) Tafel presentation of the positive scan at 900 rpm. Dashed red line is the Tafel fit with a slope of 118 mV dec^{-1}.*

During the negative going scan reactivation at all rotation rates occurred at an onset potential of ~ 1.3 V. This corresponded to a potential at which only a very small area of the clean gold has been reformed, since the oxide reduction has only just started at this potential. For comparison during a CV in argon purged solution, only ~1.3 % of the AuO reduction charge was transferred. At a potential where the oxidation was reactivated to almost full activity (potential on the steep increase on the negative going scan) the potential is still positive to the AuO reduction peak and only 2.1 % of the charge, associated with the surface reduction as disclosed again from the CV in argon purged solution at the same scan rate, was found to be transferred. The described reactivations at small areas of gold being reduced to neutral gold suggest that very few gold sites are required, to oxidise CO efficiently at high over-potentials. The deactivation on the positive going sweep of the CO oxidation at potentials more positive than 1.6 V suggests that the surface is already fully covered with a gold oxide layer. Clearly, surfaces with only a small fraction uncovered by oxide are very active for CO oxidation.

A Levich analysis at 1.2 V is shown in the insert of Figure 7.1(a) and, is fitted using a linear regression with an intercept very close to zero, suggesting full mass transport limitation of the current density. The slope is 0.178 mA cm^{-2} s$^{-1/2}$ which was the same as that observed experimentally for single crystal gold electrodes [141]. This value agreed within experimental errors to a two electron process, when the slope was expected to be 0.174 mA cm^{-2} s$^{-1/2}$ using the parameters of the solubility of CO in water as c^0 ~ 0.99 ·10^{-6} mol cm^{-3} [341], the diffusion coefficient D ~ 1.8 ·10^{-5} cm^2 s^{-1} [141], and the kinematic viscosity was estimated to be close to v ~ 0.01 cm^2 s^{-1} (0.5 M HClO$_4$ at T = 298 K).

7.2.2 CO oxidation on carbon supported gold nanoparticles

Figure 7.2 shows the cyclic voltammograms measured at four carbon supported Au samples from two 10 x 10 arrays. The measurements have been carried out in CO saturated (red curves) and argon purged (blue curves) 0.5 M HClO$_4$ electrolyte. The four voltammograms correspond to surfaces with different nominal thicknesses of gold; these correspond to mean particle sizes of 2.7, 3.3, 4 and 7.5 nm.

Figure 7.2. *Third cycle of a cyclic voltammetry measurement at an array of carbon supported gold electrodes (particles sizes 2.7 (a), 3.3 (b), 4 (c) and 7.5 (d) nm) in CO saturated (red curves) and Argon purged (blue curves) electrolyte (0.5 M HClO₄). The measurement was taken at room temperature at a scan rate of v = 50 mV s⁻¹.*

The argon purged voltammograms were included to show the gold surface redox behaviour, and to give an indication of the real surface area. For further discussion of the gold oxide behaviour the reader is referred to Chapter 5. Especially at the larger Au particles, the voltammogram has many of the characteristics of that for bulk Au; with decreasing size some further changes are seen. The onset of the oxidation wave occurred at 0.6 V (d) to 0.8 V (a) at a significant overpotential compared to the standard potential of the CO oxidation to CO_2 of ~ - 0.124 V in 0.5 M acid at 298 K calculated using, the standard potential of - 0.106 V under standard conditions [245]. The onset of the oxidation wave was a function of particle size, i.e. the smaller the particles the greater the overpotential of CO oxidation. The onset for the CO oxidation on model single crystal surfaces has been reported to be in the range of 0.2 to 0.45 V vs. RHE in 0.1 M HClO₄ [141].

143

The CO oxidation wave in the voltammograms of all four particle sizes had common features: an initial region of kinetic control, followed by a mixed kinetic and mass transport controlled region can be observed analogous to the RDE experiment on bulk gold. The CO oxidation peak position was strongly dependent on the particle size and/or surface area (this will be discussed in the following section) leading to a peak potential shift from ~ 0.97 V at the biggest particles of 7.5 nm mean diameter to ca. 1.3 V on the smallest mean particle size of 2.7 nm. The maximum peak currents for the particle sizes of 7.5, 4.0 and 3.3 nm were similar to those expected for diffusion controlled reactions. For the smallest particle size (2.7 nm) the maximum peak current was ~25% lower. The reason for this could be that the reaction did not reach full diffusion control and was therefore suppressed by the competing formation of gold oxide The peak potential (potential at current maximum) was observed to fall ~ 50 mV anodic to the onset of gold oxide formation at 1.25 V.

At the bigger particle sizes (e.g. 7.5 and 4 nm) a second peak was observed at around 1.4 V, associated with the charge transferred for the AuO formation (compare argon CV's). This peak decreased as the gold surface area decreased at particle sizes below 4 nm and was only visible as a shoulder at particle sizes around 3.3 nm. At even smaller particle sizes (2.7 nm) the CO oxidation peak and the gold oxide formation peak merged.

Overlay of the CV's obtained in CO saturated solution for various Au particle sizes is shown in Figure 7.3 and reveals a particle size dependent deactivation/reactivation associated with the surface redox behaviour. The larger the particle size the later the CO oxidation is deactivated by the gold oxide formation. The reactivation on the negative sweep occurs at higher positive potentials for larger particles.

Overall, it appears that the overpotential for CO oxidation increases as the Au particles decrease in size. This is a major shift as with the smallest particles, mass transport control is not reached before AuO is formed. It is also surprising since at bulk Au, only a small fraction of Au surface is needed to give a high rate of CO oxidation. This may indicate a change in the electronic properties with size of the Au centre and/or reduced

CO_{ad} mobility on smaller particles as was suggested electrochemical CO oxidation on platinum nanoparticles (assumption of L-H like mechanism).
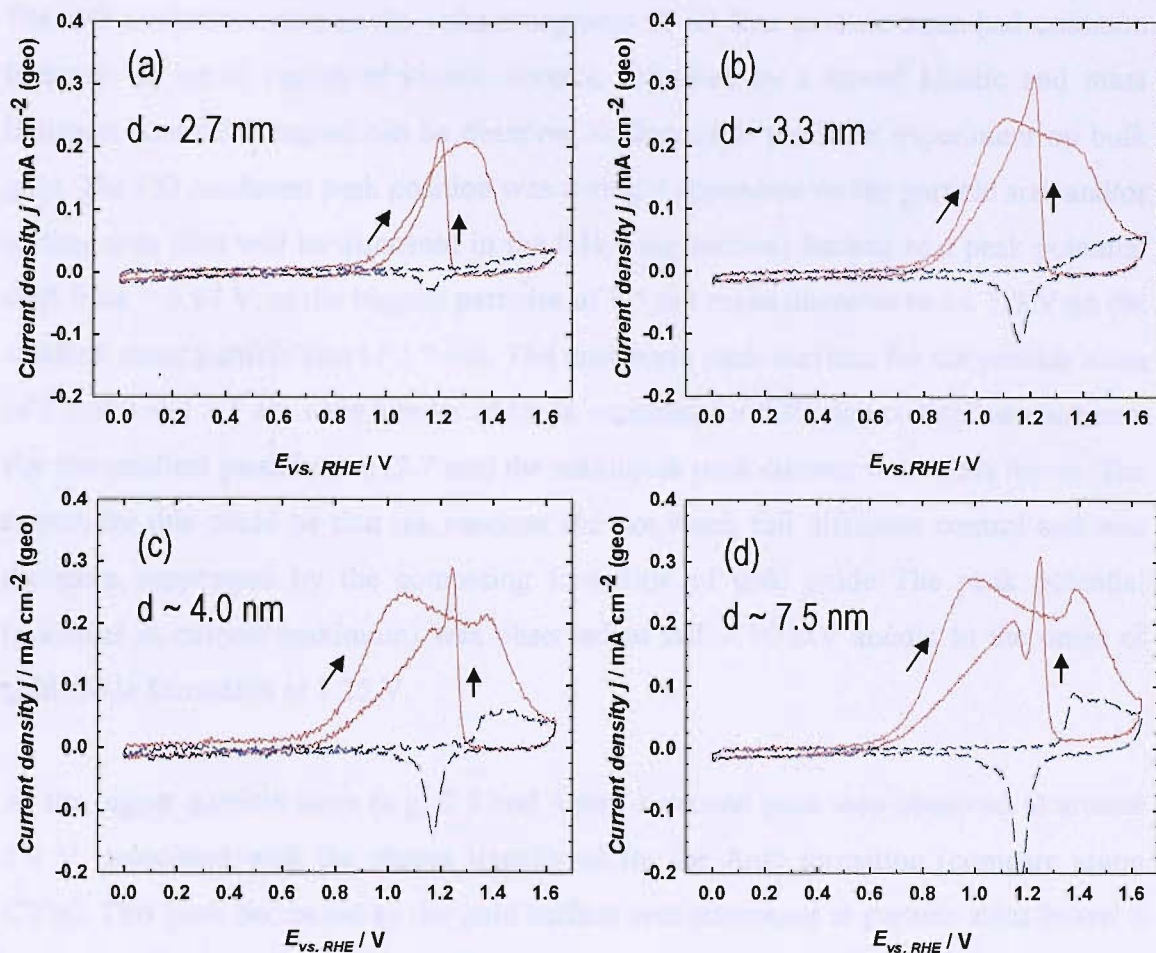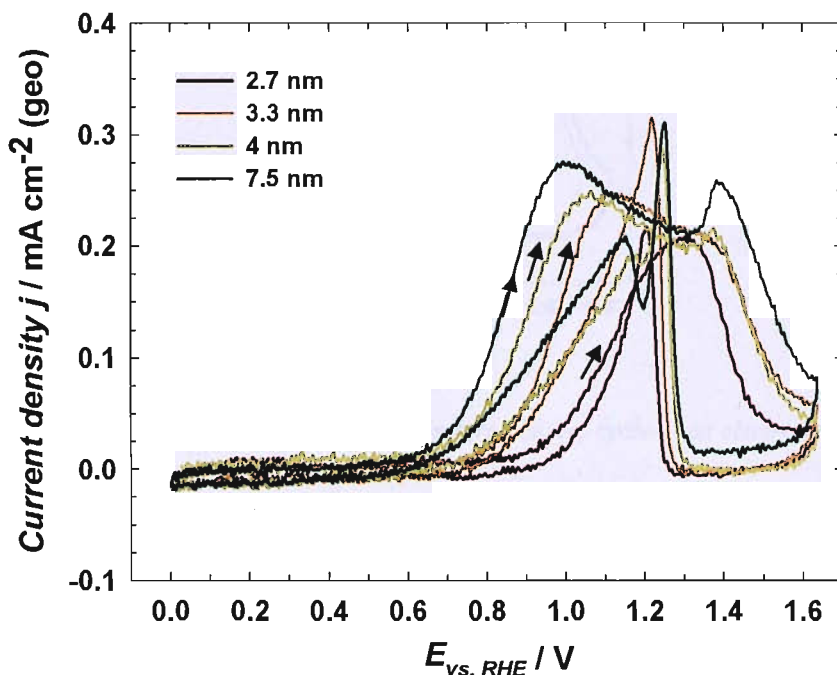

Figure 7.3. *Third cycle of a cyclic voltammetry measurement at an array of carbon supported gold electrodes (particles sizes 2.7, 3.3, 4 and 7.5 nm) in CO saturated electrolyte (0.5 M HClO$_4$). The measurement were taken at room temperature at a scan rate of v=50 mV s^{-1}.*

Figure 7.4 shows the first two cycles for a particle size of 3.3 nm. The electrolyte was saturated with CO over a period of 15 minutes, whilst the potential was held at ~ 0.7 V where CO oxidation occurs at a slow rate. The first positive scan showed a significant shift towards higher potentials and had a similar shape to the subsequent cycles for the smallest particle size of 2.7 nm. All the investigated particle sizes showed activation from the first to subsequent cycles. However, the activation was far less pronounced at larger particle sizes.
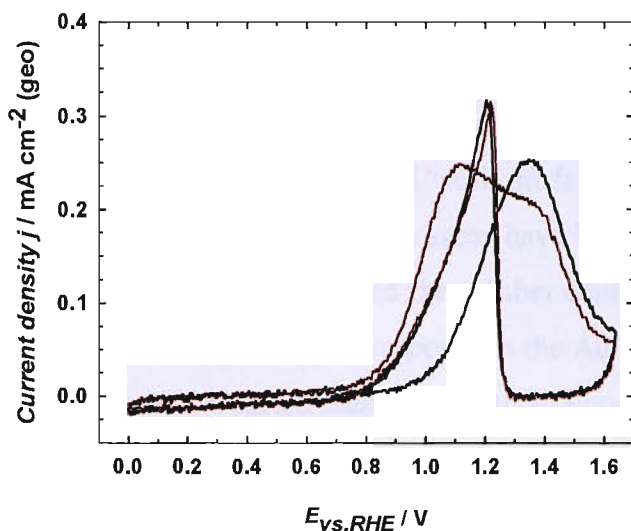
Figure 7.4. *First (black curve) and second (red curve) cycle of an electrode with an average particle size of 3.3 nm.*

The activity for CO oxidation was assessed quantitatively using a Tafel analysis and the activities at 0.8 V were compared. At lower coverage this required extrapolation of the Tafel plot from the active region (data points) to the potential of 0.8 V (see Figure 7.5). A potential of 0.8 V was chosen to minimise the distance of extrapolation/interpolation for the different Au coverage. In Figure 7.5, the Tafel presentation at three electrodes for arrays of Au/C is presented. For the determination of the Tafel slope the kinetically controlled region (approximately a range of 200 mV) at the lower part of the voltammogram was used for the regression. In the figure the slopes for the Tafel plots of the particle sizes 3 and 7.5 nm appear to have a similar slope (199 and 191 mV dec[-1]), whereas the slope of the smallest particle size 2.7 nm deviates slightly (223 mV dec[-1]).
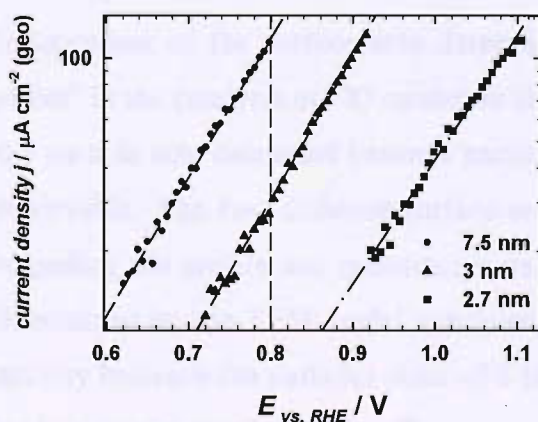
Figure 7.5. *Tafel presentation of three selected Array electrodes (particle size 2.7, 3 and 7.5 nm).*

To ease comparison of the kinetics of the CO oxidation, the current density at a constant potential had to be corrected for the influence of the surface area. For this, and analogous to the investigation on oxygen reduction in Chapter 6, the apparent currents were corrected for the estimated "real" surface area, i.e. for the catalytic sites exposed to the electrolyte. The real surface areas have been estimated both from the TEM images, using the particle diameter and the number count for hemispherical shape of the particle, or from the electrochemical response in the AuO reduction reaction in the Argon purged solution voltammogram measured, with an upper limit of 1.63 V. The data corrected for this surface area, and the results are presented in Figure 7.6 (b). The error bars are expressed as the error of an indirect measurement result, where the error of the currents and surface area are estimated from the standard deviation at the main diagonal of the same particle size. The error is than calculated using the Gaussian law of error propagation by:

$$\frac{\Delta j_{real}}{\bar{j}_{real}} = \sqrt{\left|\frac{\Delta j_{geo}}{\bar{j}_{geo}}\right|^2 + \left|\frac{\Delta A}{\bar{A}}\right|^2} , \tag{7.1}$$

Where Δj_{real} is the standard deviation of the specific activity, $\bar{j}_{real}$ the average of the specific activity, Δj_{geo} is the standard deviation of the geometric current density, $\bar{j}_{geo}$ the average of the current density, ΔA the standard deviation of the surface area and $\bar{A}$ the average electrochemical surface area (all standard deviation values are estimated at the main diagonal). The error for the TEM was for simplification assumed to be the same as for the electrochemical measurement.

Independent of the surface area determination, there appeared to be a "particle size effect" in the catalysis of CO oxidation similar to that observed for oxygen reduction. If the particle size decreased below a particle size of 3 nm a steep cut off in activity was observable. The two different surface area analysis methods showed some difference regarding the profile and quantitative values. Firstly use of the TEM surface area (as determined by the TEM model specimen) led to a slightly steeper increase of specific activity between the particles sizes of 3 to 10.1 nm, if compared to the electrochemical surface area correction. This effect was explained in chapter 5 and was probably due to the underestimation of the TEM surface area for larger particles, which are likely to agglomerate and, therefore, have a higher surface area because of an intrinsic roughness

effect. Secondly the higher quantitative values of the specific activity obtained by TEM correction are likely to occur due to the uncertainty of the positive limit during potential cycling, which will give a monolayer of gold oxide.

Irrespective of this slight difference, there seemed to be a further activation of the reaction, when the particle size is further increased in the range of 3 to 10.1 nm. This further increase would agree with the higher activity found on a bulk gold disc electrode in an identical investigation, where the specific activity at 0.8 V was found to be $\sim 250 \ \mu A \ cm^{-2}$ (EC).
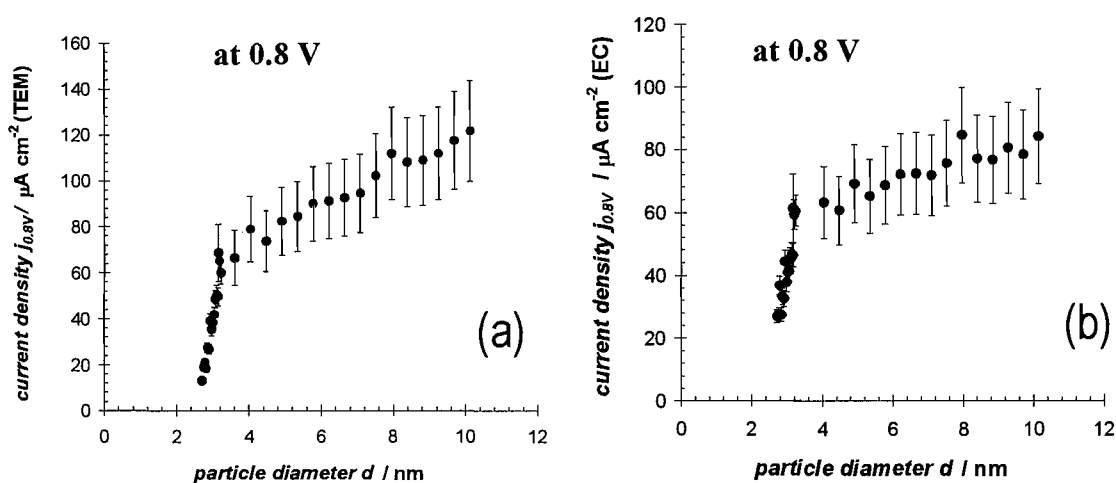
Figure 7.6. *Particle size dependent specific activity for the CO oxidation at gold nanoparticles supported on carbon. (a) Real surface area corrected currents at 0.8 V using TEM determined surface areas. (b) Currents corrected using electrochemically determined surface area.*

Further evidence for this almost linear increase in activity was evident from the mass activity plot shown in Figure 7.7 (a). Except for the characteristic decrease in activity below 3nm, the mass activity remained relatively stable and only decreased to ~ 72 % of the original value.

For a specific activity that remained at unity, i.e. was structure insensitive, a decrease as estimated from a plot of the ratio of the surface area to mass vs. the mean particle diameter would be expected with a decrease to 48 % of the maximum for a particle size of ~ 3 nm, expected for the largest particle of 10.1 nm. The shape of this plot in Figure 7.7 (b) is a function of mainly three parameters the dispersion of the metal (i.e.

148

particle/number density), particle shape (intrinsic "roughness") and particle diameter. As evident from this plot the activity in the range of 3 - 10 nm still increased and did not reach bulk gold specific activity.
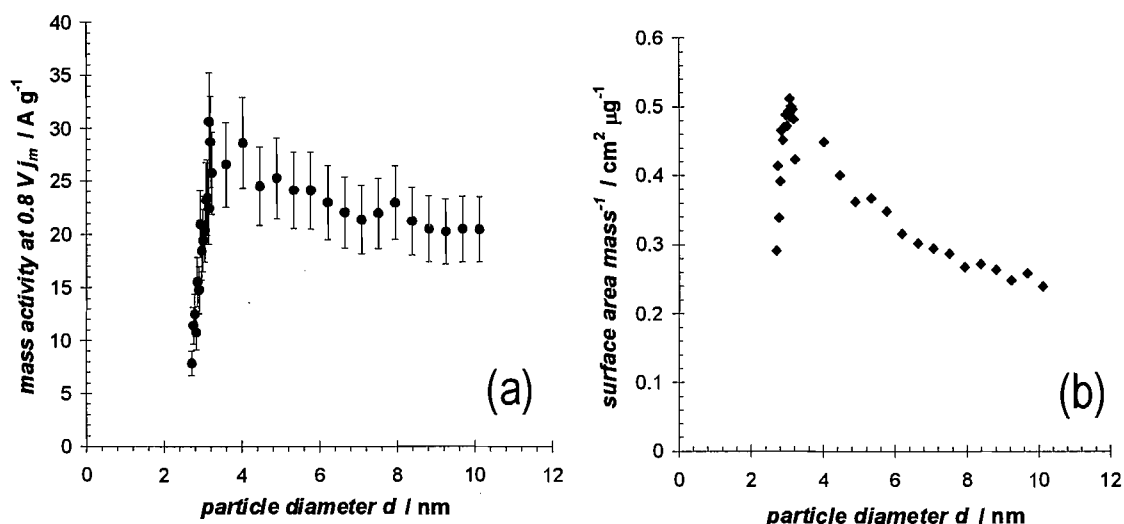
Figure 7.7. *(a) Mass activity plot for the CO oxidation at 0.8 V at carbon supported gold electrodes. (b) Ratio of the (electrochemically determined) surface area and mass of gold vs. the mean particle diameter.*

In the Tafel presentation of the voltammograms of Figure 7.5, an increase of the slope for particles of 2.7 nm was observable. Figure 7.8 summarises the average particle size dependent Tafel slopes during cyclic voltammetry with a scan rate of $v = 50$ mV s^{-1} for two array electrodes. Within experimental errors the Tafel slope was found to be constant over the particle size range of 2.6 – 10.1 nm with 207 ± 9.6 mV dec^{-1}.
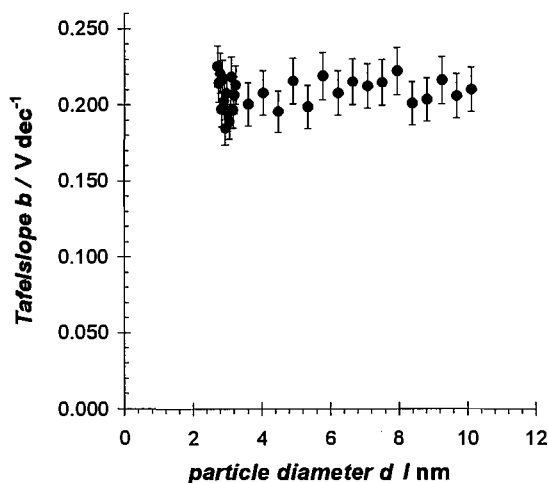
Figure 7.8. *Tafel slopes at cyclic voltammograms (v = 50 mV s⁻¹) with varying particle sizes. Error bars indicate the standard deviation of the main diagonal and the error was calculated to be ~ 6 - 7 % (depending on the array).*

7.2.3 CO oxidation on sub-stoichiometric titanium dioxide supported gold nanoparticles

7.2.3.1 CO oxidation on RDE disc electrodes

In the red and blue curves in Figure 7.9 (a), the oxidation of CO was investigated in 0.5 M $HClO_4$ at gold nanoparticles with an average particle size of 2.8 nm, supported on sub-stoichiometric titanium dioxide. Also shown in the figure is the i-E response for CO oxidation on bulk gold electrode (turquoise) for comparison. The estimated surface area by TEM of the Au/TiOx electrode was ~ 0.4 cm^2, and the electrochemically determined surface area of the bulk gold disc was found to be ~ 3 cm^2. The direct comparison of these electrodes, even though the surface area was significantly larger on the polycrystalline gold, showed that the titania supported gold particles were more active at lower overpotentials. As the overpotential increased a cross over in activity occurred at around 0.625 V. In the literature the onset potential of CO oxidation on single crystals was reported to occur at values as low as ~ 0.2 (face 110) and ~ 0.45 (face 111) $V_{vs. RHE}$ in acidic solution but only with very low current densities. This was confirmed by an observable CO_2 band in the infrared spectra and a Faradaic current during CO electro-oxidation [141]. A close inspection of the Tafel-like presentation of the titania

150

supported gold particle electrochemistry in Figure 7.9 (b) indicated, that the onset potential, if compared to a polarisation curve recorded in argon purged solution started at potentials as low as 0.1 to 0.15 V this was 50 to 300 mV before CO electrooxidation occurs at single crystal gold surfaces.

Another finding of Figure 7.9 (b) showed that the slope (if fitted) would not lie in the region of the theoretical 118 mV dec^{-1} ($\alpha = 0.5$). The observed slope was at 328 mV dec^{-1} (in the range of 0.25 to 0.4 V), much higher than expected for a one electron rate determined transfer reaction.
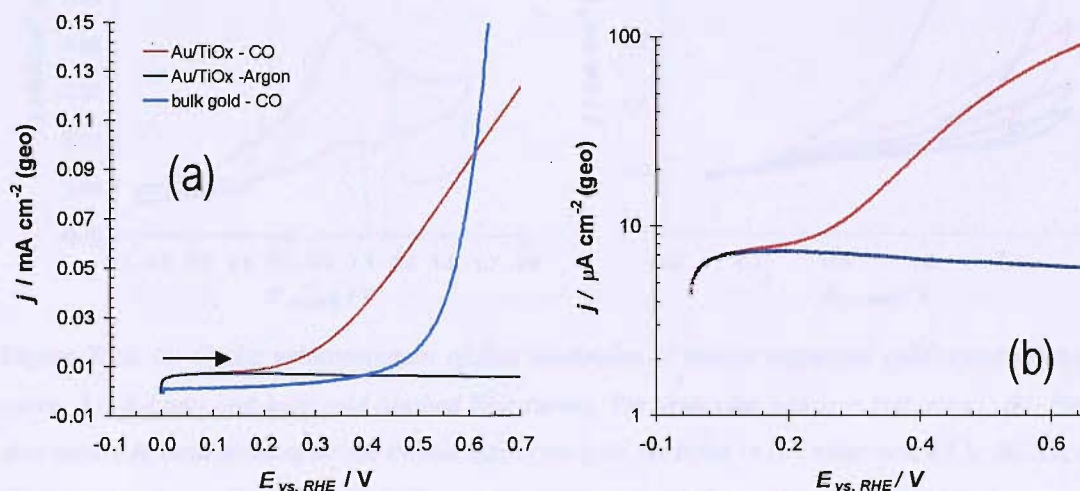
Figure 7.9. *(a) Polarization curves of bulk gold (turquoise curve) and titania supported gold nanoparticles (particle size 2.8 nm) in CO (red and light blue curve) and Argon (dark blue curve) saturated electrolyte. (b) Tafel presentation for the titania supported sample. Steady state voltammetries recorded at v = 20 mV s^{-1}, 400 rpm and an initial holding time at 0V of 120 seconds.*

After these experiments on CO oxidation, a cyclic voltammogram extended to more positive potentials did not show any Au/AuO features. Apparently the Au centre and/or support were already modified.

For particles with a mean diameter of 4.4 nm, a voltammogram in CO saturated solution was recorded after a steady state polarisation in oxygen (rotation rate 400, 900, 1600 and 2500 rpm) saturated solution, as presented in Figure 7.10 (a). During the first positive sweep there were two regions observable: (i) < 0.6 V, where an increase in current was observed that was highly activated in comparison to polycrystalline (pc) or carbon supported gold, and (ii) a region > 0.6 V (distinguishable by an inflexion point), where the current continued to increase with potential but the value was less than pc Au,

with a well defined peak at a potential of 1.04 V. The peak has the appearance of a diffusion controlled peak where the rise in current with E is rather drawn out. Interestingly the reaction was not deactivated beyond the peak if the potential reached the value where gold oxide formation was expected and observed. Only slight deactivation during AuO formation was observed as indicated by subsequent minor reactivation during the negative sweep.
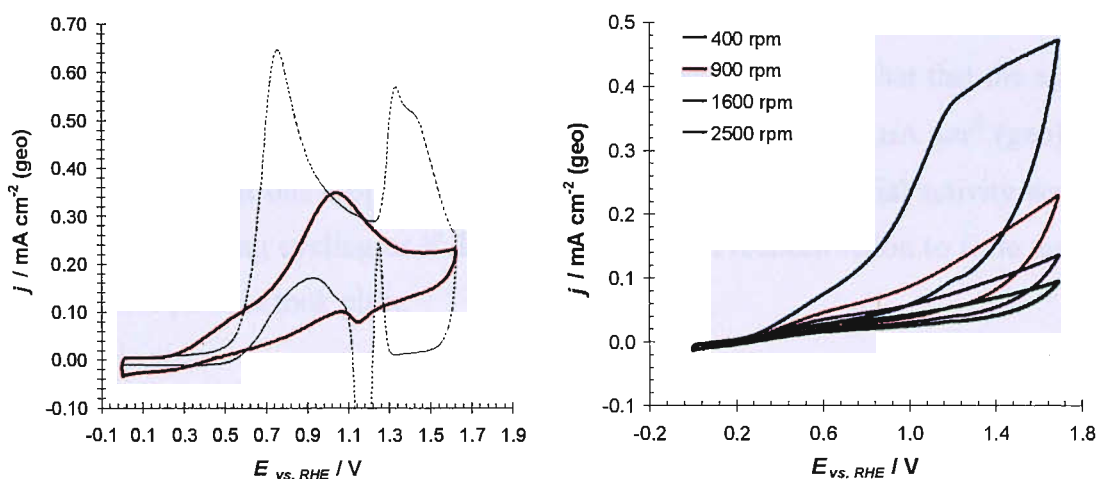
Figure 7.10. *(a) Cyclic voltammogram of disc electrodes of titania supported gold nanoparticles (red curve, d ~ 4.4 nm) and bulk gold (dashed blue curve). The scan rate was v = 100 mV s⁻¹. (b) Rotating disc electrode measurement on the titania supported gold particles in CO saturated 0.5 M HClO₄ at 298 K using a scan rate of v = 20 mV s⁻¹. The rotation rate was varied as indicated in the legend.*

In Figure 7.10 (b), a set of polarisation curves at different rotation rates (400, 900, 1600 and 2500 rpm) are shown. It can be seen that the limiting currents decrease with increasing rotation rate. This behaviour is usually only seen when the electrode reaction mechanism involves formulation of a solution free intermediate that is also a catalyst for the reaction; rotation of the electrode is then sweeping this intermediate away from the reaction layer. Whether diffusion controlled peak was observed in the measurement prior to this set of measurement with forced convection (Figure 7.10 (a)), could not be observed during the rotating disc tests. The expected mass transport limiting plateau would be expected to be ~ 1.2 mA cm^{-2} (geo) at 400 rpm (see oxidation at bulk gold beginning of this chapter). The highest current density during the scan at 400 rpm was 0.47 mA cm^{-2}, this was less than half the expected mass transport controlled faradaic current, and in subsequent cycles at higher rotation rates the current reduced even more dramatically. The observed deactivation during forced convection voltammetry might not necessarily be due to the mass transport towards the electrode, but rather an effect

due to the upper potential limit during voltammetry. It will be shown later the activity during chronoamperometric measurements at low potential did not show dramatic deactivation with time. A CV after the CO oxidation once again did not show the AuO formation/reduction couple as stated previously. To exclude the possibility of loss of the gold during this experiment a second set of steady state polarisation curves in oxygen saturated electrolyte were measured. The measurement showed "normal" gold like voltammetric responses with the typical ill-defined diffusion controlled plateaus at the different rotation rates, as for pc Au during ORR. It must be noted that that the activity at 900 rpm and 0.4 V dropped, from initial value of 218 down to 58 $\mu A\ cm^{-2}$ (geo). It is only speculative that this drop, to approximately a quarter of the initial activity was due to loss of gold during cycling or if during CO oxidation reconstruction to form an inert surface in the particle took place

The results presented above indicate, that the changes in the surface as observed from the AuO feature in the voltammogram are associated with the interaction of the gold particles with oxygenated species (hydroxide). Therefore, the role of hydroxide at the surface of the gold particles had to be further investigated. In a range of experiments, the "re"- activation of the oxidation by holding the potential at very reducing potentials (i.e. -0.3 V vs. RHE for different times e.g. 5-30 sec.) was attempted. This was not successful and the reaction continued to deactivate.

As might be indicated by the strong deactivation at higher rotation rates mass-transport was believed to be a limiting parameter as a consequence of the slow supply of hydroxide. Avramov-Ivic, et al., found, for example that methanol oxidation only occurred at very slow scan rates of 0.1 mV s^{-1} on gold (111) in acid solutions [343]. For these reason measurements at slow scan rates (2 mV s^{-1} *limit of ramp generator*) were carried out, however no reactivation and no diffusion controlled regions were observed.

7.2.3.2 CO oxidation on Array electrodes

Figure 7.11 shows the electrochemical response of four selected electrodes out of two arrays of electrodes of TiO$_x$ supported gold particles. The gold particle size varies from 2.6 nm in (a), 3.2 nm in (b), 3.9 nm in (c) and 6.1 nm in (d) as indicated in the figure. The red curves show the CV's in CO saturated electrolyte and the blue curve CV's in

argon purged electrolyte. The electrodes have been selected to be similar in particle size as in the above presented equivalent Figure 7.2 for carbon supported gold particles. The green curves for the CV's at Au/C in CO saturated electrolyte (particle sizes from (a) to (d): 2.7, 3.3, 4.0 and 7.5 nm) have been included for direct comparison.

The argon purged CV's (blue curves, first cycle/experiment on the array electrode) are again included to give an indication of the relative gold coverage on titania. The unusual behaviour of the gold oxide redox couple as discussed in Chapter 5 are again apparent in the peak broadening of the gold oxide reduction peak even in this first cycle. The gold oxide features are diminishing with consecutive electrochemical modification as shown on the discs above (not shown for the array, but the behaviour was found to be analogous). At the highest coverage with gold hence biggest particle size (d ~ 6.1 nm), a well defined gold oxide formation wave (blue curve) and gold oxide reduction peak are observable. With decreasing gold coverage/particle size the peak broadens and the recorded faradaic current decreases (Figure 7.11 (c) to (a)).

During the cyclic voltammetric experiment in CO saturated solution the potential was initially held at 50 mV (red curve) and then scanned positive at 50 mV s^{-1}. On the biggest particle size of approx. 6.1 nm shown in Figure 7.11 (d) an oxidation wave was observed with the wave onset at approximately 0.2 V and a diffusion controlled peak current at a potential of ~ 0.92 V. At around 0.6 V a change in slope was observed. At potentials, where the formation of gold oxide is to be expected the CO oxidation did not deactivate as dramatically as in the case of carbon supported gold particles (green curve) or bulk gold (see Figure 7.10). The change in slope might give indication of a change of mechanistic for different potential regions.

On the reverse negative going scan CO is still oxidized and a small gold oxide reduction peak was observed with a peak potential of ~ 1.19 V, at the same potential as in argon purged solution. A similar potential was found during gold oxide reduction on carbon supported sample and bulk gold. Most importantly, there is again no need for a reactivation phenomenon as the CO oxidation is not stopped by the AuO formation.

At smaller particle sizes Figure 7.11 (a) to (c) the positive going scan was found to be similar in shape. As a difference it should be pointed out, that the current peak potential

for the mass transport limited CO wave was shifted to more positive potentials by ~ 200 mV. Surprisingly the region before the change in slope described above was steeper in Figure 7.11 (b) and (c) for particle sizes of d ~ 3.9 and 3.2 nm. Currents at these particle sizes are higher at lower overpotentials. This is in contrast to the significant deactivation on the carbon supported samples as well as the potential region greater ~0.6 V where the peak potential was shifted more positive. Again the observation suggested that there are two processes present: at potentials below 0.6 V a mechanism which is favoured by smaller gold particles and at potentials positive this region a more irreversible as evident in a positive shifted peak.

On the negative going scan the gold oxide reduction peaks for smaller particles get smaller as expected for smaller gold surface areas until they are not apparent in Figure 7.11 (a). For particle sizes below 2 nm in diameter no mass transport limited peak during CO oxidation was observed (not shown).
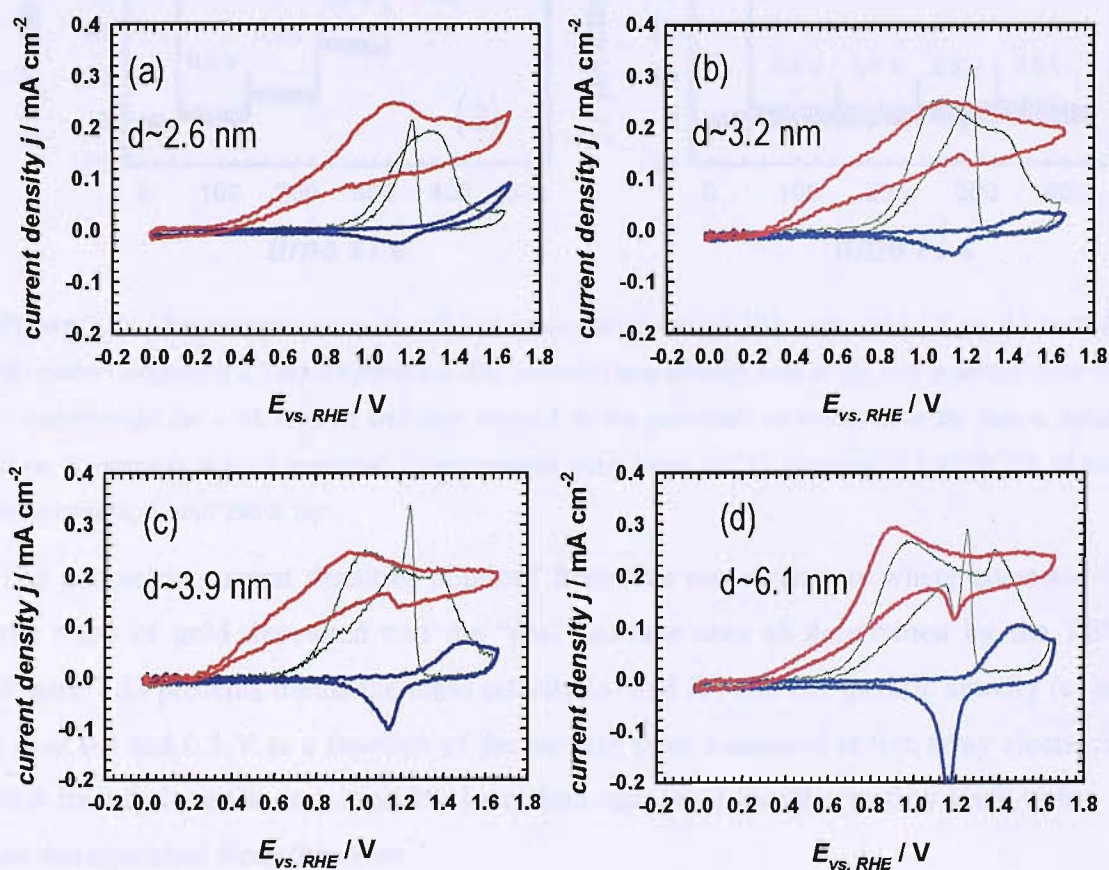
Figure 7.11. *First cycle of a cyclic voltammetry measurement at an array of titania supported gold electrodes the particles sizes was 2.62 nm (a), 3.22 nm (b), 3.94 nm (c) and 6.1nm (d) in CO saturated (red curves) and argon purged (blue curves) electrolyte (0.5 M HClO₄). The measurements were taken at a temperature of 298 K and the scan rate was of v = 50 mV s⁻¹.*

155

For the determination of the activity at different potentials chronoamperometry was used, similar as discussed for the oxygen reduction. For direct comparison chronoamperograms for an Au/TiO_x (a) and Au/C (b) array electrode with a particle size of 2.7 nm, are presented in Figure 7.12. The potential was held at either 0 V (Au/TiO_x) or 50 mV (Au/C) to produce a base line where no activity was expected, and then increased in steps to 200 (titania supported sample only), 300, 350, 400, 500 and 600 mV. The potentials were held for 90 second at each step. For the Au/TiO_x, an oxidation current is clearly seen at each potential, it increases as the potentials is made more positive and almost no deactivation is seen over 90 s in these constant potential experiments. For the carbon supported electrodes no apparent activity was observed, whilst the titania supported samples clearly showed activity.
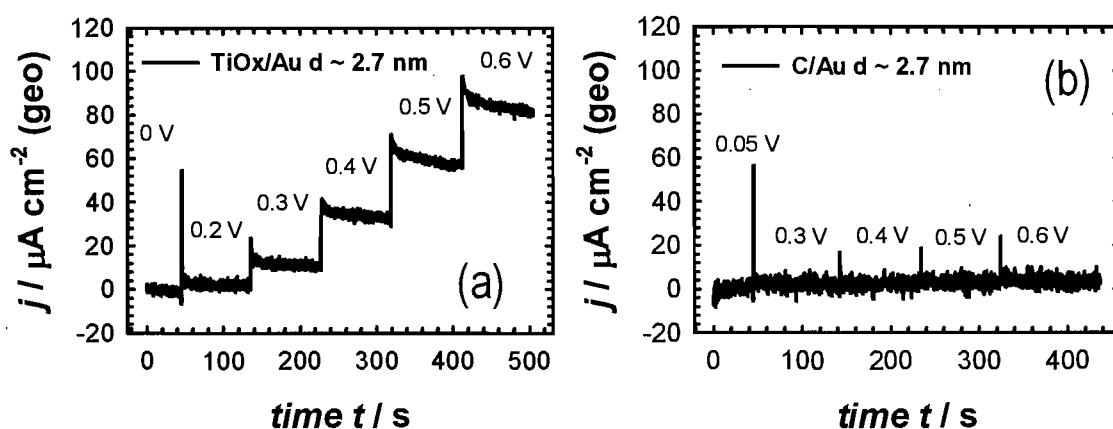
Figure 7.12. *Chronoamperometry at selected array electrodes (a) TiO_x supported 2.7 nm Au particles; (b) carbon supported 2.7 nm Au particles. The potential was initially held at the first potential (0 or 0.05 V respectively) for ~ 45 seconds and then stepped, to the potentials as indicated in the figure, holding them 90 seconds at each potential. Measurements were taken in CO saturated 0.5 M $HClO_4$ at room temperature (b) and 298 K (a).*

The geometric current densities obtained from this measurements where corrected for the mass of gold deposited and the "real" surface area as determined by the TEM. Figure 7.13 presents trends the mass activity (a) and (b) and the specific activity (c) and (d) at 0.3 and 0.5 V as a function of the particle sizes measured at five array electrodes. Not included are the activities for the carbon supported samples as they were to low to be distinguished from the noise.
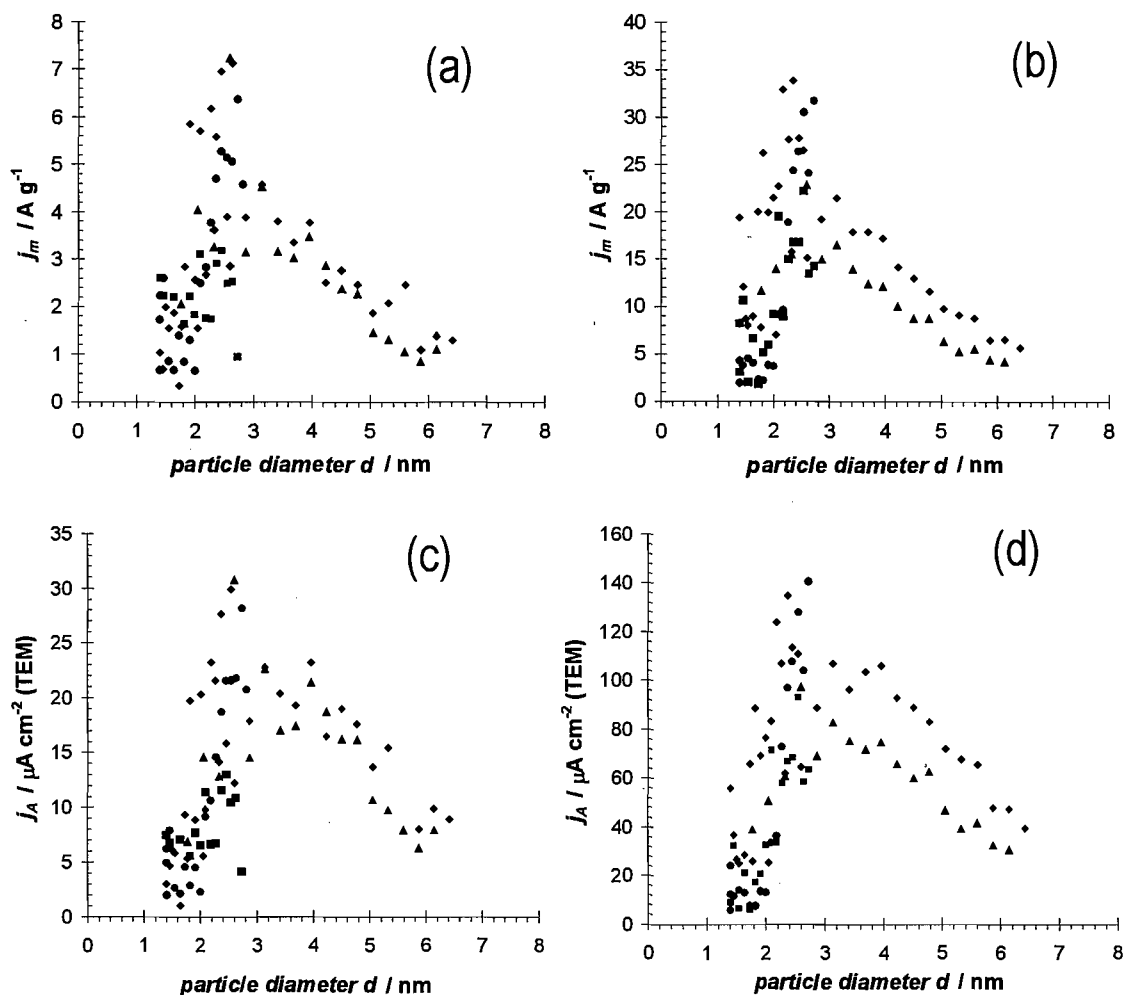
Figure 7.13. *Titania supported gold particle size dependent mass activity (a and b) and specific activity (c and d; TEM corrected) of the bulk CO oxidation in 0.5 M $HClO_4$ at potentials of 0.3 V (a and c) and 0.5 V (b and d).*

The mass activity was found to have a maximum at a particle size of ~ 2.7 nm at both potentials of 0.3 and 0.5 V. At particle sizes smaller 2.7 nm a steep decrease in activity was observed, as well as for particle sizes greater 2.7 nm. The specific activity follows a similar trend at the presented potentials, having a peak in activity at ~ 2.7 nm. Again for particle sizes smaller than this maximum the reaction strongly deactivates as it does at particle sizes after passing the maximum towards bigger particles. The most important observations for the titania supported Au nanoparticles are, that they were initially highly active for the oxidation of CO at very low overpotentials and were deactivated with subsequent electrochemical modification in experiments where an extended potential range was used. The entire gold particle seemed to be affected during

deactivation, as no CO oxidation at higher potentials was observed suggesting a non gold metal like state.

7.3 Conclusions

Gold in the *polycrystalline form* is a surprisingly good catalyst for the electro-oxidation of carbon monoxide. With CO oxidation occurring well negative to AuO formation on the other hand, in real terms the overpotential is large, > 700 mV. The results here follows behaviour which was similar to model single crystal catalysts work elsewhere [141, 216]. At some stage of gold oxide formation (between 1.4 and 1.6 V) a non-reactive oxide form is formed inhibiting the CO oxidation. This is most likely attributed to the bond strength of oxygen and was found to be reactivated during a scan in negative scan direction, when gold oxide starts to reduce. Only a few regenerated gold surface sites are apparently necessary to totally reactivate the reaction to its full activity.

Carbon support gold nanoparticles show particle size dependent catalytic properties during CO oxidation. The size dependent activity was found to have two distinct regions: (i) Particles with diameters smaller 3 nm are found to deactivated and (ii) a slow increase of activity was observed for particles in the range of 3 -10 nm. The change of activity in region (i) was not found to coincide with a change in Tafel slope suggesting no change in mechanism. Therefore the reduced activity has other sources. As in the case of oxygen reduction on carbon supported gold (see chapter 5) deactivates in the same range of particle size. Again, the similarity to ORR on platinum could be mentioned. As evident here the activation with increasing particle sizes was found to be two- to fourfold (depended on the surface area determination). Possible explanations for this activation are pure speculation. One suggested activation mechanism was a particle crystal face argument [65, 149], where it was proposed, that fcc truncated octahedral particles have predominantly (111) faces exposed at their surface. For structure sensitive reactions which are less active on (111) faces a deactivation should occur. The activity towards CO oxidation seems to decrease on single crystal surface in the order of Au(111) < Au(100) < Au(110) [141] and would therefore fulfil this criteria.

The electrooxidation of carbon monoxide on *sub-stoichiometric titanium dioxide supported gold nanoparticles* showed extraordinary high activity at low overpotential

and during constant potential experiments little deactivation is observed. The electrodes showed activity in a region, where no or only small currents for the CO oxidation was observed on Au (h,k,l) surfaces [141]. The gold nanoparticles have been found to neither behave like neutral metallic gold nor like carbon supported nanoparticles during CO oxidation, whilst the reduction of oxygen seemed to be "normal". The non gold like behaviour was manifested due to relative slow kinetics at higher potential, which prevent electrochemical modified electrodes and particle sizes < ~ 2 nm to reach mass transport limitation. Apparently two different processes are present at different potential ranges during CO oxidation. The first one highly "active" at potentials below 0.6 V and a second irreversible process at potential > 0.6 V.

8 General discussion

This section seeks to discuss the behaviour of the gold nanoparticles observed during this project. It has been reported that there is both a substrate and a particle size effect. A crucial difference of the two support materials under investigation is that carbon is conducting and titania is semiconducting. Stoichiometric titania is essentially a non-conductor.

The "inert" carbon supported gold particles showed:

- In the particle range of 3 – 7 nm essentially bulk gold-like properties
- In the particle range 2.5 – 3 nm a loss in catalytic activity for both oxygen reduction (ORR) and CO oxidation
- Au/AuO features at all particle sizes under investigation (no information was attainable for particles < 2.5 nm as during preparation this was the critical nucleus size). No loss of charge was observed with cycling.

On the semiconducting (sub-stoichiometric) titania support, two particle ranges have been identified with apparently different properties.

Nanoparticles with diameters in the range ~ 2 - 6.3 nm:

- Show much enhanced activity for the electrochemical oxidation of CO, particles at the lower end of the range showing the highest activity.
- Similar activity to bulk Au for the cathodic reduction of oxygen.
- Over most of the range, the voltammetry for the Au/AuO couple was initially similar to bulk gold. For all particle sizes the charges associated with the Au/AuO couple decreased with potential cycling and eventually vanished.
- Even when the Au/AuO peaks had disappeared, the activity for ORR was maintained and XPS showed that most of the gold remained on the surface.

Nanoparticles with diameters in the range < 2 nm

- Showed reduced activity for both ORR and CO oxidation
- No features associated with the Au/AuO couple were observed even when the positive limit was 1.63 V (and higher).

160

The observations could be discussed as "substrate only", "particle size only" and "substrate and particle size" effects as follows:

Titania (substrate) electrochemistry

Changes in titania (substrate) electrochemistry have been observed in both acidic and neutral (using a ferri/ferrocyanide model redox couple) electrolytes. In the CV of titania, oxidation current was observed, strongly suggesting the oxidation of defects in the film. CV's in 1M KCl with 4 mM $Fe_3(CN)_6$ on freshly prepared titania samples (not shown) demonstrate modification during repeated cycling experiment which is indicative of the electron transfer ability becoming more irreversible. This has been observed as a displacement of the onset potential of the reduction of ferricyanide to more negative potentials and a decrease of charge transferred during ferrocyanide re-oxidation. Nevertheless after equilibration (voltammogram was reproducible after ~20 cycles) the ferri/ferrocyanide voltammetry on titania (as presented in chapter 4) still showed some ferrocyanide oxidation current in the potential region, where no current has been observed on crystalline titania samples [330]. Hence it can be concluded that not all energy states are lost in the band gap region due to aging by cycling.

Substrate and particle size effect on titania supported gold particles: the gold redox couple

Titania supported gold particles with particle diameters > 2 nm show initially surface gold redox behaviour, where the onset potential of gold oxide formation and also the reduction peak potentials is similar to bulk gold. With subsequent cycling for all coverages, i.e. at all particles sizes in this range (d ~ 2 to 6.3 nm) the features vanish with cycle number. Even with large quantities of Au (e.g. > 10 monolayers) loss of Au/AuO features was observed with cycling. This implies that the vanishing of the gold redox couple during repeatedly cycling at all particles sizes in this range is probably best explained by an "aging" of the substrate by cycling. Under the concept of "aging" two possible effects are combined: Firstly the thin film support starts of with doping levels which are high (probably almost "quasi-metal" like) and due to partial oxidation of defects during electrochemical modification there is a loss of doping states in the band gap region. Secondly localised defect states which are likely to be present at the beginning of the amorphous thin film titania, which might be lost due to changes in

morphology. This effect was suggested to occur by ion mobility [55] in an electric field which would be present during potential cycling. It must be noted, that the authors [55] did not observe significant aging of titanium passive films, if the electrode was held at a potential of 1.5 V (vs. SHE). Both effects would form a Schottky diode like behaviour of the junction between gold and titania, where the time constant of the depletion layer is high and hence would suppress electron transfer during oxidation reactions at potentials which fall into the band gap region. Interestingly for $PtRuIr/TiO_x$ samples a deactivation towards the oxygen reduction was observed if cycled to potentials positive of 1.6 V, which was explained by a loss of conductivity and the authors overcame this by niobium doping [22].

The reasons for the complete loss of gold redox features in voltammograms for particles with mean *diameters ≤ 2 nm* is not likely to be originated solely by the loss of conduction of the support, as the initial (before aging) electron transfer ability should be high enough to enable oxidation of the gold. Also no gold was lost during the electrochemistry (as determined by XPS) [337]. The literature of metal oxide metal particle interfaces showed/suggested the following properties:

- charge transfer from gold particles to the support [99] or contradictorily charge transfer from titania to gold particles (both at particle sizes of generally ≤ 3nm) [87, 326]

- "molecule" like behaviour of small gold particles often referred as quantum size effect [89]

As the transition coincides with suggested transition of small (gold) particles to molecule like behaviour, the electronic coulomb blockade might be responsible for the effect. Moreover charge transfer at the interface might modify the gold nanoparticles and make them more susceptible to either oxidation or being inert towards oxidation. As there was no evidence for a binding energy shift in X-ray photoelectron spectroscopy before and after aging of the surface [337] it seems more likely that the surface redox behaviour becomes more irreversible. Unfortunately carbon supported gold nanoparticles nucleate at room temperature with an initial critical particle size of approximately 2.5 nm, therefre no statement of the redox behaviour at smaller particle could be made on this support. Nevertheless at particles sizes < 3 nm the oxidation and

reduction waves of gold oxide already showed an increase in irreversibility, similar to the observation for carbon supported platinum particles [19].

Substrate independent particle size effect: Oxygen reduction reaction

The oxygen electrochemistry was shown to be essentially insensitive towards the support materials of carbon and titania and changes in activity seem to be particle size induced. The substrate aging of titania does not seem to influence the electrochemistry suggesting that the electron transfer from the electrode to the electroactive species (oxygen) is not hindered. Danzfuss and Stimming [54] claim that localised states exist in the vicinity of band edges in amorphous semiconductors. The approximate conduction band edge position (on basis of literature values) of titania of ~ -0.015 V (vs. SHE) [41] and the fact that titania is a n- type semiconductor (electron donor levels positive with respect to the electrochemical scale of the conduction band edge) leads to the conclusion that up to potentials where ORR occurs electron transfer is possible.

Generally on both supports the reduction proceeded via a two electron reduction with the final product being mainly hydrogen peroxide. But a pronounced particle size effect was observed manifested in a decrease of ORR activity at particle sizes below ~ 3 nm. The similarities to the particle size effect on platinum are apparent and the statistics for small particles [149] where the activity drops due to a decrease of more active crystal planes (100) for particles smaller than 3-5 nm appear to be the most likely explanation, as the activity towards the ORR on gold single crystals was reported to be strongly dependent upon the crystallographic orientation. The activity in perchloric acid was reported to in the order (100)>>(110)>(111) [210]. Therefore it is believed that the major contribution towards the deactivation is caused by a crystallographic orientation effect on small particles exposing predominantly (111) phases to the electrolyte. Even so the role of changes in OH adsorption that has been suggested for platinum nanoparticle catalysed ORR (platinum oxide formation on Pt becomes more irreversible at smaller particles [19, 176, 178, 181]) can not be excluded, but seems unlikely as the ORR occurs on gold at potentials where no OH is believed to absorb at the surface. Nevertheless the increasing irreversibility of the gold redox couple as shown above might be indicative of a decreasing stabilisation of reaction intermediates (as was proposed in a general concept by Nørskov et al [344]) such a species could be $O_{2,ad}^{-}$ which then negatively influences the reactivity.

Substrate dependent particle size effect: CO oxidation

As presented in chapter 7 it has been found that the electrocatalytic oxidation of CO at TiO_x supported gold nanoparticles takes place at low overpotentials with a maximum in activity at 3 nm. In electrocatalytic CO oxidation it has been shown, that even gold single crystals are somewhat active [141, 216] the suggested mechanism was a Langmuir-Hinshelwood mechanism [290], with an onset potential as low as approximately ≤ 0.3 V (with very low current densities) [141]. The onset potential found here for the titania supported gold particles is centre size dependent and was at the most active particle size (d~ 2.8 nm) as low as approx. ≤ 0.2 V. The current densities during linear sweep voltammetry have been found to be significantly higher than on polycrystalline gold for potentials ≤ 0.625 V. Since in gas phase CO oxidation titania supported gold has been reported to be a highly active catalyst and also have a maximum in activity at ~ 3 nm [4], it suggests itself to comparison of the concepts developed in the gas phase discussion with the system under study here even though the reaction partner is not oxygen but hydroxide from activated water. The extraordinary high CO oxidation activity in heterogeneous catalysis has been explained in several different ways and a plenitude of factors have been reported which might influence the catalytic activity: For example it was reported [345] that the heat of adsorption of CO increased substantially at small titania supported gold particle diameters For example the heat of adsorption of bulk gold was reported to be 12.5 kcal/mol and for particles of ~2.5 nm 18.3 kcal/mol. Also oxygen seem to interact stronger with small thin gold particles as determined by an increase in desorption temperature during TPD [346]. Active sites for the resulting higher CO activity have been suggested to be:

I)   Special particle properties as for example:

♦ Low coordinated gold atoms at small particles which have a high degree of unsaturation and are specifically stabilized by the support (titania) [85, 112, 114, 347]

♦ Quantum size effects

• Most active Au particle size was observed where the a band gap of 0.2-0.6 eV was measured by STS, which are centres which are ~ 2 atomic layers thick and ~ 3 nm in diameter [4]

- In a study of monolayers of gold supported on thin TiO_x films it was shown that a "bilayer" of gold was the most active structure (and it was suggested that there is no influence by perimeter) [348]

II) Support related effects

♦ Perimeter effects, such as spill over effects of oxygen at the particle support interface, activated oxygen at the interface or facilitated charge transfer to the oxygen [101, 349, 350]

♦ Charge transfer from the gold particles to the support forming $Au^{\delta+}$ at the interface [99] (e.g. the presence of positively charged gold ions was shown to be crucial for the activity in Water Gas Shift reaction where zero-valent gold atoms were found to be inactive [351])

♦ Charge transfer from the support to gold forming negatively charged gold atoms which enhance the oxygen stabilization at the surface [103]

III) Influence of gold oxidation state

♦ Role of positively charged Au^+ on the CO oxidation activity - some authors show higher activities for partially oxidized gold clusters [113, 352]

Applying theses concepts to the electrocatalytic oxidation of CO on the basis of the presented data is difficult. The following discussion is an attempt to distinguish between "what appears to be likely and what more unlikely". Firstly a relatively high density of low coordinated sites, as well as a variety of particle structures should be present in both carbon and titania supported samples (see Introduction). Also there was no activity enhancement observed over bulk Au electrodes in the case of carbon supported Au particles, on the contrary rather a deactivation was evident at particle diameter ≤ 3 nm. As a general rule Haruta and Tsubota [17] reported that in the gas phase the smaller the gold particles become the more active they are which was explained by the increase of low coordinated sites. In electrolyte this is clearly is not the case. On the other hand a quantum size effects [4] at small particles can not be excluded as a possible explanation and there is indeed evidence for unique properties during the gold oxide formation/reduction which is probably support induced and strongest at smaller particles as discussed above.

Also effects at the perimeter cannot be excluded as the maximum perimeter between gold and titania was observed at d ~ 2.5 nm (see Figure 8.1). This is similar to the particle size where the maximum in CO oxidation is observed (d~3 nm).
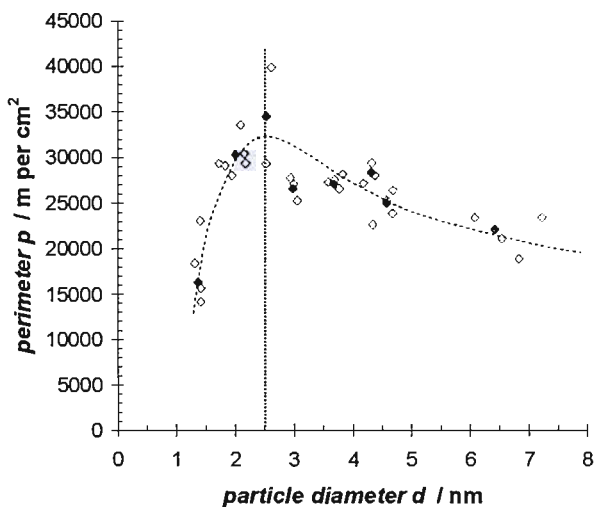
Figure 8.1. *Calculated perimeter for titania supported gold particles (the particles have been assumed to be perfect hemispheres, diameters taken from TEM images presented in Chapter 4).*

CO stripping experiments on titania supported gold particles in agreement with experiments on bulk gold did not show any adsorbed CO (the potential was held at 0 V vs. RHE for 15 minutes, experiments not shown) therefore a significant increase in surface coverages was ruled out and hence might imply that there is no significant increase in adsorption energy. Also there was no direct evidence from XPS that an oxidized gold species was present in the gold nanoparticles. Negatively charged gold sites at the particle perimeter have been reported to mediate the electron transfer to the oxygen and hence led to a stronger interaction [101-103, 350]. It is only speculative that this effect also enhances activation of water as it seems to be generally accepted to be the rate determining step during the electrocatalytic oxidation of CO. The similar onset potential to single crystal gold but with higher rates at lower overpotential implies that the key to the enhanced catalytic activity on titania supported gold is the activation of water. Interestingly Daté et al reported [118, 119] a crucial role of water during gas phase CO oxidation at metal oxide supported gold particles and proposed mechanisms, where water activates at the particle perimeter forming hydroxyl carbonyl and/or bicarbonate species. In electrocatalytic CO oxidation on both platinum and gold a hydroxyl carbonyl intermediate is believed to exist as a reaction intermediate [118, 119].

9 Conclusion and further work

A high throughput procedure [24] for investigating the influence of catalyst centre size on electrocatalytic activity has been demonstrated. The approach has required the development of physical vapour deposition (PVD) methods for the synthesis of libraries of supported metal particles and techniques for characterisation of the surfaces produced as well as the application of methodology for carrying out 100 simultaneous electrochemical experiments. It has been shown conclusively that there are both catalyst particle size effects and substrate effects on activity for cathodic oxygen reduction and CO oxidation using Au as the active metal. It has also been shown that the Au/AuO electrochemistry is influenced by both particle size and substrate.

In more detail amorphous TiO_x supports have been synthesised with a controlled range of conductivities. A range of Au nanoparticles have been synthesised as a function of position across titania substrates. TEM measurements indicate that during nucleation, a mean particle size of 1.4 nm is observed, and increasing coverage leads to an increased number of such nuclei to a maximum density of 5.5×10^{12} cm^{-2}. Particle sizes increase at higher Au coverages with a concomitant decrease in density. The small particles exhibit a binding energy shift in the Au (4f) core level of 0.3 eV from bulk gold, and the shift is 0.1 eV by the time particles grow to a mean size of 2.5 nm. Nucleation and growth of Au on carbon support is also observed, but the initial particle size is significantly larger at ca. 2.5 nm and the maximum particle density (3.1×10^{12} cm^{-2}) lower when compared to titania. Combined with suitable screening methods [24] the methodology provides a powerful route to the elucidation of particle size effects in catalysis. Applied to the study of *carbon supported gold nanoparticles* it was shown that they behave electrochemically similar to bulk gold with respect to the gold/gold oxide features, with a slight tendency of smaller particles being harder to oxidise and reduce. This was manifested in a gain of influence of the more positive anodic AuO formation peak AII over AI, as well as a slight negative shift of the AuO reduction peak towards more negative potentials (23 mV shift for particle sizes d ~ 10 nm to d ~ 2.5 nm). *Titania supported gold nanoparticles* where found to be strongly modified

electrochemically during potential sweep experiments. Although the charge for the Au/AuO electrochemistry decreased with cycling XPS measurements and oxygen reduction experiments suggested that no gold was lost from the surface. Therefore it could be concluded that the reason for inhibition of the gold redox has origin in the substrate or substrate gold interface chemistry. With decreasing size, the Au oxidation requires a higher overpotential and below a critical particle size of ~ 2 nm, the centres were found to behave non-metallic in potential sweep experiments throughout characterisation. They showed no characteristic gold oxide electrochemistry. Future experiments have to try to elucidate possible electronic changes to the substrate (loss of conductivity), particles (oxidation state) and/or possible morphology changes.

Trends in the *oxygen reduction* activity vs. particle size could be identified and data from the array and the disc electrodes on titania supported samples are identical. It was found that particles of gold with diameters below 2.5 – 3.0 nm are less active for oxygen reduction, *independent of the supporting material*. In both cases a steep deactivation of the ORR was observed. In here a maximum of the two electron reduction of oxygen reduction to hydrogen peroxide was found at particle sizes around 3 nm at *titania* supported samples and at 4 nm on carbon supported gold particles. The mechanism of the ORR on titania supported samples seems to be support and particle size independent, as the Tafel slope was always within experimental errors similar to the one found on bulk gold.

Carbon support gold nanoparticles show particle size dependent catalytic properties during *electrochemical CO oxidation*. The size dependent activity was found to have two distinct regions: (i) Particles with diameters smaller 3 nm are found to deactivated and (ii) a slow increase of activity was observed for particles in the range of 3 -10 nm. The change of activity in region (i) was not found to coincide with a change in Tafel slope suggesting no change in mechanistic. The electrooxidation of carbon monoxide on *sub-stoichiometric titanium dioxide supported gold nanoparticles* showed extraordinary high activity and during constant potential experiments little deactivation is observed. The electrodes showed activity in a region, where no or only small currents for the CO oxidation was observed on carbon supported gold, bulk gold and Au (h,k,l) surfaces [141]. The gold nanoparticles have been found to neither behave like neutral metallic

gold nor like carbon supported nanoparticles during CO oxidation, whilst the reduction of oxygen seemed to be "normal". The non gold like behaviour was manifested due to relative slow kinetics at higher potential, which prevent electrochemical modified electrodes and particle sizes < 2 nm to reach mass transport limitation. Apparently two different processes are present at different potential ranges during CO oxidation. The first one highly "active" at potentials below 0.6 V and a second irreversible process at potential > 0.6 V.

To help to answer some of the open questions future work will involve STM measurements to achieve more morphological information about the supported particles. Also the electronic properties of the TiO_x support as well as Au/TiO_x will be further studied by electrochemical impedance spectroscopy (EIS) to obtain information about the band positioning, doping level and doping level after electrochemical modification. The influence of metal doping will also be investigated.

10 References

1.   G.A. Somorjai and R.M. Rioux, *High technology catalysts towards 100% selectivity: Fabrication, characterization and reaction studies*. Catalysis Today, 2005. 100(3-4): p. 201-215.

2.   C.R. Henry, C. Chapon, S. Giorgio, and C. Goyhenex, *Size effects in heterogeneous catalysis*, in *Chemisorption and Reactivity on Supported Clusters and Thin Films*, R.M. Lambert and G. Pacchioni, Editors. 1997, Kluwer Academic Publishers: Dordrecht. p. 117-152.

3.   M. Mavrikakis, B. Hammer, and J.K. Nørskov, *Effect of strain on the reactivity of metal surfaces*. Physical Review Letters, 1998. 81(13): p. 2819-2822.

4.   M. Valden, X. Lai, and D.W. Goodman, *Onset of Catalytic Activity of Gold Clusters on Titania with the Appearance of Nonmetallic Properties*. Science, 1998. 281(5383): p. 1647-1650.

5.   T.G. Schaaff, M.N. Shafigullin, J.T. Khoury, I. Vezmar, R.L. Whetten, W.G. Cullen, P.N. First, C. Gutierrez-Wing, J. Ascensio, and M.J. Yacamán, *Isolation of Smaller Nanocrystal Au Molecules: Robust Quantum Effects in Optical Spectra*. Journal of Physical Chemistry B, 1997. 101(40): p. 7885-7891.

6.   C.R. Henry, *Surface studies of supported model catalysts*. Surface Science Reports, 1998. 31(7-8): p. 231-325.

7.   R. Balasubramanian, R. Guo, A.J. Mills, and R.W. Murray, *Reaction of $Au_{55}(PPh_3)_{12}Cl_6$ with thiols yields thiolate monolayer protected Au_{75} clusters*. Journal of the American Chemical Society, 2005. 127(22): p. 8126-8132.

8.   R. Guo and R.W. Murray, *Substituent effects on redox potentials and optical gap energies of molecule-like $Au_{38}(SPhX)_{24}$ nanoparticles*. Journal of the American Chemical Society, 2005. 127(34): p. 12140-12143.

9.   D. Lee, R.L. Donkers, G.L. Wang, A.S. Harper, and R.W. Murray, *Electrochemistry and optical absorbance and luminescence of molecule-like Au_{38} nanoparticles*. Journal of the American Chemical Society, 2004. 126(19): p. 6193-6199.

10. R.P. Andres, J.D. Bielefeld, J.I. Henderson, D.B. Janes, V.R. Kolagunta, C.P. Kubiak, W.J. Mahoney, and R.G. Osifchin, *Self-assembly of a two-dimensional superlattice of molecularly linked metal clusters.* Science, 1996. 273(5282): p. 1690-1693.

11. S.W. Chen, R.S. Ingram, M.J. Hostetler, J.J. Pietron, R.W. Murray, T.G. Schaaff, J.T. Khoury, M.M. Alvarez, and R.L. Whetten, *Gold nanoelectrodes of varied size: Transition to molecule-like charging.* Science, 1998. 280(5372): p. 2098-2101.

12. F.R.F. Fan and A.J. Bard, *An electrochemical coulomb staircase: Detection of single electron-transfer events at nanometer electrodes.* Science, 1997. 277(5333): p. 1791-1793.

13. G. Schmid and B. Corain, *Nanoparticulated gold: Syntheses, structures, electronics, and reactivities.* European Journal of Inorganic Chemistry, 2003. (17): p. 3081-3098.

14. R. Guo, D. Georganopoulou, S.W. Feldberg, R. Donkers, and R.W. Murray, *Supporting electrolyte and solvent effects on single-electron double layer capacitance charging of hexanethiolate-coated Au_{140} nanoparticles.* Analytical Chemistry, 2005. 77(8): p. 2662-2669.

15. *Catalysis and Electrocatalysis at Nanoparticle Surfaces*, ed. A. Wieckowski, E.R. Savinova, and C.G. Vayenas. 2003, New York: Marcel Dekker.

16. S.J. Tauster, S.C. Fung, and R.L. Garten, *Strong Metal-Support Interactions. Group 8 Noble Metals Supported on TiO_2.* Journal of the American Chemical Society, 1978. 100(1): p. 170-175.

17. M. Haruta and S. Tsubota, eds. *Effects of Size and Contact Structure of Supported Noble Metal Catalyst in Low-Temperature CO Oxidation.* Catalysis and Electrocatalysis at Nanoparticle Surfaces, ed. A. Wieckowski, E.R. Savinova, and C.G. Vayenas. 2003, Marcel Dekker: New York.

18. Y.P. Sun, H. Buck, and T.E. Mallouk, *Combinatorial discovery of alloy electrocatalysts for amperometric glucose sensors.* Analytical Chemistry, 2001. 73(7): p. 1599-1604.

19. S. Guerin, B.E. Hayden, C.E. Lee, C. Mormiche, J.R. Owen, A.E. Russell, B. Theobald, and D. Thompsett, *Combinatorial Electrochemical Screening of Fuel*

Cell Electrocatalysts. Journal of Combinatorial Chemistry, 2004. 6(1): p. 149-158.

20. N.D. Morris and T.E. Mallouk, *A high-throughput optical screening method for the optimization of colloidal water oxidation catalysts.* Journal of the American Chemical Society, 2002. 124(37): p. 11114-11121.

21. A.D. Spong, G. Vitins, S. Guerin, B.E. Hayden, A.E. Russell, and J.R. Owen, *Combinatorial arrays and parallel screening for positive electrode discovery.* Journal of Power Sources, 2003. 119: p. 778-783.

22. G.Y. Chen, D.A. Delafuente, S. Sarangapani, and T.E. Mallouk, *Combinatorial discovery of bifunctional oxygen reduction - water oxidation electrocatalysts for regenerative fuel cells.* Catalysis Today, 2001. 67(4): p. 341-355.

23. E. Reddington, A. Sapienza, B. Gurau, R. Viswanathan, S. Sarangapani, E.S. Smotkin, and T.E. Mallouk, *Combinatorial Electrochemistry: A Highly Parallel, Optical Screening Method for Discovery of Better Electrocatalysts.* Science, 1998. 280(5370): p. 1735-1737.

24. S. Guerin and B.E. Hayden, *Physical vapor deposition method for the high-throughput synthesis of solid-state material libraries.* Journal of Combinatorial Chemistry, 2006. 8(1): p. 66-73.

25. S. Guerin, B.E. Hayden, C.E. Lee, C. Mormiche, and A. Russell, *High-Throughput Synthesis and Screening of Ternary Metal Alloys for Electrocatalysis.* Journal of Physical Chemistry B, 2006. 110 (29): p. 14355 - 14362.

26. G. Hoogers, *Introduction,* in *Fuel Cell Technology Handbook,* G. Hoogers, Editor. 2003, CRC Press: Boca Raton.

27. G. Chen, S.R. Bare, and T.E. Mallouk, *Development of supported bifunctional electrocatalysts for unitized regenerative fuel cells.* Journal of the Electrochemical Society, 2002. 149(8): p. A1092-A1099.

28. T. Ioroi, K. Yasuda, Z. Siroma, N. Fujiwara, and Y. Miyazaki, *Enhanced CO-Tolerance of Carbon-Supported Platinum and Molybdenum Oxide Anode Catalyst.* Journal of the Electrochemical Society, 2003. 150(9): p. A1225-A1230.

29. P.K. Shen, K.Y. Chen, and A.C.C. Tseung, *CO Oxidation on Pt-Ru/WO₃ Electrodes.* Journal of the Electrochemical Society, 1995. 142: p. L85.

30. A.C.C. Tseung and K.Y. Chen, *Hydrogen spill-over effect on Pt/WO₃ anode catalysts*. Catalysis Today, 1997. 38(4): p. 439-443.

31. K.Y. Chen, Z. Sun, and A.C.C. Tseung, *Preparation and characterization of high-performance Pt- Ru/WO₃/C anode catalysts for the oxidation of impure hydrogen*. Electrochemical and Solid State Letters, 2000. 3(1): p. 10-12.

32. J. Shim, C.R. Lee, H.K. Lee, J.S. Lee, and E.J. Cairns, *Electrochemical characteristics of Pt-WO₃/C and Pt-TiO₂/C electrocatalysts in a polymer electrolyte fuel cell*. Journal of Power Sources, 2001. 102: p. 172-177.

33. T. Ioroi, Z. Siroma, N. Fujiwara, S.-i. Yamazaki, and K. Yasuda, *Sub-stoichiometric titanium oxide supported platinum electrocatalyst for polymer electrolyte fuel cells*. Electrochemistry Communications, 2005. 7: p. 183-188.

34. L. Xiong and A. Manthiram, *Synthesis and characterization of methanol tolerant Pt/TiOₓ/C nanocomposites for oxygen reduction in direct methanol fuel cells*. Electrochimica Acta, 2004. 49: p. 4163-4170.

35. U. Diebold, *The surface science of titanium dioxide*. Surface Science Reports, 2003. 48(5-8): p. 53-229.

36. H.O. Finklea, *Titanium dioxide (TiO₂) and strontium titanate (SrTiO₃)*, in *Semiconductor electrodes*, H.O. Finklea, Editor. 1988, Elsevier Science Publishers B.V. : Amsterdam.

37. R. van de Krol, A. Goossens, and J. Schoonman, *Mott-Schottky analysis of nanometer-scale thin-film anatase TiO₂*. Journal of the Electrochemical Society, 1997. 144(5): p. 1723-1727.

38. U. Diebold, *Structure and properties of TiO₂ surfaces: a brief review*. Applied Physics A - Solids and Surfaces, 2003. 76: p. 681-687.

39. H.O. Finklea, *Semiconductor electrode concepts and terminology*, in *Semiconductor electrodes*, H.O. Finklea, Editor. 1988, Elsevier Science Publishers B.V. : Amsterdam.

40. T. Bak, J. Nowotny, M. Rekas, and C.C. Sorrell, *Defect chemistry and semiconducting properties of titanium dioxide: II. Defect diagrams**. Journal of Physics and Chemistry of Solids, 2003. 64(7): p. 1057-1067.

41. Y. Xu and M.A.A. Schoonen, *The absolute energy positions of conduction and valence bands of selected semiconducting minerals*. American Mineralogist, 2000. 85(3-4): p. 543-556.

42. M. Jakob, H. Levanon, and P.V. Kamat, *Charge Distribution between UV-Irradiated TiO2 and Gold Nanoparticles: Determination of Shift in the Fermi Level.* Nano Letters, 2003. 3(3): p. 353-358.

43. C.H. Hamann, A. Hamnett, and W. Vielstich, *Electrochemistry.* 1998, Weinheim: Wiley-VCH.

44. D.C. Cronemeyer, *Electrical and Optical Properties of Rutile Single Crystals.* Physical Review, 1952. 87(5): p. 876-886.

45. P.C.S. Hayfield, *Development of a new material - Monolithic Ti4O7 Ebonex Ceramic.* 2002, Cambridge UK: RSC Publishing.

46. W.G. Lee, S.I. Woo, J.C. Kim, S.H. Choi, and K.H. Oh, *Preparation and properties of amorphous TiO2 thin films by plasma enhanced chemical vapor deposition.* Thin Solid Films, 1994. 237(1-2): p. 105-111.

47. S. Tanemura, L. Miao, W. Wunderlich, M. Tanemura, Y. Mori, S. Toh, and K. Kaneko, *Fabrication and characterization of anatase/rutile-TiO2 thin films by magnetron sputtering: a review.* Science and Technology of Advanced Materials, 2005. 6(1): p. 11-17.

48. L. Sheppard, T. Bak, J. Nowotny, C.C. Sorrell, S. Kumar, A.R. Gerson, M.C. Barnes, and C. Ball, *Effect of niobium on the structure of titanium dioxide thin films.* Thin Solid Films, 2006. 510(1-2): p. 119-124.

49. M. Lottiaux, C. Boulesteix, G. Nihoul, F. Varnier, F. Flory, R. Galindo, and E. Pelletier, *Morphology and structure of TiO2 thin layers vs. thickness and substrate temperature.* Thin Solid Films, 1989. 170(1): p. 107-126.

50. V. Mikhelashvili and G. Eisenstein, *Effects of annealing conditions on optical and electrical characteristics of titanium dioxide films deposited by electron beam evaporation.* Journal of Applied Physics, 2001. 89(6): p. 3256-3269.

51. I. Abayev, A. Zaban, F. Fabregat-Santiago, and J. Bisquert, *Electronic conductivity in nanostructured TiO2 films permeated with electrolyte.* Physica Status Solidi a-Applied Research, 2003. 196(1): p. R4-R6.

52. S.R. Morrison, *Electrochemistry at Semiconductor and Oxidized Metal Electrodes.* 1980, New York: Plenum Press.

53. H.O. Finklea, *The Preparation of TiO2 Electrodes with Minimum Mott-Schottky Frequency Dispersion.* Journal of the Electrochemical Society, 1982. 129(9): p. 2003-2008.

54.   B. Danzfuss and U. Stimming, *Iron(III)-titanium(IV)-oxide electrodes: Their structural, electrochemical and photoelectrochemical properties*. Journal of Electroanalytical Chemistry, 1984. 164(1): p. 89-119.

55.   K. Leitner, J.W. Schultze, and U. Stimming, *Photoelectrochemical Investigations of Passive Films on Titanium Electrodes*. Journal of the Electrochemical Society, 1986. 133(8): p. 1561-1568.

56.   J.W. Schultze and M.M. Lohrengel, *Stability, reactivity and breakdown of passive films. Problems of recent and future research*. Electrochimica Acta, 2000. 45(15-16): p. 2499-2513.

57.   F. Baletto and R. Ferrando, *Structural properties of nanoclusters: Energetic, thermodynamic, and kinetic effects*. Reviews of Modern Physics, 2005. 77(1): p. 371-53.

58.   M.J. Yacamán, J.A. Ascencio, H.B. Liu, and J. Gardea-Torresdey, *Structure shape and stability of nanometric sized particles*. Journal of Vacuum Science and Technology B, 2001. 19(4): p. 1091-1103.

59.   L.D. Marks, *Experimental studies of small particle structures*. Reports on Progress in Physics, 1994. 57(6): p. 603-649.

60.   F. Cosandey and T.E. Madey, *Growth, morphology, interfacial effects and catalytic properties of Au on TiO_2*. Surface Review and Letters, 2001. 8(1-2): p. 73-93.

61.   M. Bäumer and H.J. Freund, *Metal deposits on well-ordered oxide films*. Progress in Surface Science, 1999. 61(7-8): p. 127-198.

62.   A.S. Barnard, X.M. Lin, and L.A. Curtiss, *Equilibrium Morphology of Face-Centered Cubic Gold Nanoparticles >3 nm and the Shape Changes Induced by Temperature*. Journal of Physical Chemistry B, 2005. 109(51): p. 24465-24472.

63.   G. Wulff, *Zur Frage der Geschwindigkeit des Wachstums und der Auflösung der Krystallflächen*. Zeitschrift für Krystallographie, 1901. 29: p. 449-530.

64.   P.-A. Buffat, M. Flüeli, R. Spycher, P. Stadelmann, and J.-P. Borel, *Crystallographic structure of small gold particles studied by high-resolution electron microscopy*. Faraday Discussions, 1991. 92: p. 173-187.

65.   R. Van Hardeveld and F. Hartog, *The statistics of surface atoms and surface sites on metal crystals*. Surface Science, 1969. 15(2): p. 189-230.

66.   M.R. Hoare and P. Pal, *Statistics and stability of small assemblies of atoms.* Journal of Crystal Growth, 1972. 17: p. 77-96.

67.   K. Koga and K. Sugawara, *Population statistics of gold nanoparticle morphologies: direct determination by HREM observations.* Surface Science, 2003. 529(1-2): p. 23-35.

68.   H. Hofmeister, *Forty Years Study of Fivefold Twinned Structures in Small Particles and Thin Films.* Crystal Research and Technology, 1998. 33(1): p. 3-25.

69.   F. Baletto, R. Ferrando, A. Fortunelli, F. Montalenti, and C. Mottet, *Crossover among structural motifs in transition and noble-metal clusters.* The Journal of Chemical Physics, 2002. 116(9): p. 3856-3863.

70.   C.L. Cleveland, U. Landman, T.G. Schaaff, M.N. Shafigullin, P.W. Stephens, and R.L. Whetten, *Structural Evolution of Smaller Gold Nanocrystals: The Truncated Decahedral Motif.* Physical Review Letters, 1997. 79(10): p. 1873-1876.

71.   P.-A. Buffat and J.P. Borel, *Size effect on the melting temperature of gold particles.* Physical Review A, 1976. 13(6): p. 2287-2298.

72.   G.A. Somorjai, *The flexible surface: new techniques for molecular level studies of time dependent changes in metal surface structure and adsorbate structure during catalytic reactions.* Journal of Molecular Catalysis A: Chemical, 1996. 107(1-3): p. 39-53.

73.   R.D. Shannon and C.T. Prewitt, *Effective Ionic Radii in Oxides and Fluorides.* Acta Crystallographica, 1969. 25 B: p. 925-946.

74.   W.L. Winterbottom, *Equilibrium Shape of a Small Particle in Contact with a Foreign Substrate.* Acta Metallurgica, 1967. 15: p. 303-310.

75.   L. Zhang, R. Persaud, and T.E. Madey, *Ultrathin metal films on a metal oxide surface: Growth of Au on TiO_2 (110).* Physical Review B, 1997. 56(16): p. 10549-10557.

76.   I. Lopez-Salido, D.C. Lim, R. Dietsche, N. Bertram, and Y.D. Kim, *Electronic and Geometric Properties of Au Nanoparticles on Highly Ordered Pyrolytic Graphite (HOPG) Studied Using X-ray Photoelectron Spectroscopy (XPS) and Scanning Tunneling Microscopy (STM).* Journal of Physical Chemistry B, 2006. 110(3): p. 1128-1136.

77.   J.C. Heyraud and J.J. Metois, *Equilibrium shape of gold crystallites on a graphite cleavage surface: Surface energies and interfacial energy.* Acta Metallurgica, 1980. 28(12): p. 1789-1797.

78.   T. Irawan, I. Barke, and H. Hovel, *Size-dependent morphology of gold clusters grown on nanostructured graphite.* Applied Physics A-Materials Science & Processing, 2005. 80(5): p. 929-935.

79.   C. Lemire, R. Meyer, S.K. Shaikhutdinov, and H.J. Freund, *CO adsorption on oxide supported gold: from small clusters to monolayer islands and three-dimensional nanoparticles.* Surface Science, 2004. 552(1-3): p. 27-34.

80.   S.C. Parker, A.W. Grant, V.A. Bondzie, and C.T. Campbell, *Island growth kinetics during the vapor deposition of gold onto TiO$_2$(110).* Surface Science, 1999. 441(1): p. 10-20.

81.   N. Lopez and J.K. Nørskov, *Theoretical study of the Au/TiO$_2$(110) interface.* Surface Science, 2002. 515: p. 175-186.

82.   I. Hakim, O. Serdar, D.B. Nigel, and M.D. Mark, *Adsorption and diffusion of Pt and Au on the stoichiometric and reduced TiO$_2$ rutile (110) surfaces.* Physical Review B (Condensed Matter and Materials Physics), 2005. 72(8): p. 081407.

83.   A. Vijay, G. Mills, and H. Metiu, *Adsorption of gold on stoichiometric and reduced rutile TiO$_2$ (110) surfaces.* Journal of Chemical Physics, 2003. 118(14): p. 6536-6551.

84.   E. Wahlström, N. Lopez, R. Schaub, P. Thostrup, A. Ronnau, C. Africh, E. Laegsgaard, J.K. Nørskov, and F. Besenbacher, *Bonding of Gold Nanoclusters to Oxygen Vacancies on Rutile TiO$_2$ (110).* Physical Review Letters, 2003. 90(2): p. 026101.

85.   N. Lopez, J.K. Nørskov, T.V.W. Janssens, A. Carlsson, A. Puig-Molina, B.S. Clausen, and J.D. Grunwaldt, *The adhesion and shape of nanosized Au particles in a Au/TiO$_2$ catalyst.* Journal of Catalysis, 2004. 225(1): p. 86-94.

86.   Z. Yang, R. Wu, and D.W. Goodman, *Structural and electronic properties of Au on TiO$_2$(110).* Physical Review B, 2000. 61(20): p. 14066.

87.   T. Minato, T. Susaki, S. Shiraki, H.S. Kato, M. Kawai, and K.-i. Aika, *Investigation of the electronic interaction between TiO$_2$(1 1 0) surfaces and Au clusters by PES and STM.* Surface Science, 2004. 566-568(Part 2): p. 1012-1017.

88. L. Zhang, F. Cosandey, R. Persaud, and T.E. Madey, *Initial growth and morphology of thin Au films on TiO₂(110)*. Surface Science, 1999. 439(1-3): p. 73-85.

89. X. Lai, T.P.S. Clair, M. Valden, and D.W. Goodman, *Scanning tunneling microscopy studies of metal clusters supported on TiO₂ (110): Morphology and electronic structure*. Progress in Surface Science, 1998. 59(1-4): p. 25-52.

90. J.A. Venables, G.D.T. Spiller, and M. Hanbucken, *Nucleation and growth of thin films*. Reports on Progress in Physics, 1984. 47(4): p. 399-459.

91. H. Poppa, *Nucleation, Growth, and TEM Analysis of Metal Particles and Clusters Deposited in UHV*. Catalysis reviews, science and engineering, 1993. 35(3): p. 359-398.

92. B.E. Hayden, D. Pletcher, M.E. Rendall, and A.E. Russell, *Oxides as catalysts and supports in electrochemistry - A selective literature review for General Motors Inc.* Southampton Electrochemistry and Surface Science Group, 2003. p.

93. C. Kittel, *Introduction to Solid State Physics*. 5th ed. 1976, New York: John Wiley & Sons, Inc.

94. S. Trasatti, *Work function, electronegativity, and electrochemical behaviour of metals: II. Potentials of zero charge and "electrochemical" work functions*. Journal of Electroanalytical Chemistry, 1971. 33(2): p. 351-378.

95. E.W. McFarland and J. Tang, *A photovoltaic device structure based on internal electron emission*. Nature, 2003. 421(6923): p. 616-618.

96. T. Kiyonaga, T. Mitsui, M. Torikoshi, M. Takekawa, T. Soejima, and H. Tada, *Ultrafast Photosynthetic Reduction of Elemental Sulfur by Au Nanoparticle-Loaded TiO₂*. Journal of Physical Chemistry B, 2006. 110(22): p. 10771-10778.

97. G. Schmid, *The role of big metal clusters in nanoscience*. Journal of the Chemical Society-Dalton Transactions, 1998. (7): p. 1077-1082.

98. V. Subramanian, E.E. Wolf, and P.V. Kamat, *Catalysis with TiO₂/Gold Nanocomposites. Effect of Metal Particle Size on the Fermi Level Equilibration*. Journal of the American Chemical Society, 2004. 126(15): p. 4943-4950.

99. T. Okazawa, M. Kohyama, and Y. Kido, *Electronic properties of Au nano-particles supported on stoichiometric and reduced TiO₂(1 1 0) substrates*. Surface Science, 2006. 600(19): p. 4430-4437.

100. A. Vittadini and A. Selloni, *Small gold clusters on stoichiometric and defected TiO[sub 2] anatase (101) and their interaction with CO: A density functional study*. The Journal of Chemical Physics, 2002. 117(1): p. 353-361.

101. Z.-P. Liu, X.-Q. Gong, J. Kohanoff, C. Sanchez, and P. Hu, *Catalytic Role of Metal Oxides in Gold-Based Catalysts: A First Principles Study of CO Oxidation on TiO₂ Supported Au*. Physical Review Letters, 2003. 91(26): p. 266102.

102. M. Okumura, Y. Kitagawa, M. Haruta, and K. Yamaguchi, *The interaction of neutral and charged Au clusters with O₂, CO and H₂*. Applied Catalysis A: General, 2005. 291(1-2): p. 37-44.

103. A. Sanchez, S. Abbet, U. Heiz, W.D. Schneider, H. Hakkinen, R.N. Barnett, and U. Landman, *When Gold Is Not Noble: Nanoscale Gold Catalysts*. Journal of Physical Chemistry A, 1999. 103(48): p. 9573-9578.

104. B. Hammer and J.K. Nørskov, *Why gold is the noblest of all the metals*. Nature, 1995. 376(6537): p. 238-240.

105. G.C. Bond and D.T. Thompson, *Catalysis by Gold*. Catalysis reviews, science and engineering 1999. 41(3&4): p. 319-388.

106. M. Haruta, T. Kobayashi, H. Sano, and N. Yamada, *Novel Gold Catalysts for the Oxidation of Carbon-Monoxide at a Temperature Far Below 0-Degrees-C*. Chemistry Letters, 1987. (2): p. 405-408.

107. G.C. Bond and D.T. Thompson, *Gold-Catalysed Oxidation of Carbon Monoxide*. Gold Bulletin, 2000. 33(2): p. 41-51.

108. M. Haruta, *Size- and support-dependency in the catalysis of gold*. Catalysis Today, 1997. 36(1): p. 153-166.

109. L.M. Molina and B. Hammer, *Some recent theoretical advances in the understanding of the catalytic activity of Au*. Applied Catalysis A: General, 2005. 291(1-2): p. 21-31.

110. I.N. Remediakis, N. Lopez, and J.K. Nørskov, *CO oxidation on gold nanoparticles: Theoretical studies*. Applied Catalysis A: General, 2005. 291(1-2): p. 13-20.

111. Y. Iizuka, T. Tode, T. Takao, K.-i. Yatsu, T. Takeuchi, S. Tsubota, and M. Haruta, *A Kinetic and Adsorption Study of CO Oxidation over Unsupported Fine*

Gold Powder and over Gold Supported on Titanium Dioxide. Journal of Catalysis, 1999. 187(1): p. 50-58.

112.   N. Lopez and J.K. Nørskov, *Catalytic CO Oxidation by a Gold Nanoparticle: A Density Functional Study.* Journal of the American Chemical Society, 2002. 124(38): p. 11262-11263.

113.   J. Guzman and B.C. Gates, *Catalysis by Supported Gold: Correlation between Catalytic Activity for CO Oxidation and Oxidation States of Gold.* Journal of the American Chemical Society, 2004. 126(9): p. 2672-2673.

114.   J.-D. Grunwaldt, M. Maciejewski, O.S. Becker, P. Fabrizioli, and A. Baiker, *Comparative Study of Au/TiO$_2$ and Au/ZrO$_2$ Catalysts for Low-Temperature CO Oxidation.* Journal of Catalysis, 1999. 186(2): p. 458-469.

115.   Y. Xu and M. Mavrikakis, *Adsorption and Dissociation of O$_2$ on Gold Surfaces: Effect of Steps and Strain.* Journal of Physical Chemistry B, 2003. 107(35): p. 9298-9307.

116.   M. Haruta, S. Tsubota, T. Kobayashi, H. Kageyama, M.J. Genet, and B. Delmon, *Low-Temperature Oxidation of CO over Gold Supported on TiO$_2$, α-Fe$_2$O$_3$, and Co$_3$O$_4$.* Journal of Catalysis, 1993. 144(1): p. 175-192.

117.   M.M. Schubert, S. Hackenberg, A.C. van Veen, M. Muhler, V. Plzak, and R.J. Behm, *CO Oxidation over Supported Gold Catalysts --"Inert" and "Active" Support Materials and Their Role for the Oxygen Supply during Reaction.* Journal of Catalysis, 2001. 197(1): p. 113-122.

118.   M. Daté, M. Okumura, S. Tsubota, and M. Haruta, *Vital role of moisture in the catalytic activity of supported gold nanoparticles.* Angewandte Chemie-International Edition, 2004. 43(16): p. 2129-2132.

119.   M. Daté and M. Haruta, *Moisture Effect on CO Oxidation over Au/TiO$_2$ Catalyst.* Journal of Catalysis, 2001. 201(2): p. 221-224.

120.   A. Bongiorno and U. Landman, *Water-Enhanced Catalysis of CO Oxidation on Free and Supported Gold Nanoclusters.* Physical Review Letters, 2005. 95(10): p. 106102-4.

121.   N. Lopez, T.V.W. Janssens, B.S. Clausen, Y. Xu, M. Mavrikakis, T. Bligaard, and J.K. Nørskov, *On the origin of the catalytic activity of gold nanoparticles for low-temperature CO oxidation.* Journal of Catalysis, 2004. 223(1): p. 232-235.

122.	B.E. Conway, *Electrochemical oxide film formation at noble metals as a surface-chemical process.* Progress in Surface Science, 1995. 49(4): p. 331-452.

123.	L.D. Burke and P.F. Nugent, *The Electrochemistry of Gold: I The Redox Behaviour of the Metal in Aqueous Media.* Gold Bulletin, 1997. 30(2): p. 43-53.

124.	K. Juodkazis, J. Juodkazyte, V. Jasulaitiene, A. Lukinskas, and B. Sebeka, *XPS studies on the gold oxide surface layer formation.* Electrochemistry Communications, 2000. 2(7): p. 503-507.

125.	K. Juodkazis, J. Juodkazyte, B. Sebeka, and A. Lukinskas, *Cyclic voltammetric studies on the reduction of a gold oxide surface layer.* Electrochemistry Communications, 1999. 1(8): p. 315-318.

126.	S.J. Xia and V.I. Birss, *A multi-technique study of compact and hydrous Au oxide growth in 0.1 M sulfuric acid solutions.* Journal of Electroanalytical Chemistry, 2001. 500(1-2): p. 562-573.

127.	G. Tremiliosi-Filho, L.H. Dall'Antonia, and G. Jerkiewicz, *Limit of extent of formation of the quasi-two-dimensional oxide state on Au electrodes.* Journal of Electroanalytical Chemsitry, 1997. 422: p. 149-159.

128.	L.D. Burke and P.F. Nugent, *The Electrochemistry of Gold: II The Electrocatalytic Behaviour of the Metal in Aqueous Media.* Gold Bulletin, 1998. 31(2): p. 39-50.

129.	L.D. Burke, *Scope for new applications for gold arising from the electrocatalytic behaviour of its metastable surface states.* Gold Bulletin, 2004. 37(1-2): p. 125-135.

130.	G. Jerkiewicz, *Surface Oxidation of Noble Metal Electrodes*, in *Interfacial Electrochemistry*, A. Wieckowski, Editor. 1999, Marcel Dekker, Inc.: New York.

131.	H. Angerstein-Kozlowka, B.E. Conway, B. Barnett, and J. Mozota, *The role of ion adsorption in surface oxide formation and reduction at noble metals: general features of the surface process.* Journal of Electroanalytical Chemistry, 1979. 100: p. 417-446.

132.	P. Zelenay, L.M. Rice-Jackson, and A. Wieckowski, *Radioactive labeling study of sulfate/bisulfate adsorption on smooth gold electrodes.* Journal of Electroanalytical Chemistry, 1990. 283(1-2): p. 389-401.

133. T. Dretschkow and T. Wandlowski, *The kinetics of structural changes in anionic adlayers on stepped Au(111)$_s$ electrodes from sulfuric acid solutions.* Berichte Der Bunsen-Gesellschaft-Physical Chemistry Chemical Physics, 1997. 101(4): p. 749-757.

134. H. Angerstein-Kozlowska, B.E. Conway, A. Hamelin, and L. Stoicoviciu, *Elementary steps of electrochemical oxidation of single-crystal planes of Au--I. Chemical basis of processes involving geometry of anions and the electrode surfaces.* Electrochimica Acta, 1986. 31(8): p. 1051-1061.

135. H. Angerstein-Kozlowska, B.E. Conway, A. Hamelin, and L. Stoicoviciu, *Elementary steps of electrochemical oxidation of single-crystal planes of Au Part II. A chemical and structural basis of oxidation of the (111) plane.* Journal of Electroanalytical Chemistry, 1987. 228(1-2): p. 429-453.

136. K. Ataka, T. Yotsuyanagi, and M. Osawa, *Potential-Dependent Reorientation of Water Molecules at an Electrode/Electrolyte Interface Studied by Surface-Enhanced Infrared Absorption Spectroscopy.* Journal of Physical Chemistry, 1996. 100(25): p. 10664-10672.

137. H. Angerstein-Kozlowska, B.E. Conway, and A. Hamelin, *Electrocatalytic mediation of oxidation of H_2 at gold by chemisorbed states of anions.* Journal of Electroanalytical Chemistry, 1990. 277(1-2): p. 233-252.

138. M.E. Gallagher, B.B. Blizanac, C.A. Lucas, P.N. Ross, and N.M. Markovic, *Structure sensitivity of CO oxidation on gold single crystal surfaces in alkaline solution: Surface X-ray scattering and rotating disk measurements.* Surface Science, 2005. 582(1-3): p. 215-226.

139. B.M. Ocko, G. Helgesen, B. Schardt, and J. Wang, *Charge Induced (1x3) Reconstruction of the Au(110) Surface: An X-Ray Scattering Study.* Physical Review Letters, 1992. 69(23): p. 3350-3353.

140. B.M. Ocko, J. Wang, A. Davenport, and H. Isaacs, *In Situ X-ray Reflectivity Studies of the Au(001) Reconstruction in an Electrochemical Cell.* Physical Review Letters, 199. 65(12): p. 1466-1469.

141. B.B. Blizanac, M. Arenz, P.N. Ross, and N.M. Markovic, *Surface electrochemistry of CO on reconstructed gold single crystal surfaces studied by infrared reflection absorption spectroscopy and rotating disk electrode.* Journal of the American Chemical Society, 2004. 126(32): p. 10130-10141.

142. I.M. Tidswell, N.M. Markovic, C.A. Lucas, and P.N. Ross, *In situ x-ray-scattering study of the Au(001) reconstruction in alkaline and acidic electrolytes*. Physical Review B, 1993. 47(24): p. 16542.

143. S. Bruckenstein and M. Shay, *An in situ weighing study of the mechanism for the formation of the adsorbed oxygen monolayer at a gold electrode*. Journal of Electroanalytical Chemistry, 1985. 188(1-2): p. 131-136.

144. W. Stöckel and R. Schumacher, *Electrochemical Insitu Investigations on Polycrystalline Gold Electrodes with Oscillating Quartz Crystals - the Electrosorption Valency and Heterogeneity Constant of Halide and Sulfate Adlayers*. Berichte Der Bunsen-Gesellschaft-Physical Chemistry Chemical Physics, 1989. 93(5): p. 600-605.

145. J.S. Gordon and D.C. Johnson, *Application of an electrochemical quartz crystal microbalance to a study of water adsorption at gold surfaces in acidic media*. Journal of Electroanalytical Chemistry, 1994. 365(1-2): p. 267-274.

146. J. Horkans, B.D. Cahan, and E. Yeager, *Electrode potential scanning ellipsometric spectroscopy: Study of the formation of the anodic oxide film on noble metals*. Surface Science, 1974. 46(1): p. 1-23.

147. H.A. Gasteiger, J.E. Panels, and S.G. Yan, *Dependence of PEM fuel cell performance on catalyst loading*. Journal of Power Sources, 2004. 127(1-2): p. 162-171.

148. H.A. Gasteiger, S.S. Kocha, B. Sompalli, and F.T. Wagner, *Activity benchmarks and requirements for Pt, Pt-alloy, and non-Pt oxygen reduction catalysts for PEMFCs*. Applied Catalysis B-Environmental, 2005. 56(1-2): p. 9-35.

149. K. Kinoshita, *Particle-Size Effects for Oxygen Reduction on Highly Dispersed Platinum in Acid Electrolytes*. Journal of the Electrochemical Society, 1990. 137(3): p. 845-848.

150. J.P. Hoare, *Oxygen*, in *Standard Potentials in Aqueous Solution*, A.J. Bard, R. Parsons, and J. Jordan, Editors. 1985, Marcel Dekker, Inc.: New York.

151. H.S. Wroblowa, P. Yen Chi, and G. Razumney, *Electroreduction of oxygen: A new mechanistic criterion*. Journal of Electroanalytical Chemistry, 1976. 69(2): p. 195-201.

152. D.J. Schiffrin, *The Electrochemistry of Oxygen*, in *A Specialist Periodical Report; Electrochemistry*, D. Pletcher, Editor. 1983, The Royal Society of Chemistry: London.

153. E. Yeager, *Electrocatalysts for O_2 Reduction*. Electrochimica Acta, 1984. 29(11): p. 1527-1537.

154. K. Kinoshita, *Carbon Electrochemical and Phsiochemical Properties*. 1988, New York: John Wiley & Sons.

155. V.B. Baez, J.E. Graves, and D. Pletcher, *The reduction of oxygen on titanium oxide electrodes*. Journal of Electroanalytical Chemistry, 1992. 340: p. 273-286.

156. V.B. Baez and D. Pletcher, *Preparation and characterization of carbon/titanium dioxide surfaces -- the reduction of oxygen*. Journal of Electroanalytical Chemistry, 1995. 382(1-2): p. 59-64.

157. R.R. Adzic. *Surface Morphology Effects in Oxygen Electrochemistry*. in *Proceedings of the Workshop on Structural Effects in Electrocatalysis and Oxygen Electrochemistry*. 1991. Case Western Reserve University: The Electrochemical Society.

158. A.J. Appleby, *Electrocatalysis*, in *Comprhensive Treatise of Electrochemistry*, B.E. Conway, J.O.M. Bockris, E. Yeager, S.U.M. Khan, and R.E. White, Editors. 1983, Plenum Press: New York. p. 173-239.

159. J.O.M. Bockris and S.U.M. Khan, *Surface Electrochemistry, A Molecular Level Approach*. 1993, New York: Plenum Press.

160. J.K. Nørskov, J. Rossmeisl, A. Logadottir, L. Lindqvist, J.R. Kitchin, T. Bligaard, and H. Jonsson, *Origin of the overpotential for oxygen reduction at a fuel-cell cathode*. Journal of Physical Chemistry B, 2004. 108(46): p. 17886-17892.

161. J.K. Norskov, T. Bligaard, A. Logadottir, S. Bahn, L.B. Hansen, M. Bollinger, H. Bengard, B. Hammer, Z. Sljivancanin, M. Mavrikakis, Y. Xu, S. Dahl, and C.J.H. Jacobsen, *Universality in Heterogenous Catalysis*. Journal of Catalysis, 2002. 209: p. 275-278.

162. M.L.B. Rao, A. Damjanovic, and J.O.M. Bockris, *Oxygen Adsorption Related to the Unpaired d-electrons in Transition Metals* Journal of Physical Chemistry, 1963. 67(11): p. 2508-2509.

163. B. Hammer and J.K. Nørskov, *Theoretical surface science and catalysis - calculations and concepts*. Advances in Catalysis, 2000. 45: p. 71-129.

164. M.R. Tarasevich, A. Sadkowski, and E. Yeager, *Oxygen Electrochemistry*, in *Comprhensive Treatise of Electrochemistry*, B.E. Conway, J.O.M. Bockris, E. Yeager, S.U.M. Khan, and R.E. White, Editors. 1983, Plenum Press: New York. p. 301-398.

165. A. Damjanovic and V. Brusic, *Electrode Kinetics of Oxygen Reduction on Oxide-Free Platinum Electrodes*. Electrochimica Acta, 1967. 12: p. 615-628.

166. A.B. Anderson and T.V. Albu, *Catalytic Effect of Platinum on Oxygen Reduction An Ab Initio Model Including Electrode Potential Dependence*. Journal of The Electrochemical Society, 2000. 147(11): p. 4229-4238.

167. A.B. Anderson and T.V. Albu, *Ab Initio Determination of Reversible Potentials and Activation Energies for Outer-Sphere Oxygen Reduction to Water and the Reverse Oxidation Reaction*. Journal of the American Chemical Society, 1999. 121(50): p. 11855-11863.

168. N.M. Markovic and P.N. Ross, *Surface science studies of model fuel cell electrocatalysts*. Surface Science Reports, 2002. 45(4-6): p. 121-229.

169. K.L. Hsueh, E.R. Gonzalez, and S. Srinivasan, *Electrolyte Effects on Oxygen Reduction Kinetics at Platinum - a Rotating-Ring Disk Electrode Analysis*. Electrochimica Acta, 1983. 28(5): p. 691-697.

170. M. Paucirova, D.M. Drazic, and A. Damjanovic, *The effect of surface coverage by adsorbed oxygen on the kinetics of oxygen reduction at oxide free platinum*. Electrochimica Acta, 1973. 18(12): p. 945-951.

171. D.B. Sepa, M.V. Vojnovic, and A. Damjanovic, *Reaction Intermediates as a Controlling Factor in the Kinetics and Mechanism of Oxygen Reduction at Platinum-Electrodes*. Electrochimica Acta, 1981. 26(6): p. 781-793.

172. N.A. Anastasijevic, V. Vesovic, and R.R. Adzic, *Determination of the Kinetic-Parameters of the Oxygen Reduction Reaction Using the Rotating-Ring-Disk Electrode .1. Theory*. Journal of Electroanalytical Chemistry, 1987. 229(1-2): p. 305-316.

173. N.A. Anastasijevic, V. Vesovic, and R.R. Adzic, *Determination of the Kinetic-Parameters of the Oxygen Reduction Reaction Using the Rotating-Ring-Disk*

Electrode .2. Applications. Journal of Electroanalytical Chemistry, 1987. 229(1-2): p. 317-325.

174. K.L. Hsueh, D.T. Chin, and S. Srinivasan, *Electrode-Kinetics of Oxygen Reduction - a Theoretical and Experimental-Analysis of the Rotating Ring-Disc Electrode Method.* Journal of Electroanalytical Chemistry, 1983. 153(1-2): p. 79-95.

175. A. Gamez, D. Richard, P. Gallezot, F. Gloaguen, R. Faure, and R. Durand, *Oxygen reduction on well-defined platinum nanoparticles inside recast ionomer.* Electrochimica Acta, 1996. 41(2): p. 307-314.

176. Y. Takasu, N. Ohashi, X.G. Zhang, Y. Murakami, H. Minagawa, S. Sato, and K. Yahikozawa, *Size Effects of platinum particles on the electroreduction of oxygen.* Electrochimica Acta, 1996. 41(16): p. 2595-2600.

177. P. Stonehart, *The Role of Electrocatalysis in Solid Polymer Electrolyte Fuel Cells*, in *Electrochemistry and Clean Energy*, J.A.G. Drake, Editor. 1994, The Royal Society of Chemistry: Cambridge.

178. O. Antoine, Y. Bultel, and R. Durand, *Oxygen reduction reaction kinetics and mechanism on platinum nanoparticles inside Nafion(R).* Journal of Electroanalytical Chemistry, 2001. 499(1): p. 85-94.

179. X. Li, D. Heryadi, and A.A. Gewirth, *Electroreduction activity of hydrogen peroxide on Pt and Au electrodes.* Langmuir, 2005. 21(20): p. 9251-9259.

180. N.M. Markovic, H.A. Gasteiger, B.N. Grgur, and P.N. Ross, *Oxygen reduction reaction on Pt(111): effects of bromide.* Journal of Electroanalytical Chemistry, 1999. 467(1-2): p. 157-163.

181. N. Markovic, H. Gasteiger, and P.N. Ross, *Kinetics of Oxygen Reduction on Pt(hkl) Electrodes: Implications for the Crystallite Size Effect with Supported Pt Electrocatalysts.* Journal of The Electrochemical Society, 1997. 144(5): p. 1591-1597.

182. N.M. Markovic, H.A. Gasteiger, and P.N. Ross, *Oxygen Reduction on Platinum Low-Index Single-Crystal Surfaces in Sulphuric Acid Solution: Rotating Ring-Pt(hkl) Disk Studies.* The Journal of Physical Chemistry 1995. 99(11): p. 3411-3415.

183. V. Komanicky, A. Menzel, and H. You, *Investigation of Oxygen Reduction Kinetics at (111)-(100) Nanofaceted Platinum Surfaces in Acidic Media*. Journal of Physical Chemistry B, 2005. 109(49): p. 23550-23557.

184. M.D. Macía, J.M. Campiña, and J.M. Feliu, *On the kinetics of oxygen reduction on platinum stepped surfaces in acidic media*. Journal of Electroanalytical Chemistry, 2004. 564: p. 141-150.

185. H. Yano, J. Inukai, H. Uchida, M. Watanabe, P.K. Babu, T. Kobayashi, J.H. Chung, E. Oldfield, and A. Wieckowski, *Particle-size effect of nanoscale platinum catalysts in oxygen reduction reaction: an electrochemical and ^{195}Pt EC-NMR study*. Physical Chemistry Chemical Physics, 2006. 8(42): p. 4932-4939.

186. M. Watanabe, H. Sei, and P. Stonehart, *The influence of platinum crystallite size on the electroreduction of oxygen*. Journal of Electroanalytical Chemistry, 1989. 261(2, Part 2): p. 375-387.

187. V. Stamenkovic, T.J. Schmidt, P.N. Ross, and N.M. Markovic, *Surface composition effects in electrocatalysis: Kinetics of oxygen reduction on well-defined Pt_3Ni and Pt_3Co alloy surfaces*. Journal of Physical Chemistry B, 2002. 106(46): p. 11970-11979.

188. U.A. Paulus, A. Wokaun, G.G. Scherer, T.J. Schmidt, V. Stamenkovic, N.M. Markovic, and P.N. Ross, *Oxygen reduction on high surface area Pt-based alloy catalysts in comparison to well defined smooth bulk alloy electrodes*. Electrochimica Acta, 2002. 47(22-23): p. 3787-3798.

189. M.D. Obradovic, B.N. Grugur, and L.M. Vracar, *Adsorption of oxygen species and their effect on oxygen reduction on Pt_3Co*. Journal of Electroanalytical Chemistry, 2003. 548: p. 69-78.

190. T. Toda, H. Igarashi, H. Uchida, and M. Watanabe, *Enhancement of the Electroreduciton of Oxygen on Pt Alloys with Fe, Ni and Co*. Journal of the Electrochemical Society, 1999. 146(10): p. 3750-3756.

191. N. Wakabayashi, M. Takeichi, H. Uchida, and M. Watanabe, *Temperature Dependence of Oxygen Reduction Activity at Pt-Fe, Pt-Co, and Pt-Ni Alloy Electrodes*. Journal of Physical Chemistry B, 2005. 109: p. 5836-5841.

192. B.S. Mun, M. Watanabe, M. Rossi, V. Stamenkovic, N.M. Markovic, and P.N. Ross, *A study of electronic structures of Pt_3M (M = Ti,V,Cr,Fe,Co,Ni)*

polycrystalline alloys with valence-band photoemission spectroscopy. The Journal of Chemical Physics, 2005. 123(20): p. 204717.

193. J.T. Hwang and J.S. Chung, *The Morphological and Surface-Properties and Their Relationship with Oxygen Reduction Activity for Platinum-Iron Electrocatalysts.* Electrochimica Acta, 1993. 38(18): p. 2715-2723.

194. U.A. Paulus, A. Wokaun, G.G. Scherer, T.J. Schmidt, V. Stamenkovic, V. Radmilovic, N.M. Markovic, and P.N. Ross, *Oxygen reduction on carbon-supported Pt-Ni and Pt-Co alloy catalysts.* Journal of Physical Chemistry B, 2002. 106(16): p. 4181-4191.

195. D. Thompsett, *Pt alloys as oxygen reduction catalysts,* in *Handbook of Fuel Cells - Fundamentals, Technology and Applications,* W. Vielstich, A. Lamm, and H.A. Gasteiger, Editors. 2003, John Wiley & Sons: Chichester. p. 467-480.

196. J. Luo, L. Wang, D. Mott, P.N. Njoki, N. Kariuiki, C.-J. Zhong, and T. He, *Ternary alloy nanoparticles with controllable sizes and conposition and electrocatalytic activity.* Journal of Materials Chemistry, 2006. 16: p. 1665-1673.

197. V.S. Murthi, R.C. Urian, and S. Mukerjee, *Oxygen Reduction Kinetics in Low and Medium Temperature Acid Environment: Correlation of Water Activation and Surface Properties in Supported Pt and Pt Alloy Electrocatalysts.* Journal of Physical Chemistry B, 2004. 108(30): p. 11011-11023.

198. V. Stamenkovic, B.S. Mun, K.J.J. Mayrhofer, P.N. Ross, N.M. Markovic, J. Rossmeisl, J. Greeley, and J.K. Norskøv, *Changing the activity of electrocatalysts for oxygen reduction by tuning the surface electronic structure.* Angewandte Chemie-International Edition, 2006. 45(18): p. 2897-2901.

199. Y. Xu, A.V. Ruban, and M. Mavrikakis, *Adsorption and Dissociation of O_2 on Pt-Co and Pt-Fe Alloys.* Journal of the American Chemical Society, 2004. 126(14): p. 4717-4725.

200. J.R. Kitchin, J.K. Nørskov, M.A. Barteau, and J.G. Chen, *Modification of the surface electronic and chemical properties of Pt(111) by subsurface 3 d transistion metals.* Journal of Chemical Physics, 2004. 120(21): p. 10240-10246.

201. Y. Wang and P.B. Balbuena, *Design of Oxygen Reduction Bimetallic Catalysts: Ab-Initio-Derived Thermodynamic Guidelines.* Journal of Physical Chemistry B, 2005. 109(40): p. 18902-18906.

202. A.B. Anderson, J. Roques, S. Mukerjee, V.S. Murthi, N.M. Markovic, and V. Stamenkovic, *Activation Energies for Oxygen Reduction on Platinum Alloys: Theory and Experiment*. Journal of Physical Chemistry B, 2005. 109(3): p. 1198-1203.

203. X. Li and A.A. Gewirth, *Peroxide Electroreduction on Bi-Modified Au Surfaces: Vibrational Spectroscopy and Density Functional Calculations*. Journal of the American Chemical Society, 2003. 125(23): p. 7086-7099.

204. X. Li and A.A. Gewirth, *Oxygen Electroreduction through a Superoxide Intermediate on Bi-Modified Au Surfaces*. Journal of the American Chemical Society, 2005. 127(14): p. 5252-5260.

205. M.A. Genshaw, A. Damjanovic, and J.O.M. Bockris, *Hydrogen peroxide formation in oxygen reduction at gold electrodes : I. Acid solution*. Journal of Electroanalytical Chemistry, 1967. 15: p. 163-172.

206. M.A. Genshaw, A. Damjanovic, and J.O.M. Bockris, *Hydrogen peroxide formation in oxygen reduction at gold electrodes : II. Alkaline solution*. Journal of Electroanalytical Chemistry, 1967. 15: p. 173-180.

207. R.R. Adzic, N.M. Markovic, and V.B. Vesovic, *Structural effects in electrocatalysis: Oxygen reduction on the Au (100) single crystal electrode*. Journal of Electroanalytical Chemistry, 1984. 165(1-2): p. 105-120.

208. N.M. Markovic, R.R. Adzic, and V.B. Vesovic, *Structural effects in electrocatalysis: Oxygen reduction on the gold single crystal electrodes with (110) and (111) orientations*. Journal of Electroanalytical Chemistry, 1984. 165(1-2): p. 121-133.

209. A. Prieto, J. Hernández, E. Herrero, and J.M. Feliu, *The role of anions in oxygen reduction in neutral and basic media on gold single-crystal electrodes*. Journal of Solid State Electrochemistry, 2003. 7(9): p. 599-606.

210. M. Alvarez-Rizatti and K. Jüttner, *Electrocatalysis of Oxygen Reduction by UPD of Lead on Gold Single-Crystal Surfaces*. Journal of Electroanalytical Chemistry, 1983. 144: p. 351-363.

211. T.J. Schmidt, V. Stamenkovic, M. Arenz, N.M. Markovic, and P.N. Ross, *Oxygen electrocatalysis in alkaline electrolyte: Pt(hkl), Au(hkl) and the effect of Pd-modification*. Electrochimica Acta, 2002. 47(22-23): p. 3765-3776.

212. R.R. Adzic and N.M. Markovic, *Structural effects in electrocatalysis: Oxygen and hydrogen peroxide reduction on single crystal gold electrodes and the effects of lead ad-atoms*. Journal of Electroanalytical Chemistry, 1982. 138(2): p. 443-447.

213. N.M. Markovic, I.M. Tidswell, and P.N. Ross, *Oxygen and hydrogen peroxide reduction on the gold(100) surface in alkaline electrolyte: the roles of surface structure and hydroxide adsorption* Langmuir, 1994. 10(1): p. 1-4.

214. S. Strbac and R.R. Adzic, *The influence of pH on reaction pathways for O_2 reduction on the Au(100) face*. Electrochimica Acta, 1996. 41(18): p. 2903-2908.

215. S. Strbac and R.R. Adzic, *The influence of OH$^-$ chemisorption on the catalytic properties of gold single crystal surfaces for oxygen reduction in alkaline solutions*. Journal of Electroanalytical Chemistry, 1996. 403(1-2): p. 169-181.

216. B.B. Blizanac, C.A. Lucas, M.E. Gallagher, M. Arenz, P.N. Ross, and N.M. Markovic, *Anion adsorption, CO oxidation, and oxygen reduction reaction on a Au(100) surface: The pH effect*. Journal of Physical Chemistry B, 2004. 108(2): p. 625-634.

217. G. Kokkinidis and D. Sazou, *Electrocatalysis of O_2 Reduction on Au Surfaces Modified by Underpotential Pb and Tl Adsorbates in Acetonitrile*. Journal of Electroanalytical Chemistry, 1986. 199: p. 165-176.

218. M.H. Shao and R.R. Adzic, *Spectroscopic Identification of the Reaction Intermediates in Oxygen Reduction on Gold in Alkaline Solutions*. Journal of Physical Chemistry B, 2005. 109(35): p. 16563-16566.

219. M.S. El-Deab and T. Ohsaka, *An extraordinary electrocatalytic reduction of oxygen on gold nanoparticles-electrodeposited gold electrodes*. Electrochemistry Communications, 2002. 4: p. 288-292.

220. M.S. El-Deab and T. Ohsaka, *Electrocatalysis by nanoparticles: oxygen reduction on gold nanoparticles-electrodeposited platinum electrodes*. Journal of Electroanalytical Chemistry, 2003. 553: p. 107-115.

221. M.S. El-Deab, T. Okajima, and T. Ohsaka, *Electrochemical Reduction of Oxygen on Gold Nanoparticle-Electrodeposited Glassy Carbon Electrodes*. Journal of the Electrochemical Society, 2003. 150(7): p. A851-A857.

222. M. El-Deab and T. Ohsaka, *Hydrodynamic voltammetric studies of the oxygen reduction at gold nanoparticles-electrodeposited gold.* Electrochimica Acta, 2002. 47: p. 4255-4261.

223. F. Gao, M. El-Deab, T. Okajima, and T. Ohsaka, *Electrochemical Preparation of a Au Crystal with Peculiar Morphology and Unique Growth Orientation and Its Catalysis for Oxygen Reduction.* Journal of the Electrochemical Society, 2005. 152(6): p. A1226-A1232.

224. M. El-Deab, T. Sotomura, and T. Ohsaka, *Size Crystallographic Orientation of Gold Nanoparticles Electrodeposited on GC Electrodes.* Journal of the Electrochemical Society, 2006. 152(1): p. C1-C6.

225. M. El-Deab, T. Sotomura, and T. Ohsaka, *Oxygen reduction at electrochemically deposited crystallographically oriented Au(1 0 0)-like gold nanoparticles.* Electrochemistry Communications, 2005. 7: p. 29-34.

226. J. Hernández, J. Solla-Gullón, and E. Herrero, *Gold nanoparticles synthesized in a water-in-oil microemulsion: electrochemical characterization and effect of the surface structure on the oxygen reduction reaction.* Journal of Electroanalytical Chemistry, 2004. 574: p. 185-196.

227. J. Hernández, J. Solla-Gullón, E. Herrero, A. Aldaz, and J.M. Feliu, *Characteriszation of the Surface Structure of Gold Nanoparticles and Nanorods Using Structure Sensitive Reactions.* Journal of Physical Chemistry B, 2005. 109(26): p. 12651-12654.

228. I. Yagi, T. Ishida, and K. Uosaki, *Electrocatalytic reduction of oxygen to water at Au nanoclusters vacuum-evaporated on boron-doped diamond in acidic solution.* Electrochemistry Communications, 2004. 6: p. 773-779.

229. Y. Zhang, S. Asahina, S. Yoshihara, and T. Shirakashi, *Oxygen reduction on Au nanoparticle deposited boron-doped diamond films.* Electrochimica Acta, 2003. 48: p. 741-747.

230. Y. Zhang, V. Suryanarayanan, I. Nakazawa, S. Yoshihara, and T. Shirakashi, *Electrochemical behaviour of Au nanoparticle deposited on as-grown and O-terminated diamond electrodes for oxygen reduction in alkaline solution.* Electrochimica Acta, 2004. 2004: p. 5235-5240.

231. N. Alexeyeva, T. Laaksonen, K. Kontturi, F. Mirkhalaf, D.J. Schiffrin, and K. Tammeveski, *Oxygen reduction on gold nanoparticle/multi-walled carbon*

nanotubes modified glassy carbon electrodes in acid solution. Electrochemistry Communications, 2006. 8(9): p. 1475-1480.

232. A. Sarapuu, K. Tammeveski, T.T. Tenno, V. Sammelselg, K. Kontturi, and D.J. Schiffrin, *Electrochemical reduction of oxygen on thin-film Au electrodes in acid solution.* Electrochemistry Communications, 2001. 3: p. 446-450.

233. M.M. Maye, N.N. Kariuiki, J. Luo, L. Han, P.N. Njoki, L. Wang, Y. Lin, R. Naslund, and C.-J. Zhong, *Electrocatalytic Reduction of Oxygen: Gold and Gold-Platinum Nanoparticle Catalysts Prepared by Two-Phase Protocol.* Gold Bulletin, 2004. 37(3-4): p. 217-223.

234. C.R. Raj, A.I. Abdelrahman, and T. Ohsaka, *Gold nanoparticle-assisted electroreduction of oxygen* Electrochemistry Communications, 2005. 7: p. 888-893.

235. W.S. Baker, J.J. Pietron, M.E. Teliska, P.J. Bouwman, D.E. Ramaker, and K.E. Swider-Lyons, *Enhanced Oxygen Reduction Activity in Acid by Tin-Oxide Supported Au Nanoparticle Catalysts.* Journal of the Electrochemical Society, 2006. 153(9): p. A1702-A1707.

236. M. El-Deab, T. Sotomura, and T. Ohsaka, *Size Crystallographic Orientation of Gold Nanoparticles Electrodeposited on GC Electrodes.* Journal of the Electrochemical Society, 2005. 152(1): p. C1-C6.

237. S. Trasatti, *Electrodes of conductive metallic oxides.* 1980, Amsterdam: Elsevier.

238. E.J.M. O'Sullivan and E.J. Calvo, *Reactions at metal oxide electrodes*, in *Electrode kinetics: Reactions*, R.G. Compton, Editor. 1987: Amsterdam.

239. S. Trasatti, *Transition Metal Oxides: Versatile Materials for Electrocatalysis*, in *Electrochemistry of Novel Materials*, J. Lipkowski and P.N. Ross, Editors. 1994, VCH: Weinheim.

240. B. Parkinson, F. Decker, J.F. Julião, M. Abramovich, and H.C. Chagas, *The reduction of molecular oxygen at single crystal rutile electrodes.* Electrochimica Acta, 1980. 25(5): p. 521-525.

241. M. Van Brussel, G. Kokkinidis, I. Vandendael, and C. Buess-Herman, *High performance gold-supported platinum electrocatalyst for oxygen reduction.* Electrochemistry Communications, 2002. 4: p. 808-813.

242. M. Van Brussel, G. Kokkinidis, A. Hubin, and C. Buess-Herman, *Oxygen reduction at platinum modified gold electrodes*. Electrochimica Acta, 2003. 48: p. 3909-3919.

243. Q. Li, R. He, J.-A. Gao, J.O. Jensen, and N.J. Bjerrum, *The CO Poisoning Effect in PEMFCs Operational at Temperatures up to 200 °C*. Journal of the Electrochemical Society, 2003. 150(12): p. A 1599 - A 1605.

244. G. Blyholder, *Molecular Orbital View of Chemisorbed Carbon Monoxide*. Journal of Physical Chemistry, 1964. 68(10): p. 2772-2778.

245. Z. Galus, *Carbon, Silicon, Germanium, Tin, and Lead*, in *Standard Potentials in Aqueous Solution*, A.J. Bard, R. Parsons, and J. Jordan, Editors. 1985, Marcel Dekker, Inc.: New York.

246. P.W. Atkins, *Physical Chemistry*. 6th ed. 1998, Oxford: Oxford University Press.

247. S. Gilman, *The mechanism of Electrochemical Oxidation of Carbon Monoxide and Methanol on Platinum. II. The "Reactant-Pair" Mechanism for Electrochemical Oxidation of Carbon Monoxide and Methanol*. Journal of Physical Chemistry 1964. 68(1): p. 70-80.

248. C. McCallum and D. Pletcher, *An investigation of the mechanism of the oxidation of carbon monoxide adsorbed onto a smooth Pt electrode in aqueous acid*. Journal of Electroanalytical Chemistry, 1976. 70(3): p. 277-290.

249. M. Bergelin, J.M. Feliu, and M. Wasberg, *Study of carbon monoxide adsorption and oxidation on Pt(111) by using an electrochemical impinging jet cell*. Electrochimica Acta, 1998. 44(6-7): p. 1069-1075.

250. M. Bergelin, E. Herrero, J.M. Feliu, and M. Wasberg, *Oxidation of CO adlayers on Pt(111) at low potentials: an impinging jet study in H_2SO_4 electrolyte with mathematical modeling of the current transients*. Journal of Electroanalytical Chemistry, 1999. 467(1-2): p. 74-84.

251. E. Herrero, J.M. Feliu, S. Blais, Z. Radovic-Hrapovic, and G. Jerkiewicz, *Temperature Dependence of CO Chemisorption and Its Oxidative Desorption on the Pt(111) Electrode*. Langmuir, 2000. 16(11): p. 4779-4783.

252. M. Watanabe, Y. Zhu, and H. Uchida, *Oxidation of CO on a Pt-Fe Alloy Electrode Studied by Surface Enhanced Infrared Reflection-Absorption Spectroscopy*. J. Phys. Chem. B, 2000. 104(8): p. 1762-1768.

253. Y. Zhu, H. Uchida, and M. Watanabe, *Oxidation of Carbon Monoxide at a Platinum Film Electrode Studied by Fourier Transform Infrared Spectroscopy with Attenuated Total Reflection Technique*. Langmuir, 1999. 15(25): p. 8757-8764.

254. E. Santos, E.P.M. Leiva, and W. Vielstich, *CO adsorbate on Pt(111) single crystal surfaces*. Electrochimica Acta, 1991. 36(3-4): p. 555-561.

255. A.V. Petukhov, W. Akemann, K.A. Friedrich, and U. Stimming, *Kinetics of electrooxidation of a CO monolayer at the platinum/electrolyte interface*. Surface Science, 1998. 402-404: p. 182-186.

256. T.E. Shubina, C. Hartnig, and M.T.M. Koper, *Density functional theory study of the oxidation of CO by OH on Au(110) and Pt(111) surfaces*. Physical Chemistry Chemical Physics, 2004. 6(16): p. 4215-4221.

257. A.B. Anderson and E. Grantscharova, *Potential Dependence of CO_{ads} Oxidation by OH_{ads} on Platinum Anodes. Molecular Orbital Theory* Journal of Physical Chemistry 1995. 99(22): p. 9143-9148.

258. C. Korzeniewski and D. Kardash, *Use of a Dynamic Monte Carlo Simulation in the Study of Nucleation-and-Growth Models for CO Electrochemical Oxidation*. Journal of Physical Chemistry B, 2001. 105(37): p. 8663-8671.

259. N.P. Lebedeva, M.T.M. Koper, J.M. Feliu, and R.A. van Santen, *Mechanism and kinetics of the electrochemical CO adlayer oxidation on Pt(111)*. Journal of Electroanalytical Chemistry, 2002. 524-525: p. 242-251.

260. N.P. Lebedeva, M.T.M. Koper, J.M. Feliu, and R.A. van Santen, *Role of Crystalline Defects in Electrocatalysis: Mechanism and Kinetics of CO Adlayer Oxidation on Stepped Platinum Electrodes*. Journal of Physical Chemistry B, 2002. 106(50): p. 12938-12947.

261. N.P. Lebedeva, A. Rodes, J.M. Feliu, M.T.M. Koper, and R.A. van Santen, *Role of crystalline defects in electrocatalysis: CO adsorption and oxidation on stepped platinum electrodes as studied by in situ infrared spectroscopy*. Journal of Physical Chemistry B, 2002. 106(38): p. 9863-9872.

262. M.T.M. Koper, N.P. Lebedeva, and C.G.M. Hermse, *Dynamics of CO at the solid/liquid interface studied by modeling and simulation of CO electro-oxidation on Pt and PtRu electrodes*. Faraday Discussions, 2002. 121: p. 301-311.

263. B.E. Hayden, M.E. Rendall, and O. South, *Electro-oxidation of carbon monoxide on well-ordered pt(111)/Sn surface alloys*. Journal of the American Chemical Society, 2003. 125(25): p. 7738-7742.

264. H.A. Gasteiger, N.M. Markovic, and P.N. Ross, *Electrooxidation of CO and H_2/CO Mixtures on a Well-Characterized Pt_3Sn Electrode Surface*. Journal of Physical Chemistry, 1995. 99(22): p. 8945-8949.

265. S. Motoo and M. Watanabe, *Electrocatalysis by Sn and Ge ad-atoms*. Journal of Electroanalytical Chemistry, 1976. 69: p. 429-431.

266. J.C. Davies, B.E. Hayden, and D.J. Pegg, *The electrooxidation of carbon monoxide on ruthenium modified Pt(110)*. Electrochimica Acta, 1998. 44(6-7): p. 1181-1190.

267. J.C. Davies, B.E. Hayden, and D.J. Pegg, *The modification of Pt(110) by ruthenium: CO adsorption and electro-oxidation*. Surface Science, 2000. 467(1-3): p. 118-130.

268. J.C. Davies, B.E. Hayden, D.J. Pegg, and M.E. Rendall, *The electro-oxidation of carbon monoxide on ruthenium modified Pt(111)*. Surf. Sci., 2002. 496(1-2): p. 110-120.

269. T.J. Schmidt, M. Noeske, H.A. Gasteiger, R.J. Behm, P. Britz, W. Brijoux, and H. Bonnemann, *Electrocatalytic activity of PtRu alloy colloids for CO and CO/H_2 electrooxidation: Stripping voltammetry and rotating disk measurements*. Langmuir, 1997. 13(10): p. 2591-2595.

270. G.-Q. Lu, P. Waszczuk, and A. Wieckowski, *Oxidation of CO adsorbed from CO saturated solutions on the Pt(111)/Ru electrode*. Journal of Electroanalytical Chemistry, 2002. 532: p. 49-55.

271. J. Jiang and A. Kucernak, *Electrooxidation of small organic molecules on mesoporous precious metal catalysts: II: CO and methanol on platinum-ruthenium alloy*. Journal of Electroanalytical Chemistry, 2003. 543(2): p. 187-199.

272. K.A. Friedrich, K.P. Geyzers, U. Linke, U. Stimming, and J. Stumper, *CO adsorption and oxidation on a Pt(111) electrode modified by ruthenium deposition: an IR spectroscopic study*. Journal of Electroanalytical Chemistry, 1996. 402(1-2): p. 123-128.

273. B. Hammer, Y. Morikawa, and J.K. Nørskov, *CO Chemisorption at Metal Surfaces and Overlayers*. Physical Review Letters, 1996. 76(12): p. 2141.

274. B. Hammer and J.K. Nørskov, *Electronic factors determining the reactivity of metal surfaces*. Surface Science, 1995. 343(3): p. 211-220.

275. M. Tsuda and H. Kasai, *Ab initio study of alloying and straining effects on CO interaction with Pt*. Physical Review B (Condensed Matter and Materials Physics), 2006. 73(15): p. 155405.

276. T.E. Shubina and M.T.M. Koper, *Quantum-chemical calculations of CO and OH interacting with bimetallic surfaces*. Electrochimica Acta, 2002. 47(22-23): p. 3621-3628.

277. M. Watanabe and S. Motoo, *Electrocatalysis by ad-atoms. Part 3. Enhancement of the oxidation of carbon monoxide on platinum by ruthenium ad-atoms*. Journal of Electroanalytical Chemistry 1975. 60: p. 275 - 283.

278. M. Watanabe and S. Motoo, *Electrocatalysis by ad-atoms. Part 2. Enhancement of the oxidation of methanol on platinum by ruthenium ad-atoms*. Journal of Electroanalytical Chemistry, 1975. 60: p. 267.

279. F. Maillard, S. Schreier, M. Hanzlik, E.R. Savinova, S. Weinkauf, and U. Stimming, *Influence of particle agglomeration on the catalytic activity of carbon-supported Pt nanoparticles in CO monolayer oxidation*. Physical Chemistry Chemical Physics, 2005. 7(2): p. 385-393.

280. F. Maillard, E.R. Savinova, P.A. Simonov, V.I. Zaikovskii, and U. Stimming, *Infrared spectroscopic study of CO adsorption and electro-oxidation on carbon-supported Pt nanoparticles: Interparticle versus intraparticle heterogeneity*. Journal of Physical Chemistry B, 2004. 108(46): p. 17893-17904.

281. F. Maillard, M. Eikerling, O.V. Cherstiouk, S. Schreier, E. Savinova, and U. Stimming, *Size effects on reactivity of Pt nanoparticles in CO monolayer oxidation: The role of surface mobility*. Faraday Discussions, 2004. 125: p. 357-377.

282. K.J.J. Mayrhofer, M. Arenz, B.B. Blizanac, V. Stamenkovic, P.N. Ross, and N.M. Markovic, *CO surface electrochemistry on Pt-nanoparticles: A selective review*. Electrochimica Acta, 2005. 50(25-26): p. 5144-5154.

283. M. Arenz, K.J.J. Mayrhofer, V. Stamenkovic, B.B. Blizanac, T. Tomoyuki, P.N. Ross, and N.M. Markovic, *The effect of the particle size on the kinetics of CO*

electrooxidation on high surface area Pt catalysts. Journal of the American Chemical Society, 2005. 127(18): p. 6819-6829.

284. K.J.J. Mayrhofer, B.B. Blizanac, M. Arenz, V.R. Stamenkovic, P.N. Ross, and N.M. Markovic, *The impact of geometric and surface electronic properties of Pt-catalysts on the particle size effect in electocatalysis.* Journal of Physical Chemistry B, 2005. 109(30): p. 14433-14440.

285. F. Maillard, E.R. Savinova, and U. Stimming, *CO monolayer oxidation on Pt nanoparticles: Further insights into the particle size effects.* Journal of Electroanalytical Chemistry. In Press, Corrected Proof: p.

286. S.G. Sun, W.B. Cai, L.J. Wan, and M. Osawa, *Infrared Absorption Enhancement for CO Adsorbed on Au Films in Perchloric Acid Solutions and Effects of Surface Structure Studied by Cyclic Voltammetry, Scanning Tunneling Microscopy, and Surface-Enhanced IR Spectroscopy.* Journal of Physical Chemistry B, 1999. 103(13): p. 2460-2466.

287. J.A. Caram and C. Gutierrez, *Study by UV-visible potential-modulated reflectance spectroscopy and cyclic voltammetry of the electroadsorption and electro-oxidation of CO on Au in a.* Journal of Electroanalytical Chemistry, 1991. 314(1-2): p. 259-278.

288. S.C. Chang, A. Hamelin, and M.J. Weaver, *Dependence of the Electrooxidation Rates of Carbon-Monoxide at Gold on the Surface Crystallographic Orientation - a Combined Kinetic-Surface Infrared Spectroscopic Study.* Journal of Physical Chemistry, 1991. 95(14): p. 5560-5567.

289. S.C. Chang, A. Hamelin, and M.J. Weaver, *Reactive and Inhibiting Adsorbates for the Catalytic Electrooxidation of Carbon-Monoxide on Gold (210) as Characterized by Surface Infrared-Spectroscopy.* Surface Science, 1990. 239(3): p. L543-L547.

290. G.J. Edens, A. Hamelin, and M.J. Weaver, *Mechanism of carbon monoxide electrooxidation on monocrystalline gold surfaces: Identification of a hydroxycarbonyl intermediate.* Journal of Physical Chemistry, 1996. 100(6): p. 2322-2329.

291. A. Cuesta, N. Lopez, and C. Gutierrez, *Electrolyte electroreflectance study of carbon monoxide adsorption on polycrystalline silver and gold electrodes.* Electrochimica Acta, 2003. 48(20-22): p. 2949-2956.

292. G.J. Edens, X. Gao, M.J. Weaver, N.M. Markovic, and P.N. Ross, *Influence of adsorbed hydroxyl and carbon monoxide on potential-induced reconstruction of Au(100) as examined by scanning tunneling microscopy*. Surface Science, 1994. 302(1-2): p. L275-L282.

293. T.F. Jaramillo, S.H. Baeck, B.R. Cuenya, and E.W. McFarland, *Catalytic Activity of Supported Au Nanoparticles Deposited from Block Copolymer Micelles*. Journal of the American Chemical Society, 2003. 125(24): p. 7148-7149.

294. B.R. Cuenya, S.H. Baeck, T.F. Jaramillo, and E.W. McFarland, *Size- and Support-Dependent Electronic and Catalytic Properties of Au^0/Au^{3+} Nanoparticles Synthesized from Block Copolymer Micelles*. Journal of the American Chemical Society, 2003. 125(42): p. 12928-12934.

295. S. Kumar and S. Zou, *Electrooxidation of Carbon Monoxide on Gold Nanoparticle Ensemble Electrodes: Effects of Particle Coverage*. Journal of Physical Chemistry B, 2005. 109(33): p. 15707-15713.

296. M. Watanabe, *New CO-tolerant catalyst concepts*, in *Handbook of Fuel Cells*, W. Vielstich, H.A. Gasteiger, and A. Lamm, Editors. 2003, John Wiley & Sons: Chichester.

297. T. Iwasita, *Methanol and CO electrooxidation*, in *Handbook of Fuel Cells*, W. Vielstich, H.A. Gasteiger, and A. Lamm, Editors. 2003, John Wiley & Sons: Chichester.

298. G. Hoogers, *The Fueling Problem: Fuel Cell Systems*, in *Fuel Cell Technology Handbook*, G. Hoogers, Editor. 2003, CRC Press: Boca Raton.

299. D. Cameron, R. Holliday, and D. Thompson, *Gold's future role in fuel cell systems*. Journal of Power Sources, 2003. 118: p. 298-303.

300. G. Hoogers, *Fuel Cell Components and Their Impact on Performance*, in *Fuel Cell Technology Handbook*, G. Hoogers, Editor. 2003, CRC Press: Boca Raton.

301. D. Thompsett, *Catalysts for the Proton Exchange Membrane Fuel Cell*, in *Fuel Cell Technology Handbook*, G. Hoogers, Editor. 2003, CRC Press: Boca Raton.

302. V. Stamenkovic, B.N. Grgur, P.N. Ross, and N.M. Markovic, *Oxygen reduction reaction on Pt and Pt-bimetallic electrodes covered by CO - Mechanism of the air bleed effect with reformate*. Journal of the Electrochemical Society, 2005. 152(2): p. A277-A282.

303. K.Y. Chen, P.K. Shen, and A.C.C. Tseung, *Anodic oxidation of impure H2 on teflon bonded Pt-Ru/WO₃/C electrodes*. Journal of the Electrochemical Society, 1995. 142: p. L185.

304. F. Maillard, E. Peyrelade, Y. Soldo-Olivier, M. Chatenet, E. Chainet, and R. Faure, *Is carbon-supported Pt-WO$_x$ composite a CO-tolerant material?* Electrochimica Acta, 2007. 52(5): p. 1958-1967.

305. Y.-H. Chu, S.-W. Ahn, D.-Y. Kim, H.-J. Kim, Y.-G. Shul, and H. Han, *Combinatorial investigation of Pt-Ru-M as anode electrocatalyst for direct methanol fuel cell*. Catalysis Today, 2006. 111(3-4): p. 176-181.

306. P.S. Hauge and F.H. Dill, *Rotating-Compensator Fourier Ellipsometer*. Optics Communications, 1975. 14(4): p. 431-437.

307. A. Uhlir, *The Potentials of Infinite Systems of Sources and Numerical Solutions of Problems in Semiconductor Engineering*. The Bell System Technical Journal, 1955. 34: p. 105-128.

308. D.K. Schroder, *Semiconductor Material and Device Characterization*. John Wiley & Sons, 1990. p.

309. F.M. Smits, *Measurement of Sheet Resistivities with the Four-Point Probe*. The Bell System Technical Journal, 1958. 38: p. 711-718.

310. H. Wormeester, E. Stefan Kooij, A. Mewe, S. Rekveld, and B. Poelsema, *Ellipsometric characterisation of heterogeneous 2D layers*. Thin Solid Films, 2004. 455-456: p. 323-334.

311. A. Bendavid, P.J. Martin, and L. Wieczorek, *Morphology and optical properties of gold thin films prepared by filtered arc deposition*. Thin Solid Films, 1999. 354(1-2): p. 169-175.

312. K. Mümmler and P. Wissmann, *Ellipsometrical studies on the Au/Si(111) system*. Thin Solid Films, 1998. 317(1-2): p. 193-197.

313. F. Mirkhalaf and D.J. Schiffrin, *Metal-ion sensing by surface plasmon resonance on film electrodes*. Journal of Electroanalytical Chemistry, 2000. 484(2): p. 182-188.

314. D. Krause, C.W. Teplin, and C.T. Rogers, *Optical surface second harmonic measurements of isotropic thin-film metals: Gold, silver, copper, aluminum, and tantalum*. Journal of Applied Physics, 2004. 96(7): p. 3626-3634.

315. A.J. Bard and L.R. Faulkner, *Electrochemical methods: fundamentals and applications*. 2 ed. John Wiley & Sons. 2001.

316. E. Yagi, R.R. Hasiguti, and M. Aono, *Electronic conduction above 4 K of slightly reduced oxygen- deficient rutile TiO_{2-x}*. Physical Review B, 1996. 54(11): p. 7945-7956.

317. R.C. Weast, *Handbook of Chemistry and Physics*. C R C Press, 1974. p.

318. M. Flueli and J.P. Borel, *Surface energy anisotropy measurements on a small cuboctahedron of gold observed by high resolution electron microscopy (HREM)*. Journal of Crystal Growth, 1988. 91(1-2): p. 67-70.

319. J.A. Ascencio, C. Gutierrez-Wing, M.E. Espinosa, M. Marin, S. Tehuacanero, C. Zorrilla, and M.J. Yacamán, *Structure determination of small particles by HREM imaging: theory and experiment*. Surface Science, 1998. 396(1-3): p. 349-368.

320. A.I. Kirkland, D.A. Jefferson, D. Tang, and P.P. Edwards, *High-resolution image simulations of small particles*. Proceedings of the Royal Society of London. Series A, Mathematical and Physical Sciences, 1991. 434(1891): p. 279-296.

321. M. Mavrikakis, P. Stoltze, and J.K. Nørskov, *Making gold less noble*. Catalysis Letters, 2000. 64(2-4): p. 101-106.

322. E.C.H. Sykes, F.J. Williams, M.S. Tikhov, and R.M. Lambert, *Nucleation, growth, sintering, mobility, and adsorption properties of small gold particles on polycrystalline titania*. Journal of Physical Chemistry B, 2002. 106(21): p. 5390-5394.

323. W.T. Wallace, B.K. Min, and D.W. Goodman, *The stabilization of supported gold clusters by surface defects*. Journal of Molecular Catalysis A: Chemical, 2005. 228(1-2): p. 3-10.

324. J. Vesenka, S. Manne, R. Giberson, T. Marsh, and E. Henderson, *Colloidal gold particles as an incompressible atomic force microscope imaging standard for assessing the compressibility of biomolecules*. Biophysical Journal, 1993. 65: p. 992-997.

325. D. Briggs and M. Seah, *Practical Surface Analysis by Auger and X-ray Photoelectron Spectroscopy*. 1983, Chichester: John Wiley & Sons Ltd.

326. A. Howard, D.N.S. Clark, C.E.J. Mitchell, R.G. Egdell, and V.R. Dhanak, *Initial and final state effects in photoemission from Au nanoclusters on TiO_2(1 1 0)*. Surface Science, 2002. 518(3): p. 210-224.

327. W.J. James and J.W. Johnson, *Titanium, Zirconium and Hafnium*, in *Standard Potentials in Aqueous Solution*, A.J. Bard, R. Parsons, and J. Jordan, Editors. 1985, Marcel Dekker, Inc.: New York.

328. S.V. Mentus, *Oxygen reduction on anodically formed titanium dioxide*. Electrochimica Acta, 2004. 50(1): p. 27-32.

329. B.E. Hayden, D.V. Malevich, and D. Pletcher, *Electrode coatings from sprayed titanium dioxide nanoparticles - behaviour in NaOH solutions*. Electrochemistry Communications, 2001. 3(8): p. 390-394.

330. R.N. Noufi, P.A. Kohl, S.N. Frank, and A.J. Bard, *Semiconductor Electrodes XIV. Electrochemistry and Electroluminescence at n-Type TiO_2 in Aqueous Solutions*. Journal of the Electrochemical Society, 1978. 125(2): p. 246-252.

331. K.E. Heusler and W.J. Lorenz, *Iron, Ruthenium, and Osmium*, in *Standard Potentials in Aqueous Solution*, A.J. Bard, R. Parsons, and J. Jordan, Editors. 1985, Marcel Dekker, Inc.: New York.

332. C. Beriet, *Microelectrode studies in low ionic strength media*, in *School of Chemistry*. 1993, University of Southampton: Southampton. p. 33.

333. H. Angerstein-Kozlowska, B.E. Conway, K. Tellefsen, and B. Barnett, *Stochastically-gated surface processes involving anions in oxidation of Au: time-resolution of processes down to 0.25% coverages and 50 μs time-scales*. Electrochimica Acta, 1989. 34(8): p. 1045-1056.

334. R. Woods, *Chemisorption at electrodes: Hydrogen and oxygen on noble metals and their alloys*, in *Electroanalytical Chemistry* A.J. Bard, Editor. 1976, Marcel Dekker Inc.: New York. p. 119-125.

335. G. Tremiliosi-Filho, L.H. Dall'Antonia, and G. Jerkiewicz, *Growth of oxides on gold electrodes under well-defined potential, time and temperature conditions*. Journal of Electroanalytical Chemsitry, 2005. 578: p. 1-8.

336. D. Dickertmann, J.W. Schultze, and K.J. Vetter, *Electrochemical formation and reduction of monomolecular oxide layers on (111) and (100) planes of gold single crystals*. Journal of Electroanalytical Chemistry, 1974. 55(3): p. 429-443.

337. L.J. Williams, *Investigation of reduced titania as a support for fuel cell electrocatalysts*, in *Transfer report*. September 2005, University of Southampton: Southampton.

338. Z. Yang and R. Wu, *Origin of positive core-level shifts in Au clusters on oxides.* Physical Review B (Condensed Matter and Materials Physics), 2003. 67(8): p. 081403.

339. L. Fu, N.Q. Wu, J.H. Yang, F. Qu, D.L. Johnson, M.C. Kung, H.H. Kung, and V.P. Dravid, *Direct evidence of oxidized gold on supported gold catalysts.* Journal of Physical Chemistry B Letters, 2005. 109(9): p. 3704-3706.

340. N. Wakabayashi, M. Takeichi, M. Itagaki, H. Uchida, and M. Watanabe, *Temperature-dependence of oxygen reduction activity at a platinum electrode in an acidic electrolyte solution investigated with a channel flow double electrode.* Journal of Electroanalytical Chemistry, 2005. 574(2): p. 339-346.

341. *GRC Handbook of Chemistry and Physics.* 75 ed, ed. D.R. Lide. 1994, Boca Raton: CRC Press.

342. I.M. Maruyama J, Ogumi Z, *Rotating ring-disk electrode study on the cathodic oxygen reduction at Nafion (R)-coated gold electrodes.* Journal of Electroanalytical Chemistry, 1998. 458(1-2): p. 175-182.

343. M. Avramov-Ivic, S. Strbac, and V. Mitrovic, *The electrocatalytic properties of the oxides of noble metals in the electrooxidation of methanol and formic acid.* Electrochimica Acta, 2001. 46(20-21): p. 3175-3180.

344. J.K. Nørskov, T. Bligaard, A. Logadottir, S. Bahn, L.B. Hansen, M. Bollinger, H. Bengard, B. Hammer, Z. Sljivancanin, M. Mavrikakis, Y. Xu, S. Dahl, and C.J.H. Jacobsen, *Universality in Heterogenous Catalysis.* Journal of Catalysis, 2002. 209: p. 275-278.

345. D.C. Meier and D.W. Goodman, *The Influence of Metal Cluster Size on Adsorption Energies: CO Adsorbed on Au Clusters Supported on TiO₂.* Journal of the American Chemical Society, 2004. 126(6): p. 1892-1899.

346. V.A. Bondzie, S.C. Parker, and C.T. Campbell, *The kinetics of CO oxidation by adsorbed oxygen on well-defined gold particles on TiO₂(110).* Catalysis Letters, 1999. 63(3-4): p. 143-151.

347. C. Lemire, R. Meyer, S. Shaikhutdinov, and H.J. Freund, *Do quantum size effects control CO adsorption on gold nanoparticles?* Angewandte Chemie-International Edition, 2004. 43(1): p. 118-121.

348. M.S. Chen and D.W. Goodman, *The Structure of Catalytically Active Gold on Titania.* Science, 2004. 306: p. 252-255.

349. F. Boccuzzi, A. Chiorino, M. Manzoli, P. Lu, T. Akita, S. Ichikawa, and M. Haruta, *Au/TiO₂ Nanosized Samples: A Catalytic, TEM, and FTIR Study of the Effect of Calcination Temperature on the CO Oxidation.* Journal of Catalysis, 2001. 202(2): p. 256-267.

350. L.M. Molina, M.D. Rasmussen, and B. Hammer, *Adsorption of O₂ and oxidation of CO at Au nanoparticles supported by TiO₂(110).* The Journal of Chemical Physics, 2004. 120(16): p. 7673-7680.

351. Q. Fu, H. Saltsburg, and M. Flytzani-Stephanopoulos, *Active Nonmetallic Au and Pt Species on Ceria-Based Water-Gas Shift Catalysts.* Science, 2003. 301(5635): p. 935-938.

352. E.D. Park and J.S. Lee, *Effects of Pretreatment Conditions on CO Oxidation over Supported Au Catalysts.* Journal of Catalysis, 1999. 186(1): p. 1-11.